New peptide-type tripodal ligands and their metal complexes : synthesis, thermodynamic and structural study, application in catalytic function

Ágnes Dancs

UNIVERSITÉ DE LORRAINE
Laboratoire SRSMC UMR 7565
Ecole doctorale SESAMES

UNIVERSITY OF SZEGED
Department of Inorganic and Analytical Chemistry
Doctoral School of Chemistry

THESIS

Presented in order to obtain the title **Doctor in Chemistry** of

UNIVERSITE DE LORRAINE
and
UNIVERSITY OF SZEGED

by

Ágnes DANCS

NEW PEPTIDE-TYPE TRIPODAL LIGANDS AND THEIR METAL COMPLEXES: SYNTHESIS, THERMODYNAMIC AND STRUCTURAL STUDY, APPLICATION IN CATALYTIC FUNCTION

Defense expected on 13 December 2017

Supervisors:

Dr. Tamás GAJDA	Full professor University of Szeged, Hungary
Dr. Florence DUMARÇAY	Maitre de Conférences HDR Université de Lorraine, France
Dr. Katalin SELMECZI	Maitre de Conférences Université de Lorraine, France

Members of the examining board:

Reviewers:	Dr. Katalin VÁRNAGY	Full professor University of Debrecen, Hungary
	Dr. Marius RÉGLIER	Full professor Aix-Marseille Université, France
Examiners:	Dr. Dezső HORVÁTH	Full professor University of Szeged, Hungary
	Dr. Tamás SZABÓ	Assistant professor University of Szeged, Hungary
Supervisors:	Dr. Florence DUMARÇAY	Maitre de Conférences HDR Université de Lorraine, France
	Dr. Katalin SELMECZI	Maitre de Conférences Université de Lorraine, France

TABLE OF CONTENT

Table of content **1**

List of abbreviations **3**

1. Introduction **4**

1.1. Coordination chemistry of basic tripodal ligands 4
1.1.1. N-donor tripodal ligands 5
1.1.2. O-donor tripodal ligands 6
1.2. Tripodal ligands functionalized by peptide coupling 7
1.3. Histidine containing peptide ligands towards copper(II) and zinc(II) ions 8
1.3.1. The role of histidines in the peptide chain 9
1.3.2. The role of terminal histidines 11
1.4. Enzyme mimicking using metal complexes 12
1.4.1. General approaches 12
1.4.2. Catechol oxidation 13
1.4.3. Superoxide dismutation 16
1.4.4. Hydrolysis of phosphoesters 18

2. Aims **20**

3. Materials and methods **21**

3.1. Synthesis of the ligands 21
3.1.1. Synthesis of the N-terminal tris-His-ligand: tren3his (**L**^{1}) 21
3.1.2. Synthesis of the N-terminal asymmetric His-ligands: tren2his (**L**^{3}), tren1his (**L**^{4}) 21
3.1.3. Synthesis of the C-terminal tris-His-ligand: nta3his (**L**^{2}) 23
3.1.4. Syntheses attempted on solid phases: nta1his and nta1his-NH_2 24
3.2. Characterization techniques of solution equilibrium and structure 26
3.2.1. pH potentiometry 26
3.2.2. UV-visible (UV-Vis) spectroscopy 26
3.2.3. Circular dichroism (CD) spectroscopy 27
3.2.4. Electron Paramagnetic Resonance (EPR) spectroscopy 28
3.2.5. Nuclear Magnetic Resonance (NMR) spectroscopy 30
3.2.6. Mass Spectrometry (MS) 31
3.3. Kinetic experiments 32
3.3.1. Catechol oxidation measurements 33
3.3.2. Superoxide dismutase (SOD) measurements 34
3.3.3. Activated phosphoester hydrolytic measurements 35

4. Results and discussion **36**

4.1. Protonation and coordination properties of tren3his (**L**^{1}) 36
4.1.1. Protonation of tren3his 36
4.1.2. Copper(II) complexes of tren3his 38
4.1.3. Zinc(II) complexes of tren3his 45
4.2. Protonation and coordination properties of nta3his (**L**^{2}) 51
4.2.1. Protonation of nta3his 51
4.2.2. Copper(II) complexes of nta3his 53
4.2.3. Zinc(II) complexes of nta3his 59

4.3. Protonation and complex formation of nta1His-NH_2 62
4.3.1. Protonation of the ligands 62
4.3.2. Copper(II) and zinc(II) complexes of the ligand nta1his-NH_2 63
4.4. Protonation and coordination properties of tren2his (**L**^{3}) and tren1his (**L**^{4}) 65
4.4.1. Protonation of tren2his and tren1his 65
4.4.2. Copper(II) complexes of tren2his 67
4.4.3. Zinc(II) complexes of tren2his 72
4.4.4. Copper(II) complexes of tren1his 78
4.4.5. Zinc(II) complexes of tren1his 81
4.5. Assessment of the metal binding properties of tripodal peptides 84
4.6. Catechol oxidase mimicking with the metal-ligand complexes 87
4.6.1. Kinetic study of Cu(II)-**L**^{1}, -**L**^{2} and -**L**^{3} systems 87
4.6.2. Substrate binding study in Cu(II)-**L**^{1} 3:2, Cu(II)-**L**^{2} 2:1 and Cu(II)-**L**^{3} 2:1 systems 92
4.6.3. Peroxide, *o*-benzoquinone and radical formation in Cu(II)-**L**^{1} and -**L**^{2} systems. Mechanism of catecholase-like activities in the studied Cu(II)-**L** systems 95
4.6.4. Catechol oxidation: linear vs. tripodal peptide complexes 99
4.7. Superoxide dismutase (SOD) mimicking with the metal-ligand complexes 102

5. Summary 105

6. Összefoglalás 108

Résumé français 111

List of references 132

Acknowledgements 138

Appendix 139

LIST OF ABBREVIATIONS

Materials

Boc – *tert*-butyloxycarbonyl
Boc-His(Boc)-OH · DCHA – *N*-α-*N*-im-di-Boc-L-histidine dicyclohexylammonium salt
Boc_2O – di-*tert*-butyl dicarbonate
BNPP – *bis*(4-nitrophenyl) phosphate
CHES – *N*-cyclohexyl-2-aminoethanesulfonic acid
COx – catechol oxidase
DCC – dicyclohexyl carbodiimide
DCM – dichloromethane
DIPEA – *N,N*-diisopropylethylamine
DMF – *N,N*-dimethylformamide
DNPEP – 2,4-dinitrophenylethyl phosphate
DTBSQ – 3,5-di-*tert*-butyl benzosemiquinone
DTBQ – 3,5-di-*tert*-butyl-*o*-benzoquinone
EtOH – ethanol
Fmoc – 9-fluorenylmethyloxycarbonyl
HEPES – 4-(2-hydroxyethyl)-1-piperazineethanesulfonic acid
His – histidine
HOBt – *N*-hydroxybenzotriazole
HPNP – 2-hydroxypropyl-*p*-nitrophenyl phosphate
$H_2$4NP – 4-nitrocatechol
H_2DTBC – 3,5-di-*tert*-butylcatechol
MeCN – acetonitrile
MeOH – methanol
MES – 2-(*N*-morpholino)ethanesulfonic acid
NMP – *N*-methyl-2-pirrolidone
NBT – nitrotetrazolium Blue chloride
NPP – 4-nitrophenyl phosphate
NP – 4-nitrophenol
nta – nitrilotriacetic acid
SOD – superoxide dismutase
TEA – triethylamine
TFA – trifluoroacetic acid
TIS – triisopropylsilane
tren – *tris*(2-aminoethyl)amine
Trt – trityl

Methods

CD – Circular Dichroism
EPR – Electron Paramagnetic Resonance
ESI-MS – Electrospray Ionization Mass Spectrometry
HPLC – High Performance Liquid Chromatography
MALDI-TOF-MS – Matrix-Assisted Laser Desorption Ionization Time-of-Flight Mass Spectrometry
NMR – Nuclear Magnetic Resonance
SPPS – Solid Phase Peptide Synthesis
UV-Vis – Ultraviolet-Visible

1. INTRODUCTION

1.1. COORDINATION CHEMISTRY OF BASIC TRIPODAL LIGANDS

Tripodal ligands are specially structured molecules with three coordinating arms, containing several (usually at least three) donor groups. Due to their structural properties, they are extensively used in coordination chemistry as complexing agents for various transition metal ions. The key to their versatile applicability is the tripodal scaffold, which is able to organize the donor groups in space, leading to strong and controllable metal binding. Metal complexes of tripodal ligands usually possess elevated thermodynamic stability due to the forming fused chelate rings, which, depending on the denticity and symmetry of the ligand, may also help stabilize several coordination geometries. Targeted functionalization of the tripodal ligand allows the fine-tuning of metal binding, and also the development of additional functions, *e.g.* molecular recognition sites, secondary (allosteric) metal binding sites or substrate binding sites, etc.

For these reasons, metal complexes of tripodal ligands are targets of scientific interest in many fields, such as metal sensing [1], metalloenzyme modeling [2-4], stabilization of reactive species and intermediates [5, 6] or development of molecular motors [7]. Tripodal ligands have recently risen the attention of supramolecular chemistry, since they present exceptional tendency to self-assembly creating metallocages with colorful compositions [8], hydrogels [9] or other mesophase structures [10].

With respect to the structure of tripodal ligand complexes, the center of the tripod is of great importance: it can be either a coordinating, trivalent heteroatom itself (such as nitrogen, phosphorous or boron) or a functionalized central group (*e.g.* benzene or cyclohexane platforms). Rigid scaffolds as benzene tend to stabilize unusual geometries, while a tertiary amino center provides flexibility to the ligand, often resulting oligomerization. These features, of course, are also dependent on the quality of the donor groups and the metal ion, and the length of the tripodal arms.

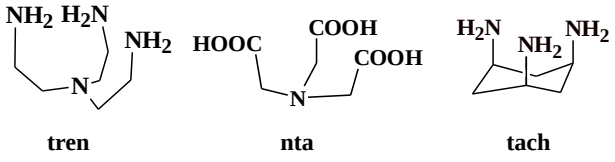

Figure 1.1. Examples for basic tripodal ligands: tren *(tris(2-aminoethyl)amine)*, nta *(nitrilotriacetic acid)* and tach *(1,3,5-triaminocyclohexane)*.

Figure 1.1. presents examples for some basic, extensively described and used tripodal ligands. The structure of the mentioned basic tripods, having one donor group per arm in a chelating position, normally allows tri- or tetradentate binding to a transition metal ion, and the free coordination sites can be occupied by solvent molecules or counter ions. With respect to geometry, the quality of the metal ion, the solvent and the flexibility of the ligand together determines coordination number and thus the structure of the complexes:

while rigid molecules like tach usually provide a relatively fixed, trigonal-based structure for metal ions, more flexible ligands like tren or nta may stabilize more than one type of geometry.

Tripodal ligands can be classified by many features: their symmetry (identical or different arms), the chemical property of the pendant donor groups (aromatic or aliphatic), the length of the arms, the type of the donor atoms, denticity, etc. Since a main aspect of this work is to compare the C- and N-terminally functionalized histidine-containing tripodal ligands, the N- and O-donor tripodal ligands are briefly reviewed below, focusing on the two most important target molecules, tren and nta, which were used as base tripodal scaffolds for the studied ligands.

1.1.1. N-donor tripodal ligands

Tripodal ligands containing N-donor atoms have enormous literature background, which denotes their high significance in coordination chemistry [11-14]. Being the most frequent donor group of biorelevant ligands, tripods with nitrogen donor functions are extensively researched in bioinorganic chemistry, thus their coordination properties towards copper(II), zinc(II) and iron(II/III) ions are studied in details.

The most widely investigated N-donor tripodal ligand is *tren*, *tris*(2-aminoethyl amine). It was first synthesized by *Eugen Ristenpart* in 1896, as trihydrochloride salt, in the reaction of 2-bromoethylphtalimide and ammonia, followed by deprotection with HCl [15]. Tren has four amino groups, of which the three primary amino nitrogen can be protonated between pH 2-11, therefore only those can be determined potentiometrically ($pK_{NH_3^+}$ = 8.43, 9.47 and 10.17 at 25 °C, in 0.1 M KCl) [11]. The low basicity of the tertiary amino nitrogen ($pK < 2$) is due to the relatively close proximity of the primal amino groups.

The aptitude of tren for chelating metal ions has been discovered soon after its first successful synthesis; metal complex formation in presence of tren has been studied within various conditions ever since. Most of its 3d metal complexes have been characterized in solution and solid phase as well. Metal coordination by tren results in thermodynamically favored, 5-membered, fused chelate ring system, which prevents classical four-coordination (tetrahedral, square planar) geometries, and causes the formation of distorted five-coordinate complexes instead (Figure 1.2). The scale of this distortion is described by the τ value ($0 < \tau < 1$), where the two extrema correspond to the symmetric trigonal bipyramidal ($\tau = 1$) and the symmetric square pyramidal ($\tau = 0$) geometries [16]. In most of the cases, the central donor atom occupies the apical position, and the fifth coordination site is taken by a rapidly exchanging ligand such as water molecule or background/counter ion.

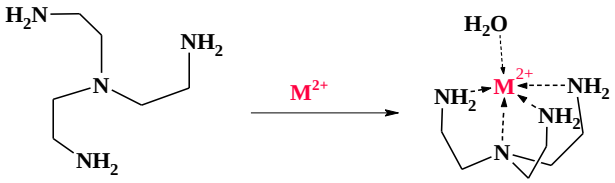

Figure 1.2. Metal complex formation of tren in aqueous media.

In presence of certain metals (*e.g.* Co(III) ions) and/or co-ligands, tren may form octahedral complexes in a $[M(tren)(X)(Y)]^{n+}$ manner, in which case two stereoisomers can be distinguished, *p*- and *t*-isomers, often having very different physicochemical properties. In case of asymmetric tripods (bearing arms with different length), this isomerism can become more complex, depending on the position of the longer/shorter arm with respect to the X and Y ligands. 4d and 5d metal complexes of tren are of lesser significance as compared to 3d metal complexes, reflecting their strong preference for square planar geometries, which is disfavored by tren. Therefore, hypodentate coordination is not rare in such 4d/5d metal-tren complexes [11].

Tren forms the most stable ML-type metal complexes among tripodal tetramine ligands, due to the optimal size of chelate rings (5-membered) around the metal ion. Tripods with longer arms result in less favorable chelate systems, therefore substitution of aminoethylamine arm(s) with aminopropylamine moieties causes a gradual decrease in stability. Copper(II) complexes of the 3-aminopropyl-*bis*(2-aminoethyl)amine (baep), 2-aminoethyl-*bis*(3-aminopropyl)amine (abap) and *tris*(3-aminopropyl)amine (trpn) ligand series convincingly represent this tendency: $\log K_{Cu(tren)}$ (= 18.5) > $\log K_{Cu(baep)}$ (= 16.55 [17]) > $\log K_{Cu(abap)}$ (= 15.98 [18]) > $\log K_{Cu(trpn)}$ (= 13.117 [19]).

1.1.2. O-donor tripodal ligands

Tripods bearing oxygen donor groups are not as profoundly studied as the N-donor counterparts. Oxygen containing functional groups are mostly present as carboxylic or hydroxyl groups, beside additional nitrogen functions in many cases.

The most important representative of O-donor tripodal ligands is the nitrilotriacetic acid, generally abbreviated as *nta*. Nta was synthesized from ammonia and chloroacetic acid in 1862 by *Heintz* [20], but its strong metal sequestering properties were not discovered until the 20th century. Nta possesses four (de)protonable functional groups, yet only three can be determined in aqueous solutions: pK_1 = 1.65, pK_2 = 2.94 and pK_3 = 10.33 at 20°C [21], of which the first two corresponds to the carboxylic moieties, while the last p*K* is the result of the increased basicity of the tertiary nitrogen, most probably due to intramolecular hydrogen bonding between the N_{tert}-H and a deprotonated carboxylic O.

Similarly to tren, nta binds most metal ions in a tetradentate way, resulting highly stable mononuclear complexes (see Table 1.1). In case of most metal ions, the great stability of the complexes does not allow direct potentiometric determination, another competitor ligand (*e.g.* tren) must be used to reach full decomplexation of nta. Table 1.1. exhibits a comparison in stability constants of ML complexes of tren, nta and EDTA.

Table 1.1. Stability constants of ML complexes of tren [11], nta [22] and EDTA [23] at I = 0.1 M, T = 25 °C or 20 °C*.

M(II)	logK_{ML} / L = tren	logK_{ML} / L = nta	logK_{ML} / L = EDTA
Cu(II)	18.5	12.96*	18.86*
Zn(II)	14.5	10.66*	16.68*
Mn(II)	5.77	7.44*	13.95*
Fe(II)	8.8	8.83*	14.33*
Fe(III)		16.26*	25.1*
Co(II)	12.69	10.4*	16.49*
Co(III)			41.5
Ni(II)	14.6	11.54*	18.52

The geometry preference of nta is interestingly much less straightforward than that of tren. For example, as described earlier, tren forms 5-coordinate $[M(tren)(H_2O)]^{n+}$ complexes with 3d transition metal ions, while nta-metal complexes are usually thought of as octahedral species, in a $[M(nta)(H_2O)_2]^{n+}$ manner. In the last fifteen years, however, experimental and theoretical studies revealed that the second water molecule is coordinatively weakly bound. This also goes for other $[M(nta)L_2]^{n+}$ complexes; they easily lose a monodentate L ligand to result the five-coordinate, trigonal bipyramidal complex [24]. However, this process is highly dependent on the nature of the co-ligand; bidentate ligands or steric hindrances (*e.g.* immobilization in IMAC chromatography) suppress its significance.

1.2. TRIPODAL LIGANDS FUNCTIONALIZED BY PEPTIDE COUPLING

Although functionalized tripodal ligands and their metal complexes are extensively studied for various goals, only a relatively small group of these products contains amide or peptide functions. This might be partly due to the inevitable technical difficulties regarding the synthesis of these compounds: the peptide coupling has to take place in solution phase (except for a few special solid-phase techniques [25, 26]), in presence of at least one co-agent (coupling agent), therefore further purification step(s) are required. Peptide-type ligands are often not easy to handle in solid state due to *e.g.* hygroscopic properties even as salts; furthermore, tripodal peptides, especially on benzene or cyclohexane-type platforms and/or bearing aliphatic side chains have been shown to act as hydrogels [9]. The few examples of peptide-type tripods, however, generally present some interesting properties of biological/biomimetic relevance, proving the worth of this direction in bioinorganic research – despite all preparation-related hardship.

The advantages of peptide-type tripodal ligands in coordination chemistry have been recognized in the last decades: they proved to be useful in *e.g.* the development of allosteric binding cavities in supramolecular assemblies [27], targeted metal chelation [28],

structural or functional enzyme modeling [25, 29], and catalytic applications [30]. *Herr* and co-workers reported equilibrium and structural study on zinc(II) complexes of two histidine containing tripodal peptides ($N(BzGly*ValHisOMe)_3$ and $N(BzGly*ValHisSerOMe)_3$); both were found to be structural mimics of the active center of carbonic anhydrase enzyme [31]. *Ichikawa's* research group synthesized a tren-based tripodal ligand containing benzyl-protected histidyl moieties, and described the complex formation properties in presence of Zn(II) ions. Beside the imidazole-coordinated complexes, they found evidence of 'extra' deprotonated species above pH 7, which was attributed to mixed hydroxo complexes, and was found to possess considerable hydrolytic activity towards activated phosphoester substrates such as BNPP and TNPP (*bis* and *tris*(4-nitrophenyl) phosphate) [32]. Later on, the C-terminal analog of this ligand has been prepared as well, but despite the presence of a OH^--containing 'extra' deprotonated species above pH 6, hydrolytic activity was not detected in this ligand system [30].

In the last decade *Delangle's* research group studied several cysteine containing ligands on, among others, tripodal platforms such as nitrilotriacetic acid (nta), in order to create efficient chelators for Cu(I) and other soft-type (potentially toxic) metal ions [28, 33-36]. *Vahrenkamp et al.* also studied histidine and cysteine containing tripods with benzene-1,3,5-carboxylic acid and *tris*(carboxyethyl)-nitromethane platforms; the zinc(II) complexes of these compounds showed high tendency towards oligo- and polymerization [29].

Some copper(II) complexes can also be found in the literature of peptide-type tripodal ligands: *Albada* and co-workers were able to build a structural model of type-3 copper(II) binding sites using a triazacyclophane (TAC) scaffold functionalized by histidine amino acids: oxygen uptake and reactivity of the oxygenated intermediate have also been shown in H_2DTBC oxidation [25]. Branched peptides investigated by *Szyrwiel* and colleagues can be considered as close relatives of tripodal peptides; they – especially the trihistidyl compound 3H – were shown to possess remarkable binding affinity towards Cu(II) ions [37, 38]. They also described a Asp-functionalized ligand, which forms catalytically active copper(II) complexes for electrocatalytic water oxidation [39]. As example for non-histidyl compounds, a tren-based alanine ligand has been synthesized by *Mohamadou et al.*, and characterized in presence of Cu(II) and Ni(II) ions. Interestingly, formation of dinuclear copper(II) complexes has been detected at metal excess, which, beside UV-Vis and EPR analyses, was also confirmed by ESI-MS results [40].

1.3. HISTIDINE CONTAINING PEPTIDE LIGANDS TOWARDS COPPER(II) AND ZINC(II) IONS

Histidine plays an essential role in the mechanism of the majority of native enzymes and metalloproteins, participating in *e.g.* proton transfer, metal or substrate binding. The key to its utmost importance in biological systems is the imidazole side chain, which possesses a highly basic (pyrrolic) N1 nitrogen, and an easily protonable N3 (pyridinic)

nitrogen. The deprotonation constant of the conjugate acidic form of histidine is p*K* ~ 6, which provides an ideal acid-base catalytic site in peptides and proteins, meanwhile transition metal ions can easily exchange the N3-H proton, providing a strong metal-ligand interaction in the physiological pH range. Metal binding of His residues is further improved when occupying a terminal position, although this binding mode has lower importance in native proteins. Occasionally, the imidazole group can act as a bidentate ligand, serving as a bridge between two metal ions, as *e.g.* in the active center of Cu,Zn-superoxide dismutase (Cu,Zn-SOD) enzymes. In summary, the presence of histidine(s) in a peptide sequence not only alters but usually determines the metal binding properties.

1.3.1. The role of histidines in the peptide chain

The imidazole group of histidine amino acid inside the peptide chain enables metal binding at relatively low pH, depending on the nature of the metal ion. Coordination properties of imidazole-coordinated complexes are highly dependent on many factors [41]: for example, the number and position of the histidyl moieties in the peptide, the presence of other potentially coordinative side chains such as carboxylic groups (Asp, Glu), thiol groups (Cys), or the presence of free termini. If the peptide contains separated His amino acids in the sequence (proximity in the chain > 3 amino acids), the simultaneously coordinating N_{im} groups allow the formation of macrochelate structures in the acidic-neutral pH range, as it is frequently observed for large natural peptide fragments as well, including prions or amyloid-β peptides [42].

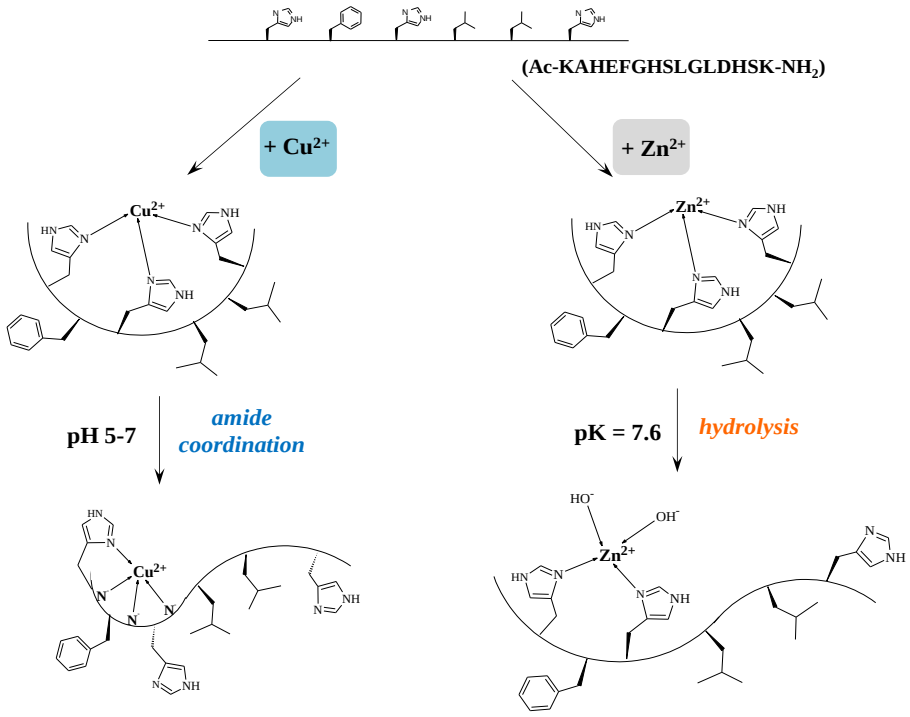

Figure 1.3. Examples for destabilization of multiimidazole-metal complexes (from previous work in our laboratory [43]).

With increasing pH, the multiimidazole environment competes less and less with (1) the metal-induced deprotonation of the backbone amide nitrogens, or (2) the (partial) hydrolysis of the metal ion (Figure 1.3). The former process occurs mostly in metal complexes prone to form square planar geometries, such as Ni(II), Cu(II) and several 4d and 5d metals. Histidine can facilitate the amide coordination to the metal center by acting as anchoring group: a coordinating imidazole N3 atom forms highly stable six-membered chelate ring with a neighboring amide N^- towards the N-terminus. The coordination of the next amide nitrogen occurs co-operatively in almost all cases, creating a new five-membered chelate ring. In this fashion, two or three amide nitrogens can be present in the coordination sphere of the metal ion beside the anchoring group. Without another characteristic driving force of coordination, this process takes place already below neutral pH for most copper(II)-oligopeptide complexes, around pH 8 for Ni(II) complexes and at extremely acidic pH for palladium(II) complexes [42]. Another result of N^- coordination in peptides containing separated histidines is the formation of multinuclear species, since each His provides an individual $\{N_{im},xN^-\}$ type binding site.

Hydrolysis of the metal ion, *i.e.* the deprotonation of coordinated water molecule(s), occurs in peptide complexes where amide nitrogen coordination is not an option. Unsaturated coordination sphere generally facilitates the process, but in many cases, such as in Zn(II) or Fe(III) complexes, hydroxide molecules are able to force out donor groups from the coordination sphere, or trigger oligomerization, resulting insoluble mixed hydroxo oligomer formation. In absence of additional stabilization, precipitation is usually observed at mildly basic pH [41].

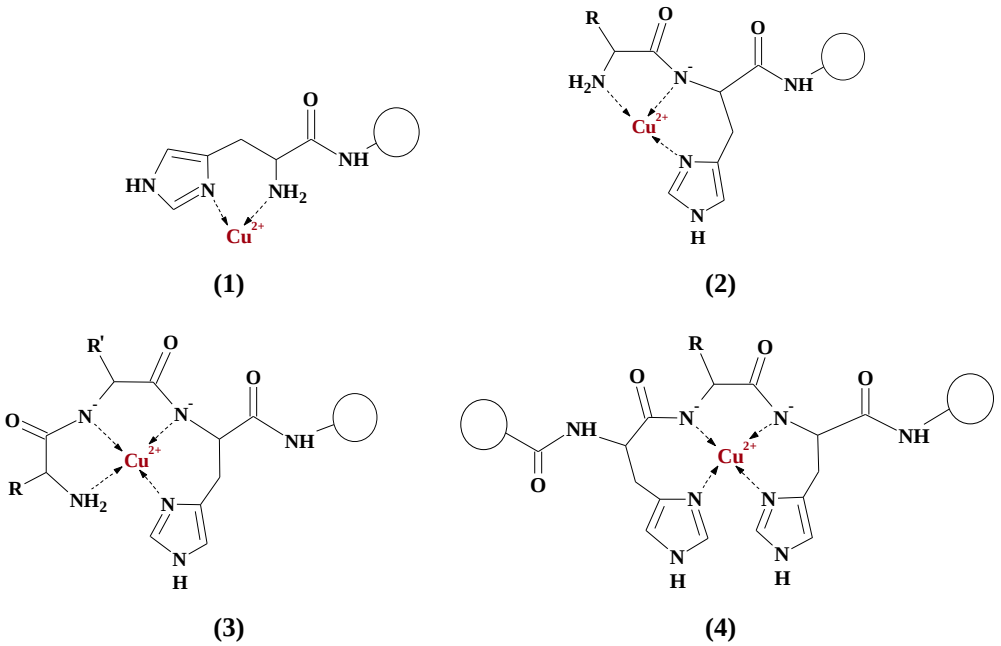

Figure 1.4. Structure of copper(II) complexes in presence of (1) terminal His, (2) NH_2-X-His, (3) NH_2-X-X-His and (4) His-X-His type sequences.

The stability of His-containing peptide complexes are generally increased if His occupies special position(s) in the peptide chain: terminal His, NH_2-X-His, NH_2-X-X-His

and alternating $H(XH)_n$ type sequences provide elevated stability for their metal complexes compared to terminally protected, separate His-containing peptide species [41]. Figure 1.4. depicts the dominant binding modes in these peptide sequences for Cu^{2+} ions. Peptides containing such structural motifs often serve as target ligands in biomimetic studies.

1.3.2. The role of terminal histidines

Terminally unprotected peptides generally form complexes with relatively high thermodynamic stability, since $-NH_2$ and $-COO^-$ functions can behave as anchoring group in metal binding. Histidine in the terminal positions, especially located at the N-terminus, further enhances the observed complex stabilities. While C-terminal histidine mainly facilitates amide deprotonation, a N-terminal imidazole forms highly stable six-membered chelate ring with the terminal $-NH_2$ group, creating a *histamine-type binding* mode (Figure 1.4, structure (1)), which dominates in a very wide pH range. The monocopper(II) complex of the simplest N-terminal His-peptide, His-Gly, is dominant between pH 3.7 and 6, while at ligand excess the *bis*-histamine-type CuL_2 complex (Figure 1.5, left) does not deprotonate until pH ~ 10.5 [44]. Both analogous Zn(II) complexes form predominantly until basic pH, however their logβ values ($\log\beta_{ZnL}$ = 5.07, $\log\beta_{ZnL_2}$ = 9.54 [45]) are significantly lower than that of the copper(II) complexes (8.85 and 15.06, respectively). It is worth mentioning that, even though Zn(II) supports the symmetrical octahedral geometry, *tris*-histamine-type complexes in Zn(II)-His-Gly system are not produced at any metal-to-ligand ratio.

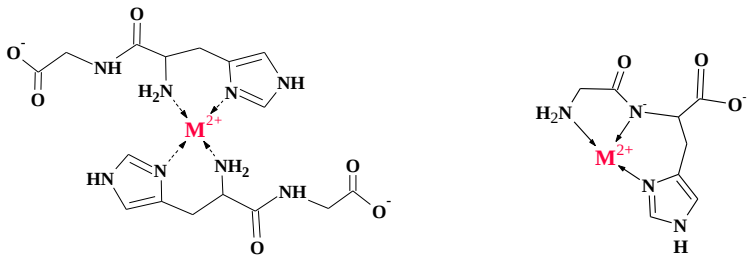

Figure 1.5. Dominant binding modes in terminal His-peptide complexes: CuL_2 (left) and $CuH_{-1}L$ (right) complexes of His-Gly and Gly-His peptides, respectively (coordinating water molecules omitted).

The smallest model of the C-terminal His containing peptides, namely the Gly-His ligand, also presents a characteristic metal binding ability (Figure 1.5. right). Due to the formation of a (5,6)-membered fused chelate ring system, the deprotonation constant of the C-terminal amide group decreases significantly:

$$CuL \rightarrow CuH_{-1}L + H^+ \qquad pK = 3.39 \text{ [44]}$$
$$ZnL \rightarrow ZnH_{-1}L + H^+ \qquad pK = 6.73 \text{ [45]}.$$

In fact, this is one of the very few cases when Zn^{2+} ions are capable of promoting the deprotonation of amide nitrogens in peptides; aside of Gly-His, zinc(II) complexes of Ala-His and βAla-His also present similar coordination behavior [46].

1.4. ENZYME MIMICKING USING METAL COMPLEXES

A very relevant direction of modern bioinorganic research is the design of low-molecular models of metalloenzymes and -proteins. Native enzymes are the most efficient catalysts, accelerating biochemical reactions by several thousand times. This catalytic performance, along with their remarkable selectivity, has become highly desirable with the rapid development of biochemical industry. The usage of native enzymes in biochemical production, however, poses several difficulties: they are expensive, their structure is highly sensitive to the reaction conditions (pH, *T*, concentration of substrate(s), co-agents, product(s), *etc.*) causing eventual degradation, and their recovery is also problematic. Therefore, there is a constant need for the development of enzyme alternatives possessing similar (or at least sufficient) catalytic properties, more robustness, less expensive procurement; but they should also be environmentally friendly, and preferably recyclable.

The key to the tremendous efficiency of enzymes is their well-defined three dimensional structure, perfected by millions of years of evolution, in order to function in a very specific environment in living organisms. If we drastically change this environment, the tertiary structure might get damaged, leading to the loss of catalytic activity. The utmost challenge of enzyme mimicking is to substitute the great and sensitive polypeptide structure with a simpler, robust organic ligand, which can provide similar coordination environment to the active center of the metalloenzyme. It is clear that there is no general solution for this problem; each different enzyme family requires different metals, ligands, environment, etc., targeting a specific substrate molecule (or molecule family). As consequence, research of such enzyme mimetic ligand-metal complexes will probably not lose relevance for a long time.

1.4.1. General approaches

There are two distinctively different directions of metalloenzyme modeling, namely the structural and the functional enzyme model design. Model compounds are much easier to study than the whole native enzyme, and they can help gaining a better understanding over the structure-catalytic activity relationship. In structural enzyme modeling the main goal is to build molecular structures similar to the active site of the selected metalloenzyme, which can provide important spectroscopic and structural data relevant to the native active site. This can be achieved through *e.g.* comparison of smaller and larger peptide sequences responsible for metal binding, with respect to metal-ligand interactions or catalytic activity.

Functional enzyme models target most importantly the catalytic performance and its mechanism, not necessarily aiming for the active center-like structure. However, structural models often provide inspiration for functional enzyme model design, and the best enzyme mimetic complexes are engineered based on similarities to the active sites in *e.g.* substrate recognition, substrate activation or metal-metal interaction.

Structurally enhanced peptide compounds can serve as ‘in-between’ examples as enzyme models. Due to the amino acidic functions, the donor groups are identical to that of

the metalloenzyme center, and other functional groups can facilitate substrate binding or acid/base catalysis, similarly to the native enzyme. Unlike linear peptide fragments, their structure is organized by a non-peptide-type scaffold, which may provide the rigidity necessary for a well-defined metal binding site. These structurally improved peptide derivatives can retain hydrolysis of the metal or the loss of the physiologically relevant binding mode, which are often the main sources of catalytic inefficiency in linear peptide-metal systems.

The literature can serve with countless examples on enzyme mimicking complexes. With respect to this work, three catalytic processes are presented below: oxidation of catechol, dismutation of superoxide radical anion and hydrolysis of activated phosphoesters.

1.4.2. Catechol oxidation

Catechol oxidases (COx) are monomeric enzymes with ~40 kDa molar mass. They contain a type-3 copper center with a Cu(II)-Cu(II) distance of approximately 2.9 Å in the native *met* form. Catechol oxidase enzyme was isolated by *Krebs* and co-workers in 1998 from sweet potato *(Ipomoea batatas)* [47], and its structural and catalytic analyses have been carried out.

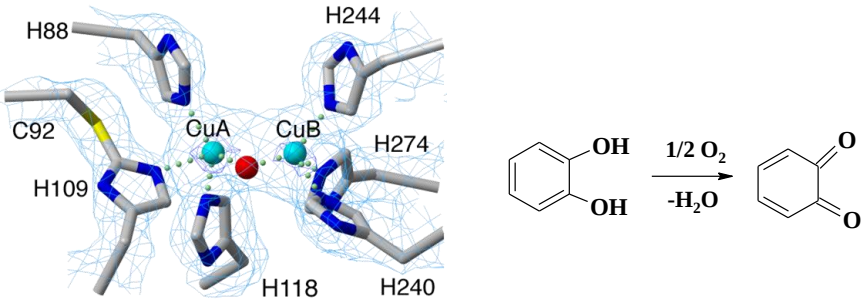

Figure 1.6. Left: *Met* form of the active center of catechol oxidase (COx) isolated from sweet potato *(Ipomoea batatas)* [48]; right: the reaction catalyzed by COx.

COx enzyme catalyzes the oxidation of *ortho*-diphenolic (catechol) compounds to the corresponding *ortho*-benzoquinones (Figure 1.6). The mechanism of the oxidation pathway was proposed by *Eicken, Krebs* and *Sacchettini* [49] (see Appendix A.1). During the catalytic cycle two substrate molecules are converted; one dioxygen molecule is consumed while two *o*-benzoquinone and two water molecules are released. Both copper(II) centers in the *met* form are surrounded by three His imidazole N atoms, along with a μ-hydroxo bridge between the two metal ions, altogether forming trigonal pyramidal coordination sphere per Cu(II). The bridging OH^- group conducts a strong antiferromagnetic interaction between the copper centers, hence, the *met* form is EPR silent. After the oxidation of one substrate molecule, the *deoxy* state of the enzyme is formed with two Cu(I): their distance is significantly increased (~4 Å), one copper is in square planar geometry with an empty coordination site, the other remains in a distorted trigonal pyramidal structure with an

additional water molecule. According to the suggested mechanism, oxygen uptake occurs through the formation of a peroxo μ-η^2:η^2 intermediate, resulting the *oxy* form (Cu(II)-Cu(II) distance: 3.8 Å), which binds the second substrate molecule as well (Appendix A.1). Intramolecular electron transfer from the catechol to the peroxo-bridge results in the formation of the product and water, and the hydroxo-bridged oxidized form of the enzyme is recovered. The above described coordination modes of the copper centers and the fashion of the oxygen uptake is well preserved among other type-3 copper cores, as it was found in hemocyanin (Hc) or tyrosinase (Tyr) [50]. The conformation of the active center is only weakly influenced by the oxidation state of the metal ions, which emphasizes the importance of the robust, fixed three dimensional structure at the active site.

Catechol oxidation is an extensively used test reaction in enzyme mimicking studies, thus it has a large literature background. An often applied model substrate for catechol oxidase mimicking is the 3,5-di-*tert*-butylcatechol (H_2DTBC), which is selectively oxidized to 3,5-di-*tert*-butyl-*o*-benzoquinone in presence of oxygen and copper(II) containing catalysts, without the cleavage of the aromatic ring. Such enzyme mimicking studies have been summarized in several review articles [51-54], presenting catalytic performance of mono- and multicopper(II) species, mechanistic considerations and substrate binding studies. Based on these informations, a few general observations can be established regarding catechol oxidase mimicking:

(1) Unlike the native enzyme, catechol oxidizing model complexes mostly release H_2O_2 side-product instead of water, carrying out two electron reduction of dioxygen. There are a few examples where water formation is proposed [55, 56] based on insufficient amount of H_2O_2 formation detected; however, this finding can also be due to H_2O_2 consumption along the catalytic oxidation, which indeed has been proven in some cases [56-58].

(2) The most active complexes were found among dinuclear copper(II) complexes, indicating that the close proximity of two copper centers is a necessity for highly efficient COx activity; however, numerous mononuclear copper(II) complexes also exhibit (lesser, but notable) catechol oxidase activity [54, 59-65].

(3) Anaerobic and aerobic substrate or substrate analog binding measurements revealed that binuclear complexes generally perform catechol oxidation through co-operation of metal centers (except binuclear complexes with distant copper(II) centers [56]) involving the formation of a μ-peroxo dicopper(II) intermediate, similarly to the native enzyme [57, 66-73]. Monocopper complexes, however, exhibit one electron oxidation of the substrate through the formation of a Cu(I)-semiquinonato adduct. This adduct reacts with O_2 leading to benzoquinone production.

(4) According to the one-electronic mechanistic pathway involving the formation of a semiquinone-type adduct, catalytic oxidation of catechol is also possible in absence of redox active metal ions: several zinc(II) complexes were found to show catechol oxidase-like activity [74-78], often in case of redox non-innocent (*e.g.* Schiff-base) ligand systems.

Copper(II) containing COx model systems have been summarized recently [54]. According to the Michaelis-Menten enzyme kinetic model, k_{cat} (s^{-1}) and K_M (M) parameters

represent the rate of product formation from the catalyst-substrate adduct and the stability of the latter adduct, respectively. Catalytic performance of enzyme mimics is often demonstrated by the k_{cat}/K_M ratio, conveniently representing the overall effectiveness of the catalyst. The most powerful catalyst to date has been synthesized by *Das* and co-workers [71], based on a Schiff-base ligand (see Figure 1.7. (a)); report on H_2DTBC oxidase activity has been supplemented by substrate binding measurements. The k_{cat}/K_M value for the above-mentioned complex is 3913 $M^{-1}s^{-1}$, which is still two orders of magnitude lower than the value calculated for the native COx enzyme isolated from sweet potato [47]. Several other compounds exhibit outstanding catalytic activities in presence of copper(II); mostly symmetrical, N-donor ligands, and all of them provides the formation of dinuclear, μ-bridged copper(II) complexes (some important examples are presented in Figure 1.7).

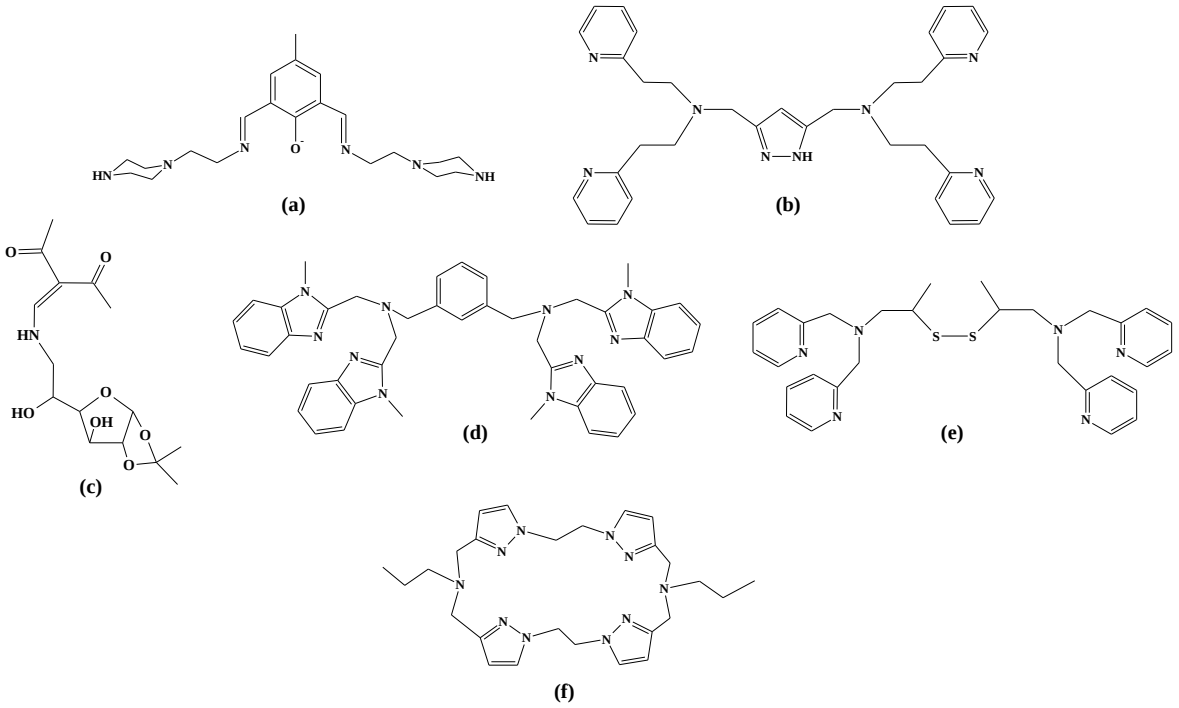

Figure 1.7. Structures of ligand precursors of some highly active catecholase mimicking model complexes. Redrawn after (a) Das [71], (b) Meyer [67], (c) Klemm [69], (d) Casella [79], (e) Bouwman [68], (f) Reedijk [56] and co-workers.

Although these catecholase mimics are excellent functional models of the native catechol oxidase, there is hardly any resemblance in the nature of donor groups to the enzyme itself. In order to gain better understanding on the enzymatic reaction, and to design more high-performance catalysts in the future, catecholase mimicking capabilities of peptide-type ligand-metal complexes ought to be investigated.

Not many peptide-metal complexes have been studied so far for that purpose. Kinetic characterization of the copper(II)-Ac-His-His-Gly-His-OH tetrapeptide system has been carried out previously in our laboratory [65] using H_2DTBC substrate; this study revealed that the $\{3N_{im},OH^-\}$ coordinated $CuH_{-1}L$ complex acts as efficient COx mimic in 86 wt% methanol-water medium (k_{cat} = 0.063 s^{-1}). Another investigated system is the

copper(II)-Ac-His-Pro-His-His-NH_2; similarly, the 'extra' deprotonated $CuH_{-1}L$ was assigned as the catalytically active complex, with a relatively high k_{cat} = 0.12 s^{-1}, and with K_M = 3.5 mM, implying moderate substrate binding. A few other peptide-copper(II) complexes were also shown to possess catalytic activity in oxidation of H_2DTBC or catechol substrates [58, 80, 81], showing moderate k_{cat}/K_M values.

Aside of these separate examples, there are no comparative investigations or mechanistic arguments on the catecholase mimicking properties of copper(II)-peptide complexes in the literature. Therefore, their role and function as catechol oxidase mimics is to be further explored.

1.4.3. Superoxide dismutation

Superoxide dismutase (SOD) enzymes catalyze the disproportion of superoxide radical anion ($O_2^{\bullet-}$) forming upon monovalent reduction of dioxygen. Cu,Zn-SOD is a homodimeric enzyme of 2×16 kDa present in eukaryotic organisms. Both domains contain a copper and a zinc ion in the active site, which are linked via a μ-imidazolato bridge ligand in the oxidized form. The remaining coordination sites of copper are occupied by three histidine side chains forming a distorted five-coordination geometry with a free coordination site, while the zinc(II) is surrounded by two imidazole rings and an aspartic -COO^- group in a tetrahedral structure (Figure 1.8).

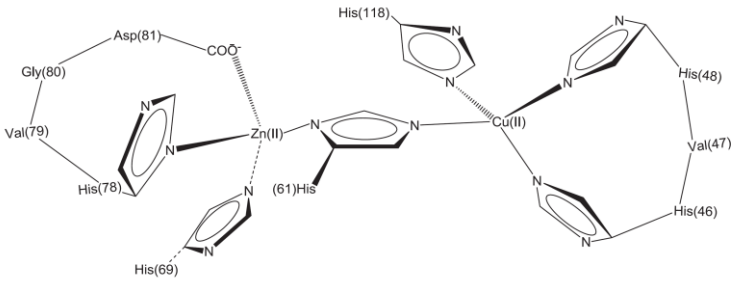

Figure 1.8. Schematic structure of the active center of Cu,Zn-SOD enzyme. Redrawn after Várnagy and co-workers [82].

Superoxide radical is bound by the Cu(II) in the active site; superoxide decomposition is achieved by the reaction with both the oxidized and reduced copper center as following:

$$Zn(Im^-)Cu(II) + O_2^{\bullet-} \rightarrow Zn(Im^-)Cu(I) + O_2$$
$$Zn(Im^-)Cu(I) + H^+ \rightarrow Zn(ImH) + Cu(I)$$
$$Cu(I) + O_2^{\bullet-} \rightarrow Cu(II)–O_2^{2-}$$
$$Cu(II)–O_2^{2-} + H^+ + Zn(ImH) \rightarrow Zn(Im^-)Cu(II) + H_2O_2$$

The reaction rate is tremendously high ($k = 2\times10^9$ $M^{-1}s^{-1}$), near the verge of diffusion limit, allowing Cu,Zn-SOD to protect the living cells from oxidative stress and uncontrolled mutations.

Superoxide dismutation is a frequently targeted subject in biochemical studies. The rate of the reaction is usually measured indirectly due to the high reactivity of $O_2^{\bullet -}$. One of the most often used test reaction for SOD activity determination is a modified version of the McCord-Fridovich method [83]: superoxide radicals are produced *in situ* by the xanthine-xanthine oxidase system, and they subsequently react with the chromophoric nitrotetrazolium Blue choride (NBT), causing an increasing absorption band at 560 nm. Compounds with SOD activity inhibit this reaction by abstracting the superoxide reactant, therefore SOD performance of a complex can be given as IC_{50} value (concentration of the complex where inhibition of the reaction NBT $\rightarrow$ NBT-diformazan is 50%). When comparing systems studied under different concentration conditions, SOD activity may be expressed as k, calculated as $k_{NBT} \times [NBT]/IC_{50}$ [84], in order to obtain [NBT]-independent parameters. The scheme of the NBT model reaction is depicted on Figure 1.9.

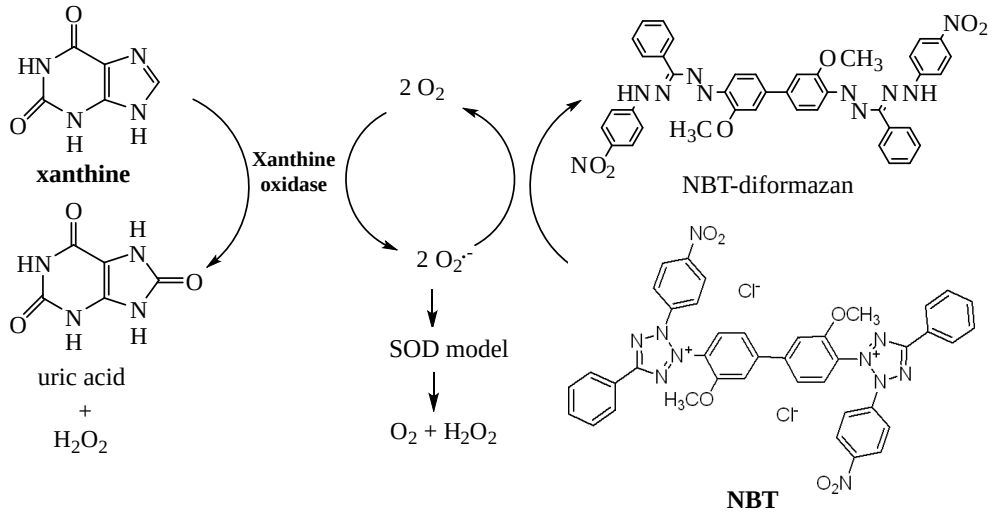

Figure 1.9. The model reaction used for SOD activity determination.

A huge variety of metal complexes has been investigated as antioxidants, including copper(II)-peptide SOD models. Table 1.2. presents IC_{50} and k values of some investigated copper(II)-peptide complexes, along with that of free Cu^{2+} (in phosphate buffer), and the native Cu,Zn-SOD as comparison.

Table 1.2. Superoxide dismutase activity of some copper(II)-ligand complexes.

Cu(II)-ligand systems	IC_{50} (μM)	references	k ($M^{-1}s^{-1}$)
Cu,Zn-SOD (pH 6.8)	0.0045	[65]	3.3×10^{8}
Cu(II)–Ac-HSarHSarHSarH-NH_2 1:1 (pH 7.4)	0.0442	[82]	3.4×10^{7}
Cu(II)–His-BIMA 3:2 (pH 7.4)	0.070	[85]	2.1×10^{7}
Cu(II)–Ac-HGHG-OH 1:1 (pH 7.4)	0.083	[86]	3.6×10^{7}
Cu(II)–HAHPH-NH_2 1:1 (pH 6.8)	0.0841	[82]	1.8×10^{7}
Cu(II)–apz-pn 1:1 (pH 7.4)	0.0902	[87]	[NBT] not reported
Cu(II)–HADHDHKK-NH_2 1:1 (pH 7.0)	0.11	[88]	1.4×10^{7}
Cu(II)–Ac-$(PHGGGWGQ)_4$-NH_2 1:1 (pH 6.6)	0.12	[89]	1.3×10^{7}
Cu(II)–Ac-HHGH-OH; 1:1 (pH 7.5)	0.15	[65]	1.0×10^{7}
Cu(II)–HGDHMHNHDTK-OH 1:1 (pH 7.0)	0.19	[90]	7.9×10^{6}
Cu(II)–Ac-HVH-NH_2; 1:1 (pH 7.4)	0.20	[91]	7.5×10^{6}
Cu(II)– HGHG-OH 1:1 (pH 7.4)	0.67	[86]	4.5×10^{6}
Cu(HPO_4) (pH 7.4)	1.06	[91]	6.2×10^{6}

It appears that copper(II) complexes of histidine-containing peptides perform superoxide dismutation in a very effective manner; some of them can be considered as good structural models of the native enzyme, too. As it was mentioned before, the real challenge in the design of structural SOD models with peptides is the suppression of early amide nitrogen coordination. This was successfully achieved by *Várnagy* and co-workers, using sarcosine (N-methylglycine) in alternating positions with histidines; the CuL complex of $\{3N_{im}\}$ coordination forms in practically 100% at pH 7.4. The SOD activity of this species is only one order of magnitude lower than that of the native Cu,Zn-SOD [82].

1.4.4. Hydrolysis of phosphoesters

Hydrolase mimicking complexes are able to increase the rate of hydrolysis in activated phosphoesters by (1) providing the nucleophilic OH^- group at relatively low pH, (2) by binding and activating the substrate, making it more vulnerable to nucleophilic attack and (3) destabilizing the binding of the product, forcing it to dissociate from the active site. Beside electronic effects, the orientation of the substrate by the metal center is also important: steric preferences can result advantageous specificity/selectivity for the catalytic complex.

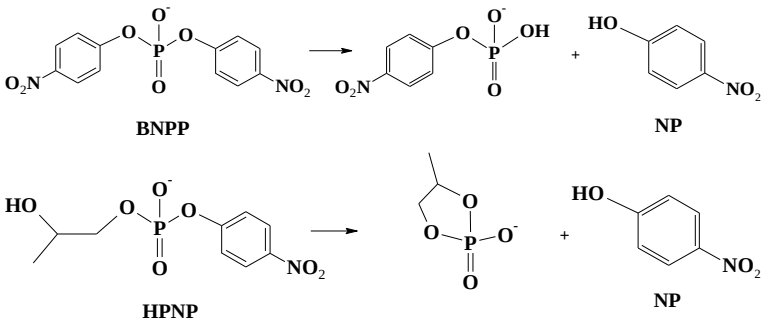

Figure 1.10. Hydrolysis of DNA and RNA model compounds (BNPP: *bis*(4-nitrophenyl) phosphate, HPNP: 2-hydroxypropyl-*p*-nitrophenyl phosphate, NP: *p*-nitrophenol).

Phosphoester hydrolysis is frequently targeted as subject of catalytic studies (Figure 1.10), since the reaction can be considered as a model for RNA or DNA cleavage. The most commonly studied activated phosphoester substrates are the minimalist DNA models *bis*(4-nitrophenyl) phosphate (BNPP) and 4-nitrophenyl phosphate (NPP), and 2-hydroxypropyl-*p*-nitrophenyl phosphate (HPNP) as a simplified model of RNA.

Many copper(II) and zinc(II) complexes are reported as efficient catalysts in phosphoester hydrolysis, along with lanthanide species. Dinuclear complexes might be especially adequate as hydrolase mimics, due to the dual activation of the substrate by the dinuclear core: μ-hydroxo/alkoxo species are often found to be excellent candidates [92-95]. Mononuclear complexes can also exhibit hydrolase function; in this case, coordinated OH^- group(s) or free coordination site(s) facilitate substrate binding and activation.

2. AIMS

The overall goal of this work was to design, synthesize and characterize new tripodal peptide-type ligands and their complexes with biologically relevant transition metal ions. With the combination of the structuring effect of tripodal scaffolds and the advantageous coordination properties of histidine, a new class of ligands can be obtained with advanced metal binding capabilities, suitable for potential catalytic applications. The main points of interest arisen within the scope of this thesis can be categorized as following:

(1) We wished to confirm that tripodal platforms are capable of improving metal binding of peptides, peptide-type ligands, as expected. Tripodal ligands provide exceptional stability for their metal complexes due to their enhanced chelating effect. Their suitable modification can open a window towards new functionalities based on appropriate metal binding. Therefore, detailed pH potentiometric measurements were carried out in order to determine the stability of the forming metal complexes, comparing them with structurally relevant examples from the literature.

(2) We wanted to reveal the significance of the tripodal and the amino acid moiety, with respect to the structure of the forming species. Beside thermodynamic stability, structural characterization of the metal complexes were equally important: ^{1}H and 2D nuclear magnetic resonance (NMR) studies were used to assign the coordinating groups in Zn(II) complexes, while combined UV-visible (UV-Vis), circular dichroism (CD) and electron paramagnetic resonance (EPR) spectroscopy was applied to study the coordination properties of Cu(II) complexes.

(3) The effect of N- and C-terminus, asymmetric functionalization and terminal protection in the ligands was to be investigated. The varying number of functionalized 'legs' provides varying number of donor groups available to metal ions. This, along with symmetry, is a leading force in the formation of multinuclear complexes, self-assembly and other interesting coordination features.

(4) The forming metal complexes were to be tested in simple enzymatic model reactions, including oxidoreductase and hydrolase functions. Pseudopeptide ligands with enhanced stability are promising candidates as components of enzyme mimics; therefore all ligand-metal systems were tested as catalysts in oxidative and hydrolytic reactions. We were interested in kinetic description of the catalytic systems, as well as in mechanistic details (substrate binding, effects of reaction partners *etc.*).

(5) We meant to draw conclusions regarding the relation of the experienced catalytic behavior and the structure of the applied ligand. Catalytically active peptide-metal complexes have great relevance from the point of view of structural enzyme modeling. Studying several tripodal peptides, we wanted to learn more about the development of catalytic performance of peptide complexes. Such findings, connecting structural properties and activity, can be powerful tools in future enzyme mimic design.

3. MATERIALS AND METHODS

3.1. SYNTHESIS OF THE LIGANDS

Preparation and characterization of the investigated ligands has been performed in our laboratories, at the University of Szeged. The quality and purity of all synthesized materials has been verified by ESI-MS, ^{1}H and ^{13}C NMR methods (see Appendix A.2-A.20). Starting materials were all analytically pure reagents and were used without further purification.

3.1.1. Synthesis of the N-terminal tris-His-ligand: tren3his (L^1)

Pre-treatment of Boc-His(Boc)-OH. Boc-His(Boc)-OH starting material was obtained from acidic treatment of Boc-His(Boc)-OH dicyclohexylammonium (DCHA) salt precursor (Sigma-Aldrich) according to the following procedure: 3 g Boc-His(Boc)-OH · DCHA (5.59 mmol) was suspended in 100 ml ethyl acetate, washed with 30 ml ice cold phosphorous acid solution (10 (m/m)%) and cold water until neutral pH. The acidic phase was washed with 40 ml fresh cold ethyl acetate. The organic phases were combined, free Boc-His(Boc)-OH was obtained after evaporation of ethyl acetate solvent.

Synthesis of $\mathbf{L^1}$. 1.38 g Boc-His(Boc)-OH (3.88 mmol), 0.225 g tren (1.54 mmol, Sigma-Aldrich), 0.55 g HOBt (4.07 mmol, NovaBiochem) and 0.83 g DCC (4.02 mmol, Sigma-Aldrich) was dissolved in 40 ml dichloromethane with stirring. The reaction was followed by thin-layer chromatography (eluent: 10% MeOH-90% chloroform +3% DIPEA). After 3 h at room temperature the white precipitate (dicyclohexylurea) was removed by filtration and dichloromethane was evaporated from the remaining solution. The residue was treated with a mixture of 95 (V/V)% trifluoroacetic acid (TFA), 2.5 (V/V)% triisopropylsilane (TIS) and 2.5 (V/V)% distilled water in order to remove N-protecting Boc-groups. TFA was evaporated using liquid nitrogen trap, the oily product was dissolved in water, neutralized with NaOH, filtered and purified by preparative HPLC (reverse-phase (RP) column: Supelco C18 5 μm, 25 cm × 10 mm geometry, 0 to 4.1% MeCN +0.05% TFA/20 min. gradient elution mode, 3 ml/min flow rate, t_R' = 8.6 min). After lyophilization the trifluoroacetate salt of $\mathbf{L^1}$ was obtained as white hygroscopic solid (61% yield). ^{1}H NMR (500 MHz, D_2O/H_2O, pH 7.19) δ (ppm): 2.46 (m, 6H, N_{tert}-C*H*$_2$), 2.98 (m, 6H, βC*H*$_2$), 3.18 (m, 6H, C*H*$_2$-NHCO), 3.88 (t, 3H, *J* = 7.0 Hz, αC*H*), 6.96 (s, 3H, im C^5*H*), 7.74 (s, 3H, im C^2*H*). ESI-MS *m/z* calcd for $C_{24}H_{40}N_{13}O_3$ $[M+H]^+$ 558.34, found 557.97 (*z* = 1) and $[M+2H]^{2+}$ 278.98 (*z* = 2).

3.1.2. Synthesis of the N-terminal asymmetric His-ligands: tren2his (L^3), tren1his (L^4)

Preparation of the asymmetric trenXhis ligands was realized in two steps, since the partial protection of tren had to be accomplished first, in order to carry out an effective asymmetric peptide coupling in solution phase.

Synthesis of mono-Boc tren. Mono-Boc protected tren was necessary for the selective synthesis of tren2his. 25.5 ml tren (175 mmol) was dissolved in 150 ml dioxane. To that solution, 6.0 g di-*tert*-butyl dicarbonate (Boc_2O, 27.5 mmol) in 150 ml dioxane was added dropwise applying N_2 atmosphere. After 17 h of stirring at r.t., a white precipitate was formed. Dioxane was evaporated, the white solid was dissolved in water. The aqueous solution was extracted by 6×75 ml dichloromethane. Organic phases were combined, the evaporation of DCM solvent resulted the mono-Boc protected tren as pale yellow oily product of high viscosity. Purity was checked by thin-layer chromatography (eluent: 75% MeCN-15% H_2O-10% $ccNH_3$ solution) and NMR. ^{1}H NMR (500 MHz, $CDCl_3$) δ (ppm): 1.44 (s, 9H, Boc-C*H*$_3$), 2.52 (t, 4H, N_{tert}-C*H*$_2^{unprot}$), 2.54 (t, 2H, N_{tert}-C*H*$_2^{prot}$), 2.75 (t, 4H, C*H*$_2$-NH_2), 3.17 (br t, 2H, C*H*$_2$-NH^{prot}), 5.56 (br s, 1H, N*H*).

Synthesis of di-Boc tren. Di-Boc protected tren, as a starting material for tren1his was synthesized following the description below: 2.34 g tren (16.0 mmol) was dissolved in 800 ml dry MeOH, to that a solution of 5.94 g Boc_2O (27.2 mmol) in 140 ml dry MeOH was added slowly, dropwise, at 0 °C. The mixture was put on ice for two days, enabling a slow reaction between the components. After the reaction time, thin-layer chromatograms indicated the presence of free, mono-, di- and tri-Boc tren accordingly. MeOH was evaporated, the residue was dissolved in chloroform, and the mixture was washed with four portions of 10% $NaHCO_3$ solution, removing mono-Boc and free tren from the organic phase. Di-Boc tren was obtained after chromatography on silica normal phase column (eluent: 50% MeOH-50% chloroform +2% $ccNH_3$ solution) and evaporation, as a pale yellow oily product. The purity of the compound was verified by NMR. ^{1}H NMR (500 MHz, $CDCl_3$) δ (ppm): 1.36 (s, 18H), 2.54 (br t, 4H), 2.65 (br t, 2H), 3.09 (br t, 6H).

Synthesis of Boc-His(Boc)-OH. Boc-His(Boc)-OH starting material was also prepared for these syntheses based on a general literature procedure [96], as following: 1.8 g L-His (11.6 mmol, Sigma-Aldrich) was suspended in 80 ml 50% tetrahydrofurane/water mixture. 3 g $NaHCO_3$ (35.7 mmol) and 6 g Boc_2O (27.5 mmol) was added at 0 °C. The turbid reaction mixture was stirred for 30 min at this temperature, then for further 14 h at r.t., becoming a clear solution. The mixture was washed with diethyl ether (2×50 ml), followed by careful addition of ~7 M solution of citric acid until pH reached 4.5. The aqueous solution was extracted with DCM (3×50 ml), the organic phases were combined and the solvent was evaporated. Boc-His(Boc)-OH was obtained as sticky white solid (31% yield), purity was confirmed by HPLC, by comparison with a standard Boc-His(Boc)-OH sample (RP column description in section 3.1.1. Eluent: isocratic 65% MeCN-35% water, t_R = 9.1 min).

Synthesis of L^3. 0.84 g Boc-His(Boc)-OH (2.36 mmol) and 0.27 g mono-Boc tren (1.10 mmol) were dissolved together in 50 ml dichloromethane, 0.47 g DCC (2.30 mmol) and 0.31 g HOBt (2.30 mmol) were added subsequently. The mixture was stirred overnight at rt. After filtration and evaporation of the solvent, the cleavage of Boc protecting groups was accomplished by a treatment of 95%-2.5%-2.5% TFA/TIS/water mixture. The

cleaving mixture was evaporated using liquid nitrogen trap, the oily residue was dissolved in water, neutralized and purified by preparative HPLC (RP column description in section 3.1.1., eluent: 0 to 3.2% MeCN +0.1% TFA/20 min gradient elution mode, 3 ml/min flow rate, t_R' = 9.2 min). After lyophilization the trifluoroacetate salt of **L^3** (62.7% yield) was obtained as white solid. ^{1}H NMR (500 MHz, D_2O/H_2O, pH 6.70) δ (ppm): 2.47 (t, 4H, *J* = 6.9 Hz, N_{tert}-CH_2^{funct}), 2.69 (t, 2H, *J* = 6.2 Hz, N_{tert}-CH_2^{free}), 2.98 (m, 4H, βCH_2), 2.97 (m, 2H, CH_2-NH_2), 3.17 (m, 4H, CH_2–NHCO), 3.91 (t, 2H, *J* = 7.0 Hz, αC*H*), 6.97 (s, 2H, im C^5*H*), 7.75 (s, 2H, im C^2*H*). ^{13}C NMR δ (ppm): 29.9, 37.0, 37.1, 50.4, 52.0, 54.0, 117.0, 131.5, 136.1, 171.9. ESI-MS *m/z* calcd for $C_{18}H_{33}N_{10}O_2$ $[M+H]^+$ 421.26, found 421.32 (*z* = 1).

Synthesis of L^4. 0.42 g Boc-His(Boc)-OH (1.18 mmol) and 0.38 g di-Boc tren (1.09 mmol) were dissolved together in 50 ml dichloromethane, 0.25 g DCC (1.20 mmol) and 0.16 g HOBt (1.20 mmol) were added subsequently. The mixture was stirred overnight at r.t. After filtration and evaporation of the solvent, the cleavage of Boc protecting groups was accomplished by a treatment of 95%-2.5%-2.5% TFA/TIS/water mixture. The cleaving mixture was evaporated using liquid nitrogen trap, the oily residue was dissolved in water, neutralized and purified by preparative HPLC (RP column description in section 3.1.1., eluent: 0 to 2% MeCN +0.1% TFA/15 min gradient elution mode, 3 ml/min flow rate, t_R' = 3.7 min). After lyophilization the trifluoroacetate salt of **L^4** (70.6% yield) was obtained as white solid. ^{1}H NMR of **L^4** (500 MHz, D_2O/H_2O, pH 7.12) δ (ppm): 2.53 (t, 2H, *J* = 7.0 Hz, N_{tert}-CH_2^{funct}), 2.75 (t, 4H, *J* = 6.3 Hz, N_{tert}-CH_2^{free}), 2.94 (m, 2H, βCH_2), 3.03 (t, 4H, *J* = 6.3 Hz, CH_2-NH_2), 3.22 (m, 2H, CH_2–NHCO), 3.79 (t, 1H, *J* = 6.9 Hz, αC*H*), 6.95 (s, 1H, im C^5*H*), 7.73 (s, 1H, im C^2*H*). ^{13}C NMR δ (ppm): 30.8, 36.5, 37.1, 50.5, 51.3, 55.2, 117.1, 132.2, 136.2, 173.6. ESI-MS *m/z* calcd for $C_{12}H_{26}N_7O$ $[M+H]^+$ 284.24, found 284.23 (*z* = 1).

3.1.3. Synthesis of the C-terminal tris-His-ligand: nta3his (L^2)

General issues. The preparation and purification of the C-terminal nta3his was found to be rather challenging. The tripodal scaffold molecule nta has a poor solubility in most of the common solvents, especially those being suitable media for peptide coupling in solution phase (*e.g.* DCM, chloroform). For that reason, reaction time became undesirably long, in respect of the relatively low stability of the coupling agents used in the procedures. In addition, as a C-terminally protected His precursor was necessary for the synthesis, the commercially available L-His-methylester · 2HCl was applied. This raised the need of using a base, in order to deprotonate the N-terminus of the amino acid and thus generating the nucleophilic group. The usage of bases in the carbodiimide coupling strategy, however, was proved to inhibit the activation of the carboxylic function [97], slowing down the reaction even further. The application of the commonly used organic base diisopropylethylamine (DIPEA) caused additional problems, as it was impossible to find an appropriate gradient program to separate it entirely from the product: yet HPLC

chromatograms indicated a single peak, traces of DIPEA were found in the sample of purified nta3his by ^{1}H NMR and ESI-MS as well. To avoid this, triethylamine (TEA) was used instead as base in small quantities during the following syntheses, resulting a product of eligible purity. However, it must be remarked that despite the various attempts for optimization, the yield of the reaction remained considerably low, the purification process was extremely long and the amount of obtained product was very limited.

Synthesis of $\mathbf{L^2}$. 1 g L-His-methyl ester · 2HCl (4.13 mmol, Sigma-Aldrich) and 0.852 g DCC (4.13 mmol), 0.558 g HOBt (4.13 mmol) coupling agents were dissolved in 60 ml chloroform in presence of triethylamine (1.2 ml). A suspension of nitrilotriacetic acid (0.26 g, 1.36 mmol) was added to the mixture and stirred at room temperature overnight. Chloroform was evaporated, the oily residue was treated with 5 eq. NaOH solution (H_2O:MeOH 2:1), in order to remove the C-terminal protecting group. The hydrolysis of methyl ester group was completed in 17 h at r.t. Excess base was neutralized, the mixture was filtered and purified by preparative HPLC (RP column described in section 3.1.1, eluent: 0 to 5% MeCN +0.1% TFA/20 min. gradient elution mode, 3 ml/min flow rate, t_R' = 14.8 min). After purification and lyophilization, $\mathbf{L^2}$ was obtained as a trifluoroacetate salt (yield 53%). ^{1}H NMR (500 MHz, D_2O/H_2O, pH 7.08) δ (ppm): 2.95 (dd, 3H, J_{AB} = 15.3 Hz, J_{HH} = 4.5 Hz, βCH_2), 2.96 (d, 3H, J_{AB} = 15.3 Hz, N_{tert}-CH_2), 3.06 (d, 3H, J_{AB} = 15.3 Hz, N_{tert}-CH_2), 3.16 (dd, 3H, J_{AB} = 15.3 Hz, J_{HH} = 4.5 Hz, βCH_2), 7.00 (s, 3H, im C^5H), 7.99 (s, 3H, im C^2H), 8.30 (d, 3H, CONH). ESI-MS *m/z* calcd for $C_{24}H_{31}N_{10}O_9$ $[M + H]^+$ 603.23, found 603.2 (z = 1) and $[M+2H]^{2+}$ 302.0 (z = 2).

3.1.4. Syntheses attempted on solid phases: nta1his and nta1his-NH_2

The encountered difficulties regarding the synthetic strategy of C-terminal His compounds forced us to open towards different synthetic procedures. Beside the optimizations of solution phase peptide coupling, solid phase synthetic methods were also experimented with. Attempts for such kind of preparations for tripodal ligands were already reported in the literature [26, 98]; it is a convenient method for synthesizing partially functionalized compounds, since small tripodal scaffold molecules are being attached by only one 'arm' to the resin. Therefore we applied the Fmoc-strategy for creating the *mono*-His functionalized, C-terminally free and protected nta1his and nta1his-NH_2 ligands, respectively.

Although early ^{1}H NMR and ESI-MS measurements indicated unified, pure products following the syntheses, the materials turned out to be degrading slowly, even after repurification. This eventual degradation could not be prevented even by careful storage in solid state, at -4 °C. Therefore, experimental data regarding these compounds are limited.

Synthesis of nta1his. The mono-functionalized C-terminal nta1his was prepared using Wang resin (100-200 mesh, Merck). 1 g of resin was left to swell together with 2 eq. Fmoc-His(Trt)-OH (Sigma-Aldrich) in DMF for 15 min. 3.3 eq. pyridine (Sigma-Aldrich)

and 2 eq. 2,6-dichlorobenzoyl chloride (Molar Chemicals) was added and stirred overnight. DMF was filtered, the resin was rinsed with *N*-methyl-2-pirrolidone (NMP), as in every following rinsing step. Remaining active sites on the Wang resin have been blocked by treatment with 4 eq. pyridine/benzoyl chloride (Molar Chemicals) mixture. Fmoc group of His was removed by 20% piperidine solution, the presence of the free NH_2 groups were confirmed by Kaiser-test [99]. Nta (4 eq.) was coupled then to the amino functions using HOBt (4 eq., Novabiochem), HBTU (4 eq., Novabiochem) and DIPEA, stirred together for 4 h. The coupling reaction was repeated, negative Kaiser-test attested for the absence of residual free amino groups. The ligand was cleaved from the resin using a mixture of 95%-2.5%-2.5% TFA/TIS/water. After the evaporation of TFA, the residue was dissolved in water, neutralized and purified by preparative HPLC (RP column described in section 3.1.1, eluent: 100% H_2O+0.1% TFA/10 min. isocratic elution mode, 3 ml/min flow rate, t_R' = 2.2 min). After lyophilization the trifluoroacetate salt of nta1his was obtained as white hygroscopic solid. ^{1}H NMR (500 MHz, D_2O/H_2O) δ (ppm): 3.03, 3.22, 3.69, 4.00, 7.16, 8.47.

Synthesis of nta1his-NH_2. The C-terminally protected compound was synthesized similarly to nta1His, except for the followings: Rink Amide AM resin (0.68 mmol/g) was used for the preparation, to which Fmoc-His(Trt)-OH was coupled straightforwardly after the removal of Fmoc protecting group, using 4 eq. HOBt, 4 eq. HBTU coupling agents in presence of 8 eq. DIPEA. The coupling step was repeated, after 45 min stirring Kaiser-test supported the absence of residual free amino groups. Fmoc group of His moiety was removed and the coupling of nta followed as described previously. HPLC purification (RP column described in section 3.1.1, eluent: 100% H_2O+0.1% TFA/10 min. isocratic elution mode, 3 ml/min flow rate, t_R' = 2.7 min) and lyophilization resulted nta1his-NH_2 trifluoroacetate salt as white solid. ^{1}H NMR (500 MHz, D_2O/H_2O) δ (ppm): 3.19 (q, 2H), 3.86 (s, 4H), 4.01 (q, 2H), 7.27 (s, 1H), 8.57 (s, 1H). ESI-MS *m/z* calcd for $C_{12}H_{18}N_5O_6$ $[M+H]^+$ 328.29, found 327.88 (z = 1).

3.2. CHARACTERIZATION TECHNIQUES OF SOLUTION EQUILIBRIUM AND STRUCTURE

3.2.1. pH potentiometry

The protonation and coordination equilibria were investigated by pH-potentiometric titrations in aqueous solutions (I = 0.1 M NaCl and T = 298.0 ± 0.1 K) under argon atmosphere. The titrations were performed using a PC controlled Dosimat 665 (Metrohm) automatic burette and an Orion 710A precision digital pH-meter. The Metrohm micro glass electrode (125 mm) was calibrated by the titration of hydrochloric acid and the data were fitted using the modified Nernst-equation [100]:

$$E = E_0 + K \cdot \log[\mathrm{H}^+] + J_{\mathrm{H}} \cdot [\mathrm{H}^+] + \frac{J_{\mathrm{OH}} \cdot K_{\mathrm{w}}}{[\mathrm{H}^+]}$$

where J_{H} and J_{OH} are the fitting parameters representing the acidic and alkaline error of the glass electrode, respectively ($K_{\mathrm{w}} = 10^{-13.75}$ is the autoprotolysis constant of water [101]). The parameters were calculated by the non-linear least squares method. The formation of the complexes was characterized by the general equilibrium process:

$$\mathrm{pM} + \mathrm{qH} + \mathrm{rL} \overset{\beta_{\mathrm{M_pH_qL_r}}}{\rightleftharpoons} \mathrm{M_pH_qL_r}$$

$$\beta_{\mathrm{M_pH_qL_r}} = \frac{[\mathrm{M_pH_qL_r}]}{[\mathrm{M}]^{\mathrm{p}}[\mathrm{H}]^{\mathrm{q}}[\mathrm{L}]^{\mathrm{r}}}$$

where M denotes the metal ion and L the fully deprotonated ligand molecule. Charges are omitted for simplicity. The protonation constants of the ligands and the formation constants of the complexes were calculated by the PSEQUAD computer program [102] from 4, and 6-8 independent titrations respectively (*ca*. 90 data points per titration). The metal ion concentrations varied between 0.5-3.3×10^{-3} M, using 2:1, 3:2, 1:1 and 1:2 metal-to-ligand ratios.

3.2.2. UV-visible (UV-Vis) spectroscopy

In order to gather information about the number and quality of the coordinating groups around the metal ion(s), UV-Vis spectrometric measurements were performed. Changes in the coordination sphere can be monitored by the appropriate interpretation of pH-dependent UV-Vis spectra series.

Light absorption of a complex can be originated from either the ligand (chromophoric groups, n–σ*, π–π*, n–π* transitions), the metal (d-d transitions) or both (M-L or L-M type charge transfer (CT) bands). Newly appearing absorption bands or displacements imply a change in coordination environment around the metal ion. However, qualitative interpretation of spectral changes is not always simple, since the d-d transitions and HOMO-LUMO energy gap is dependent of many factors, such as the quality of the donor

groups, the coordination geometry, symmetry and distortions of the coordination spheres, temperature, solvent, etc.

Regarding metal complexes with relatively simple donor groups, there has been an effort in the literature to state some useful empirical 'rules', guidelines for treating and comparing the behavior of different metal-peptide systems. The most important of these works concerned the relation between the energy of the d-d band of Cu(II), expressed as wavenumbers (ν/cm^{-1}) and the quality/number of donor groups in the equatorial plane. This was first published by Billo and co-workers [103] and later extended by Sigel and Martin [104], Pettit [105] and Prenesti [106], who afterwards continued researching on the effects of axially coordinating donor groups to the visible spectra of Cu(II) complexes as well, estimating their contribution to the λ_{max} [107].

Optical spectroscopic methods such as UV-Vis and CD spectroscopy enable the possibility of quantitative characterization: the Beer-Lambert law defines the relationship between the concentration of the absorbing species (c) and the measured absorbance (A) according to the following equation:

$$A = \lg(I_0/I) = \varepsilon \times c \times l,$$

where I_0 denotes the intensity of the incoming light, I the intensity of the transmitted light, ε is the molar extinction coefficient ($M^{-1}cm^{-1}$) of the absorbing species and l (cm) is the optical pathlength.

UV-Vis spectra were recorded on a Unicam Helios α spectrophotometer, a MOS 450 (BioLogic) spectrometer and a PerkinElmer Lambda 1050 spectrophotometer, using a quartz cuvette with 1 cm optical pathlength. Spectral changes were monitored between pH 2 and 11 for all Cu(II)-ligand systems, at all relevant Cu(II)-to-ligand ratios. The metal ion concentration varied between 8.8×10^{-4} -2.4×10^{-3} M. The pH-dependent UV-Vis spectra were processed together with the pH-potentiometric data using the PSEQUAD computer program [102], resulting $\log\beta$ values as well as individual UV-Vis spectra of the Cu(II) complexes.

3.2.3. Circular dichroism (CD) spectroscopy

Similar qualitative and quantitative information can be extracted from CD spectra. CD spectroscopy uses plane polarized light which can be split to left- and right-handed circularly polarized components. Optically active molecules absorb different quantities of these components, this phenomenon is called circular dichroism. In CD spectroscopy we obtain a spectrum by the difference of extinction coefficients of the two components ($\Delta\varepsilon = \varepsilon_{left} - \varepsilon_{right}$) at each scanned wavelength (λ). The Beer-Lambert law is applicable for the qualitative treatment of the data, enabling to calculate individual CD spectra for light absorbing chiral metal complexes.

Chirality of transition-metal complexes can be assigned to the asymmetry sources summarized below:

(1) Central chirality, which corresponds to the chiral distribution of donor groups around the metal ion,

(2) Helical chirality, which is caused by the chirally positioned chelate rings around the metal center,

(3) Conformational chirality of the chelate rings

(4) Chirality of the coordinating ligand, which is conducted towards the metal ion through chemical bonds.

While effects (1)-(3) have significance in case of kinetically inert complexes (mainly Co(III), Cr(III), Rh(III), Ir(III) and Pt(IV) complexes), chirality of copper(II) containing complexes are usually originated from the chiral ligand. In a CD-active complex, at least one of the conformers of the forming chelate ring must be stabilized, otherwise racemization would occur, resulting zero overall signal on the CD spectrum. The shape of a CD spectrum is unique of the three-dimensional environment of the central metal ion.

CD spectra were measured on a Jasco J-710 spectropolarimeter and a MOS 450 (BioLogic) spectrometer, in the wavelength interval from 300 to 900/830 nm, in a cell with 1 cm optical pathlength. Spectral changes were monitored between pH 2 and 11 for all Cu(II)-ligand systems, at all relevant Cu(II)-to-ligand ratios. The metal ion concentration varied between 8.8×10^{-4} -2.4×10^{-3} M. pH-dependent CD spectra were processed together with the pH-potentiometric data using the PSEQUAD computer program [102], resulting logβ values as well as individual CD spectra of the Cu(II) complexes.

3.2.4. Electron Paramagnetic Resonance (EPR) spectroscopy

EPR spectroscopy can be used to structural characterization of systems bearing unpaired electron(s) such as radicals or paramagnetic metal complexes. The method is based on the Zeeman effect, namely that an external magnetic field splits the energy levels of an unpaired electron. This energy separation corresponds to the energy of microwave frequency.

EPR signals are dependent of the interactions between the unpaired electron and all non-zero nuclear spin(s) or other unpaired electron(s). The main interactions which must be taken into account in complex systems, are the following:

(1) Interaction of unpaired electron(s) of the metal ion with its non-zero nuclear spin ($I\neq0$): EPR signal is split into a number of $2I+1$ components. This interaction is characterized by the hyperfine coupling constant (A).

(2) Interaction of the unpaired electron with a non-zero nuclear spin of a different atom (donoratom of the ligand): EPR signal can be split into a number of $2nI+1$ components. This interaction is characterized by the super hiperfine coupling constant (A).

(3) Dinuclear complexes can produce antiferromagnetic interaction between the metal centers, which denotes the interchange of electron spins. This interaction is highly sensitive to the proximity of the interacting metals, and can cause extreme broadening or quenching of the EPR signal.

EPR spectra of the copper(II) complexes were recorded on a BRUKER EleXsys E500 spectrometer (microwave frequency 9.81 GHz, microwave power 10 mW, modulation amplitude 5 G, modulation frequency 100 kHz), or a continuous wave Bruker EMXplus 10/12 spectrometer (microwave frequency 9.412 GHz). Since common copper(II) perchlorate was used for all measurements, the spectra were calculated by the summation of spectra ^{63}Cu and ^{65}Cu weighted by their natural abundances. The hyperfine and the relaxation parameters were obtained in field units (Gauss = 10^{-4} T).

We applied EPR titrations in case of Cu(II)-$\mathbf{L^1}$: pH-dependent (pH = 2.3-11.3) series of EPR spectra were collected under argon atmosphere at room temperature, in both equimolar solution ($0.95\times[\mathbf{L^1}]_{tot}$ = $[Cu(II)]_{tot}$ = 1.6×10^{-3} M) and at metal ion excess ($1.40\times[\mathbf{L^1}]_{tot}$ = $[Cu(II)]_{tot}$ = 2.31×10^{-3} M) in a circulating system using a Heidolph Pumpdrive 5101 peristaltic pump. The ionic strength was adjusted to 0.1 M with NaCl. The two series of room-temperature CW-EPR spectra were simulated by the 2D_EPR program [108]. The parameters g_o, A_o^{Cu} copper hyperfine (I_{Cu}= 3/2) and A_o^{N} nitrogen (I_N = 1) hyperfine coupling has been taken into account to describe each component curve. The relaxation parameters, α, β, and γ defined the linewidths through the equation $\sigma_{MI} = \alpha + \beta M_I + \gamma M_I^2$, where M_I denotes the magnetic quantum number of copper(II) ion.

EPR spectra of Cu(II)-$\mathbf{L^2}$, -$\mathbf{L^3}$ and -$\mathbf{L^4}$ systems have been measured using individually prepared and pH-adjusted solutions (0.1 M NaCl ionic strength) in a capillary, at 1:1 and 2:1 metal-to-ligand ratios ($[Cu(II)]_{tot}$ = 0.8×10^{-4}-3.3×10^{-3} M). Samples were prepared as aqueous solutions; 100 µl volumes were put in capillary, 20 µl methanol was added to each sample in order to avoid water crystallization. The frozen solution EPR spectra were simulated by the "EPR" program [109], rhombic g-tensor (g_x, g_y, g_z), copper hyperfine tensor (A_x, A_y, A_z) and the orientation dependent linewidth parameters were fitted to set up the spectra. In cases when well resolved superhyperfine lines were detected, a rhombic nitrogen coupling was taken into account (a_x^N, a_y^N, a_z^N) as well. The linewidths have been described by the above-mentioned equation using orientation dependent α, β and γ parameters. Isotropic EPR spectra, recorded at room temperature, could only be obtained for Cu(II)-$\mathbf{L^2}$ complexes; they were fitted by the "EPR" program [109] using the parameters: g_o, A_o^{Cu} copper hyperfine (I_{Cu}= 3/2) and A_o^{N} nitrogen (I_N = 1) hyperfine couplings.

Detection of the oxygenated radical intermediate in Cu(II)-$\mathbf{L^1}$-H_2DTBC system was carried out using a Bruker ECS106 X-band EPR spectrometer (modulation amplitude 0.84 G, microwave power 5 mW). After mixing the reaction solution under aerobic conditions (in EtOH/H_2O 50/50 HEPES/CHES buffer, I = 0.1 M, $[complex]_{tot}$ = 5×10^{-5} M, $[H_2DTBC]$ = 2×10^{-3} M, pH = 8), a sample of 4-5 µl was put in a capillary tube, and measured in presence of 2,2-diphenyl-1-picrylhydrazyl (DPPH) internal reference.

3.2.5. Nuclear Magnetic Resonance (NMR) spectroscopy

One of the most powerful structural characterization techniques is the NMR spectroscopy. It can be applied to species possessing non-zero nuclear spin ($I \neq 0$), and is based on the fact that external magnetic field induces the splitting of the energy levels of these nuclear spins (number of energy levels is $2I+1$). Resonance between the split energy levels can be achieved by radiofrequency irradiation. This frequency (also called Larmor frequency) is unique for each nuclear spin and is dependent of the external magnetic field.

The high number of signals on a simple NMR spectrum is due to the sensitivity of the resonance frequency to the chemical environment of a nuclear spin. This effect is called the chemical shift (δ), usually given in Hz or ppm, and it is in strict relation with the electronic shielding of the nuclei. Generally, the intensity of the signals is corresponding to the number of nuclei the signals are originated from, which contributes to the important structural information. Moreover, the spins are sensitive to the chemical environment of the neighboring atoms, resulting characteristic splitting ($nI+1$) of each signals. The interaction between the neighboring nuclei and therefore the induced splitting of the signals can be described by the coupling constant (J) in Hz.

Although NMR spectroscopy provides various and detailed structural information as it is, investigation of more complicated systems (*e.g.* proteins, multicomponent mixtures) often requires special techniques providing complementary data. 2D NMR techniques are based on transfer of magnetism between different groups, which results additional information about the interactions between further (not neighboring) functional groups via chemical bonds (*e.g.* COSY = *correlation spectroscopy*, TOCSY = *total correlation spectroscopy*) or space (ROESY = *rotating-frame Overhauser spectroscopy*). It is possible to execute resonance transfer between nuclei of different elements (HMQC = *heteronuclear multiple-quantum correlation*, HMBC = *heteronuclear multiple bond correlation*), and thus to assign every peak of the 1D spectra to the corresponding groups. In a system prone to aggregation, the measurement of diffusion processes can be extremely helpful in order to estimate the size of species occurring in the solution (DOSY = *diffusion-ordered spectroscopy*), which can be achieved by monitoring the different relaxation times of the species with different size.

The width of NMR signals depends on many factors; some of them are practical (frequency of the instrument, homogeneity of the magnetic field, etc.). However, in case of diamagnetic metal complexes, the kinetics of complex formation has major importance on the matter. Basically, the relation between the rate of complex formation and the relaxation time of the studied nucleus determines the width of the signal.

(I) In case the ligand exchange rate around the metal is considerably faster than the relaxation time of the observed nuclei, the obtained peak will be in fact a superposition of many different states (conformation, chemical environment) regarding the nucleus. Signals are usually narrow, free and complexed ligand peaks can not be differentiated.

(II) In case the ligand exchange rate is much slower than the relaxation of the studied nuclei, the obtained spectra will represent a single state corresponding to the metal complex. Signals are very sharp and multiplication of them often occurs, indicating chemically different environments (for each complexes and free ligand).

(III) If the ligand exchange rate is very close (in the same order of magnitude) to the rate of relaxation, signals are broadened. It is considered an intermediate exchange rate in respect of the NMR time scale and usually indicates some sort of interaction, which causes the loss of free motion of the molecule part involved, and therefore a retarded exchange rate.

(IV) Presence of paramagnetic compounds (*e.g.* paramagnetic transition metal ions) causes significant changes on the NMR signals. In presence of copper(II), due to its slow electronic relaxations, important broadening of the signals can be observed. Although, some information (like *J*-couplings) might be lost by the decreased resolution of the spectra, the selective broadening may help to identify the binding site(s) of metal ions.

NMR spectra were recorded in Szeged (Hungary), on a Bruker Avance DRX500 spectrometer (500.13 MHz frequency), and in Nancy (France), on a Bruker DRX400 spectrometer (400 MHz frequency). All samples were aqueous solutions with 10-20% D_2O unless it is marked otherwise. Water signal suppression on ^1H spectra has been achieved using presat or watergate pulse sequences. Dioxane was used at internal reference ($\delta_{dioxane}$ = 3.70 (^1H) and 66.5 (^{13}C) ppm). Ligand concentrations have been adjusted to 1-2 mM unless stated otherwise. The assignment of the proton and carbon signals of the ligands was based on ^1H-^1H COSY, ^1H-^{13}C HMQC and ^1H-^{13}C HMBC 2D spectra (see Appendix A.9-A.20). DOSY measurements of Zn(II)-$\mathbf{L^1}$ 3:2 system were performed at the University of Debrecen, with solvent suppression, using 64 gradient step at 293 K. Three sets of spectra were recorded, following the preparation of the complex solution and after 90 and 156 h, in order to verify the kinetic stability and reproducibility of the system during the experiment. Data were processed using the Topspin 2.0 software package (Bruker).

3.2.6. Mass Spectrometry (MS)

Mass spectrometric measurements were carried out in order to verify the presence our synthesized ligand molecules and their metal complexes forming at various metal-to-ligand ratios. In most cases, free ligand molecules and monocomplexes were analyzed using electrospray ionization (ESI) quadrupole MS coupled to a liquid chromatography column. Di- or trinuclear complexes were detected by matrix-assisted laser desorption/ionization time-of-flight (MALDI-TOF) MS method, either in the Biological Research Centre of Szeged (Hungary), or in the University of Lorraine (Metz, France). The samples were prepared in aqueous solutions at the desired metal-to-ligand ratios, pH was adjusted using NaOH and HCl solutions. ESI-MS measurements were carried out by direct injection of the samples to the LC column. In case of MALDI measurements, 1 µl of the samples was spotted onto the target plate and let dry before adding 0.5 µl of the matrix solution (20 mg/ml 2,5-dihydroxybenzoic acid (DHB) in water or 2,6-dihydroxyacetophenone

(DHAP) in MeCN-water 1:1). Mass spectra were recorded in the positive (**L**^{1}, **L**^{3} and **L**^{4} complexes) and negative (**L**^{2}, nta1his-NH_2 complexes) reflectron modes collecting multiple shots for each sample (*m/z* range: 900-2000). External calibration affording ±200 or 100 ppm mass accuracy was performed using peptide standards, or polyethylene glycol standard (Aldrich). DHB and DHAP matrices were obtained from Sigma-Aldrich.

The mass spectrometers used in this work are the following: Finnigan TSQ 7000 ESI-LC-MS with triple quadrupole analyzer (University of Szeged, Department of Medical Chemistry, Szeged), Bruker MicroTOFq high-resolution ESI-MS (Université de Lorraine SRSMC UMR 7565, Nancy), Bruker REFLEX III MALDI-TOF MS (Biological Research Centre, Szeged), Bruker REFLEX IV MALDI-TOF MS (Université de Lorraine LCP-A2MC, Metz).

3.3. KINETIC EXPERIMENTS

In order to characterize the potential catalytic abilities of our complexes, kinetic experiments have been carried out, testing redox (SOD, catechol oxidation) and hydrolytic functions (phosphoester hydrolysis) as well. In all cases we used spectrophotometric detection of the forming product, resulting absorbance vs. time data series. All kinetic experiments were executed and treated according to the initial reaction rates method.

The *initial reaction rates method* presumes that the conversion of the substrate does not exceed 3-5%, where the quantity of product increases linearly in function of time. Initial reaction rate (v_i) can be calculated from the slope of this region of the absorbance-time curve:

$$dA/dt = \varepsilon_\lambda \times l \times d[P]/dt$$

$$v_i = d[P]/dt = -d[S]/dt = (dA/dt)/(\varepsilon_\lambda \times l)$$

where dA/dt is the observed time-dependent absorbance (slope), [P] is the concentration of the product, [S] is the concentration of the substrate, ε_λ is the molar extinction coefficient of the forming product at the absorption maximum and l is the optical pathlength in cm.

Under pseudo-first order conditions, a pseudo-first order reaction rate constant (k_{obs}) can be introduced. Presentation of kinetic data usually includes the second order rate constant k', which is independent of the concentration of the catalyst, therefore can be used for correlating data from different concentration conditions.

$$v_i = d[P]/dt = k_{obs} \times [S] = k' \times [\text{catalyst}] \times [S]$$

The *Michaelis-Menten kinetic method* was originally introduced to enzymatic reactions. In such reactions (considering only the most simple case as model) the enzyme (E) and the substrate (S) molecules form an adduct (ES) in a pre-equilibrium step, followed by the conversion of the substrate to product (P) with the regeneration of the enzyme.

$$E + S \underset{k'_a}{\overset{k_a}{\rightleftharpoons}} ES \xrightarrow{k_b} P + E$$

Presuming steady-state approximation to the formation and consumption of ES, product formation can be expressed in differential equations as following:

$$\frac{d[P]}{dt} = k[E]_o, \qquad k = \frac{k_b[S]}{K_M + [S]},$$

where **[***E***]**$_o$ is the total concentration of the enzyme and K_M is the *Michaelis constant*:

$$K_M = \frac{k_b + k'_a}{k_a}.$$

In order to apply this methodology in our complex catalyzed reactions (where the complex = E), the following conditions must be settled:
(I) Substrate concentration exceeds considerably the enzyme concentration.
(II) The variation of substrate concentration is negligible during the reaction (which meets the prerequisites of the initial reaction rates method).
(III) Product does not form a stable adduct with the enzyme.
(IV) One substrate molecule binds to the enzyme.

Michaelis-Menten mechanism states a linear correlation between the reaction rate and $[E]_o$, but the substrate-dependence is more complex: if $[S] >> K_M$, then the reaction rate becomes independent on [S]:

$$d[P]/dt = k_b[E]_o$$

If $[S] << K_M$, the reaction rate increases linearly with [S]:

$$d[P]/dt = (k_b/K_M)[E]_o[S]$$

According to these boundary statements, the experimental substrate-dependent reaction rate curve is a saturation curve, which can be used to calculate K_M and k_b (often cited as k_{cat}) parameters by *e.g.* least squares methods.

3.3.1. Catechol oxidation measurements

Kinetics. The oxidation of 3,5-di-*tert*-butylcatechol (H_2DTBC) was followed in buffered solutions (0.02 M HEPES/CHES, I = 0.1 M (0.08 M NaCl), T = 298 K) by detecting the increase in absorption at 400 nm of 3,5-di-*tert*-butyl-*o*-benzoquinone (DTBQ, ε = 1900 $M^{-1}cm^{-1}$). 50% EtOH-50% aqueous solutions were used to prevent the precipitation of DTBQ. The actual pH (used as pH_{corr}) in this mixed solvent was determined by substracting 0.21 units from the pH-meter reading [110], the auto-ionization constant of water in this medium is pK_w = 14.84 [111]. Precise concentrations of O_2 were obtained by addition of EtOH saturated by O_2 gas to the reaction solutions (the solubility of O_2 is 250 $mgdm^{-3}$ and 41 $mgdm^{-3}$ in ethanol and water, respectively [112]). After mixing the ethanol and the aqueous phases, the solutions were thermostated at 298 K for 2-3 minutes, then the reaction was initiated by the addition of H_2DTBC as ethanolic solution.

Autooxidation of H_2DTBC was taken into account in every experiments, resulting $k_{obs,corr}$ values ($k_{obs,corr} = k_{obs} - k_{obs,auto}$). The parameters of the Michaelis-Menten model (K_M and k_{cat}) were calculated by non-linear least square method. All kinetic data are averages of at least three parallel measurements.

Substrate binding. Substrate binding experiments were carried out in buffered 50% EtOH-H_2O solutions (0.05 M HEPES/CHES, I = 0.1 M (0.05 M NaCl), T = 298 K), using 4-nitrocatechol ($H_2$4NC) and H_2DTBC. During the study of $H_2$4NC binding the complex concentrations varied between 0.8 - 2.5×10^{-4} M or was held constant on 2.1×10^{-5} M. Deprotonation constants and spectroscopic parameters of 4NC species were calculated using PSEQUAD program [102].

Anaerobic H_2DTBC binding UV-Vis measurements were executed under argon atmosphere, in closed quartz cuvette equipped with a septum, with 1 cm optical pathlength. Different volumes of H_2DTBC stock solution was added to deoxygenized, buffered complex solutions using a Hamilton syringe. Complex concentrations were adjusted to 2.4×10^{-4} M in case of each ligand system, substrate concentration varied between 0-1.2×10^{-2} M. 'Blank' experiments, in the absence of metal complexes, were also carried out. Each measurement was performed twice in order to confirm reproducibility.

Detection of H_2O_2. The formation of hydrogen peroxide during the oxidation of H_2DTBC was identified and quantified spectrophotometrically, as $[Ti(O_2)(OH)]^+$ complex (ε^{408nm} = 935 $M^{-1}cm^{-1}$), in aqueous solutions. In a typical experiment, 20 ml reaction solution has been prepared (0.02 M HEPES/CHES, I = 0.1 M (0.08 M NaCl), T = 298 K); 4.5 ml aliquots have been removed and extracted with 2×5 ml dichloromethane, after different reaction times (t = 1, 6, 12 and 30 min). After the removal of residual substrate and benzoquinone product by extraction, the aqueous phases were treated with excess H_2SO_4 and $TiOSO_4$ solutions, and subsequently measured in a quartz cuvette of 1 cm pathlength. Complex concentrations were 5×10^{-5} M, the initial H_2DTBC concentration was 2×10^{-3} M. The production of DTBQ has been also determined under identical conditions, but without the extraction step. After a given time interval 1:1 HCl solution was added to stop the reaction, and the solution was mixed with EtOH to obtain 50% EtOH-water mixture.

3.3.2. Superoxide dismutase (SOD) measurements

Superoxide dismutase activity of copper(II) complexes were measured using the McCord-Fridovich reaction (see section 1.4.3.). The formation of the blue product NBT-diformazan (λ_{max} = 560 nm) was followed by a Unicam Helios α spectrophotometer, in function of complex concentrations ($[Cu^{2+}]_{tot}$ = 0-1×10^{-6} M). In every experiment two reaction mixtures were measured simultaneously along with a blank (without complex) sample, in cuvettes of 1 cm pathlength. The reaction solutions were buffered at pH 7.4 (0.05 M Na_2HPO_4/NaH_2PO_4), samples contained 1.0×10^{-4} M NBT and 1.2×10^{-4} M

xanthine. Xanthine oxidase enzyme was stored on ice, and was applied in a sufficient quantity for producing $\Delta A \sim 0.025\text{-}0.028$ min^{-1}.

SOD activity was defined using IC_{50} values according to relevant literature, which denotes the concentration of the complex at 50% inhibition. %inhibition values were calculated as following:

$$\%\,\text{inhibition} = \frac{\left(\frac{\Delta A}{\min}\right)^{blank} - \left(\frac{\Delta A}{\min}\right)^{complex}}{\left(\frac{\Delta A}{\min}\right)^{blank}} \times 100$$

When comparing systems studied under different concentration conditions, it must be taken into account that IC_{50} is dependent on the used detector (NBT in our case) and its concentration. Therefore, SOD activity may be expressed as *k*, calculated as $k_{NBT} \times [NBT]/IC_{50}$ (k_{NBT} = 3×10^4 $M^{-1}s^{-1}$ [113], as later corrected by the authors: http://kinetics.nist.gov/solution/Detail?id=1977BIE/RIC3019-3023:16). However, these *k* values are only approximate values, since the above k_{NBT} was determined at pH 9.8. Nevertheless, it allows the comparison of SOD activities of different complex systems, regardless of the applied NBT concentrations.

3.3.3. Activated phosphoester hydrolytic measurements

Chromophoric phosphoester compounds were used to characterize potential hydrolytic activities of the metal complexes; the activated phosphoesters: BNPP – *bis*(4-nitrophenyl) phosphate, NPP – 4-nitrophenyl phosphate, DNPEP – 2,4-dinitrophenylethyl phosphate and HPNP – 2-hydroxypropyl *p*-nitrophenyl phosphate substrates were tested in presence of some of the metal-ligand complexes, as hydrolytic catalysts. Aqueous, buffered solutions were used (0.02 M HEPES/CHES, I = 0.1 M (0.08 M NaCl), T = 298 K) for following the reaction by detecting the increase in absorption at 400 nm of 4-nitrophenolate (4NP, ε^{400nm} = 18900 $M^{-1}cm^{-1}$) or 2,4-dinitrophenolate in case of DNPEP (ε^{400nm} = 12100 $M^{-1}cm^{-1}$). Complex concentrations were set to 1×10^{-4} M, initial substrate concentrations were 2×10^{-4} M. Data points were collected for 240 min, the autohydrolysis was taken into account at the given pH in every experiments ($k_{obs,corr} = k_{obs} - k_{obs,auto}$). Table of the observed reaction rate constants and related discussion can be found in Appendix section A.26. and Table A.2.

4. RESULTS AND DISCUSSION

4.1. PROTONATION AND COORDINATION PROPERTIES OF TREN3HIS (L^1)

In the first stages of my PhD work, we were interested in synthesizing free terminal histidine-containing tripodal ligands with C_3 symmetry. The first accomplished preparation resulted the ligand tren3his ($\mathbf{L}^1$), bearing solely *N*-functional groups.

4.1.1. Protonation of tren3his

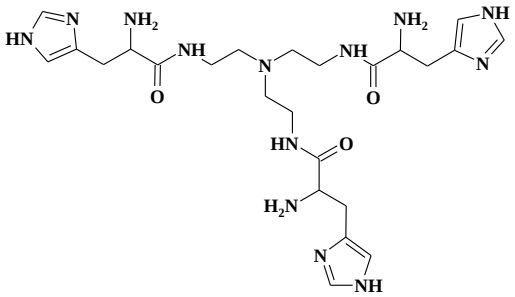

Scheme 4.1. Schematic structure of the ligand tren3his ($\mathbf{L}^1$).

Although seven p*K* values can be expected for tren3his (one tertiary, three primary amino groups and three imidazole rings, Scheme 4.1), only six could be determined in the studied pH range, since the tertiary amino nitrogen probably has a p*K* < 2, similarly to tren itself [11] (Figure 4.1). Nevertheless, the ^{1}H NMR spectra of tren3his (Figure 4.2.) show considerable shift between pH 2-6, for both the signals of imidazole rings and the CH_2 protons related to the tren moiety. Consequently, the tertiary amine is involved in a strong H-bonding network with the imidazole rings. Although the imidazole p*K* values are notably lower than for histamine itself (p*K* = 6.08, [114]), the values determined are close to those of the related *N*-(π)-benzyl substituted derivative [32], and the structurally similar *N,N'*-di-L-histidylethane-1,2-diamine [114]. Above pH 6 only the αCH protons of histidines undergo notable pH-shift (Figure 4.2), hence these processes are related to the deprotonation of primary amino groups.

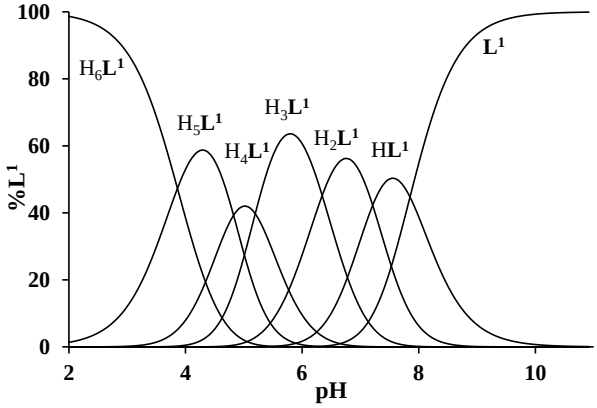

	logβ	pK
$H_6\mathbf{L}^1$	35.29(1)	3.87
$H_5\mathbf{L}^1$	31.42(1)	4.82
$H_4\mathbf{L}^1$	26.60(1)	5.20
$H_3\mathbf{L}^1$	21.40(1)	6.34
$H_2\mathbf{L}^1$	15.06(1)	7.21
$H\mathbf{L}^1$	7.85(1)	7.85

Figure 4.1. Speciation diagram (left) and table of formation and deprotonation constants (right) of the tren3his ligand system ($[\mathbf{L}^1]_{tot}$ = 0.001 M, I = 0.1 M NaCl, T = 298 K).

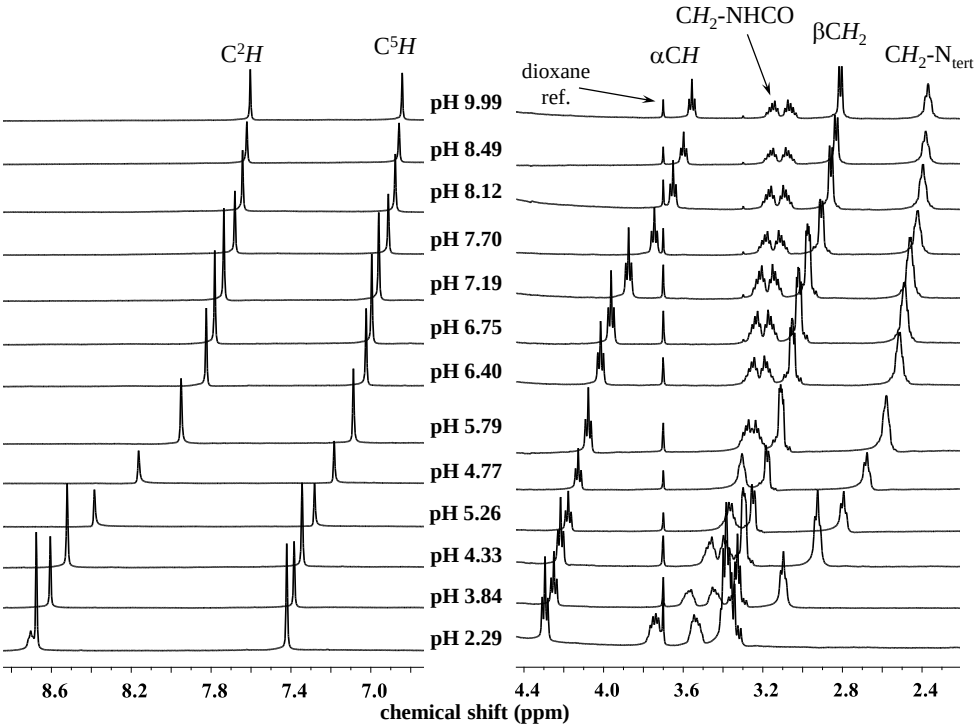

Figure 4.2. pH-dependent ^{1}H NMR spectra of ligand tren3his ($[\mathbf{L}^{1}]_{tot}$ = 0.0019 M, I = 0.1 M NaCl, T = 298 K).

4.1.2. Copper(II) complexes of tren3his

The speciation in the copper(II)-$\mathbf{L^1}$ system proved to be rather complicated. Therefore, beside the combined evaluation of potentiometric and CD data, pH-dependent EPR titrations were also used to uncover the equilibrium properties. The two independent sets of formation constants, derived from our potentiometric/CD and EPR titrations, are in good agreement (Table 4.1). These formation constants are related to a given composition, which in turn may exist in forms of structural isomers. Based on the spectroscopic information discussed later, we were able to identify the main isomers, but due to the polydentate nature of the ligand others with smaller mole fraction may also exist.

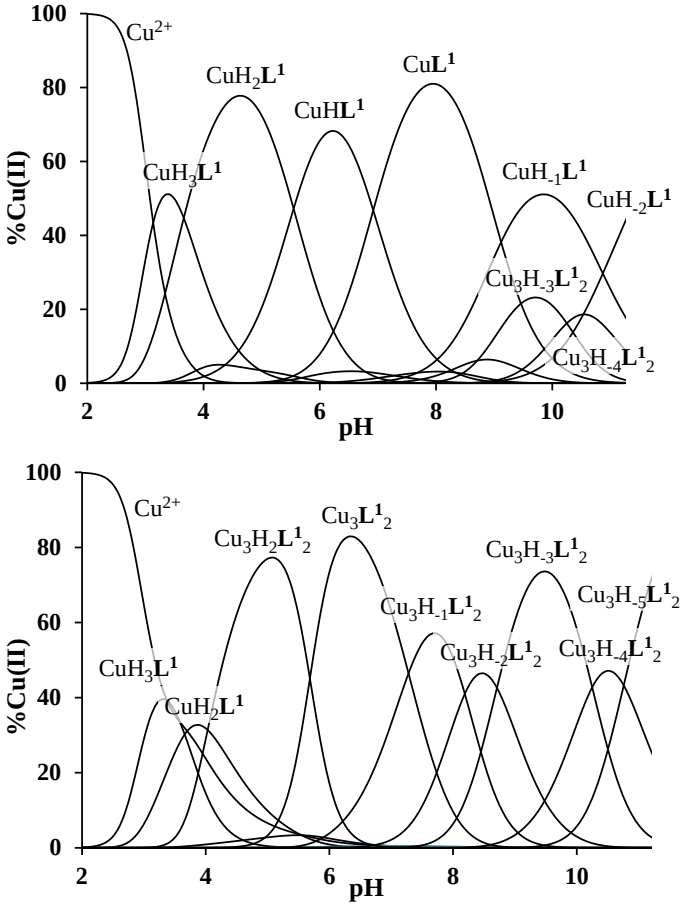

Figure 4.3. Speciation diagrams of Cu(II)-$\mathbf{L^1}$ 1:1 (up) and 3:2 (down) systems ($[\mathbf{L^1}]_{tot}$ = $[Cu(II)]_{tot}$ = 0.001 M and 1.5×$[\mathbf{L^1}]_{tot}$ = $[Cu(II)]_{tot}$ = 0.001 M respectively, I = 0.1 M NaCl, T = 298 K).

Table 4.1. Formation constants and spectroscopic (UV-Vis, CD and EPR) parameters of copper(II)-$\mathbf{L^1}$ complexes (estimated errors in parentheses (last digit), I = 0.1 M NaCl, T = 298 K).

$Cu_pH_qL_r$	$\log\beta_{pqr}$ [a]	$\lambda^{d\text{-}d}_{max}$ (nm), ε ($M^{-1}cm^{-1}$)	λ^{CD}_{max} (nm), $\Delta\varepsilon$ ($M^{-1}cm^{-1}$)	g_o	A_o (G)
131	29.32(1)[a] [29.21(3)][b]	650, 56.3	630, 0.41 312, -0.42	2.136(2)	61(1)
121	25.66(1)[a] [25.54(4)][b]	602, 99.9	624, 0.96 318, -0.93	2.109(6)	71.3(7)
111	20.11(1)[a] [19.95(9)][b]	614, 107.7	654, 0.76 318, -0.77	2.112(6)	68.7(6)
101	13.19(1)[a] [13.18(9)][b]	638, 100.5	690, 0.65 318, -0.55	2.111(6)	59.5(6)
1-11	4.07(2)[a] [4.01(6)][b]	626, 155.0	715, 0.64 612, -0.15	2.106(3)	9(5)
1-21	-6.80(2)[a] [-6.84(5)][b]	596, 200.8	708, -0.62 582, 0.60 312, 1.64	2.089(3)	63(3)
322	49.57(2)[a] [49.60(4)][b]	626, 189.0	636, 1.82 318, -1.82	2.102(3)[c] 2.133(2)[c]	64.1(7)[c] 48.7(6)[c]
302	38.20(3)[a,d]	630, 198.2	678, 1.57 318, -1.30	2.103(2)	57(3)
3-12	30.93(4)[a,d]	638, 264.7	702, 1.46 546, 0.30 312, -1.09	2.124(3)	60(2)
3-22	22.73(4)[a,d]	632, 262.2	708, 1.92 594, -0.49	2.106(4)	61(3)
3-32	14.03(4)[a,d]	616, 304.3	714, 1.57 612, -0.05 312, 0.42	2.099(2)	51(4)
3-42	3.77(4)[a,d]	614, 329.5	690, -0.88 576, 1.57 318, 5.20	2.107(3)	52(3)
3-52	-6.99(3)[a,d]	610, 320.5	702, -0.38 582, 1.57 318, 4.40	2.097(3)	56(2)

[a] $\log\beta$ values derived from the combined potentiometric and CD spectroscopic data
[b] $\log\beta$ values derived from the pH-dependent EPR data
[c] EPR parameters of $Cu_3H_2\mathbf{L^1}_2$ component spectra; see text in details
[d] during the evaluation of EPR spectra, the formation constants of these species were taken from the potentiometric data, due to their weakly resolved and nearly identical spectra.

In equimolar solution, four differently protonated mononuclear complexes are formed up to pH 8 (Figure 4.3). Both the spectroscopic data ($\lambda^{d\text{-}d}_{max}$ = 650 nm, weak positive CD peak at ~ 630 nm, g_o = 2.136, A_o = 61 G) and the equilibrium constant of the reaction $Cu^{2+} + H_3\mathbf{L^1} = CuH_3\mathbf{L^1}$ ($\log K = \log\beta_{131} - \log\beta_{031} = 7.92$) are consistent with a $\{3N_{im}\}$ coordination in $CuH_3\mathbf{L^1}$ [41, 65]. In case of peptides with N-terminal histidine, the *bis*-histamine-like $\{2NH_2,2N_{im}\}$ coordination is preferred in the neutral pH range [42, 115]. In principle, this binding mode may appear already in $CuH_2\mathbf{L^1}$. However, during the

successive deprotonations $CuH_3\mathbf{L^1} \rightarrow CuH_2\mathbf{L^1} \rightarrow CuH\mathbf{L^1} \rightarrow Cu\mathbf{L^1}$ the visible, CD and EPR spectra all show significant changes (Figures 4.4, 4.5, 4.6). Moreover, the pK values of the above-mentioned successive deprotonations (p$K_{CuH_3\mathbf{L^1}}$ = 3.71, p$K_{CuH_2\mathbf{L^1}}$ = 5.55, p$K_{CuH\mathbf{L^1}}$ = 6.92) are considerably smaller than the corresponding values of the free ligand (p$K_{H_3\mathbf{L^1}}$ = 6.34, p$K_{H_2\mathbf{L^1}}$ = 7.25, p$K_{H\mathbf{L^1}}$ = 7.85), indicating copper(II) promoted deprotonations. All these facts suggest continuous changes in the coordination environment of the metal ion during the processes $CuH_3\mathbf{L^1} \rightarrow CuH_2\mathbf{L^1} \rightarrow CuH\mathbf{L^1} \rightarrow Cu\mathbf{L^1}$.

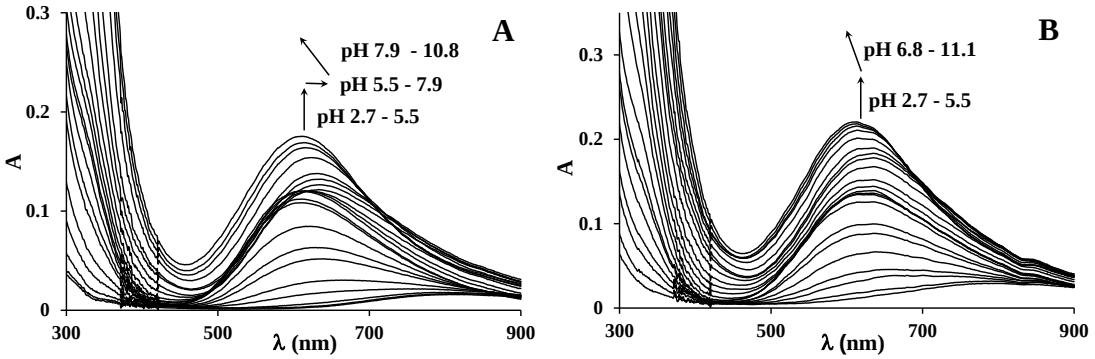

Figure 4.4. pH-dependent UV-Vis spectra of Cu(II)-$\mathbf{L^1}$ 1:1 (**A**) and 3:2 (**B**) systems (**A**: $[\mathbf{L^1}]_{tot}$ = $[Cu(II)]_{tot}$ = 0.0013 M, **B**: 1.5×$[\mathbf{L^1}]_{tot}$ = $[Cu(II)]_{tot}$ = 0.0019 M, I = 0.1 M NaCl, T = 298 K). Corresponding calculated individual molar spectra can be found in Figure 4.8.

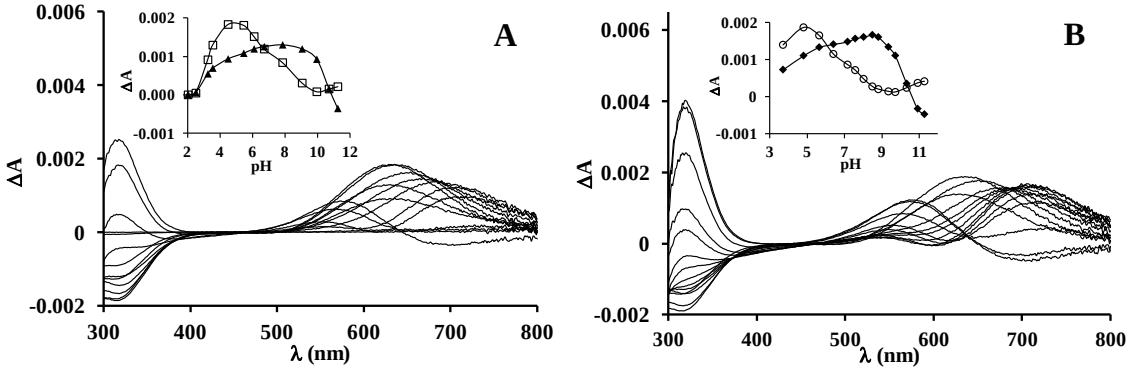

Figure 4.5. pH-dependent CD spectra of Cu(II)-$\mathbf{L^1}$ 1:1 (**A**) and 3:2 (**B**) systems ($[\mathbf{L^1}]_{tot}$ = $[Cu(II)]_{tot}$ = 0.0025 M and 1.5×$[\mathbf{L^1}]_{tot}$ = $[Cu(II)]_{tot}$ = 0.0037 M respectively, I = 0.1 M NaCl, T = 298 K). Insert: pH-dependence of ΔA at 630 nm (□ and ○) and 700 nm (▲ and ♦). Corresponding calculated individual molar spectra can be found in Figure 4.9.

The spectroscopic parameters of $CuH_2\mathbf{L^1}$ ($\lambda^{d\text{-}d}_{max}$ = 602 nm, g_o = 2.109, A_o = 71.3 G, Table 4.1.) indicate considerably increased ligand field strength as compared to $CuH_3\mathbf{L^1}$, which supports the coordination of four nitrogens in $CuH_2\mathbf{L^1}$, thus a $\{NH_2,3N_{im}\}$ binding mode in the equatorial plane of copper(II). The copper(II) promoted deprotonation of the second amino nitrogen of $\mathbf{L^1}$ should lead to the highly stable *bis*-histamine-like $\{2NH_2,2N_{im}\}$ coordination in the equatorial plane of $CuH\mathbf{L^1}$. However, the slight red shift of the d-d transitions and the decrease of A_o of this species ($\lambda^{d\text{-}d}_{max}$ = 614 nm, g_o = 2.112, A_o = 68.7 G, Table 4.1.) as compared to $CuH_2\mathbf{L^1}$, indicate some distortion of the crystal field around the metal ion. Considering that five N-donors are available for metal ion

binding in CuH$\mathbf{L}^{\mathbf{1}}$, this distortion is most likely caused by the axial coordination of the third imidazole nitrogen {$2NH_2$,$2N_{im}$+N_{im}}. During the next copper(II) promoted deprotonation (CuH$\mathbf{L}^{\mathbf{1}}$ → Cu$\mathbf{L}^{\mathbf{1}}$) an even more important red shift of the visible/CD spectra and decrease of A_o was observed ($\lambda^{d\text{-}d}_{max}$ = 638 nm, g_o = 2.111, A_o = 59.5 G, Table 4.1). Since the 6N coordinated *tris*-histamine-like complex of copper(II) is not known even in the case of histamine [114], the observed spectral changes are due to the replacement of the axially coordinated imidazole ring by the third amino group in Cu$\mathbf{L}^{\mathbf{1}}$ ({$2NH_2$,$2N_{im}$+NH_2}, Scheme 4.2).

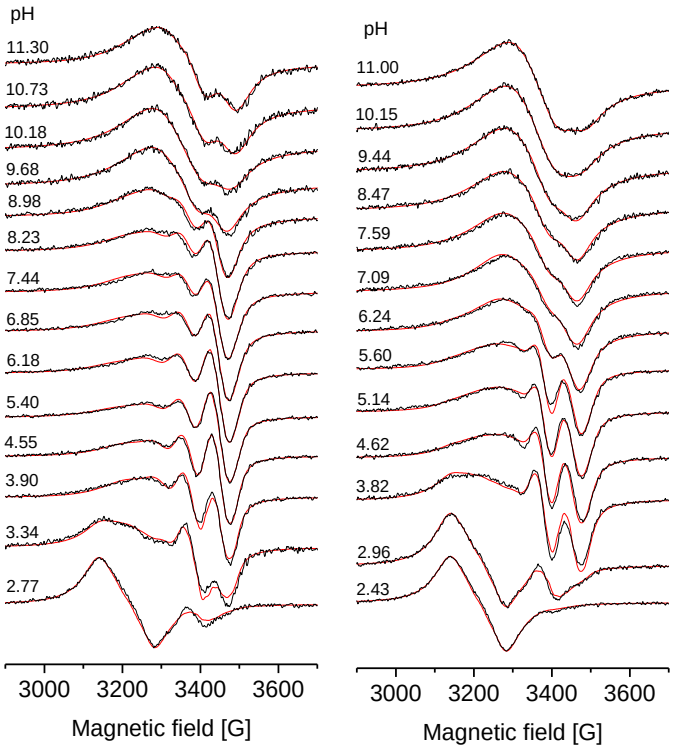

Figure 4.6. pH-dependent EPR spectra of Cu(II)-$\mathbf{L}^{\mathbf{1}}$ 1:1 (left) and 3:2 (right) system (0.95×$[\mathbf{L}^{\mathbf{1}}]_{tot}$ = $[Cu(II)]_{tot}$ = 0.0016 M and 1.4×$[\mathbf{L}^{\mathbf{1}}]_{tot}$ = $[Cu(II)]_{tot}$ = 0.0023 M respectively, *I* = 0.1 M NaCl, *T* = 298 K). Black: measured, red: simulated spectra.

At higher pH, further deprotonations were observed leading to the species $CuH_{-1}\mathbf{L}^{\mathbf{1}}$ and $CuH_{-2}\mathbf{L}^{\mathbf{1}}$. Due to the notable stability of Cu$\mathbf{L}^{\mathbf{1}}$ (log*K* = 13.19), these deprotonations take place only above pH 8 (p$K_{Cu\mathbf{L}^{\mathbf{1}}}$ = 9.12 and p$K_{CuH_{-1}\mathbf{L}^{\mathbf{1}}}$ = 10.87), at higher pH than usual for peptides with N-terminal His moieties [38, 114]. Such processes can be related to the metal ion promoted deprotonation of amide nitrogen(s), water molecule(s), or, in certain cases, coordinated imidazole ring(s) [116]. The increasing negative contribution in the visible CD spectra of $CuH_{-1}\mathbf{L}^{\mathbf{1}}$ and $CuH_{-2}\mathbf{L}^{\mathbf{1}}$ indicates metal ion induced deprotonation and coordination of amide nitrogen(s) in our system [117], according to the high affinity of copper(II) toward amide nitrogens. The rather unique visible CD spectrum ('inverse couplet', Figure 4.9 A), as well as the visible and EPR spectra, determined for the species $CuH_{-2}\mathbf{L}^{\mathbf{1}}$ is nearly identical to those of the CuH_{-2}L complexes of Ac-HGG-NH_2, Ac-HGGG-NH_2, Ac-HGGGW-NH_2 and several other analogs of prion protein octarepeat

domain [118-120]. Based on this similarity, we suggest $\{N_{im},N^{-},N_{tert},N^{-}\}$ coordination in the equatorial plane of $CuH_{-2}\mathbf{L^1}$ (Scheme 4.2).

The presence of at least ten potential nitrogen donors in $\mathbf{L^1}$ provides the possibility to the formation of oligonuclear complexes, too. Indeed, at 3:2 metal-to-ligand ratio the solution was clear in the whole studied pH range, but precipitate was observed above pH 6 at 2:1 metal-to-ligand ratio. This observation indicates the formation of trinuclear complexes with $Cu_3H_x\mathbf{L^1}_2$ stoichiometry. The presence of such species, beside the mononuclear complexes, was confirmed by MALDI-TOF MS (Figure 4.7). The obtained isotopic distribution patterns are in very good agreement with those calculated for the molecular ions $[CuH_{-1}\mathbf{L^1}]^+$ (=$[C_{24}H_{38}\ N_{13}O_3Cu]^+$) and $[Cu_3H_{-5}\mathbf{L^1}_2]^+$ (=$[C_{48}H_{73}N_{26}O_6Cu_3]^+$). There are differences, however, between the estimated and measured molecular weights (619.24/620.36 and 1298.41/1301.32), which corresponds to the uptake of one and three protons, respectively. The measured higher molecular weights are due to the reduction of Cu^{2+} to Cu^+ and the corresponding uptake of one proton per metal ion during the ionization process. Identical observations were reported in the literature related to MALDI-TOF MS studies of other copper(II) complexes, formed with cyclen/cyclam derivatives [121], some pseudo-peptides [122] and peptides [123].

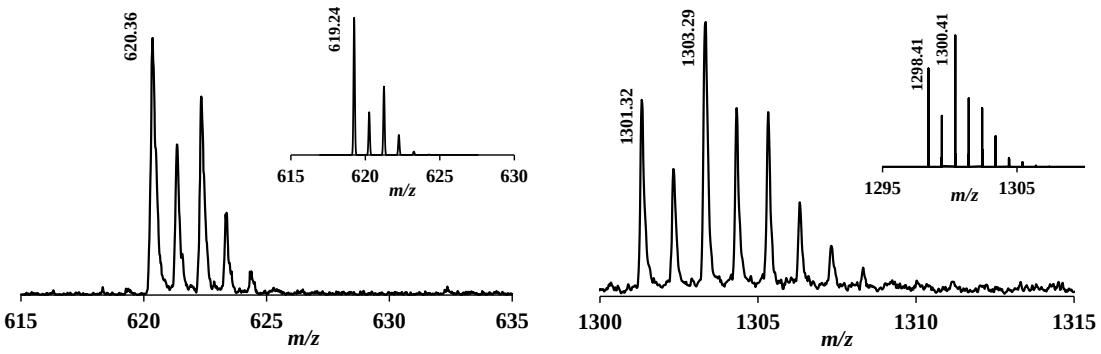

Figure 4.7. MALDI-TOF MS spectra measured in the Cu(II)-$\mathbf{L^1}$ 1:1 (left) and 3:2 (right) systems. Insert: Calculated spectra of the corresponding complexes ($[C_{24}H_{38}N_{13}O_3Cu]^+$ and $[C_{48}H_{73}N_{26}O_6Cu_3]^+$, respectively).

Since trinuclear complexes may have several protonation states, the copper(II)-$\mathbf{L^1}$ 3:2 system presents a complicated, but rather obvious speciation behavior (Figure 4.3). $Cu_3H_2\mathbf{L^1}_2$ is the first trinuclear complex formed around pH 5. Considering the ten available N-donors (the additional two are still protonated), the three copper(II) ions have 3/4N coordination environments, similarly to those in the mononuclear complexes $CuH_3\mathbf{L^1}$ and $CuH_2\mathbf{L^1}$. Indeed, the evaluation of the pH-dependent EPR spectra indicated that the spectrum of $Cu_3H_2\mathbf{L^1}_2$ is the superposition of two, rather distinct component spectra having similar g_0 values to $CuH_3\mathbf{L^1}$ and $CuH_2\mathbf{L^1}$ (Table 4.1). All trinuclear complexes have detectable EPR spectra (Figures 4.6. and A.22), indicating weakly interacting metal ions. Nevertheless, only the spectra of $Cu_3H_2\mathbf{L^1}_2$ and $Cu_3\mathbf{L^1}_2$ show comparatively well-resolved hyperfine structures. In $Cu_3\mathbf{L^1}_2$ the six N-terminal His units create *bis*-histamine-like coordination environment around the three metal ions. This is similar to that observed in

Cu$\mathbf{L}^{\mathbf{1}}$, except the axially coordinated amino group present in the latter. Accordingly, the UV-Vis (and CD) spectra of $Cu_3\mathbf{L}^{\mathbf{1}}_2$ shows ~ 20 nm blue shift as compared to that of Cu$\mathbf{L}^{\mathbf{1}}$ (Table 4.1). Although other alternatives are also possible, the most likely structure of $Cu_3\mathbf{L}^{\mathbf{1}}_2$ is depicted in Scheme 4.2. In principle, the three legs of $\mathbf{L}^{\mathbf{1}}$ may induce the formation of higher oligomers with the composition $(Cu_3\mathbf{L}^{\mathbf{1}}_2)_n$ (n > 1), too. However, the linewidth of the isotropic EPR spectra, especially at lower magnetic fields, is sensitive to the radius of the complex molecules. Since intensity loss was not observed, and the linewidth of the EPR spectrum of $Cu_3\mathbf{L}^{\mathbf{1}}_2$ is similar to that of the analogous $Cu_2(dhen)_2$ complex [114], the formation of higher oligomers is at least negligible.

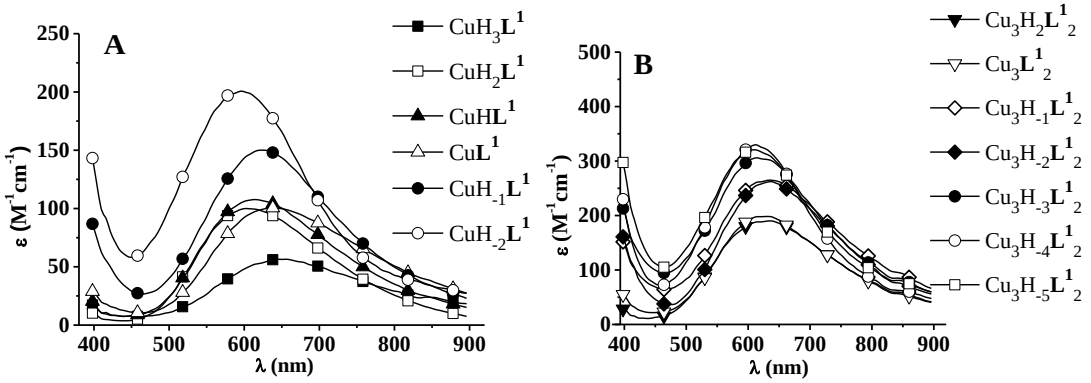

Figure 4.8. Individual molar UV-Vis spectra of mononuclear (**A**) and trinuclear (**B**) Cu(II)-$\mathbf{L}^{\mathbf{1}}$ complexes.

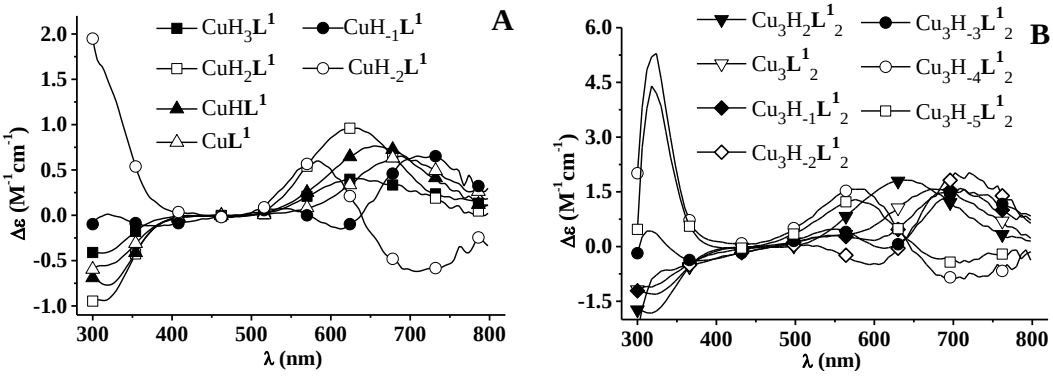

Figure 4.9. Individual molar CD spectra of mononuclear (**A**) and trinuclear (**B**) Cu(II)-$\mathbf{L}^{\mathbf{1}}$ complexes.

Above pH 6, consecutive deprotonations of the trinuclear complexes were observed (Figure 4.3). The characteristic CD spectra of $CuH_{-1}\mathbf{L}^{\mathbf{1}}$ and $CuH_{-2}\mathbf{L}^{\mathbf{1}}$ are very similar to those of $Cu_3H_{-2}\mathbf{L}^{\mathbf{1}}_2$ and $Cu_3H_{-4}\mathbf{L}^{\mathbf{1}}_2$, respectively (Figure 4.9). Accordingly, in the latter species two copper(II) ions have similar $\{N_{im},N^-,N_{tert},N^-\}$ coordination environment to the corresponding mononuclear complexes. This in turn means that similar deprotonation processes take place at more than one pH unit lower in the trinuclear complexes as compared to the mononuclear ones. This is probably due to the stabilization by the axial nitrogen coordination, which is present only in the mononuclear Cu$\mathbf{L}^{\mathbf{1}}$ and $CuH_{-1}\mathbf{L}^{\mathbf{1}}$ complexes. The fifth deprotonation ($Cu_3H_{-4}\mathbf{L}^{\mathbf{1}}_2 \rightarrow Cu_3H_{-5}\mathbf{L}^{\mathbf{1}}_2 + H^+$, p$K$ = 10.76) does not

cause considerable change of spectral properties. The central metal ion in the trinuclear complexes, bound to both ligands (Scheme 4.2), has clearly different coordination environment from the other two, since the histamine-like chelate rings belong to two different molecules, and thus fused chelates cannot be formed between them. This coordination mode is identical to that in Cu(His-Gly)$_2$ complex, which also undergoes a single deprotonation step at high pH [44, 115].

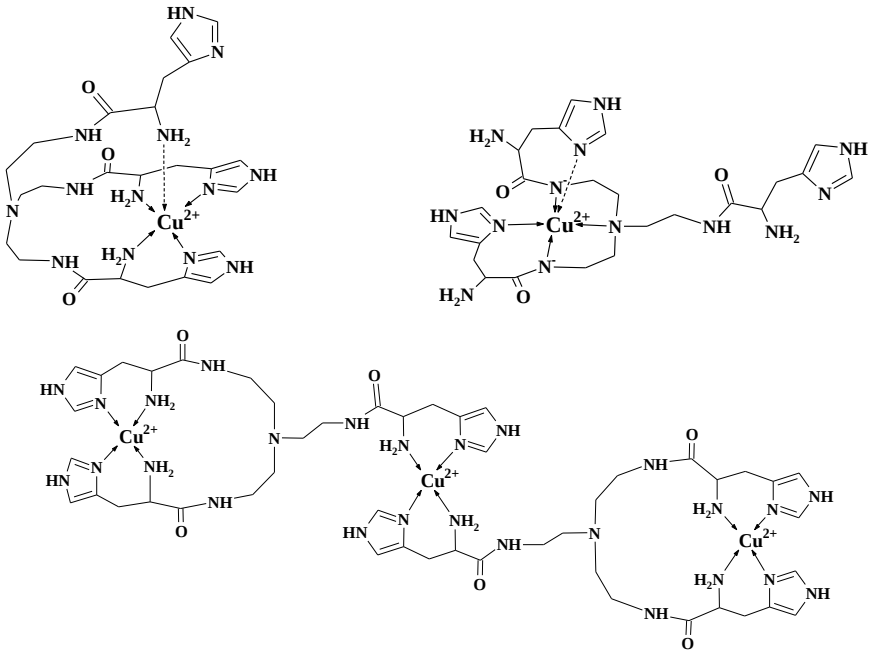

Scheme 4.2. Proposed schematic structure of copper(II)-**L**$^{\mathbf{1}}$ complexes Cu**L**$^{\mathbf{1}}$, CuH$_{-2}$**L**$^{\mathbf{1}}$ and Cu$_3$**L**$^{\mathbf{1}}{}_2$ (dashed arrow line indicates possible axial coordination).

4.1.3. Zinc(II) complexes of tren3his

Potentiometric titrations, MALDI-TOF MS and ^{1}H NMR measurements were carried out in order to obtain information on the Zn(II)-**L^1** complexes. Similarly to the copper(II)-**L^1** system, clear solution was obtained in the whole studied pH range up to 3:2 metal-to-ligand ratio, but precipitation was observed at higher metal ion excess. The titration curves of Zn(II)-**L^1** 0:1, 1:1 and 3:2 systems, along with the formation constants of the metal complexes are presented on Figure 4.10.

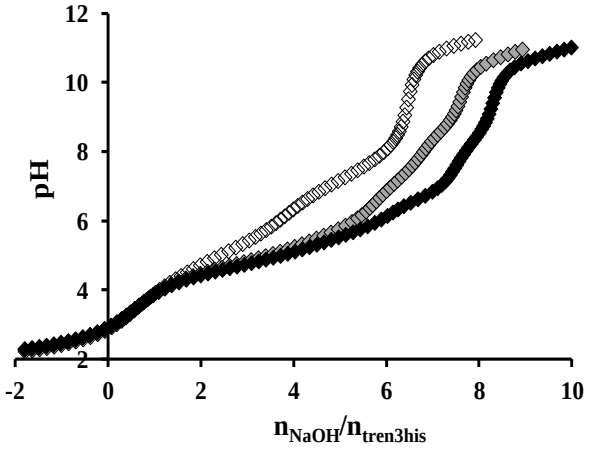

$Zn_pH_qL_r$	log β_{pqr}	pK
131	24.76(2)	4.90
121	19.86(1)	5.42
111	14.44(1)	6.49
101	7.95(1)	8.10
1-11	-0.15(2)	10.24
1-21	-10.39(3)	
302	22.87(4)	
3-22	9.62(3)	8.04
3-32	1.58(4)	8.90
3-42	-7.32(4)	

Figure 4.10. Titration curves in Zn(II)-**L^1** 0:1 (white), 1:1 (gray) and 3:2 (black) systems (left); formation and deprotonation constants of zinc(II) complexes (right). Estimated errors in parentheses (last digit), I = 0.1 M NaCl, T = 298 K.

The evaluation of potentiometric data indicated the formation of complexes with ZnH_x**L^1** and Zn_3H_x**L$^1_2$** stoichiometries. The presence of such complexes has been verified by MALDI-TOF MS measurements (Figure 4.11). The detected *m/z* values and isotopic distribution patterns are in very good agreement with the calculated spectra for $[ZnH_{-1}$**L^1**$]^+$ (= $[C_{24}H_{38}N_{13}O_3Zn]^+$) and $[Zn_3H_{-4}$**L$^1_2$**$(ClO_4)]^+$ (= $[C_{48}H_{74}N_{26}O_{10}ClZn_3]^+$).

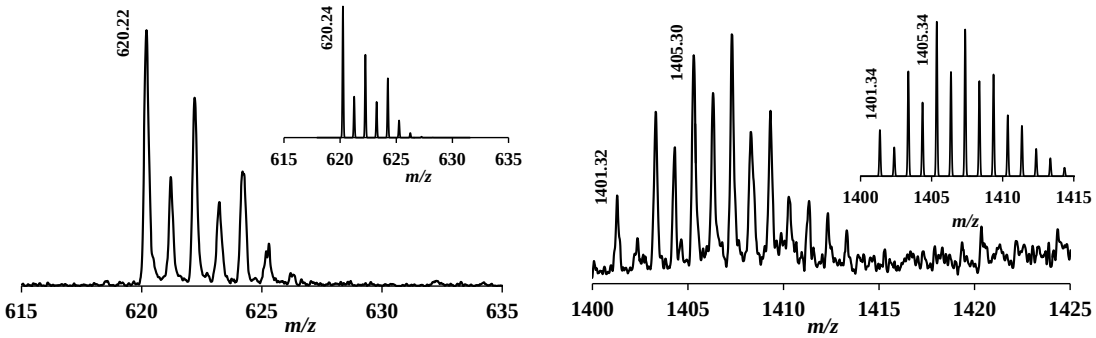

Figure 4.11. MALDI-TOF MS spectra measured in the Zn(II)-**L^1** 1:1 (left) and 3:2 (right) systems. Insert: Calculated spectra of the corresponding complexes ($[C_{24}H_{38}N_{13}O_3Zn]^+$ and $[C_{48}H_{74}N_{26}O_{10}ClZn_3]^+$).

The distribution of the differently protonated complexes is presented on Figure 4.12. The monocomplexes ZnH_3**L^1** and ZnH_2**L^1** are formed around pH 4-5 in a strongly

overlapped manner. The selective broadening of ^{1}H NMR signals of the imidazole protons (C^2H, C^5H) around pH 5 (Figure 4.13.) indicates imidazole coordination in these species.

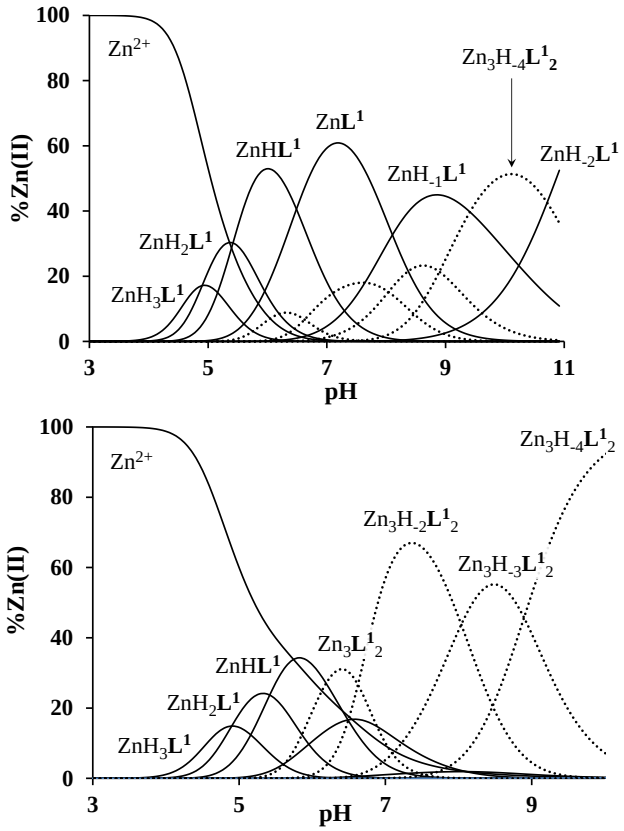

Figure 4.12. Speciation diagrams of Zn(II)-$\mathbf{L^1}$ 1:1 (up) and 3:2 (down) systems; dotted lines represent the trinuclear species ($[\mathbf{L^1}]_{tot}$ = $[Zn(II)]_{tot}$ = 0.001 M and 1.5×$[\mathbf{L^1}]_{tot}$ = $[Zn(II)]_{tot}$ = 0.001 M, I = 0.1 M NaCl, T = 298 K).

After three overlapped deprotonations, the major species ZnH$\mathbf{L^1}$ (at pH ~ 5.8) and Zn$\mathbf{L^1}$ (at pH ~ 7.2) are formed. Approaching pH 7, the ^{1}H NMR spectra show downfield shift upon coordination of both imidazole and αCH signals, and an interesting duplication of a tren CH_2 signal at ~ 2.4 ppm can be observed, too (Figure 4.13 dashed frame). This phenomenon is most likely due to the formation of a macrochelate ring associated with a {$2N_{im}$,$2NH_2$} *bis*-histamine-like binding, which causes inequivalence of the N_{tert}-CH_2 protons participating in the macrochelate structure. The relations of the deprotonation constants indicate the additional coordination of the third histidine 'pod' in ZnH$\mathbf{L^1}$ and Zn$\mathbf{L^1}$ complexes, too. The pK values of the protonated complexes (p$K_{ZnH_2\mathbf{L^1}}$ = 5.42, p$K_{ZnH\mathbf{L^1}}$ = 6.49) are lower than those of the free ligand (p$K_{H_2\mathbf{L^1}}$ = 7.21, p$K_{H\mathbf{L^1}}$ = 7.85), and also than the analogous copper(II) containing species (p$K_{CuH_2\mathbf{L^1}}$ = 5.55, p$K_{CuH\mathbf{L^1}}$ = 6.92). As a consequence, 5N coordination can be proposed in Zn$\mathbf{L^1}$ (Scheme 4.3).

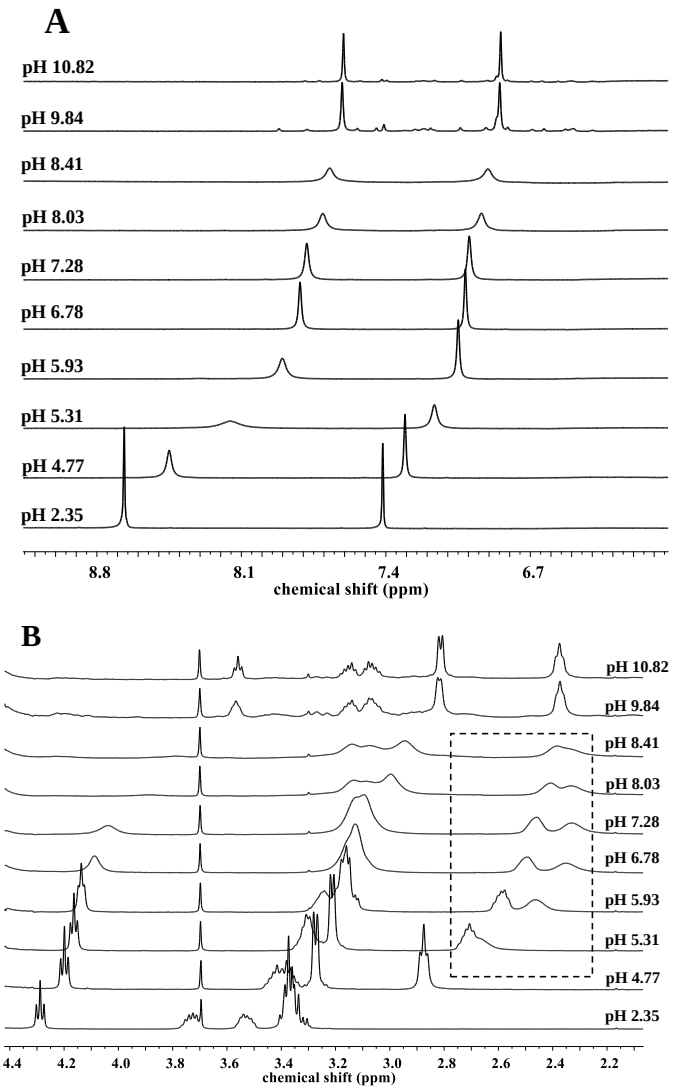

Figure 4.13. Aromatic (**A**) and aliphatic (**B**) region of pH-dependent ^{1}H NMR spectra of Zn(II)-$\mathbf{L}^{\mathbf{1}}$ 1:1 system (in H_2O/D_2O, $[\mathbf{L}^{\mathbf{1}}]_{tot} = [Zn(II)]_{tot} = 0.0017$ M, $I = 0.1$ M NaCl, $T = 298$ K).

Under basic conditions the complex Zn$\mathbf{L}^{\mathbf{1}}$ releases two additional protons (pK = 8.10 and 10.24). Above pH 7 the mentioned inequivalence of N_{tert}-CH_2 protons ceases, and the signals of αCH protons are strongly upfield shifted on the ^{1}H NMR spectra (Figure 4.13). The formation of slow exchanging complexes was not detected. The coordination of amide nitrogen(s) is indeed unlikely, since N-terminal histidines with $\{N_{im},NH_2\}$ binding site do not act as anchor for amide deprotonations, and such processes have never been observed in zinc(II)-His-Gly and related systems [42, 45, 88, 124]. These deprotonations are more likely related to the formation of mixed hydroxo complexes ($ZnH_{-1}\mathbf{L}^{\mathbf{1}}$ = Zn$\mathbf{L}^{\mathbf{1}}$(OH) and $ZnH_{-2}\mathbf{L}^{\mathbf{1}} = Zn\mathbf{L}^{\mathbf{1}}(OH)_2$).

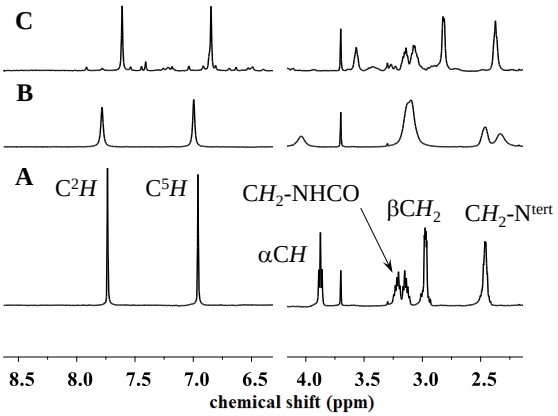

Figure 4.14. ^{1}H NMR spectra of $\mathbf{L^1}$ (**A**) and Zn(II)-$\mathbf{L^1}$ 1:1 (**B,C**) systems. pH = 7.2 (**A**), 7.3 (**B**) and 9.8 (**C**). (in H_2O/D_2O, $[\mathbf{L^1}]_{tot}$ = 0.0023 M, I = 0.1 M NaCl, T = 298 K).

Interestingly, considerable amount of trinuclear complexes is already formed in equimolar solution, according to potentiometric and NMR data (Figures 4.12-4.14, small peaks around pH 10). This indicates that $\mathbf{L^1}$ is able to bind more than one Zn^{2+} with nearly equivalent binding affinities, resulting a significant amount of unbound $\mathbf{L^1}$ above pH 7 in equimolar solution (signals of the free ligand and that of the fast exchanging monocomplexes manifest as average). At 3:2 metal-to-ligand ratio, trinuclear complexes become dominant in neutral and basic solutions (Figure 4.12). At pH 6 the parent $Zn_3\mathbf{L^1}_2$ is formed; this stoichiometry implies that the zinc(II) ions are coordinated by two arms of the tripod, originated from either the same or two different ligand molecules (Scheme 4.3). Such M_3L_2 type cluster formation is well described in the literature regarding tripodal ligand complexes [125], and a similar species was detected in the copper(II)-$\mathbf{L^1}$ system, too.

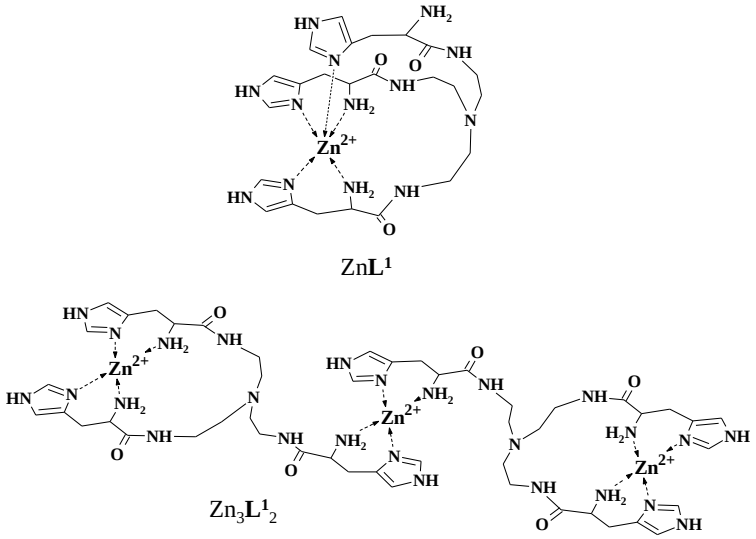

Scheme 4.3. Proposed structures of mono- and trinuclear Zn(II)-$\mathbf{L^1}$ complexes.

Since the metal ions in $Zn_3\mathbf{L^1}_2$ are coordinated by less nitrogen donors than in $Zn\mathbf{L^1}$, the trinuclear complex is more prone to deprotonation. The formation of $Zn_3H_{-2}\mathbf{L^1}_2$ and

$Zn_3H_{-3}\mathbf{L^1}_2$ results in considerably broadened ^{1}H NMR spectra. On the other hand, parallel with the formation of $Zn_3H_{-4}\mathbf{L^1}_2$ (pH 8-10) numerous narrow signals appear on the aromatic region (Figure 4.15). The number of peaks cannot be explained by the speciation of the complexes based on the potentiometric model; at pH 10, the observed at least 22 different imidazole signals seem to correspond to a single (de)protonation state (at this pH ~95% of zinc(II) is bound in $Zn_3H_{-4}\mathbf{L^1}_2$). Among them, at least 7 different C^2H/C^5H imidazole proton pairs can be identified on the corresponding TOCSY spectrum (Figure 4.16).

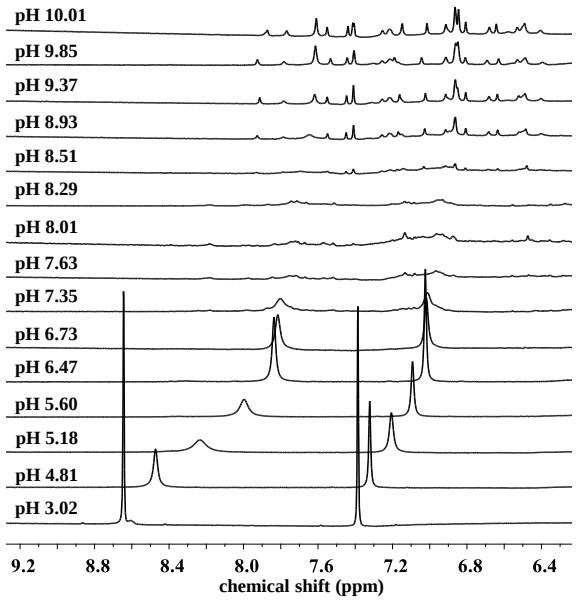

Figure 4.15. Aromatic region of the pH-dependent ^{1}H NMR spectra of Zn(II)-$\mathbf{L^1}$ 3:2 system (in H_2O/D_2O, $[\mathbf{L^1}]_{tot}$ = 0.0023 M, I = 0.1 M NaCl, T = 298 K).

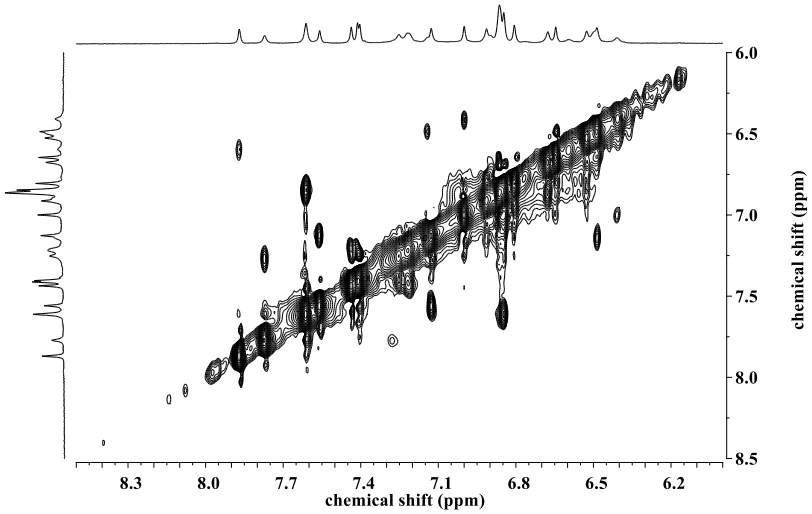

Figure 4.16. ^{1}H-^{1}H TOCSY NMR spectrum of Zn(II)-$\mathbf{L^1}$ 3:2 system at pH = 9.8 (in H_2O/D_2O, I = 0.1 M NaCl, T = 298 K).

The observed multiplication of the signals can imply either the inequivalence of imidazole protons in the trinuclear species due to the conformational differences, or the formation of differently composed ($Zn_{3n}H_{-4n}\mathbf{L^1}_{2n}$, n ≥ 1) oligomer complexes (Scheme 4.4) with the same metal-to-ligand ratio. The size of such oligomers would be high enough to have detectable variance in their hydrodynamic radii. Accordingly, ^{1}H DOSY measurements indicate the presence of several complexes with moderately different diffusion parameters, which are, however, clearly distinct from that of the free ligand (at 7.61 and 6.85 ppm, Figure 4.17). This observation supports the presence of several oligomers with different compositions. Applying the approximate rule $(D_{ref}/D_x)^3 = M_x/M_{ref}$ (where *D* and M stands for the diffusion coefficient and molar mass, ref. values: dioxane and acetonitrile), one can estimate several oligomers formed by the association of 2-8 trinuclear complexes (although uncertainties must be taken into account due to the non-spherical geometry and different hydration of the ligand and its Zn(II) complexes).

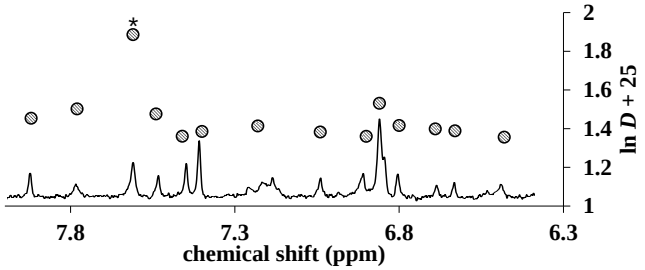

Figure 4.17. Aromatic region of ^{1}H NMR spectra in Zn(II)-$\mathbf{L^1}$ 3:2 system, and the measured diffusion coefficients by ^{1}H DOSY NMR. * indicates the C^2H signal of the free ligand, the corresponding C^5H signal at 6.85 ppm is not resolved (pH = 10, $[\mathbf{L^1}]_{tot}$ = 0.0019 M, $[Zn(II)]_{tot}$ = 0.0027 M, *I* = 0.1 M NaCl, *T* = 298 K).

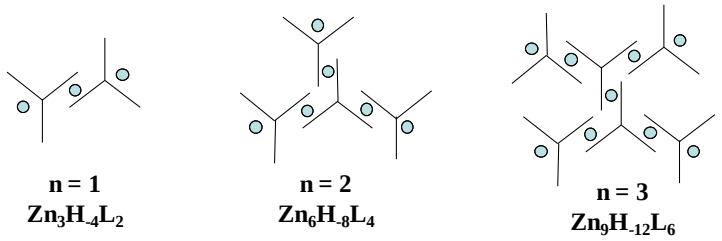

Scheme 4.4. Possibilities of oligomer formation in Zn(II)-$\mathbf{L^1}$ 3:2 system.

Although the presence of several oligomers and the complexity of the NMR spectra do not allow doubtless identification of the coordinating groups and complex compositions, the broadened signals around pH 8 may indicate mixed hydroxo complexes and even their oligomerization through hydroxo bridges. However, it seems clear that the formation of $Zn_3H_{-4}\mathbf{L^1}_2$ involves a new type of bridging unit. The TOCSY spectrum (Figure 4.16) indicates that the imidazole C^2H/C^5H signals are scattered in a wide range; some of the imidazole signals are considerably upfield-shifted (Figure 4.15). This may imply the presence of imidazolato bridges in these species, participating in the assembly of $(Zn_3H_{-4}\mathbf{L^1}_2)_n$ complexes, which results in slow ligand exchange processes.

4.2. PROTONATION AND COORDINATION PROPERTIES OF NTA3HIS (L^2)

The second prepared ligand during my work was the C_3 symmetrical nta3his, the C-terminal counterpart of tren3his. Accordingly, N- and O-donor groups are present in this compound, and the position of the amide group is inversed as compared to $\mathbf{L^1}$.

4.2.1. Protonation of nta3his

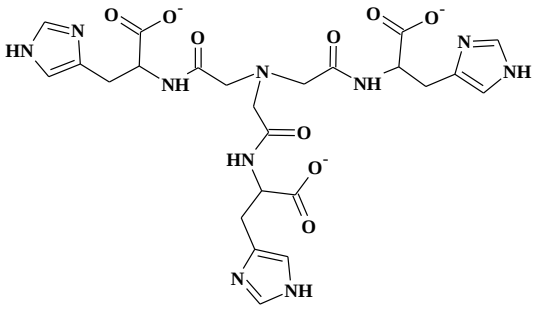

Scheme 4.5. Schematic structure of the ligand nta3his ($\mathbf{L^2}$).

For the C-terminal histidine containing $\mathbf{L^2}$ ligand (Scheme 4.5), six p*K* values could be determined between pH 2-11 (Figure 4.18). The deprotonation processes in the acidic and neutral pH range are more separated than that observed in the tren3his system: in the acidic region the carboxylic, above pH 6 the imidazolium groups deprotonate distinctively. The average imidazole p*K* values of the two ligands ($pK_{im,\mathbf{L^1}}$ = 4.63, $pK_{im,\mathbf{L^2}}$ = 7.11) show notable basicity difference. This indicates that, in the latter case, the imidazolium rings are involved in strong H-bonding network with either the negatively charged carboxylates or the nonbonding electron-pair of N_{tert}. Unlike in case of nta, the protonation of the tertiary amine was not detected in the studied pH range.

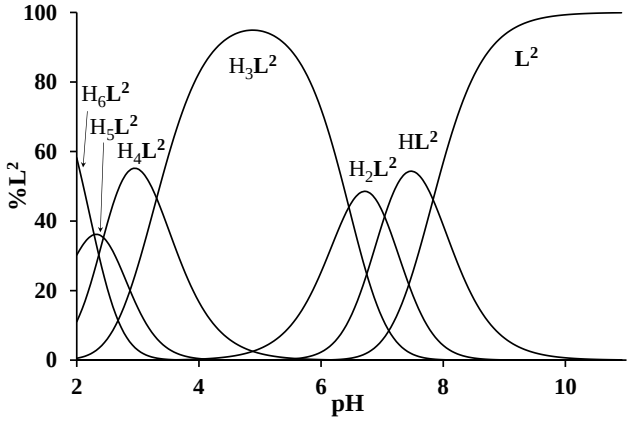

	logβ	pK
$H_6\mathbf{L^2}$	29.36(1)	2.29
$H_5\mathbf{L^2}$	27.07(1)	2.43
$H_4\mathbf{L^2}$	24.64(1)	3.31
$H_3\mathbf{L^2}$	21.33(1)	6.46
$H_2\mathbf{L^2}$	14.87(1)	7.04
$H\mathbf{L^2}$	7.83(1)	7.83

Figure 4.18. Speciation diagram (left) and table of formation and deprotonation constants (right) of the nta3his ligand system ($[\mathbf{L^2}]_{tot}$ = 0.001 M, I = 0.1 M NaCl, T = 298 K).

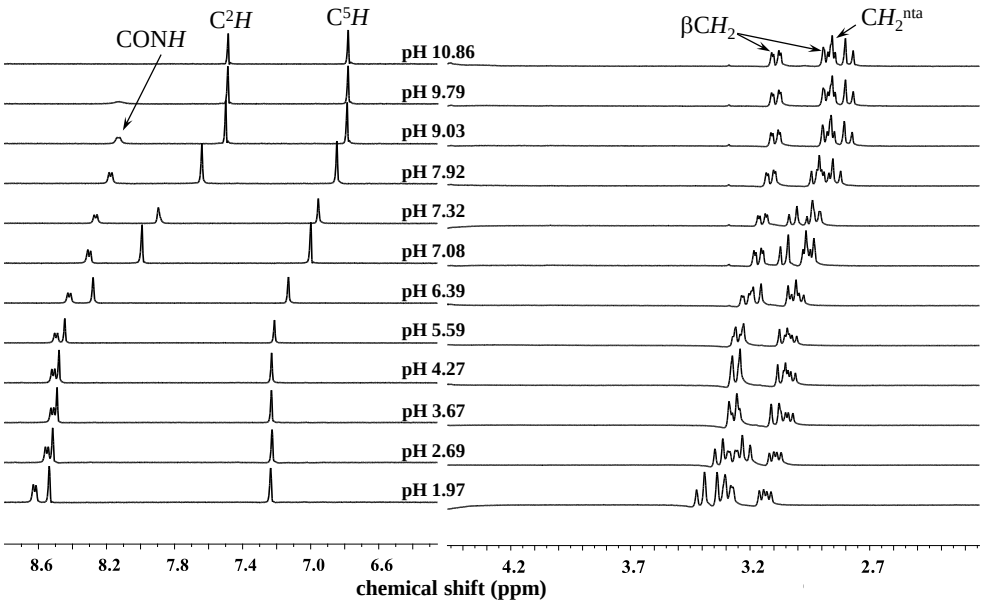

Figure 4.19. pH-dependent ^{1}H NMR spectra of ligand nta3his ($[\mathbf{L}^2]_{tot}$ = 0.0019 M, I = 0.1 M NaCl, T = 298 K).

Figure 4.19. shows the ^{1}H NMR spectra recorded at different pH values in presence of $\mathbf{L}^2$. Both the nta CH_2 and the βCH_2 protons are magnetically inequivalent, resulting (highly overlapping) AB-quartet signals in the whole pH range. The αCH proton is not visible at any pH: it remains concealed by the water signal. This surprisingly high chemical shift is most probably due to the electron withdrawing effect of the neighboring amide NH group; similarly high (4.4-4.5 ppm) chemical shifts were observed for αCH signal in Gly-His and Ala-His peptides [46, 126]. The pH-dependent changes are in agreement with the potentiometrically observed deprotonation processes: the imidazole C^2H, C^5H and the amide NH proton signals shift considerably upfield between pH 6 and 9. Interestingly, the nta CH_2 signal also shifts during the deprotonation of the imidazole moiety; the increased electron density on these groups can be explained by a ceasing H-bond between the N_{tert} and imidazolium groups. It is worth mentioning that the amide NH signal is visible almost up to pH 10, indicating unusually slow proton exchange processes for this group.

4.2.2. Copper(II) complexes of nta3his

In presence of copper(II) ions, $\mathbf{L^2}$ forms mono- and dinuclear complexes at 1:1 and 2:1 metal-to-ligand ratio, respectively. The evaluation of potentiometric measurements did not require the inclusion of trinuclear (3:2) species (Figure 4.20); this itself indicates that nta3his does not provide equivalent binding sites observed for the N-terminal His ligand tren3his.

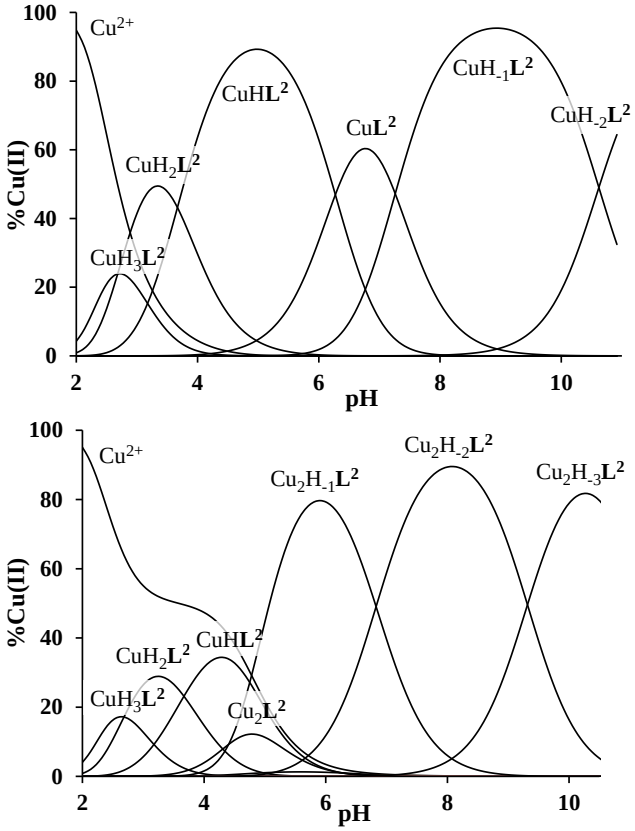

Figure 4.20. Speciation diagrams of Cu(II)-$\mathbf{L^2}$ 1:1 (up) and 2:1 (down) systems ($[\mathbf{L^2}]_{tot}$ = $[Cu(II)]_{tot}$ = 0.001 M and $2\times[\mathbf{L^2}]_{tot}$ = $[Cu(II)]_{tot}$ = 0.001 M respectively, I = 0.1 M NaCl, T = 298 K).

Potentiometric data and pH-dependent UV-Vis spectra were evaluated together in order to calculate the formation constants of the copper(II) species of $\mathbf{L^2}$: logβ and pK values are presented in Table 4.2. along with the characteristic UV-Vis and CD spectroscopic parameters of the complexes.

Table 4.2. Formation constants and spectroscopic (UV-Vis and CD) parameters of copper(II)-$\mathbf{L^2}$ complexes (estimated errors in parentheses (last digit), I = 0.1 M NaCl, T = 298 K).

	logβ	**$\lambda^{d\text{-}d}_{max}$ (nm), ε ($M^{-1}cm^{-1}$)**	**λ^{CD}_{max} (nm), $\Delta\varepsilon$ ($M^{-1}cm^{-1}$)**
$CuH_3\mathbf{L^2}$	25.64(1)	640, 71.6	305, -0.64 545, 0.27 635, -0.17
$CuH_2\mathbf{L^2}$	22.50(2)	625, 91.6	305, -1.19 545, 0.59 630, -0.31
$CuH\mathbf{L^2}$	18.97(2)	625, 88.5	310, -0.89 545, 0.73 635, -0.22
$Cu\mathbf{L^2}$	12.77(3)	625, 90.3	310, -0.85 550, 0.74 635, -0.20
$CuH_{-1}\mathbf{L^2}$	5.40(3)	627, 91.9	310, -0.69 550, 0.66 640, -0.18
$CuH_{-2}\mathbf{L^2}$	-5.21(4)	650, 109.5	630, -1.53 780, 0.82
$Cu_2\mathbf{L^2}$	17.84(1)	650, 118.4	310, -0.80 550, 0.66
$Cu_2H_{-1}\mathbf{L^2}$	12.56(1)	665, 142.3	315, -0.61 560, 0.90 705, 0.47
$Cu_2H_{-2}\mathbf{L^2}$	5.91(1)	605, 179.5	305, -3.09 525, 1.01 665, -0.59
$Cu_2H_{-3}\mathbf{L^2}$	-3.42(1)	630, 180.8	310, -2.34 570, 1.01 650, 0.96

In equimolar solution, the visible and CD spectra are practically unchanged between pH 4 and 10 (Figure 4.21), and consequently the calculated individual visible and CD spectra of the species $CuH\mathbf{L^2}$, $Cu\mathbf{L^2}$, $CuH_{-1}\mathbf{L^2}$ are identical, and even those of $CuH_2\mathbf{L^2}$ are very similar (Figure 4.22). This means that the coordination environment of copper(II) in these complexes is also identical, and the four successive deprotonations are related to non-coordinating side chains. Indeed, the pK values of these deprotonations (pK = 3.14, 3.54, 6.20, 7.34, Table 4.2.) are consistent with the proton loss of two carboxylic and two imidazole groups of the free ligand. The 'extra' deprotonation detected for $CuH_{-1}\mathbf{L^2}$ and its intense CD spectra indicate the presence of a coordinated amide nitrogen in this, and therefore in all mentioned complexes. The spectroscopic parameters of $CuH_{-1}\mathbf{L^2}$ ($\lambda^{d\text{-}d}_{max}$ = 627 nm, g_o = 2.1121, A_o = 71.5 G, Tables 4.2. and 4.3.) are consistent with a $\{N_{tert},N^-,N_{im},O\}$ type coordination with slight rombic distortion, similarly to the $CuH_{-1}L$ complex of Gly-His [44, 127] or glycyl-histamine [128].

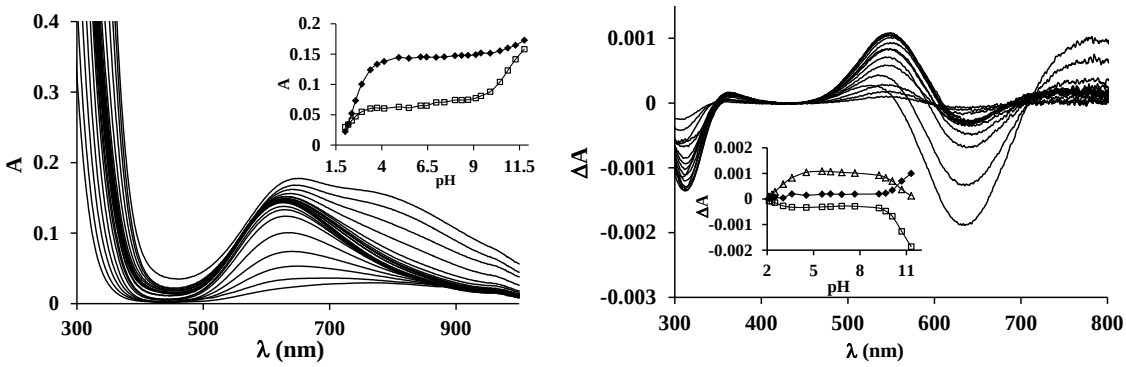

Figure 4.21. pH-dependent UV-Vis (left) and CD spectra (right) of Cu(II)-$\mathbf{L}^2$ 1:1 system ($[\mathbf{L}^2]_{tot}$ = $[Cu(II)]_{tot}$ = 0.0015 M and 0.0016 M, respectively, I = 0.1 M NaCl, T = 298 K). UV-Vis insert: pH-dependent absorbances at 628 (♦) and 770 nm (□). CD insert: pH-dependence of ΔA at 550 (Δ), 640 (□) and 780 nm (♦).

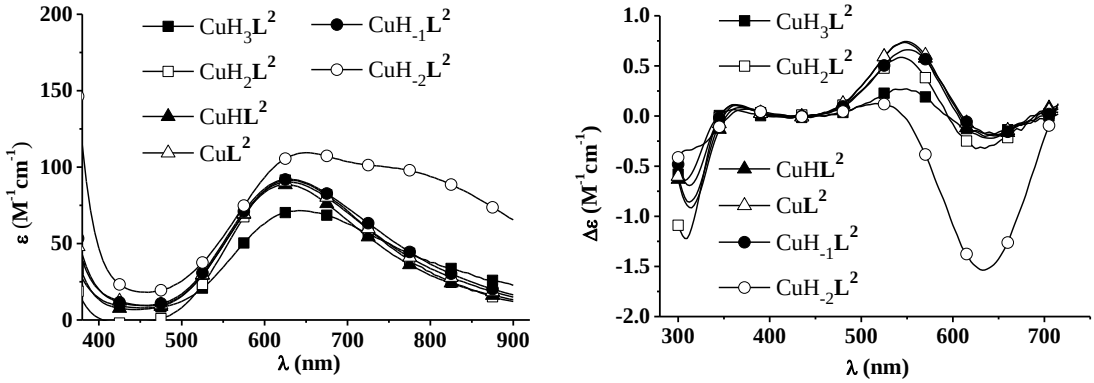

Figure 4.22. Individual molar UV-Vis (left) and CD (right) spectra of mononuclear Cu(II)-$\mathbf{L}^2$ complexes.

The high stability of the Gly-His-like coordination explains the unchanged binding mode during four successive deprotonations of non-coordinated side chains. The formation of the Gly-His-like $\{N_{tert},N^-,N_{im},O\}$ coordination mode in the present system takes place at somewhat lower pH ($pK_{CuH_3L^2}$ = 3.14) than in the case of Gly-His itself (pK_{CuL} = 4.15 [44]), which can be explained by the important basicity difference of the tertiary ($\mathbf{L}^2$) and primary (Gly-His) amines involved in the metal binding. In the copper(II)-Gly-His and related systems, the fourth equatorial position is occupied by a water molecule, which deprotonates with a pK = 9.2–9.4 [115]. Such deprotonation was not observed in our system, indicating that the fourth equatorial position in $CuH_{-1}\mathbf{L}^2$ is more likely occupied by an amide oxygen in chelating position (Scheme 4.6).

Above pH 10, the formation of $CuH_{-2}\mathbf{L}^2$ results in fundamental changes of the spectroscopic behaviors. On the individual visible spectrum of this species two bands appear with nearly equal intensities at 645 and 765 nm (Figure 4.22. left), suggesting an intermediate structure between square pyramidal and trigonal bipyramidal geometries [129], which is rare in the case of copper(II)-peptide complexes. The intensity of the CD bands increases considerably in the d–d region, indicating the metal coordination of a further amide nitrogen, since only this binding can induce strong chiral perturbation (Figures 4.21 and 4.22 right).

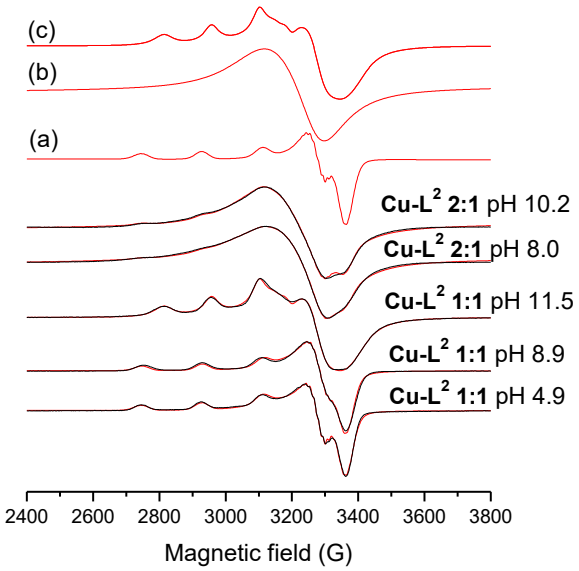

Figure 4.23. Anisotropic EPR spectra recorded at 77 K in Cu(II)-$\mathbf{L}^2$ 1:1 and 2:1 systems ($[\mathbf{L}^2]_{tot}$ = $[Cu(II)]_{tot}$ = 0.0017 M and 1.9×$[\mathbf{L}^2]_{tot}$ = $[Cu(II)]_{tot}$ = 0.0033 M, respectively, I = 0.1 M NaCl. Red: simulated, black: measured). Calculated EPR parameters of (a), (b) and (c) component spectra (related to the complexes $CuH_x\mathbf{L}^2$ (x = 2, 1, 0, -1), $Cu_2H_x\mathbf{L}^2$ (x = -1, -2, -3) and $CuH_{-2}\mathbf{L}^2$, respectively) are listed in Table 4.3.

Table 4.3. Calculated EPR parameters of component spectra detected in the Cu(II)-$\mathbf{L}^2$ system. The component spectra (a), (b) and (c) are related to the complexes $CuH_x\mathbf{L}^2$ (x = 2, 1, 0, -1), $Cu_2H_x\mathbf{L}^2$ (x = -1, -2, -3) and $CuH_{-2}\mathbf{L}^2$, respectively.

	g_o	A_o /G	a_N	g_x	g_y	g_z	A_x /G	A_y /G	A_z /G	a_x^N	a_y^N	a_z^N
(a)	2.1121	71.5	11.6 11.6 11.6	2.0448	2.0526	2.2285	17.4	8.6	178.9	12.0 12.0 13.1	10.0 10.0 11.3	10.0 10.0 9.3
(b)	2.105	w=165 G		2.106			w=180G					
(c)	2.1117	61.8	13.9 13.9 13.9	2.097(1)	2.012(1)	2.225(1)	34.2(2)	20.0(4)	140.9(2)			

In general, the amide coordination results in an increase of the EPR parameter A_o, due to the increased ligand field around the metal ion. However, in the present case, A_o of $CuH_{-2}\mathbf{L}^2$ (g_o = 2.1117, A_o = 61.8 G) is considerably smaller than that of the former species, indicating an axially coordinated nitrogen. Considering these facts and the available unbound imidazole rings, a $\{N_{tert},2N^-,N_{im}+N_{im}\}$ type coordination is the most probable in $CuH_{-2}\mathbf{L}^2$. The alternative binding mode without the tertiary amine (*i.e.* $\{2N^-,2N_{im}\}$), which is rather common in the case of peptides containing the –HXH– sequence, has distinctly different spectral properties [65, 91].

The two non-coordinating C-terminal histidine legs in $CuH_x\mathbf{L^2}$ (x = 2, 1, 0, -1) obviously may bind a further metal ion. Indeed, our experimental data indicate the formation of four dinuclear complexes above pH 4 (Figure 4.20.) at 2:1 metal-to-ligand ratio. The presence of dicopper(II) complexes was also confirmed by MALDI-TOF MS (Figure 4.24). The obtained isotopic distribution pattern is in good agreement with that calculated for the molecular ion $[Cu\mathbf{L^2}]^-$ = $[C_{24}H_{27}N_{10}O_9Cu]^-$ and $[Cu_2H_{-2}\mathbf{L^2}]^-$ = $[C_{24}H_{25}N_{10}O_9Cu_2]^-$. However, differences between the estimated (662.13, 723.04) and measured (663.26, 725.21) molecular weights were observed, which were attributed to the reduction of Cu^{2+} to Cu^+ and the corresponding uptake of a proton during the ionization process (see Section 4.1.2).

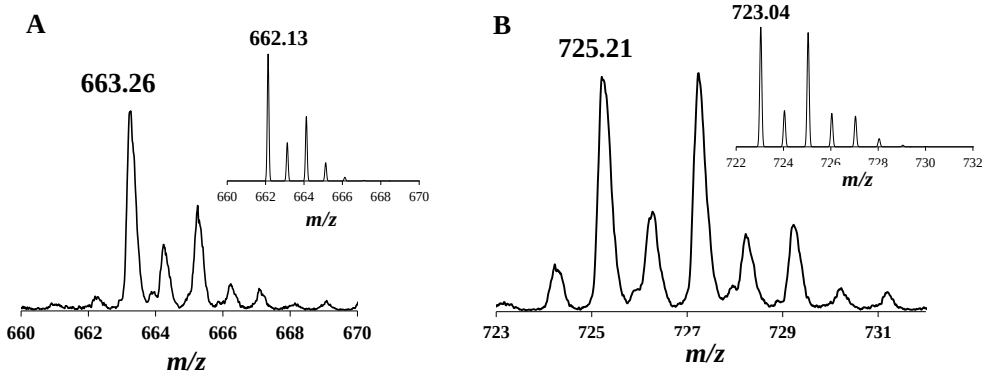

Figure 4.24. MALDI-TOF MS spectra measured in the Cu(II)-$\mathbf{L^2}$ 1:1 (**A**) and 2:1 (**B**) systems. Insert: calculated spectra of the corresponding complexes ($[C_{24}H_{27}N_{10}O_9Cu]^-$ and $[C_{24}H_{25}N_{10}O_9Cu_2]^-$).

Considering the high stability of the above-mentioned Gly-His-like $\{N_{tert},N^-,N_{im},O\}$ coordination, this binding mode should be preserved in the dinuclear $Cu_2H_{-1}\mathbf{L^2}$ species. Indeed, the equilibrium constant for the process $CuH_{-1}\mathbf{L^2} + Cu^{2+} = Cu_2H_{-1}\mathbf{L^2}$ (log$K$ = 7.2), as well as the visible and CD difference spectra between $Cu_2H_{-1}\mathbf{L^2}$ and $CuH_{-1}\mathbf{L^2}$ ($\lambda^{d\text{-}d}_{max}$ ~ 700 nm, positive CD band around 640 nm, Figure 4.26.) are in accordance with a $\{2N_{im},2COO^-\}$ type coordination of the second metal ion in $Cu_2H_{-1}\mathbf{L^2}$ [106].

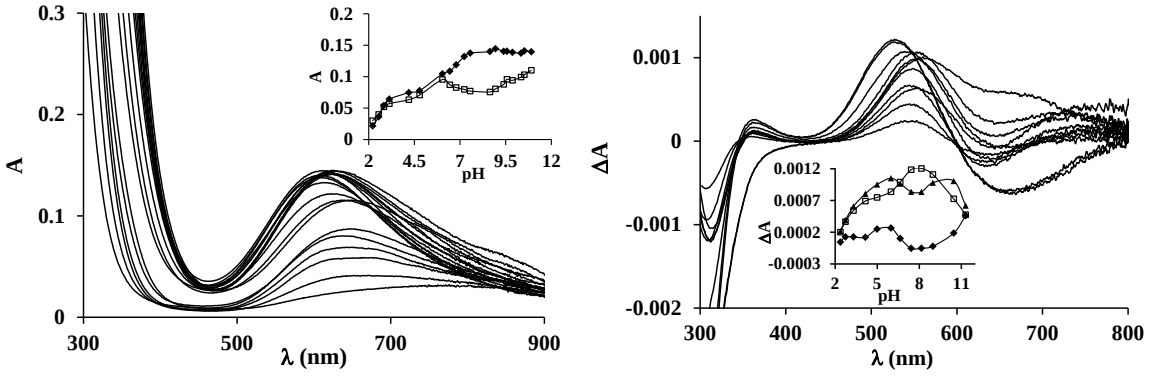

Figure 4.25. pH-dependent UV-Vis (left) and CD (right) spectra of Cu(II)-$\mathbf{L^2}$ 2:1 systems ($1.95\times[\mathbf{L^2}]_{tot}$ = $[Cu(II)]_{tot}$ = 0.0029 M and 0.0031 M, respectively, I = 0.1 M NaCl, T = 298 K). UV-Vis insert: pH-dependent absorbances at 607 (♦) and 720 nm (□); CD insert: pH-dependent absorbances at 525 (□), 560 (▲) and 780 nm (♦).

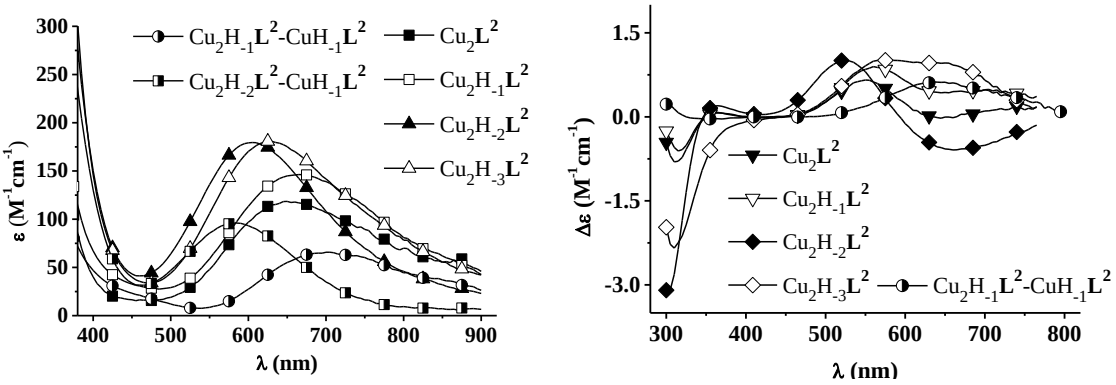

Figure 4.26. Individual molar UV-Vis (left) and CD (right) spectra of dinuclear Cu(II)-$\mathbf{L}^2$ complexes, along with some difference spectra.

The following deprotonation ($pK_{Cu_2H_{-1}L^2}$ = 6.65) results in ~ 60 nm blue shift of the d-d maximum and important change on the CD spectra, which indicates amide nitrogen coordination to the second metal ion (the Gly-His-like coordination in the mononuclear complexes is unchanged up to pH 9). Indeed, the visible difference spectra between $Cu_2H_{-2}\mathbf{L}^2$ and $CuH_{-1}\mathbf{L}^2$ ($\lambda^{d\text{-}d}_{max}$ ~ 585 nm, Figure 4.26.) is again in accordance with a $\{2N_{im},N^-,COO^-\}$ type coordination [106] in the equatorial plane of the second copper(II) (Scheme 4.6). This species has surprisingly high stability: it is the dominant complex over nearly 3 pH units. The next deprotonation ($pK_{Cu_2H_{-2}L^2}$ = 9.35) induces further characteristic changes on CD spectra both in the UV and visible region (Figure 4.26), which reflects the metal coordination of the third amide nitrogen. On the other hand, the visible spectrum shows ~ 20 nm red shift between pH 8-10.3 (Figure 4.25). The spectral changes exclude the formation of a binding mode present in $CuH_{-2}\mathbf{L}^2$. The third amide nitrogen binds most likely to the second metal ion, creating a $\{N_{tert},N^-,N_{im},O;\ 2N^-,2N_{im}\}$ coordination mode in $Cu_2H_{-3}\mathbf{L}^2$. Peptides with -HXH- sequence undergo two strongly overlapping amide deprotonations, due to the preferred formation of a $\{2N^-,2N_{im}\}$ coordinated species [65, 91]. However, in the present case the two successive amide deprotonations are well separated, because they are involved in a considerably less favored, eight-membered chelate ring. Moreover, this chelate ring contains the metal-bound tertiary amine, too, which probably makes the conformational change needed for the $Cu_2H_{-2}\mathbf{L}^2 \rightarrow Cu_2H_{-3}\mathbf{L}^2 + H^+$ deprotonation more difficult, resulting in the dominant formation of $Cu_2H_{-2}\mathbf{L}^2$ at pH 8.

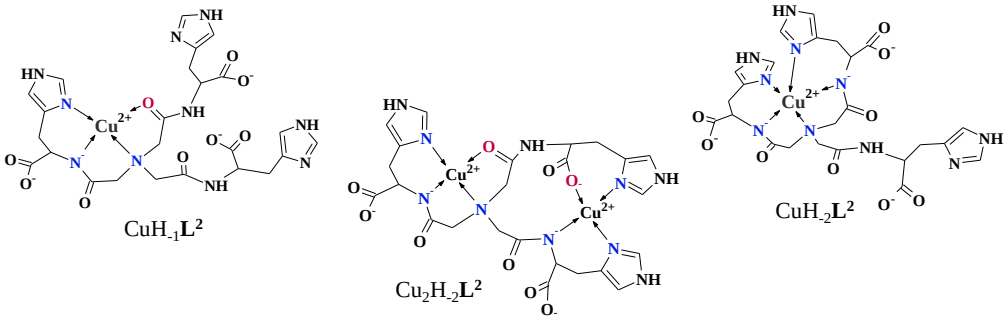

Scheme 4.6. Proposed schematic structure of copper(II)-$\mathbf{L}^2$ complexes $CuH_{-1}\mathbf{L}^2$, $CuH_{-2}\mathbf{L}^2$ and $Cu_2H_{-2}\mathbf{L}^2$.

4.2.3. Zinc(II) complexes of nta3his

Potentiometric and pH-dependent ^{1}H NMR measurements were performed to study the forming $\mathbf{L}^2$ complexes in presence of Zn(II). Surprisingly, precipitate formation was observed already at 1:1 metal-to-ligand ratio, between pH 6 and 9, even at ~1 mM complex concentration. Clear solutions could be obtained at 3.5-fold ligand excess, however, *bis*- or *tris*-ligand complexes were not needed to describe the titration curves. This, and the fact that the observed pH of the precipitation is too low for the hydrolysis of Zn(II), all suggest that the precipitate corresponds to weakly soluble zinc(II)-ligand complex(es), which can only be studied in diluted solutions.

Table 4.4. presents the formation constants of zinc(II)-$\mathbf{L}^2$ complexes, calculated on the basis of titrations at 1:3.5 metal-to-ligand ratio; Figure 4.27. shows the distribution of the species at such ligand excess (up), and at a simulated 1:1 metal-to-ligand ratio (down). By the latter simulation, it is clear that the observed precipitation in equimolar solution is most likely related to the Zn$\mathbf{L}^2$ complex (involved pH region presented as gray field).

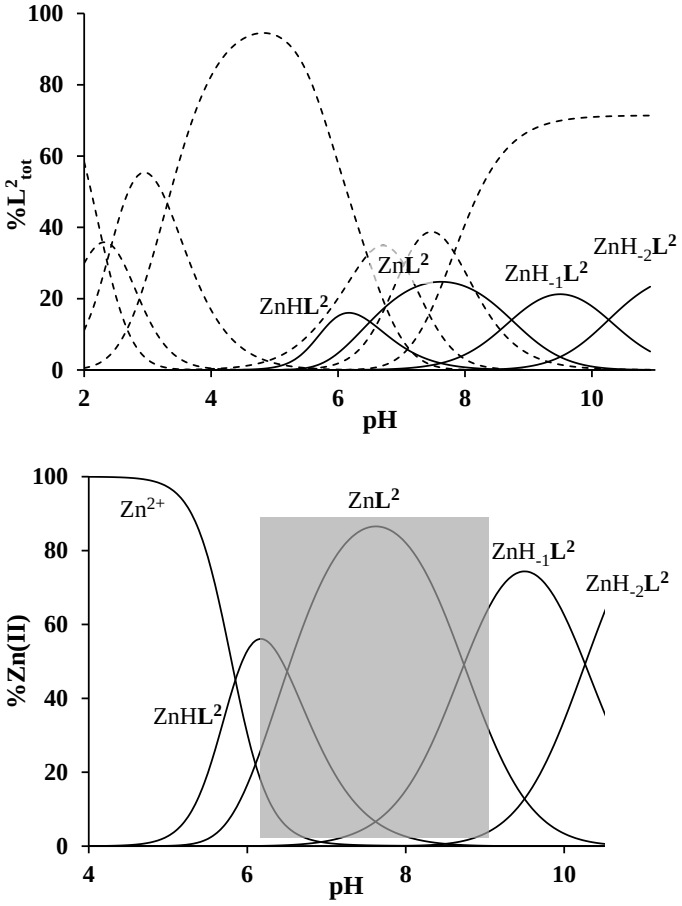

Figure 4.27. Speciation diagrams of Zn(II)-$\mathbf{L}^2$ at 1:3.5 (up) and 1:1 (down) metal-to-ligand ratios ($[\mathbf{L}^2]_{tot}$ = 0.001 M, I = 0.1 M NaCl, T = 298 K). Dashed lines represent unbound ligand species; gray field indicates pH region of precipitation.

Table 4.4. Formation and deprotonation constants of zinc(II)-$\mathbf{L}^2$ complexes (estimated errors in parentheses (last digit), I = 0.1 M NaCl, T = 298 K).

	logβ	**pK**
Zn**H**$\mathbf{L}^2$	12.26 (8)	6.50
Zn$\mathbf{L}^2$	5.76(6)	8.74
$ZnH_{-1}\mathbf{L}^2$	-2.98(8)	10.26
$ZnH_{-2}\mathbf{L}^2$	-13.24(7)	

Since a great ligand excess would have resulted nearly identical NMR spectra to that of the free ligand, pH-dependent ^{1}H NMR measurements were carried out at 1:1 zinc(II)-to-ligand ratio; the samples were centrifuged in the precipitated pH regions, and spectra of the clear solutions were recorded. Considerable intensity loss was observed for all the signals on the pH-dependent spectra (Figure 4.28); nevertheless, we could obtain structural information related to the zinc(II) complexes of $\mathbf{L}^2$.

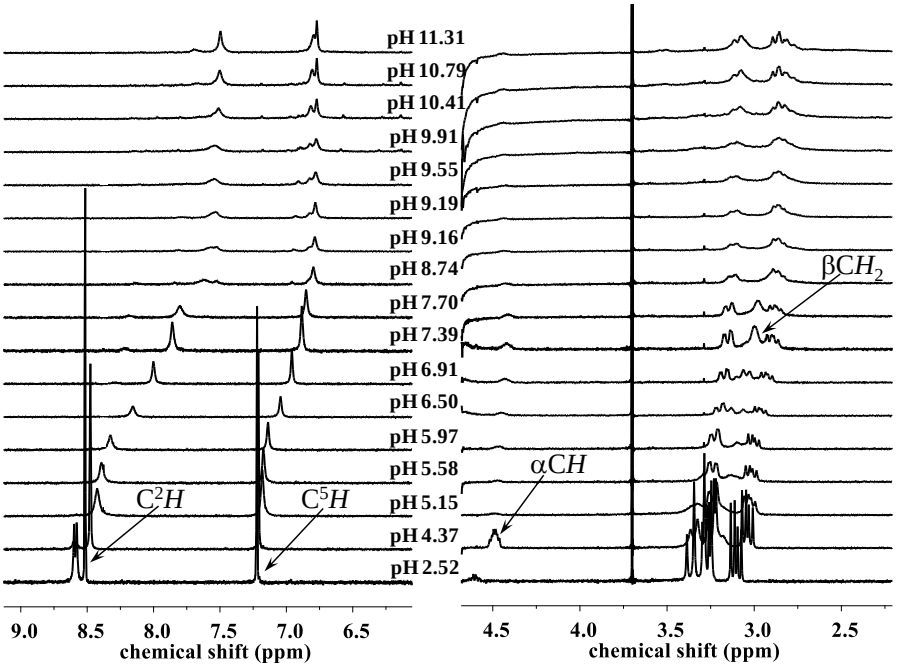

Figure 4.28. pH-dependent ^{1}H NMR spectra of Zn(II)-$\mathbf{L}^2$ 1:1 system ($[\mathbf{L}^2]_{tot}$ = 0.0029 M, I = 0.1 M NaCl, T = 298 K).

Based on potentiometric measurements, complex formation starts above pH 5. Around this pH, the broadening of the NMR signals can be observed; moreover, around neutral pH the αCH and βCH_2 signals undergo considerable changes (αCH of the free ligand was not observed at all, see Figure 4.19). All these observations indicate that in the forming complexes, Zn(II) coordination involves mostly the His moiety of the ligand (N_{im} and possibly COO^- groups). At higher pH, the broadened imidazole peaks slightly sharpen and multiply, indicating the deceleration of the ligand exchange in the forming species. This phenomenon becomes dominant above pH 9, following the deprotonation Zn$\mathbf{L}^2$ → $ZnH_{-1}\mathbf{L}^2 + H^+$.

Zinc(II)-dependent NMR spectra recorded around neutral and basic pH support these conclusions. At pH 7.9 a single, widened C^5H signal can be observed (Figure 4.29. down) indicating intermediate ligand exchange rate, implying complex(es) with multiimidazole coordination. Approaching pH 10, this structure transforms to result a slow exchanging species (Figure 4.29. up), most likely related to the Gly-His-type $\{N_{im},N^-,N_{tert}\}$ binding, since deprotonation of coordinated water molecules does not cause such deceleration of the ligand exchange process.

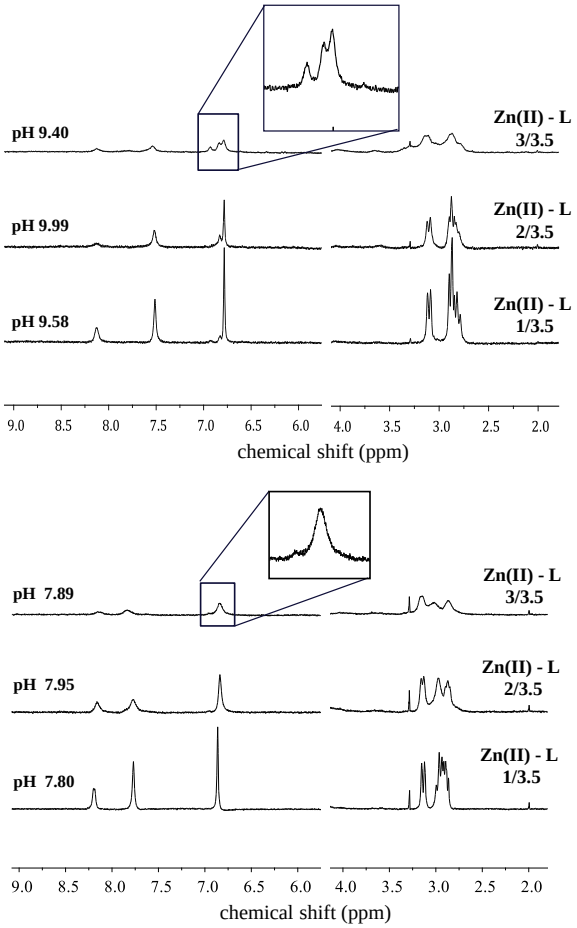

Figure 4.29. ^{1}H NMR spectra of Zn(II)-$\mathbf{L^2}$ system recorded around pH 10 (up) and 8 (down), at elevating Zn(II)-to-ligand ratios. ($[\mathbf{L^2}]_{tot}$ = 0.0012 M, I = 0.1 M NaCl, T = 298 K).

H_2N-XH-type sequences are known to promote this Gly-His-type coordination: the deprotonation of the amide NH was observed in Zn(II)-Gly/Ala-His systems [45, 46, 126]. Therefore, the formation of such species is not surprising; however, it becomes dominant at much higher pH as compared to the analogous copper(II) complex (pK_{ZnL^2} = 8.74, $pK_{CuH_2L^2}$ = 3.53). This indicates that the multiimidazolic environment competes strongly with the Gly-His binding mode up until basic pH. However, it remains unexplained, how or why this multiimidazole coordination triggers precipitation in the neutral pH range. Based on the tendency of symmetric tripodal ligands towards oligomerization [125], the most likely answer is the polymerization-aggregation of the complex, resulting in significant decrease of its solubility.

4.3. PROTONATION AND COMPLEX FORMATION OF NTA1HIS-NH$_2$

In the second part of my PhD work, our attention turned to unsymmetrical, partially functionalized tripodal ligands. Synthetic experiments were attempted in solution and solid phase as well. The latter case resulted the *mono*-His functionalized C-terminally free (nta1His) and protected (nta1His-NH$_2$) ligands (Scheme 4.7). Unfortunately, these compounds turned out to be unstable for long-term investigations (see Experimental section 3.1.4), therefore experimental data are limited mainly to potentiometric characterization of the ligands, as well as copper(II) and zinc(II) complex formation with the ligand nta1His-NH$_2$.

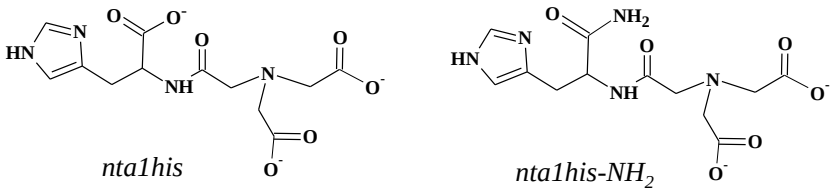

Scheme 4.7. Schematic structures of the ligands nta1his and nta1his-NH$_2$.

4.3.1. Protonation of the ligands

The ligands nta1his and nta1his-NH$_2$ have three detectable p*K* values in the studied pH range (Table 4.5). The most basic deprotonation, observed around pH 7 in both cases, most probably belongs to the proton loss of the imidazolium group. Interestingly, another relatively high p*K* was observed in both ligands (pK_{H_2L} = 6.44 and 5.66), which is probably not related to carboxylic groups. More likely they correspond to the proton loss of the N_{tert}-H^+ group, which points to an important difference between these systems and the *tris*-histidyl-functionalized nta derivative (nta3his); the protonation of N_{tert} was not observed between pH 2-10.5 in the latter case (see Section 4.2.1). This elevated p*K* can be explained by the presence of the free carboxylate groups of the nta moiety, being able to participate in a N_{tert} ---H^+---COO^- type hydrogen bonding system. Undoubtedly the same effect causes the increased acidity of the nta -COOH groups; the most acidic carboxylic groups are already deprotonated below pH 2 in both ligands.

Table 4.5. Protonation constants (logβ) and p*K* values of the ligands nta1his and nta1his-NH$_2$ (*I* = 0.1 M NaCl, *T* = 298 K, estimated error of last digits in parentheses).

	nta1his		**nta1his-NH$_2$**	
	logβ	**p*K***	**logβ**	**p*K***
H_3**L**	16.24(2)	2.30	14.80(2)	2.15
H_2**L**	13.94(1)	6.44	12.65(1)	5.66
H**L**	7.50(1)	7.50	6.99(1)	6.99

4.3.2. Copper(II) and zinc(II) complexes of the ligand nta1his-NH₂

Unfortunately, the instability of the ligand did not result accurate experimental data regarding the nta1his-metal systems, therefore complex formation could not be investigated. However, freshly prepared solutions of nta1his-NH_2 were appropriate for solution equilibrium studies, allowing to gain some information on complexation properties of *mono*-His functionalized nta derivatives. Both mononuclear copper(II)- and zinc(II) complexes were detected in ESI-MS for this ligand, too (see Appendix Figures A.7 and A.8).

Table 4.6. Formation and deprotonation constants of copper(II)- and zinc(II)-nta1his-NH_2 complexes (estimated errors in parentheses (last digit), I = 0.1 M NaCl, T = 298 K).

	logβ	**pK**
CuH**L**	13.92(4)	3.03
Cu**L**	10.89(3)	3.10
CuH_{-1}**L**	7.79(3)	8.72
CuH_{-2}**L**	-3.03(5)	10.82
ZnH**L**	13.22(2)	5.24
Zn**L**	7.98(3)	5.59
ZnH_{-1}**L**	2.39(2)	10.78
ZnH_{-2}**L**	-8.39(4)	

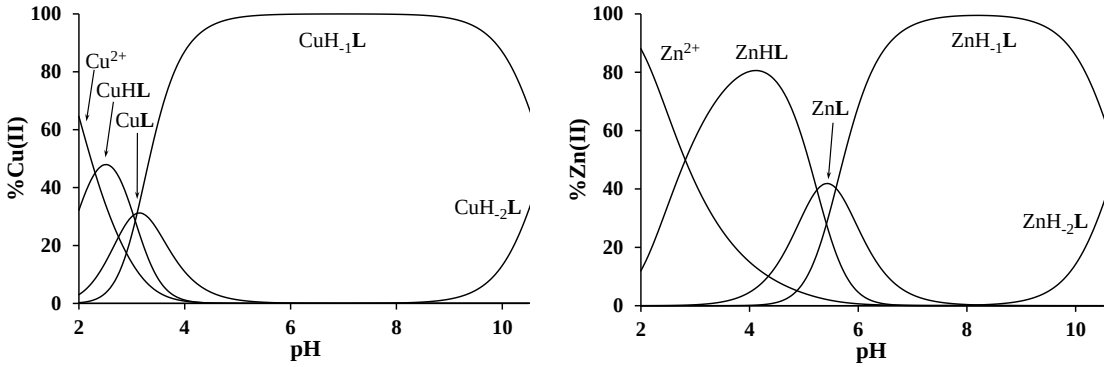

Figure 4.30. Speciation diagrams in Cu(II)-nta1his-NH_2 1:1 (left) and Zn(II)-nta1his-NH_2 1:1 (right) systems ($[\mathbf{L}]_{tot}$ = 0.001 M, $[Cu(II)]_{tot} = [Zn(II)]_{tot}$ = 0.001 M, I = 0.1 M NaCl, T = 298 K).

The distribution of the copper(II)- and zinc(II)-nta1his-NH_2 species is depicted in Figure 4.30, the calculated stability constants and deprotonation constants can be found in Table 4.6. The coordination behavior of the ligand is very similar towards Cu^{2+} and Zn^{2+} ions: the same complexes are formed with different relative stability. In presence of copper(II) ions, CuH**L** and Cu**L** species are formed at acidic pH, but their formation overlaps with that of the dominant CuH_{-1}**L** species. Spectrophotometric titration of the complex solution allowed the calculation of individual molar UV-Vis spectra for the main complexes. The absorption of CuH**L** manifests at relatively low energies, suggesting N_{im} and COO^- coordination; the $\lambda^{d\text{-}d}_{max}$ (640 nm, Figure 4.31.) of CuH_{-1}**L** is in good agreement

with that of the $CuH_{-1}\mathbf{L}^2$ complex of nta3his (615 nm, Figure 4.22). The structural analogy between the two systems and the high stability of the 'extra' deprotonated complex suggests the same, Gly-His-type $\{N_{im},N^-,N_{tert},O\}$ structure. This species deprotonates only above pH 10, most probably related to proton loss of a coordinated water molecule; the process does not cause significant perturbation in the coordination sphere (Figure 4.31).

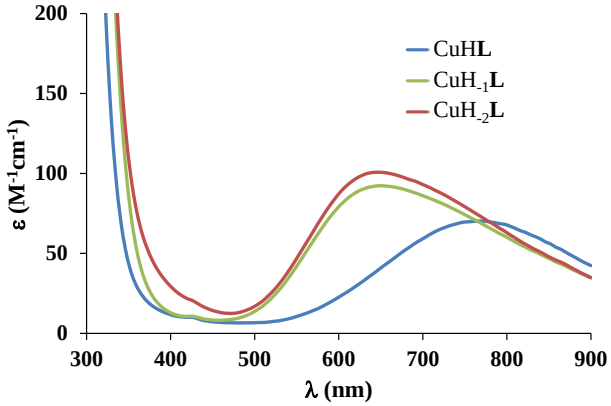

Figure 4.31. Individual molar UV-Vis spectra of the main Cu(II)-nta1his-NH_2 complexes.

In presence of Zn^{2+} ions, the protonated ZnH**L** complex forms in dominant quantities between pH 3-5; its deprotonation leads to the species Zn**L** and $ZnH_{-1}\mathbf{L}$, almost in a co-operatively fashion. Without any experimental proof, we can only assume that the highly stable Gly-His-type structure is preserved in the $ZnH_{-1}\mathbf{L}$ complex as well. Its formation takes place more than two pH units higher than in case of the analogous copper(II) complex, which is in agreement with the higher preference of copper(II) towards amide N^- coordination.

4.4. PROTONATION AND COORDINATION PROPERTIES OF TREN2HIS (L^3) AND TREN1HIS (L^4)

The most recently synthesized tripodal ligands are the asymmetric, N-terminally free His-containing tren2his (**L**^{3}) and tren1his (**L**^{4}, Scheme 4.8). These two compounds, along with tren3his, serve as a decent example for studying the impacts of gradual functionalization of tripodal platforms on metal complex formation.

4.4.1. Protonation of tren2his and tren1his

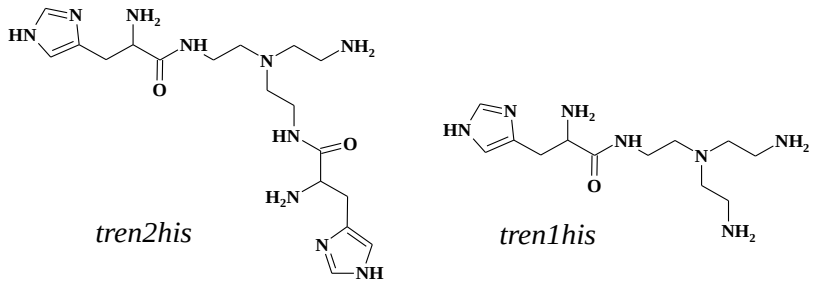

Scheme 4.8. Schematic structures of the ligands tren2his (**L**^{3}) and tren1his (**L**^{4}).

The protonation constants and p*K* values of tren2his and tren1his ligands derived from pH potentiometric titrations are collected in Table 4.7. The identification of the deprotonating groups has been supported by pH-dependent ^{1}H NMR measurements (Figures 4.32 and 4.33): the C^{2}H, C^{5}H and αCH proton signals present significant displacement in the relevant pH ranges. The p*K* values of tren-like primary and αNH$_2$ amino nitrogens are between p*K* = 9.04-9.90 and 6.82-7.69, respectively. Taking into account the *tris*-histidyl analog tren3his as well (Section 4.1.1.), the increasing overall positive charge of the ligands results in increased acidity of the imidazolium rings (p*K* = 3.87-5.41) in the trenXhis (X = 1, 2, 3) series.

Table 4.7. Protonation constants and p*K* values of tren1his and tren2his (*I* = 0.1 M NaCl, *T* = 298 K, estimated error of last digits in parentheses).

	tren1his		**tren2his**	
	log*β*	**p*K***	**log*β***	**p*K***
H$_6$**L**			36.46(1)	2.33
H$_5$**L**			34.13(1)	4.62
H$_4$**L**	31.04(1)	5.03	29.51(1)	5.41
H$_3$**L**	26.01(1)	7.07	24.10(1)	6.82
H$_2$**L**	18.94(1)	9.04	17.28(1)	7.69
H**L**	9.90(1)	9.90	9.59(1)	9.59

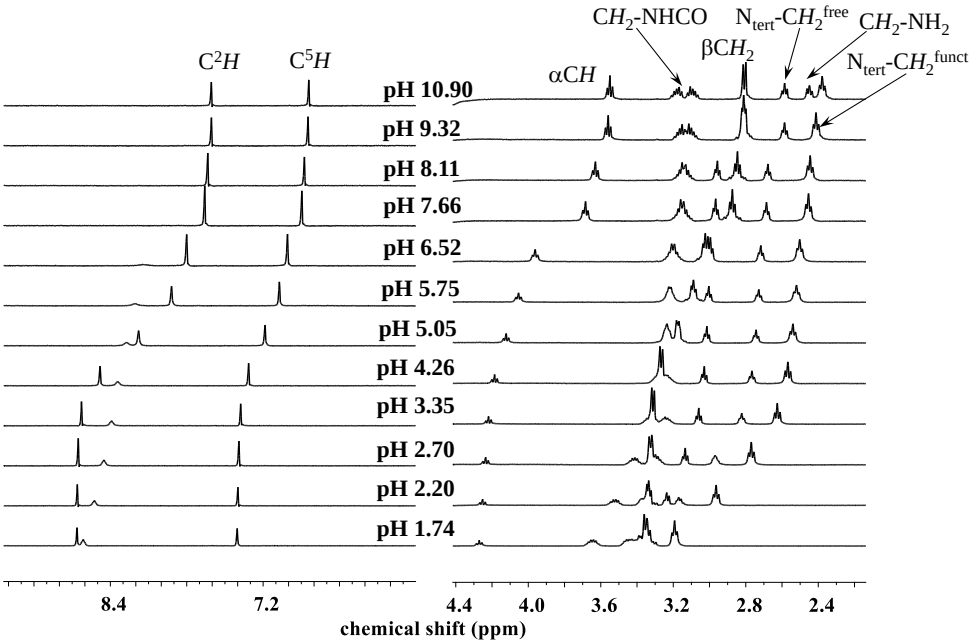

Figure 4.32. ^{1}H NMR titration of ligand $\mathbf{L}^{3}$ (in H_2O, $[\mathbf{L}^{3}]_{tot}$ = 0.0018 M, I = 0.1 M NaCl, T = 298 K).

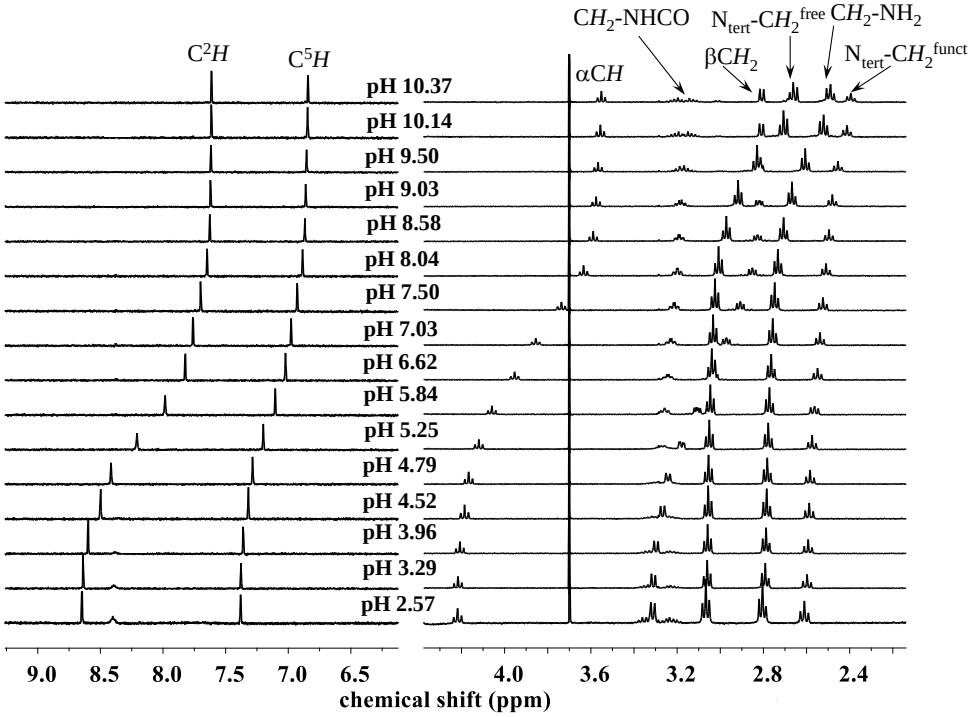

Figure 4.33. ^{1}H NMR titration of ligand $\mathbf{L}^{4}$ (in H_2O, $[\mathbf{L}^{4}]_{tot}$ = 0.0017 M, I = 0.1 M NaCl, T = 298 K).

The pK of the tertiary amino group could be determined only for $\mathbf{L}^{3}$, which was also supported by the pH-dependent ^{1}H NMR spectra (Figure 4.32): considerable shifts can be observed for the signals related to the tren moiety in the acidic pH range. Such displacements of ^{1}H NMR signals was not observed in case of tren1his (Figure 4.33), which suggests low basicity for the tertiary nitrogen in $\mathbf{L}^{4}$, similarly to tren itself [11].

4.4.2. Copper(II) complexes of tren2his

The ligand tren2his forms both mono- and oligonuclear copper(II) complexes, depending on the metal-to-ligand ratios. The distribution curves of the detected species are depicted on Figure 4.34, their formation constants and the spectroscopic parameters of the main species are listed in Table 4.8.

In equimolar solution only mononuclear complexes are formed. $CuH_2\mathbf{L}^3$ is the first major species around pH 4, its protonation state suggests 3N coordination. Indeed, the equilibrium constants for the process $Cu^{2+} + H_2\mathbf{L}^3 = CuH_2\mathbf{L}^3$ (log*K* = 10.26), its UV-Vis spectrum ($\lambda^{d\text{-}d}_{max}$ ~ 640 nm), as well as the relatively weak positive CD band between 600-800 nm are in perfect agreement with $\{2N_{im},\alpha NH_2\}$ coordinated complexes of several -HXH- [124] or -HXXH- [88] peptides.

Table 4.8. Formation constants, deprotonation constants (*I* = 0.1 M NaCl, *T* = 298 K, estimated error of last digits in parentheses) and spectroscopic (UV-Vis, CD and EPR) parameters of the main copper(II)-$\mathbf{L}^3$ complexes.

	log*β*	**p*K***	**$\lambda_{max}^{d\text{-}d}$ (nm), ε ($M^{-1}cm^{-1}$)**	**λ_{max}^{CD} (nm), Δε ($M^{-1}cm^{-1}$)**	**$g_{o,calc}$***
$CuH_3\mathbf{L}^3$	30.735(2)	3.197			
$CuH_2\mathbf{L}^3$	27.538(1)	4.984	640, 53.1	305, -0.302 635, 0.212	
$CuH\mathbf{L}^3$	22.554(4)	7.173	635, 75.6	315, -0.616 675, 0.573	2.096
$Cu\mathbf{L}^3$	15.381(6)	7.574	580, 88.0	675, 0.380	
$CuH_{-1}\mathbf{L}^3$	7.807(5)	11.077	555, 156.3	315, 0.473 595, 0.223	2.097
$CuH_{-2}\mathbf{L}^3$	-3.27(1)				
$Cu_2\mathbf{L}^3$	21.906(4)	4.741	580, 119.4	300, -0.884 750, 0.263	
$Cu_2H_{-1}\mathbf{L}^3$	17.165(3)	8.419	570, 161.1	300, 1.421 700, 0.246	2.106
$Cu_2H_{-2}\mathbf{L}^3$	8.746(4)	9.368	575, 168.4	310, 0.735 515, -0.180 670, 0.347	
$Cu_2H_{-3}\mathbf{L}^3$	-0.622(5)		585, 205.1	300, -0.698 665, 0.307	2.108
$Cu_3H_{-1}\mathbf{L}^3_2$	36.72(2)	7.38			
$Cu_3H_{-2}\mathbf{L}^3_2$	29.34(1)				
$Cu_2H_{-1}\mathbf{L}^3$ - $CuH\mathbf{L}^3$			546, 11.3		

*$g_{o,calc} = (g_x+g_y+g_z)/3$, anisotropic parameters and fitted spectra can be found in Appendix A.23. and Table A.1.

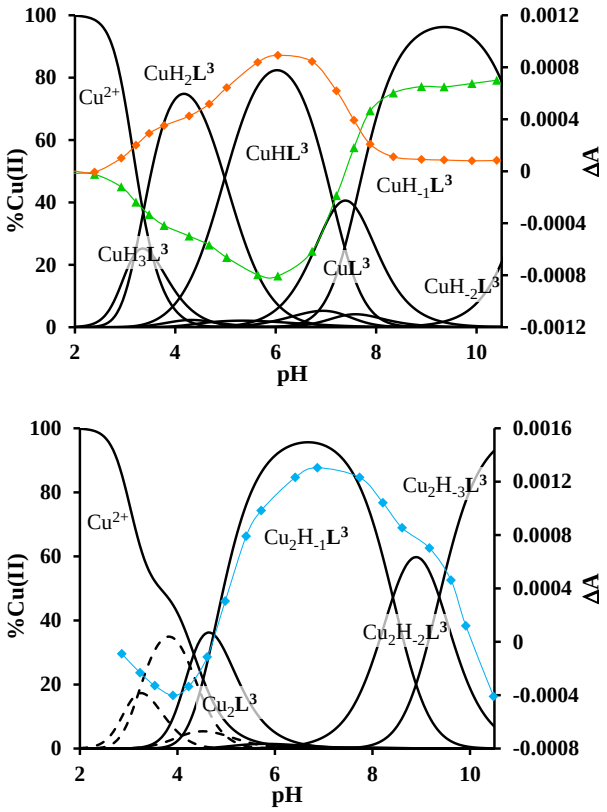

Figure 4.34. Distribution of the species in Cu(II)-$\mathbf{L}^3$ 1:1 (up) and 2:1 (down) systems ($[\mathbf{L}^3]_{tot}$ = 0.001 M, $[Cu(II)]_{tot}$ = 0.001 M and 0.002 M, respectively, I = 0.1 M NaCl, T = 298 K). Secondary axis: measured CD intensities at 325 nm (up: green, down: blue) and 675 nm (orange).

Approaching neutral pH, the next deprotonation results in the formation of Cu**H**$\mathbf{L}^3$. In this species only the tren-like NH_2 group is protonated, *i.e.* the metal ion has the highly stable *bis*-histamine-type $\{2N_{im},2\alpha NH_2\}$ coordination (Scheme 4.9). This binding mode is supported by spectral similarities with the analogous *bis*-histamine coordinated complexes: the detected d-d transitions ($\lambda^{d\text{-}d}_{max}$ = 640 nm) and CD spectra (intense positive CD band at 660 nm and a negative band around 300 nm, Figure 4.36. B) are nearly identical to those observed in the Cu(II)-His-Gly [130], Cu(II)-His-Xaa-Xaa [118], Cu(II)-*N*,*N*′-dihistidylethane-1,2-diamine [114] and in the strongly related Cu(II)-tren3his systems.

The tren-like amino group in the *bis*-histamine coordinated structure of Cu**H**$\mathbf{L}^3$ is too far from the metal ion to be axially coordinated. Nevertheless, the pK values of the subsequent two deprotonations steps are more than 2 units lower than the corresponding pK (= 9.59) in the free ligand. These facts and the fundamental spectroscopic changes during the consecutive deprotonation steps (Cu**H**$\mathbf{L}^3$ → Cu$\mathbf{L}^3$ → Cu$H_{-1}\mathbf{L}^3$, Figure 4.36. A) indicate rearrangement of the coordination sphere. The changes of CD spectra (Figure 4.36. B) support different coordination mode of the histidyl unit(s) in Cu**H**$\mathbf{L}^3$ and Cu$H_{-1}\mathbf{L}^3$. The important blue shift of the copper(II) d-d band (635 → 555 nm, Figure 4.36. A) indicates considerable increase of the ligand field around the metal ion, *i.e.* 4N coordination with at least one amide nitrogen. Indeed, since the free ligand is non-protonated around pH 10, the

protonation state of the complex suggests one coordinated amide nitrogen. Considering the preferred formation of fused chelate rings, too, a $\{\alpha NH_2,N^-,N_{tert},NH_2^{tren}\}$ coordination mode can be assumed in $CuH_{-1}\mathbf{L^3}$ (Scheme 4.9). Another evidence of the suggested coordination mode arises from the similarities of CD spectra observed for $CuH_{-1}\mathbf{L^3}$ and that reported for the $CuH_{-2}L$ complex of the HGG peptide [118], where the chiral perturbation arises from the $\{\alpha NH_2,N^-\}$ chelate ring.

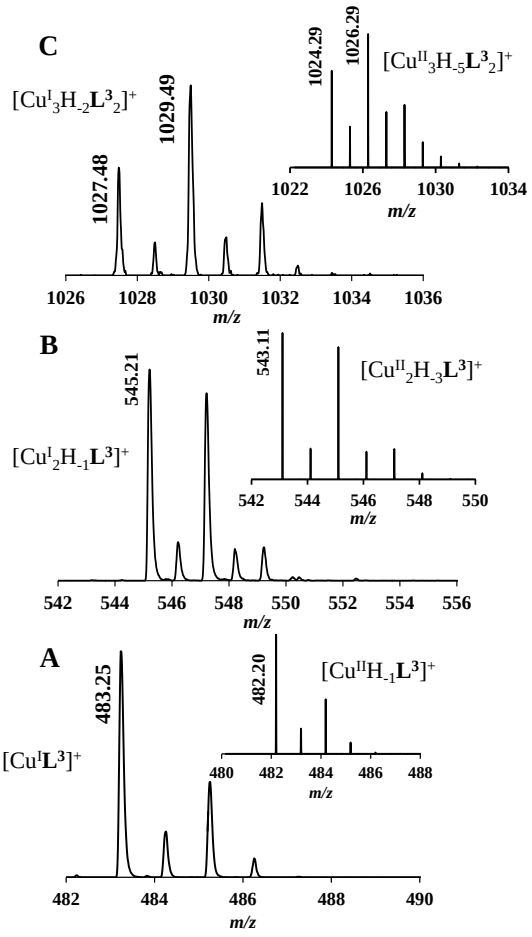

Figure 4.35. MALDI-TOF MS spectra measured at Cu(II)-$\mathbf{L^3}$ 1:1 (**A**), 2:1 (**B**) and 3:2 (**C**) ratios. Insert: calculated spectra of the corresponding complexes: $[C_{18}H_{31}N_{10}O_2Cu_2]^+$ (**A**), $[C_{18}H_{29}N_{10}O_2Cu_2]^+$ (**B**) and $[C_{36}H_{59}N_{20}O_4Cu_3]^+$ (**C**).

It must be pointed out that the proposed $\{\alpha NH_2,N^-,N_{tert},NH_2^{tren}\}$ coordination mode in $CuH_{-1}\mathbf{L^3}$ leaves a histidyl-functionalized arm free, with an unbound histamine-type binding site. As it was previously observed in case of the ligand tren3his, a free N-terminal His arm induces dimerization processes at metal ion excess via the formation of $Cu_3H_{-x}L_2$ type complexes, due to the high stability offered by the *bis*-histamine-type binding. Accordingly, the presence of trinuclear complexes was detected by MALDI-TOF MS (Figure 4.35) at 3:2 copper(II)-to-ligand ratio. Indeed, the evaluation of our potentiometric data indicated the formation of two trinuclear species ($Cu_3H_{-1}\mathbf{L^3}_2$ and $Cu_3H_{-2}\mathbf{L^3}_2$), as their consideration was found to be necessary for the successful fitting of the titration curves performed at Cu(II)-$\mathbf{L^3}$ 3:2 ratio. However, these species do not form in significant

quantities at 1:1 or 2:1 metal-to-ligand ratios, because of the high stability of both mono- and dinuclear complexes of $\mathbf{L^3}$; these were also detected by MALDI-TOF MS (Figure 4.35).

The obtained isotopic distributions are in agreement with that calculated for the one-positively charged complexes $[Cu^{II}H_{-1}\mathbf{L^3}]^+$, $[Cu^{II}{}_3H_{-5}\mathbf{L^3}{}_2]^+$ and $[Cu^{II}{}_2H_{-3}\mathbf{L^3}]^+$. The reduction of the copper(II) centers and the concomitant proton uptakes take place in this copper(II)-ligand system, too, resulting $[Cu^{I}\mathbf{L^3}]^+$, $[Cu^{I}{}_3H_{-2}\mathbf{L^3}{}_2]^+$ and $[Cu^{I}{}_2H_{-1}\mathbf{L^3}]^+$ species, as it was also observed during MALDI-TOF MS analyses of Cu(II)-$\mathbf{L^1}$ and -$\mathbf{L^2}$ complexes (Sections 4.1.2. and 4.2.2).

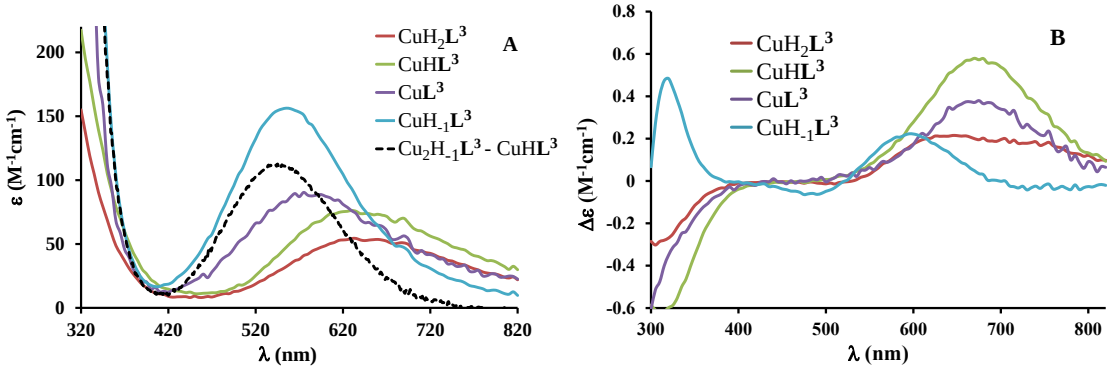

Figure 4.36. Individual molar UV-Vis (**A**) and CD (**B**) spectra of the main species in Cu(II)-$\mathbf{L^3}$ 1:1 system. Black dashed line corresponds to difference spectrum.

The fact that in equimolar solutions the dinuclear complexes form only in small quantities indicates that $\mathbf{L^3}$ provides two coordination sites for copper(II) with rather different metal binding affinities. At 2:1 metal-to-ligand ratio, the deprotonation of the first appearing minor dinuclear species $Cu_2\mathbf{L^3}$ results in the formation of $Cu_2H_{-1}\mathbf{L^3}$ (Figure 4.34. down), which predominates in the solution between pH 5-8. Taking into account that in the same pH range the *bis*-histamine-like $\{2N_{im},2\alpha NH_2\}$ coordination provides high stability in equimolar solution, the conservation of this binding site in $Cu_2H_{-1}\mathbf{L^3}$ is safe to assume. In this way, the four N donor groups of the tren-like subunit are preorganized to bind a further metal ion, and the $\{NH_2{}^{tren},N_{tert}\}$ chelate may act as an anchor to promote the deprotonation and coordination of the amide nitrogen(s). The protonation state of $Cu_2H_{-1}\mathbf{L^3}$ implies that the second copper(II) is bound to either a $\{N^-,N_{tert},NH_2{}^{tren}\}$ or $\{N^-,N_{tert},N^-\}$ donor set (with protonated tren-like amino group in the latter case, see Scheme 4.9). Assuming that the $\{2N_{im},2\alpha NH_2\}$ coordinated metal ion in $Cu_2H_{-1}\mathbf{L^3}$ has similar component Vis spectrum than that of $CuH\mathbf{L^3}$, the $Cu_2H_{-1}\mathbf{L^3}$–$CuH\mathbf{L^3}$ difference spectrum may be informative regarding the coordination environment around the second metal ion. This subtraction resulted a 'usual' Vis spectrum (Figure 4.36. A) with a relatively high energy d-d maximum ($\lambda^{d\text{-}d}{}_{max}$ = 546 nm), which favors the $\{N^-,N_{tert},N^-\}$ coordination in the equatorial plane of the second copper(II). Although, none of the above mentioned two donor sets can be ruled out, the latter one may also explain the practically unchanged UV-Vis and CD spectra during the next deprotonation, *i.e.* deprotonation of the

tren-like NH_3^+ group without metal ion assistance. In fact, the processes $Cu_2H_{-1}\mathbf{L^3} \rightarrow Cu_2H_{-2}\mathbf{L^3} \rightarrow Cu_2H_{-3}\mathbf{L^3}$ are overlapped (Figure 4.34. down), therefore a further deprotonation takes place nearly parallel. For this latter process, proton loss of either a coordinated water molecule or imidazole ring can be taken into account. In principle, both may induce structural rearrangement which would explain the observed changes on the UV-Vis and CD spectra of $Cu_2H_{-3}\mathbf{L^3}$ (Figure 4.37).

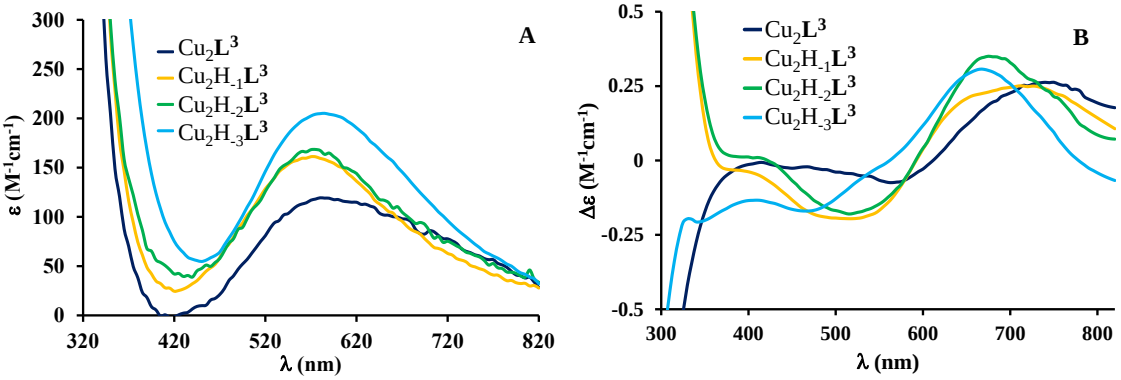

Figure 4.37. Individual molar UV-Vis (**A**) and CD (**B**) spectra of the main species in Cu(II)-$\mathbf{L^3}$ 2:1 system.

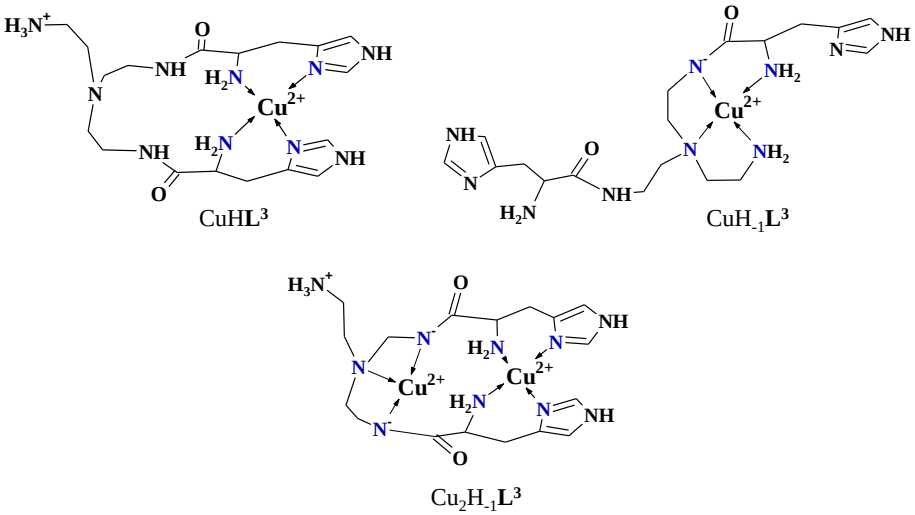

Scheme 4.9. Proposed structures of the main copper(II)-$\mathbf{L^3}$ complexes.

4.4.3. Zinc(II) complexes of tren2his

Zinc(II) complexes of $\mathbf{L}^3$ were characterized by pH potentiometric, ^{1}H and 2D NMR measurements. Water soluble complexes were found to be forming even at 2:1 zinc(II)-to-ligand ratio, indicating the presence of both mono- and dinuclear complexes. The formation constants of the complexes are listed in Table 4.9, their speciation is depicted in Figure 4.38.

Table 4.9. Formation and deprotonation constants of zinc(II)-$\mathbf{L}^3$ complexes (estimated errors in parentheses (last digit), I = 0.1 M NaCl, T = 298 K).

	logβ	**pK**
$ZnH_2\mathbf{L}^3$	22.37(1)	6.07
$ZnH\mathbf{L}^3$	16.30(1)	8.10
$Zn\mathbf{L}^3$	8.20(3)	8.72
$ZnH_{-1}\mathbf{L}^3$	-0.52(3)	9.92
$ZnH_{-2}\mathbf{L}^3$	-10.44(3)	
$Zn_2H_{-2}\mathbf{L}^3$	-2.81(2)	8.53
$Zn_2H_{-3}\mathbf{L}^3$	-11.34(2)	10.78
$Zn_2H_{-4}\mathbf{L}^3$	-22.12(4)	

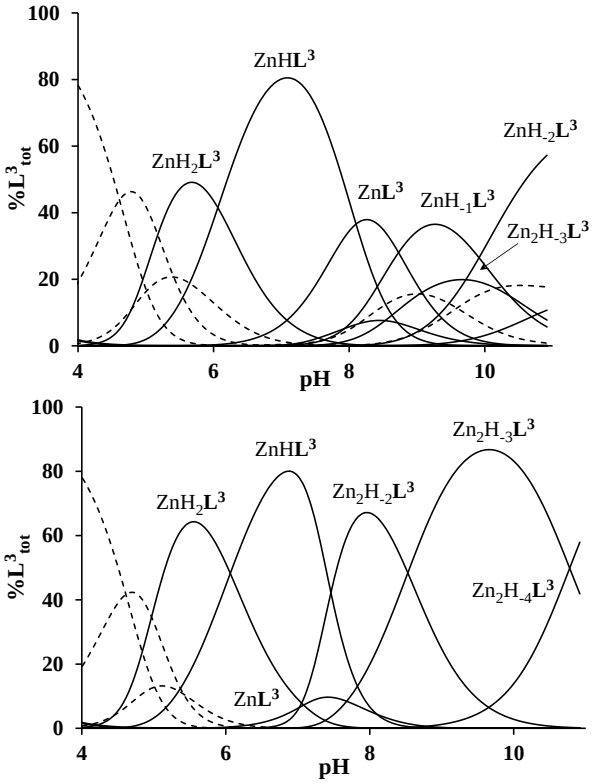

Figure 4.38. Speciation diagrams in Zn(II)-$\mathbf{L}^3$ 1:1 (up) and 2:1 (down) systems ($[\mathbf{L}^3]_{tot}$ = 0.001 M, $[Zn(II)]_{tot}$ = 0.001 and 0.002 M, I = 0.1 M NaCl, T = 298 K), dashed lines represent unbound ligand ($H_x\mathbf{L}^3$) species.

In the equimolar system, mononuclear zinc(II) complexes dominate in the whole studied pH range. The complexation starts with the formation of $ZnH_2\mathbf{L}^3$ at pH 4.5. The ^{1}H NMR spectra around pH 5 show notable broadening for the imidazole proton signals (Figure 4.39), indicating their role in the metal binding. Since both imidazole rings and one of the α-amino groups are deprotonated by metal ion assistance in $ZnH_2\mathbf{L}^3$, histamine-type binding with the additional coordination of the second imidazole ring $\{2N_{im},\alpha NH_2\}$ can be assumed in this species.

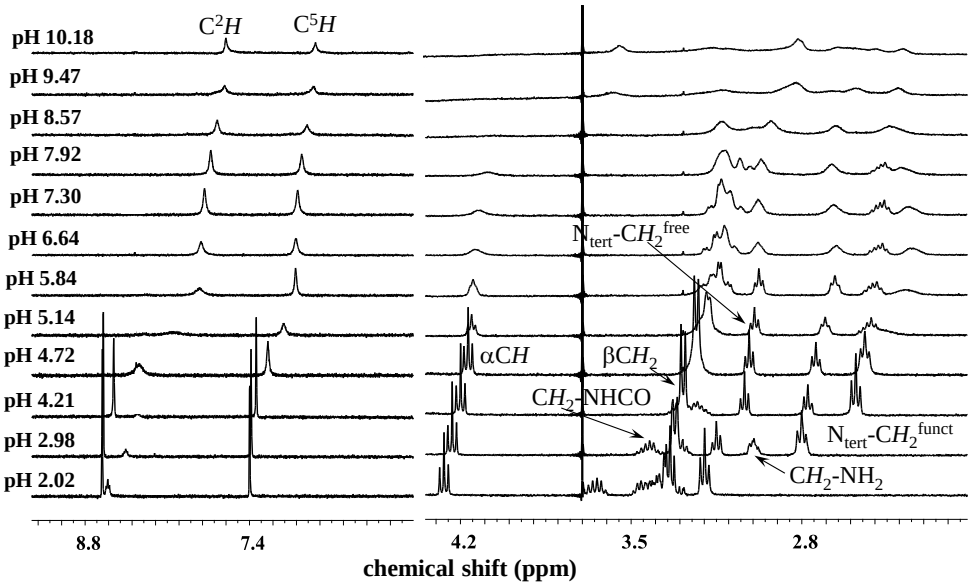

Figure 4.39. ^{1}H NMR titration of Zn(II)-$\mathbf{L}^3$ 1:1 system (in H_2O, $[\mathbf{L}^3]_{tot} = [Zn(II)]_{tot} = 0.0017$ M, $I = 0.1$ M NaCl, $T = 298$ K).

The deprotonation of $ZnH_2\mathbf{L}^3$ (pK = 6.07) results in the formation of $ZnH\mathbf{L}^3$, a dominant complex between pH 6-8. The Zn(II)-assisted deprotonation of the remaining $\alpha CH\text{-}NH_3^+$ results in the formation of *bis*-histamine-type $\{2N_{im},2\alpha NH_2\}$ coordination, which involves a macrochelate ring formation between the two His units (Scheme 4.10). The formation of this macrochelate is favorable, since the basicity corrected stability constant of $ZnH\mathbf{L}^3$ ($\log K = \log\beta_{ZnH\mathbf{L}^3} - \log\beta_{H_5\mathbf{L}^3} = -17.13$) is more than 4 units higher than that of the analogous Zn(histamine)$_2$ complex ($\log K = \log\beta_{ZnL_2} - 2\log\beta_{H_2L} = -21.71$ [114]). The presence of this macrochelate, similarly to the zinc(II)-tren3his system (see Figure 4.13. B), induces inequivalence of the CH_2 protons of the functionalized arms, which can be clearly seen on the $N_{tert}\text{-}CH_2^{funct}$ signals at ~ 2.4 ppm (Figure 4.39). The considerable downfield shift of αCH protons, close to the coordinated NH_2, as compared to the free ligand, is also noteworthy (Figure 4.40. A and B).

Above neutral pH, three overlapping deprotonation steps take place to result $Zn\mathbf{L}^3$, $ZnH_{-1}\mathbf{L}^3$ and $ZnH_{-2}\mathbf{L}^3$, beside a small amount of dinuclear complexes. During these processes the inequivalence of $N_{tert}\text{-}CH_2^{funct}$ protons ceased, and the signals of αCH protons are strongly upfield shifted (~3.5 ppm, Figure 4.40. E) indicating rearrangement in the coordination sphere. However, the general broadening of the ^{1}H NMR signals (Figures

4.39. and 4.40. D, E) allows to draw only limited conclusions. The broad spectra indicate that the 'extra' deprotonations must be related to the formation of mixed hydroxo species ($Zn\mathbf{L}^3(OH)_x$, x = 1, 2), since the deprotonation of the amide nitrogen(s) would result in slow ligand exchange (*i.e.* sharp signals, as it was observed in Zn(II)-Gly/Ala-His systems [126]).

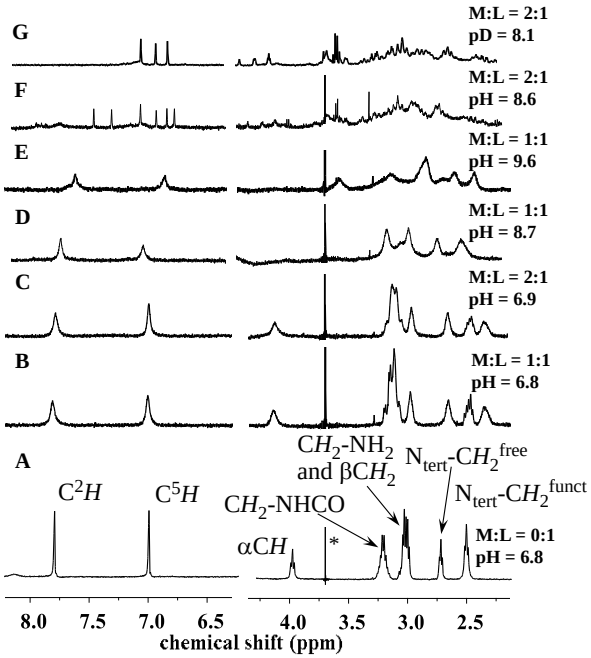

Figure 4.40. ^{1}H NMR spectra of $\mathbf{L}^3$ (**A**), Zn(II)-$\mathbf{L}^3$ 1:1 (**B**,**D**,**E**) and 2:1 (**C**,**F**, and **G** after deuteration of im-C^2 group) systems ($[\mathbf{L}^3]_{tot}$ = 0.0018 M, I = 0.1 M NaCl, T = 298 K). Marked* signal corresponds to dioxane reference at 3.70 ppm.

At metal excess, the evaluation of potentiometric data indicated the formation of three dinuclear complexes with compositions of $Zn_2H_{-2}\mathbf{L}^3$, $Zn_2H_{-3}\mathbf{L}^3$ and $Zn_2H_{-4}\mathbf{L}^3$. Their formation starts around pH 7 (Figure 4.38. down), which is in good agreement with the ^{1}H NMR spectra recorded at twofold metal excess: the spectral features are identical to that observed at Zn(II)-$\mathbf{L}^3$ 1:1 ratio until pH 7 (Figure 4.40. B, C).

Starting from neutral pH, several αCH proton signals can be seen, and more importantly, six sharp signals appear in the aromatic region of ^{1}H NMR spectrum (Figures 4.40. F and 4.41). The latter indicates three chemically different environments for the imidazole rings with nearly equal populations in the slow exchanging oligonuclear complexes. 2D TOCSY measurements and ^{1}H NMR spectrum of the complex(es) deuterated at the imidazole C^2 carbon (Figure 4.40. G) allowed the identification of the C^2H/C^5H pairs. Accordingly, at pH 8.2 the C^2H signals are strongly upfield-shifted by 0.29, 0.46 and 1.05 ppm in the slow exchanging oligonuclear complexes, as compared to the free ligand signals (Figure 4.41. right).

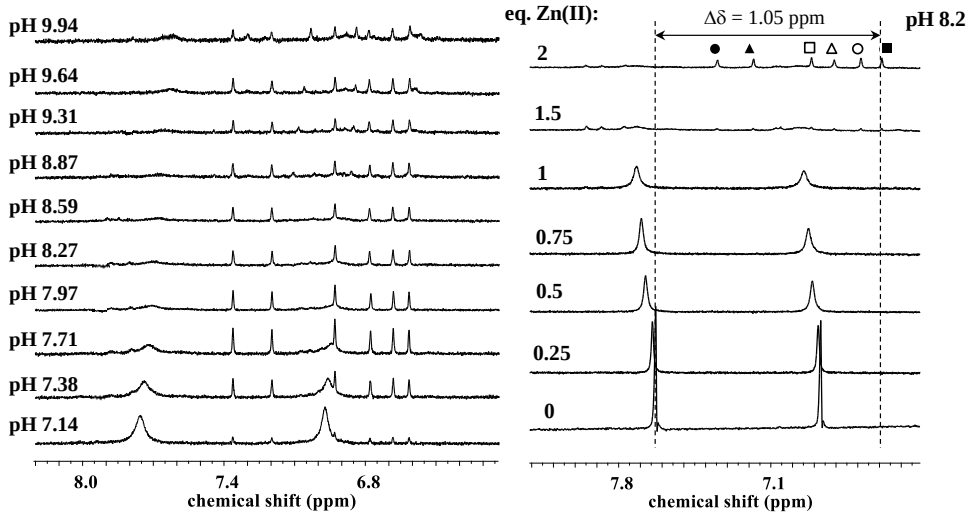

Figure 4.41. Aromatic region of ^{1}H NMR spectra of Zn(II)-$\mathbf{L}^{3}$ system. Left: pH dependence at Zn(II)-$\mathbf{L}^{3}$ 1.9:1 ratio; right: dependence on the Zn(II)-$\mathbf{L}^{3}$ ratios at pH 8.2 (in H_2O, $[\mathbf{L}^{3}]_{tot}$ = 0.0018 M, I = 0.1 M NaCl, T = 298 K). Marked signals demonstrate corresponding C^2H (black symbols) and C^5H (empty symbols) protons.

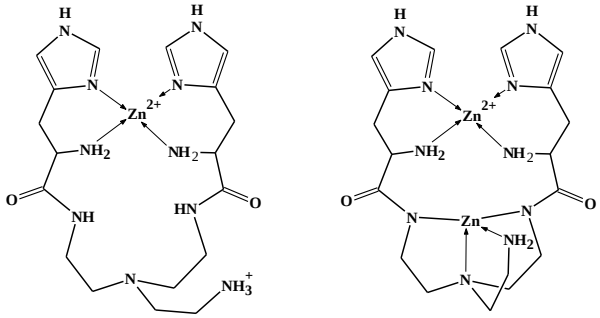

$ZnH\mathbf{L}^{3}$ $Zn_2H_{-2}\mathbf{L}^{3}$

Scheme 4.10. Proposed structures of main Zn(II)-$\mathbf{L}^{3}$ complexes.

The 'extra' deprotonation observed for the oligonuclear species between pH 7-8 could be assigned to (i) deprotonation of coordinated water molecule(s), (ii) metal-promoted deprotonation of amide nitrogen(s) or (iii) formation of μ-imidazolato-bridge between two zinc(II) ions. Among these processes only (ii) and (iii) may lead to slow ligand exchange processes and notable shift of imidazole proton signals. It is worth to mention that the strongly related *N,N'*-di-L-histidylethane-1,2-diamine (dhen) ligand also forms imidazolato-bridged oligozinc(II) complexes in the same pH range [114]. The increased electron density on the imidazolate ring obviously results in remarkable upfield shift of C^2H signals (up to ~2.2 ppm [114, 131, 132]), as compared to the free ligand. On the other hand, in the Zn(II)-GlyHis system [126] the coordination of imidazole ring and the deprotonation of nearby amide nitrogen also resulted in 0.2-0.4 ppm upfield shift of the imidazole and αCH signals. In the present system, the wide range of chemical shifts of imidazole and αCH signals upon metal ion binding (Figures 4.40. F and 4.41.) indicates the presence of both amide- and imidazolate-bound zinc centers.

The *bis*-histamine-type coordination of zinc(II) in $ZnH\mathbf{L}^{3}$ provides a preorganized tren-like $\{NH_2,N_{tert},2N^{-}\}$ binding site for the second metal ion (Scheme 4.10), *i.e.* the deprotonation of the amide nitrogens is promoted by the anchoring $\{NH_2^{tren},N_{tert}\}$ chelate. This binding mode explains the strongly cooperative deprotonations during the process $ZnH\mathbf{L}^{3} + Zn^{2+} = Zn_2H_{-2}\mathbf{L}^{3} + 3H^{+}$ (Figure 4.38. down), and also the fact that dinuclear complexes are formed only at metal ion excess, in parallel with the deprotonation of NH_2 of the free tren arm. However, the two imidazole moieties in $Zn_2H_{-2}\mathbf{L}^{3}$ cannot exist in three chemically different environments with nearly equal populations; therefore, more than one species must be present under these conditions.

In order to explain the above-mentioned observations, we assume a dimerization process of $2Zn_2H_{-2}\mathbf{L}^{3} = (Zn_2H_{-2}\mathbf{L}^{3})_2$, through the formation of two imidazolato-bridges and the re-protonation of two zinc-bound amide nitrogens. The proposed structures for $Zn_2H_{-2}\mathbf{L}^{3}$ and $(Zn_2H_{-2}\mathbf{L}^{3})_2$ are depicted in Figure 4.42.

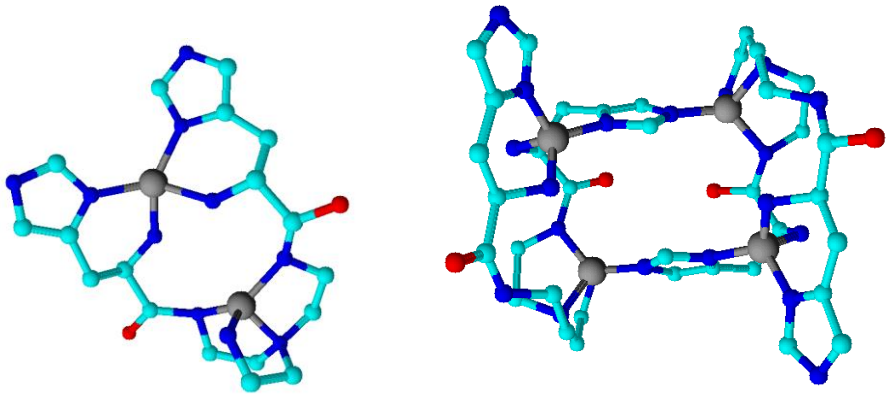

Figure 4.42. Proposed structures for $Zn_2H_{-2}\mathbf{L}^{3}$ and $(Zn_2H_{-2}\mathbf{L}^{3})_2$.

The proposed dimerization involves simple proton transfer from the imidazole N^1H to the deprotonated amide nitrogen. During this process, the imidazole C^2H protons become close to the tren CH_2 groups of the other ligand molecule in space. Accordingly, we observed ROESY correlation between two imidazole C^2H protons (Figure 4.43), tentatively assigned to $(Zn_2H_{-2}\mathbf{L}^{3})_2$, and two aliphatic signal at 2.58 and 2.78 ppm, most likely corresponding to the inequivalent protons of N_{tert}-CH_2 groups. The simultaneous presence of the two complexes ($Zn_2H_{-2}\mathbf{L}^{3}$ and $(Zn_2H_{-2}\mathbf{L}^{3})_2$) is probably the simplest way to explain the six sharp signals observed in the aromatic region of the NMR spectra at 2:1 Zn(II)-$\mathbf{L}^{3}$ ratio.

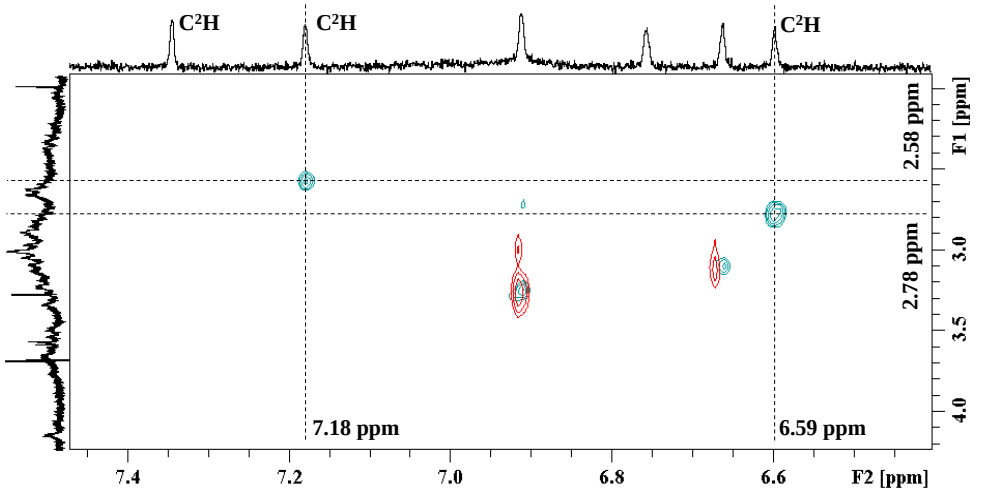

Figure 4.43. 2D ROESY (green) and TOCSY (red) spectra in Zn(II)-$\mathbf{L}^{\mathbf{3}}$ 2:1 system at pH 8.2.

The characteristic spectral patterns of the oligonuclear complexes are present in the NMR spectra over a wide pH range (pH 7-10, Figure 4.41), meaning that the basic skeletons of these species are unchanged during the next observed deprotonation ($Zn_2H_{-2}\mathbf{L}^{\mathbf{3}} \rightarrow Zn_2H_{-3}\mathbf{L}^{\mathbf{3}} + H^+$), suggesting the formation of mixed hydroxo complexes. On the other hand, new sharp peaks appear in the imidazole region around pH 10 (Figure 4.41. left), which indicates structural reorganization within the oligonuclear complexes. However, this deprotonation step ($Zn_2H_{-3}\mathbf{L}^{\mathbf{3}} \rightarrow Zn_2H_{-4}\mathbf{L}^{\mathbf{3}} + H^+$, p$K$ = 10.78) is complete only above pH 11, therefore detailed ^{1}H NMR investigations were not performed.

In consequence of all the above facts, the fitting of potentiometric data by only dinuclear complexes is an oversimplified model of the real equilibrium situation. Nevertheless, it can describe the titration curves correctly, since the equilibrium constants of reaction $ZnH\mathbf{L}^{\mathbf{3}} + Zn^{2+} = (1/n)(Zn_2H_{-x}\mathbf{L}^{\mathbf{3}})_n + (x+1)H^+$ for different values of n and different kind of deprotonation processes are nearly identical.

4.4.4. Copper(II) complexes of tren1his

The *mono*-histidyl functionalized tren1his forms only mononuclear complexes in presence of copper(II). The determined formation constants and spectroscopic parameters are listed in Table 4.10, the distribution curves of the copper(II)-$\mathbf{L}^4$ species are depicted in Figure 4.44.

Table 4.10. Formation constants, deprotonation constants (I = 0.1 M NaCl, T = 298 K, estimated error of last digits in parentheses) and spectroscopic (UV-Vis, CD and EPR) parameters of the copper(II)-$\mathbf{L}^4$ complexes.

	logβ	**pK**	**$\lambda_{max}^{d\text{-}d}$ (nm), ε ($M^{-1}cm^{-1}$)**	**λ_{max}^{CD} (nm), $\Delta\varepsilon$ ($M^{-1}cm^{-1}$)**	**$g_{o,calc}$***
$CuH_2\mathbf{L}^4$	27.181(6)	3.951	~670, 60.6	~720, 0.12	
$CuH\mathbf{L}^4$	23.230(8)	5.931	585, 118.6	535, 0.167 645, -0.188	2.113
$Cu\mathbf{L}^4$	17.299(9)	6.529	615, 142.9	545, 0.076 605, -0.016 695, 0.118	
$CuH_{-1}\mathbf{L}^4$	10.77(1)		632, 169.1	300, -1.02 635, 0.259	2.112

*$g_{o,calc} = (g_x+g_y+g_z)/3$, anisotropic parameters and fitted spectra can be found in Appendix A.23. and Table A.1.

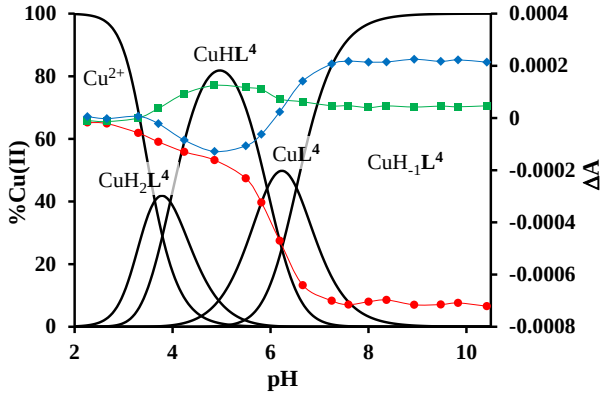

Figure 4.44. Distribution of the species in Cu(II)-$\mathbf{L}^4$ 1:1 system ($[\mathbf{L}^4]_{tot}$ = $[Cu(II)]_{tot}$ = 0.001 M, I = 0.1 M NaCl, T = 298 K). Secondary axis: measured CD intensities at 305 nm (red), 535 nm (green) and 635 nm (blue).

The equilibrium constant for the reaction $Cu^{2+} + H_2\mathbf{L}^4 = CuH_2\mathbf{L}^4$ (log$K$ = 8.24), as well as the individual UV-Vis ($\lambda^{d\text{-}d}_{max}$ ~ 670 nm) and CD (λ_{max} ~ 720 nm) spectra (Figure 4.45.) of $CuH_2\mathbf{L}^4$ complex suggest histamine-like $\{N_{im},NH_2\}$ coordination in this species (Scheme 4.11), similarly to several -HXX- peptides [118, 124].

The formation of $CuH\mathbf{L}^4$, which is the dominant species around pH 5, induces remarkable changes in the spectroscopic properties indicating a characteristically different binding mode. In principle, several binding modes are possible in this species, but the intense CD spectrum (Figure 4.45.) excludes the possibility of the sole coordination of the achiral tren-subunit $\{NH_2^{tren},N_{tert},NH_2^{tren}\}$. In fact, the observed 'inverse couplet' on the

CD spectrum of CuH**L**^{4} is unique, and characteristic for the species in which the chiral perturbation arises from a single histidine unit bound to copper(II) in a seven-membered {N_{im},N^-} chelate. This type of coordination results in a very similar CD spectrum for the copper(II) complexes of Ac-HGG-NH_2, Ac-HGGG-NH_2, Ac-HGGGW-NH_2 and several other analogs of prion protein octarepeat domain [118-120], and also for the {N_{im},N^-,N_{tert},N^-} coordinated CuH_{-2}**L**^{1} species in the copper(II)-tren3his 1:1 system (Section 4.1.2, Figure 4.9. A). Accordingly, in CuH**L**^{4} we suggest {N_{im},N^-,N_{tert},NH_2^{tren}} coordination (Scheme 4.11). The participation of a tren-like NH_2 and tertiary amino groups in the coordination is dictated by the protonation state of the complex and the enhanced stability of fused chelate rings, respectively. Indeed, the 4N-coordination is also supported by the relatively high energy of d-d transitions ($\lambda^{d\text{-}d}_{max}$ ~ 585 nm) and the corresponding EPR parameters (see Appendix, Table A.1. and Figure A.23).

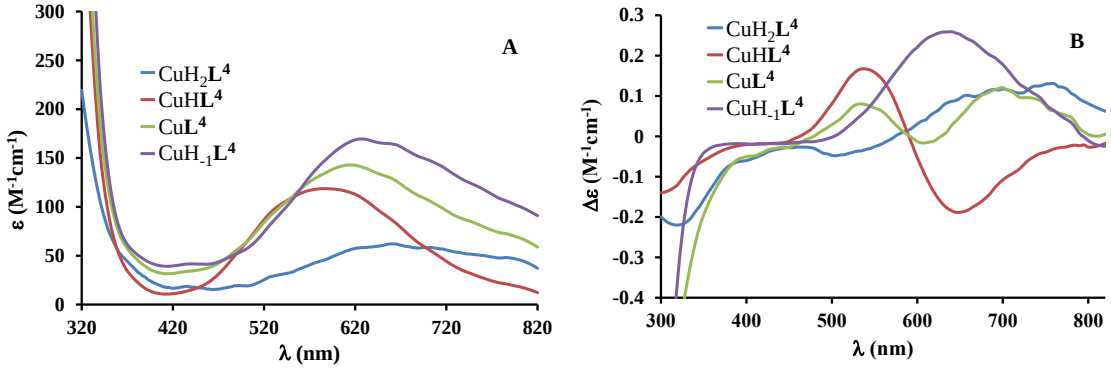

Figure 4.45. Individual molar UV-Vis (**A**) and CD (**B**) spectra of the forming species in Cu(II)-**L**^{4} 1:1 system.

Above pH 5, two overlapping deprotonations lead to CuH_{-1}**L**^{4}, which is the only species present in solution above pH 8. The UV-Vis, CD and EPR spectra indicate considerable rearrangement of the coordination sphere during these deprotonations: the d-d transitions are red-shifted by 47 nm, the g values are nearly unchanged, but A_z is considerably decreased (178 → 157 G, Appendix Table A.1). The 'inverse couplet' on the CD spectra also disappears during the CuH**L**^{4} → Cu**L**^{4} → CuH_{-1}**L**^{4} transformation. These facts indicate the coordination of a further N-donor in axial position, and therefore changes in the coordination geometry. Tren derivatives are known to prefer pentacoordinated structures, and the spectroscopic data are in accordance with the formation of square pyramidal geometry. In one of the possible structures the equatorial binding sites of CuH**L**^{4} are retained, and the second tren-like NH_2 group is coordinated in the apical position (Scheme 4.11), *i.e.* the αNH_3^+ deprotonates without metal ion assistance.

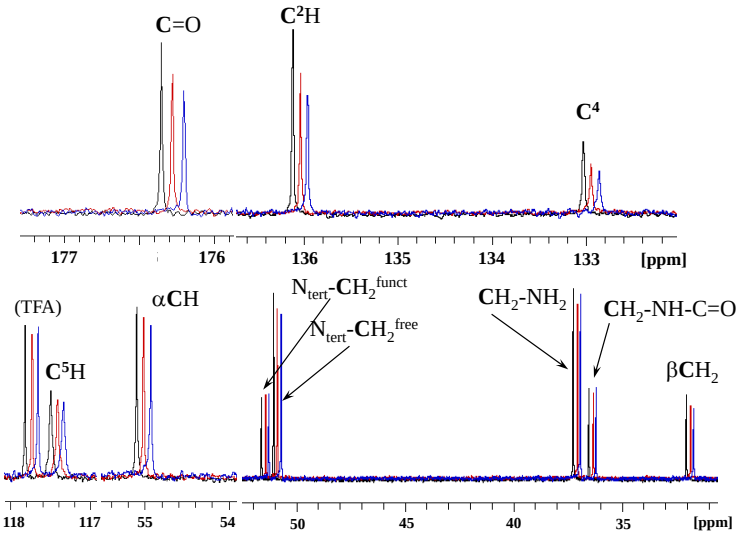

Figure 4.46. ^{13}C NMR spectra of $\mathbf{L^4}$ in presence of 0% (black), 5% (red) and 10% (blue) Cu(II) (in H_2O, pH 8.5, $[\mathbf{L^4}]_{tot}$ = 0.05 M, T = 298 K). Axis is scaled to the spectrum of the free ligand.

Obviously, in an alternative structure αNH_2 may replace the imidazole ring. In order to support one of the above mentioned binding modes, we recorded ^{1}H and ^{13}C NMR spectra of $\mathbf{L^4}$ in the presence of copper(II). On the ^{1}H NMR spectra the paramagnetic copper(II) induced only general, not selective broadening of the signals. On the other hand, the ^{13}C NMR spectra indicated notable broadening of the signals corresponding to the imidazole moiety (C^2H, C^4, Figure 4.46.) as compared to the minor broadening of the αCH signal. This observation suggests the participation of imidazole ring in the coordination in $CuH_{-1}\mathbf{L^4}$ (Scheme 4.11).

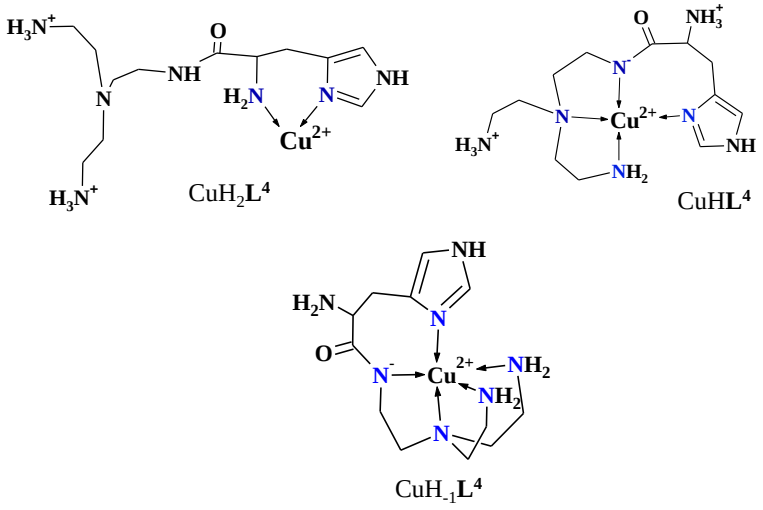

Scheme 4.11. Proposed structures of the main copper(II)-$\mathbf{L^4}$ complexes.

4.4.5. Zinc(II) complexes of tren1his

In the Zn(II)-$\mathbf{L^4}$ system, four differently protonated mononuclear species could be identified by potentiometry (Table 4.11, Figure 4.47). At the beginning of complex formation (pH 4.5-5.5) all ^{1}H NMR signals related to the histidine unit are significantly broadened (Figure 4.48). Even though $ZnH_2\mathbf{L^4}$ complex is not produced in higher quantities than 40%, the selective broadening on the ^{1}H NMR spectra indicates that zinc(II) is bound to the histidine moiety in a histamine-like binding mode ({N_{im},NH_2}, Scheme 4.12). The log*K* value for the process $Zn^{2+} + H_2\mathbf{L^4} = ZnH_2\mathbf{L^4}$ ($\log K = \log\beta_{ZnH_2\mathbf{L^4}} - \log\beta_{H_2\mathbf{L^4}} = 4.51$) also supports this type of coordination [114].

Table 4.11. Formation and deprotonation constants of Zn(II)-$\mathbf{L^4}$ complexes (I = 0.1 M NaCl, T = 298 K, estimated error of last digits in parentheses).

	logβ	**pK**
$ZnH_2\mathbf{L^4}$	23.45(3)	6.45
$ZnH\mathbf{L^4}$	17.00(3)	
$ZnH_{-1}\mathbf{L^4}$	4.16(2)	10.73
$ZnH_{-2}\mathbf{L^4}$	-6.57(4)	

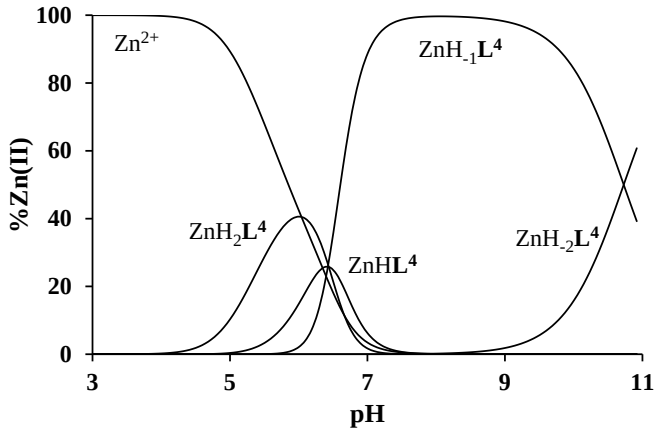

Figure 4.47. Speciation diagrams in Zn(II)-$\mathbf{L^4}$ 1:1 system ($[\mathbf{L^4}]_{tot} = [Zn(II)]_{tot}$ = 0.001 M, I = 0.1 M NaCl, T = 298 K).

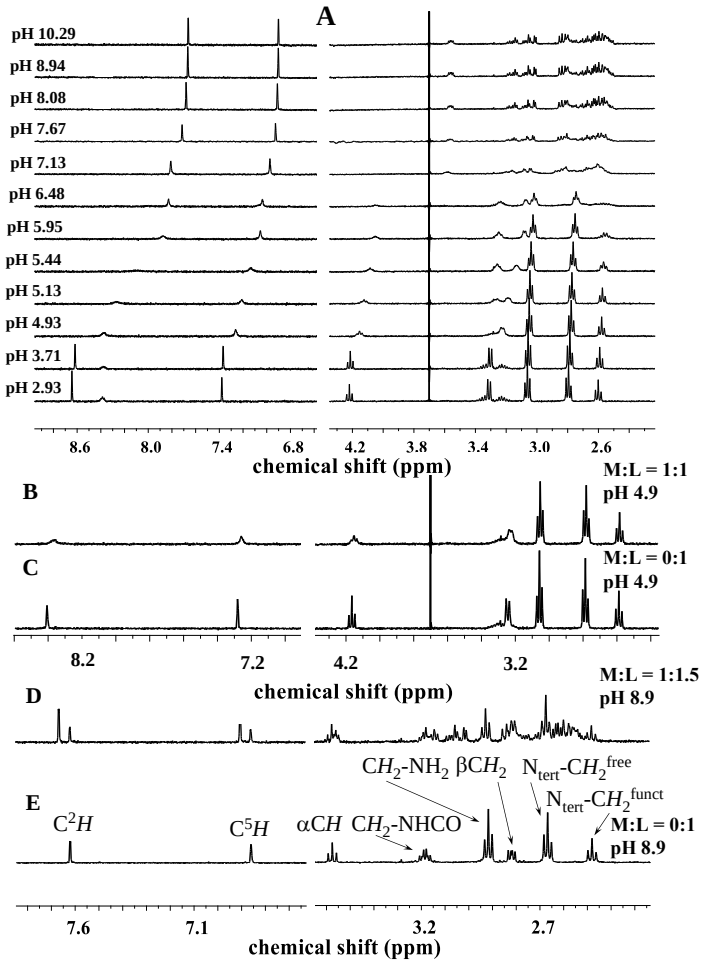

Figure 4.48. pH-dependent ^{1}H NMR spectra of Zn(II)-$\mathbf{L^4}$ 1:1 system (**A**,**B**), 1:1.5 system (**D**) and comparison with the spectra of free ligand (**C**,**E**). In H_2O, dioxane reference (3.70 ppm), $[\mathbf{L^4}]_{tot}$ = 0.0016 M, I = 0.1 M NaCl, T = 298 K.

The formation of $ZnH_{-1}\mathbf{L^4}$, a dominant complex between pH 7-10, occurs through three strongly overlapped deprotonations ($ZnH_2\mathbf{L^4} \rightarrow ZnH_{-1}\mathbf{L^4} + 3H^+$), which are so cooperative that $Zn\mathbf{L^4}$ could not be detected at all. In parallel (pH 6.0-7.5), remarkable changes can be observed on the NMR spectra. All CH_2 signals first broaden then sharpen to result a complex spectrum in the basic pH range (Figure 4.48. A,D). The source of this complicated peak set is the slow ligand exchange rate of $ZnH_{-1}\mathbf{L^4}$, and the inequivalence of all CH_2 protons related to the metal-bound ligand.

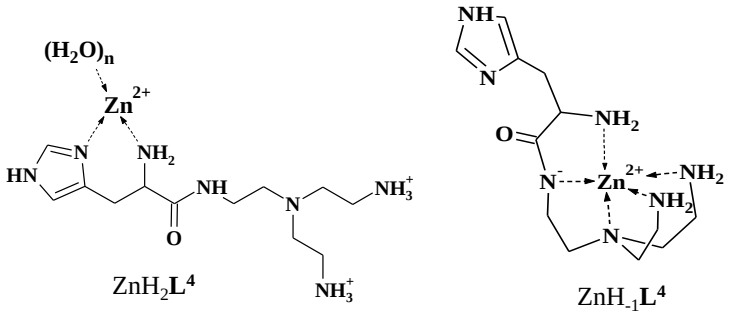

Scheme 4.12. Proposed structure of the main Zn(II)-$\mathbf{L^4}$ complexes.

The slow ligand exchange observed for $ZnH_{-1}\mathbf{L}^{4}$ indicates that the 'extra' deprotonation is related to the formation of amide-bound species (and not to mixed hydroxo complexes) [126]. Beside the amide group, the complete formation of $ZnH_{-1}\mathbf{L}^{4}$ at pH 7 suggests zinc(II) protomoted deprotonation and coordination of all three primary amino groups (their p*K* values in the free ligand are 7.07, 9.04, 9.90). Although the tertiary amino group is deprotonated at pH 7 even in the absence of zinc(II), the preferred formation of fused chelate rings and the inequivalence of all tren-CH_2 protons support its coordination. The simultaneous coordination of amide-, αNH_2- and imidazole nitrogens is unlikely in the case of N-terminal His fragments [42, 133], therefore the axial coordination site can be occupied by either the N_{im} or the αNH_2 group. Considering the thermodynamically favorable 5-membered $\{N^{-},\alpha NH_2\}$ chelate ring and the above-mentioned deprotonation processes, we suggest $\{3NH_2,N^{-},N_{tert}\}$ type binding in $ZnH_{-1}\mathbf{L}^{4}$ (Scheme 4.12). In consequence of the saturated coordination sphere in $ZnH_{-1}\mathbf{L}^{4}$, the p*K* of the subsequent deprotonation is rather high (10.73), since the coordinating hydroxide ion should displace one of the bound nitrogens.

4.5. ASSESSMENT OF THE METAL BINDING PROPERTIES OF TRIPODAL PEPTIDES

An important aim of this work was to enhance the metal binding capabilities of linear peptides with the assistance of functionalized tripodal platforms. The comparison of metal ion sequestering ability of different ligands based on simply the formation/stability constants, however, can be misleading, due to the different basicity of the compared ligands. In order to demonstrate the increased metal ion sequestering ability of our tripodal ligands, predominance diagrams were simulated in presence of our ligand systems, and also of other structurally relevant ligands.

The impact of gradual functionalization of tren scaffold on metal ion affinity can be well studied in the trenXhis (X = 1, 2, 3) series. Based on the predominance diagrams in Cu(II)- and Zn(II)-trenXhis equimolar systems (Figure 4.49), it can be stated that the metal ion is bound most importantly by tren3his ($\mathbf{L}^1$) in the acidic-neutral, and by tren1his ($\mathbf{L}^4$) in the basic pH range. This tendency stands for both copper(II) and zinc(II) complexes. Interestingly, tren2his ($\mathbf{L}^3$) does not become dominant metal binding ligand next to the other two at any pH. These findings point to the two highly dominant binding modes in the trenXhis series, which in fact predominate in different pH ranges. The *bis*-histamine-type binding - supplemented by axial coordination in case of $\mathbf{L}^1$ - is major binding site up to neutral pH, while the involvement of the tren-type binding site (N_{tert}, NH_2 and/or N^- groups) becomes more and more important in the basic pH range with decreasing functionalization of the tripodal scaffold. The ligand tren1his can be considered as a 'maximum' in copper(II) binding capability in this ligand series above pH 7: simulations demonstrated that its copper complexes dominate even over copper(II)-tren species at 1:1:1 Cu(II)-$\mathbf{L}^4$-tren ratio.

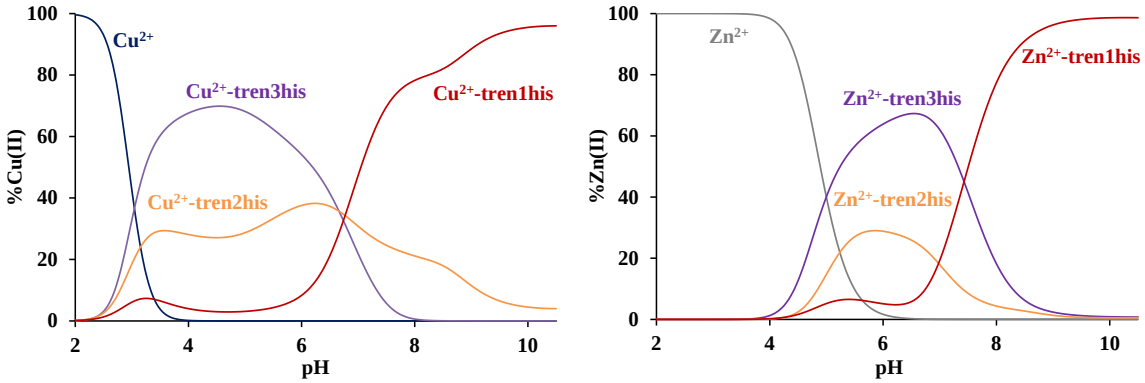

Figure 4.49. Simulated predominance diagrams in the Cu(II)- (left) and Zn(II)- (right) $\mathbf{L}^1$-$\mathbf{L}^3$-$\mathbf{L}^4$ 1:1:1:1 quaternary systems. $[Cu(II)]_{tot} = [Zn(II)]_{tot} = [\mathbf{L}^1]_{tot} = [\mathbf{L}^3]_{tot} = [\mathbf{L}^4]_{tot} = 0.001$ M.

Even though the two symmetrically functionalized tren3his and nta3his ($\mathbf{L}^2$) ligands are very different in terms of basicity and nature of donor groups, their metal binding capabilities are worth comparing (Figure 4.50). $\mathbf{L}^2$ bears carboxylic groups which are capable of binding copper(II) ions strongly at relatively low pH. In agreement with the

previous statements, the *bis*-histamine-type coordination provides exceptional binding site for copper(II) in the acidic-neutral pH range. As this binding mode loses significance above pH 8, the nta3his ligand becomes the dominant copper(II) binding agent. Based on these observations, we can state that the Gly-His-type $\{N_{im},N_{tert},N^-,O\}$ structure of nta3his is not able to compete with the *bis*-histamine-type coordination, but provides a more stable coordination environment than that of the $\{N_{im},N^-,N_{tert},N^-\}$ structure in $CuH_{-2}\mathbf{L}^1$.

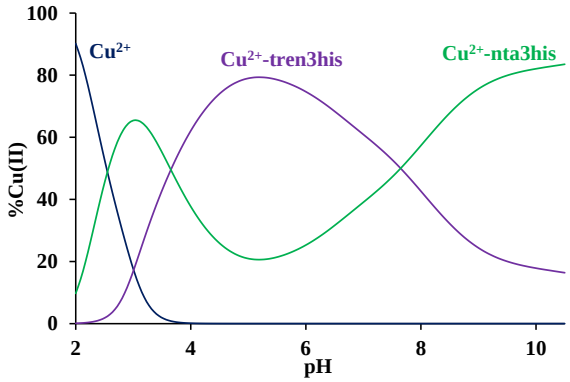

Figure 4.50. Simulated predominance diagrams in the Cu(II)-$\mathbf{L}^1$-$\mathbf{L}^2$ 1:1:1 ternary system. $[Cu(II)]_{tot} = [\mathbf{L}^1]_{tot} = [\mathbf{L}^2]_{tot} = 0.001$ M.

Considering the structural organization of the metal binding moieties provided by the tripodal scaffold, it might not be surprising that the two symmetrical *tris*-His ligands demonstrate higher metal binding abilities in the whole pH range than that of their 'structural models', histamine and Gly-His (Figure 4.51). This dominance is so important that the Zn(II) complex of histamine does not produce in notable quantities in the Zn(II)-$\mathbf{L}^1$-histamine 1:1:1 equimolar system.

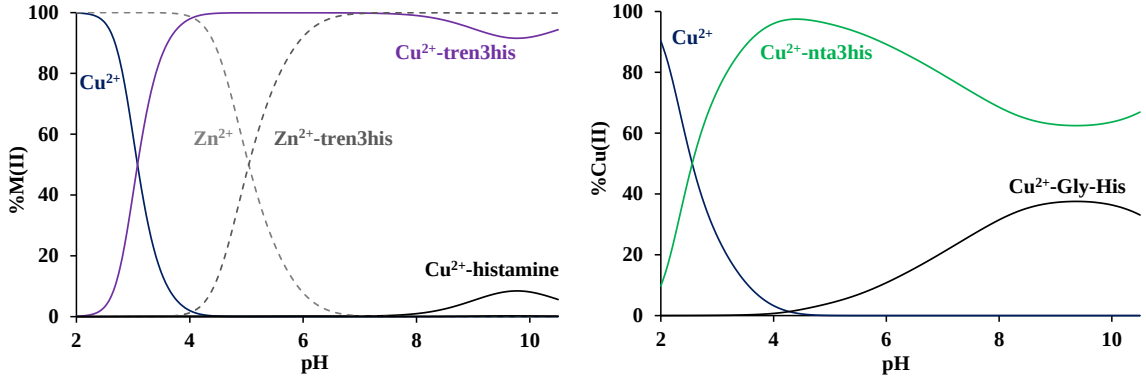

Figure 4.51. Simulated predominance diagrams in the Cu(II)/Zn(II)-$\mathbf{L}^1$-histamine 1:1:3 (left) and Cu(II)-$\mathbf{L}^2$-Gly-His 1:1:1 (right) ternary systems. $[Cu(II)]_{tot} = [Zn(II)]_{tot} = [\mathbf{L}^1]_{tot} = 0.001$ M, $[histamine]_{tot} = 0.003$ M, $[Cu(II)]_{tot} = [\mathbf{L}^2]_{tot} = [Gly\text{-}His]_{tot} = 0.001$ M.

If we mean to draw conclusions on enhanced metal binding with respect to linear peptides, probably the most convincing example is the comparison of our systems with the simplest H_2N-XXH-type peptide ligand, Gly-Gly-His (GGH), which can be considered as one of the strongest copper(II) binding peptide sequence providing $\{NH_2,N^-,N^-,N_{im}\}$ binding site in aqueous solutions [134]. Simulated predominance curves of

Cu(II)-**L**^{1}-**L**^{3}-**L**^{4} 1:1:1:1 system show that the copper(II) complex of GGH does not form in dominant quantities at any pH (Figure 4.52). In fact, the presence of 1 eq. GGH does not alter significantly the distribution of copper(II) among the trenXhis ligands, implying that it is unable to compete in copper(II) binding with the above-described, highly stable coordination environments provided by the trenXhis series. This observation proves convincingly that metal binding capabilities of peptides can be significantly improved by the functionalization with tripodal scaffold.

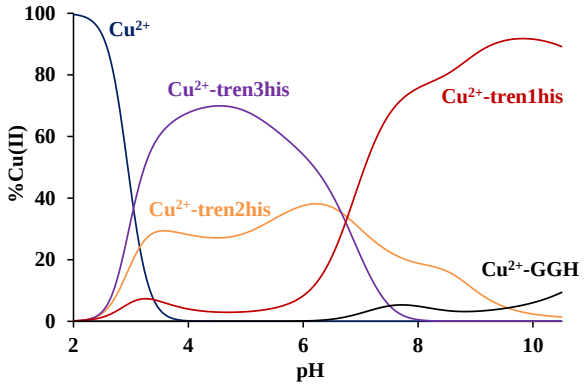

Figure 4.52. Simulated predominance diagrams in the Cu(II)-**L**^{1}-**L**^{3}-**L**^{4}-GGH 1:1:1:1:1 system. $[Cu(II)]_{tot} = [\mathbf{L}^{1}]_{tot} = [\mathbf{L}^{3}]_{tot} = [\mathbf{L}^{4}]_{tot} = [GGH]_{tot} = 0.001$ M.

4.6. CATECHOL OXIDASE MIMICKING WITH THE METAL-LIGAND COMPLEXES

One of our main goals was to explore the effect of increasing histidyl functionalization of tripodal platforms on enzyme mimicking properties of the formed copper(II) complexes. To this end we tested our copper(II) complexes as catechol oxidase mimics. For that purpose, we chose the widely investigated 3,5-di-*tert*-butylcatechol (H_2DTBC) substrate, which is selectively converted to 3,5-di-*tert*-butyl-*o*-benzoquinone (DTBQ) in presence of copper(II) containing catalysts and dioxygen. Catechol oxidases are type-3 copper enzymes [48, 135], therefore the copper(II) complexes of trenXhis (X = 1, 2, 3) ligands are well suited for such biomimetic studies, and provide a decent possibility for structure/nuclearity/activity comparison.

We performed detailed kinetic measurements in order to establish kinetic parameters (Section 4.6.1), whereas substrate binding studies helped us to reveal mechanistic information (Sections 4.6.2-4.6.4). Experimental conditions of kinetic studies are collected in Table 4.12; further experimental details can be found in Section 3.3.1.

4.6.1. Kinetic study of Cu(II)-L^1, -L^2 and -L^3 systems

In case of all copper(II)-ligand systems, pH-dependent kinetic measurements were carried out to reveal the pH optimum of the reaction; further experiments were performed at this pH, in buffered solutions. Of all investigated systems, the copper(II) complexes of tren3his (**L^1**), nta3his (**L^2**) and tren2his (**L^3**) ligands were found to possess high catechol oxidase activity. In every cases, the multinuclear (Cu(II)-**L^1** 3:2, Cu(II)-**L^2** and -**L^3** 2:1) complexes showed the highest catechol oxidase mimicking capability. Although we observed activity for the Cu(II)-**L^1** 1:1 system in the basic pH range, the presence of trinuclear complexes in solution makes it impossible to distinguish the catalytic performance of the mono- and the trinuclear species. Therefore, further kinetic experiments were performed only at 3:2 copper(II)-to-ligand ratio, where trinuclear complexes dominate in the studied pH region.

Table 4.12. Experimental conditions used in the kinetic measurements of H_2DTBC oxidation by Cu(II)-**L** systems (in H_2O/EtOH 50/50%, I = 0.1 M NaCl-buffer (MES/HEPES/CHES), T = 298 K in all experiments).

system	$[S]_o$ (M)	$[complex]_{tot}$ (M)	pH_{corr}	varying condition
Cu(II)-$\mathbf{L^1}$ 3:2	1.5×10^{-3}	5.0×10^{-5}		pH_{corr}
		5.0×10^{-5}	7.8	$[S]_o$
	5.0×10^{-3}		7.8	$[complex]_{tot}$
	5.0×10^{-4}	4.8×10^{-5}	7.8	$[O_2]$
Cu(II)-$\mathbf{L^2}$ 2:1	7.0×10^{-4}	5.0×10^{-5}		pH_{corr}
		1.0×10^{-5}	8.9	$[S]_o$
	4.0×10^{-4}		8.9	$[complex]_{tot}$
	8.0×10^{-4}	5.0×10^{-5}	8.9	$[O_2]$
Cu(II)-$\mathbf{L^3}$ 1:1	8.0×10^{-4}	5.0×10^{-5}		pH_{corr}
		1.0×10^{-5}	7.4	$[S]_o$
Cu(II)-$\mathbf{L^3}$ 2:1	4.0×10^{-4}	1.0×10^{-5}		pH_{corr}
		5.3×10^{-6}	8.7	$[S]_o$
	5.4×10^{-4}		8.7	$[complex]_{tot}$
	5.5×10^{-4}	1.0×10^{-5}	8.7	$[O_2]$

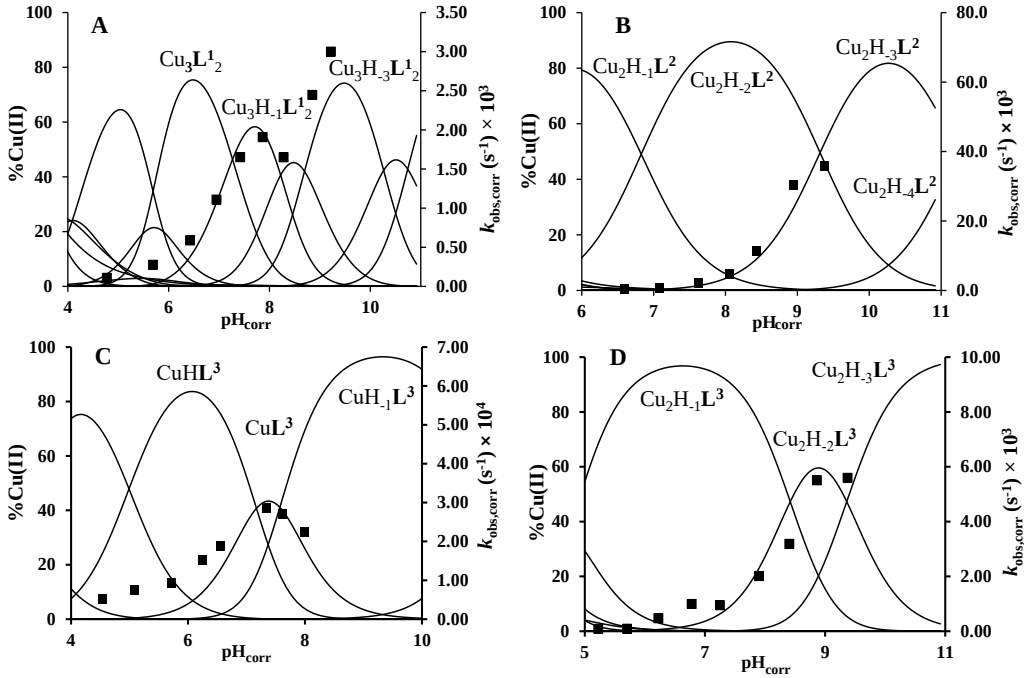

Figure 4.53. pH-dependent reaction rate constants ($k_{obs,corr}$, secondary axis) in the investigated Cu(II)-$\mathbf{L^1}$ 3:2 (**A**), Cu(II)-$\mathbf{L^2}$ 2:1 (**B**), Cu(II)-$\mathbf{L^3}$ 1:1 (**C**) and Cu(II)-$\mathbf{L^3}$ 2:1 (**D**) systems, with the corresponding speciation diagrams (primary axis). Applied concentrations in Table 4.12.

The pH_{corr}–$k_{obs,corr}$ profiles of catalytic H_2DTBC oxidation are presented on Figure 4.53. In case of Cu(II)-$\mathbf{L^1}$ 3:2 system we observed a reproducible local maximum around pH 7.8, and increasing rate constants above pH 8.3. In presence of Cu(II)-$\mathbf{L^2}$ 2:1 system, a continuous increase of rate constants was observed above pH 7, and their values are higher

at any pH than in the former case. Both Cu(II)-$\mathbf{L}^3$ 1:1 and 2:1 systems resulted a pH optimum (pH_{corr} 7.4 and 8.7, Figure 4.53), however the observed reaction rates are very different in the two cases. The speciation of the complexes in 50% ethanol-water solvent mixture is generally similar to those determined in pure aqueous solutions, thus the observed catalytic activities are mainly related to the complexes $Cu_3H_{-1}\mathbf{L}^1_2$/$Cu_3H_{-3}\mathbf{L}^1_2$, $Cu_2H_{-3}\mathbf{L}^2$, $Cu\mathbf{L}^3$ and $Cu_2H_{-2}\mathbf{L}^3$. Based on these data (and to avoid the high rate of autooxidation of H_2DTBC), the further kinetic measurements have been performed at pH_{corr} = 7.8 ($\mathbf{L}^1$), 8.9 ($\mathbf{L}^2$), 7.4 ($\mathbf{L}^3$ mononuclear system) and 8.7 ($\mathbf{L}^3$ dinuclear system).

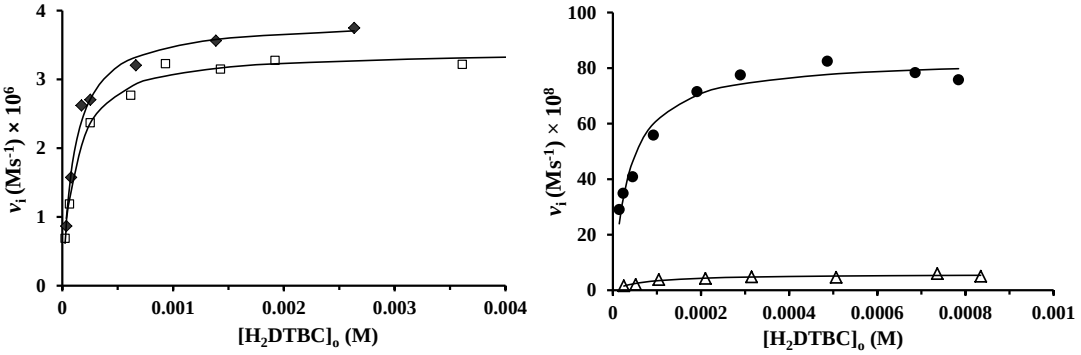

Figure 4.54. Dependence of the initial reaction rates on H_2DTBC concentration promoted by Cu(II)-**L** systems (♦: Cu(II)-$\mathbf{L}^1$ 3:2, pH_{corr} 7.8, □: Cu(II)-$\mathbf{L}^2$ 2:1, pH_{corr} 8.9, Δ: Cu(II)-$\mathbf{L}^3$ 1:1, pH_{corr} 7.4, ●: Cu(II)-$\mathbf{L}^3$ 2:1, pH_{corr} 8.7); applied concentrations in Table 4.12. Solid lines correspond to fitted curves.

The initial reaction rates of the catalytic oxidation as a function of H_2DTBC concentration show saturation kinetics above 10-50-fold excess of substrate over the complexes (Figure 4.54). This indicates a fast pre-equilibrium between the complex and the substrate molecules before the rate determining redox processes, therefore the Michaelis-Menten enzyme kinetic model is applicable in our systems. Table 4.13. lists the calculated Michaelis-Menten parameters, along with those of some previously reported model complexes. Although the comparison with literature data is complicated by the many different conditions used, it can be stated that the multinuclear complexes of $\mathbf{L}^1$, $\mathbf{L}^2$ and $\mathbf{L}^3$ possess high activities, outperforming the few copper(II)-peptide complexes studied earlier [65, 80]. It is interesting to note, that in all cases amide coordinated complexes are the pre-active species for H_2DTBC oxidation (further discussion in Section 4.6.4).

Regarding the non-peptide complexes, the k_{cat} values determined for our copper(II)-ligand systems can be considered average; the activities are ~4 orders of magnitude lower than that of the native enzyme isolated from sweet potato [47]. However, the k_{cat}/K_M ratios, especially in case of Cu(II)-$\mathbf{L}^2$ 2:1 and Cu(II)-$\mathbf{L}^3$ 2:1, support the high catalytic efficiency of the present systems: the k_{cat}/K_M determined for Cu(II)-$\mathbf{L}^3$ 2:1 system exceeds the same value of the catechol oxidase model possessing the highest k_{cat} value reported so far (see Table 4.13). This elevated efficiency can be attributed to the impressively strong substrate binding ability of the tripodal peptide complexes (*i.e.* low K_M), representing a unique and very advantageous feature among catechol oxidase mimicking model complexes.

Table 4.13. Comparison of catecholase activity of some previously investigated copper(II)-ligand systems along with the catechol oxidase enzyme.

Cu(II)-ligand systems (*pH*)	k_{cat} (s^{-1})	K_M (M)	k_{cat}/K_M ($M^{-1}s^{-1}$)	**solvent, *T* (°C)**	**ref.**
Cu(II)-Ac-HHGH 1:1 (*10.18*)	0.063	not rep.	not rep.	MeOH/H_2O 86/14, 25	[65]
Cu(II)-MDVFMKGLSKAKEGV-NH_2 1:2 (*7.4*)	0.009	1.8×10^{-3}	5.0	MeOH/H_2O 80/20, 25	[80]
Cu(II)-B1[a] 2:1 (*8.50*)	0.051	9.44×10^{-3}	5.47	MeOH/H_2O 97/13, 25	[136]
Cu(II)-B2[a] 2:1 (*8.50*)	0.0078	9.5×10^{-4}	8.1	MeOH/H_2O 97/13, 25	[136]
Cu(II)-B3[b] 1:2	0.00596	2.6×10^{-4}	23.37	DMF, 20	[64]
Cu(II)-B4[c] 2:1	0.25	6.4×10^{-3}	39.1	MeCN, 25	[137]
Cu(II)-L^3 1:1 (*7.4*)	**0.0056**	**7.09×10^{-5}**	**79.4**	**EtOH/H_2O 50/50, 25**	
Cu(II)-B5[d] 2:4:2	0.0426	1.45×10^{-4}	293.8	MeOH, 25	[138]
Cu(II)-B6[e] 2:2	2.63	5.90×10^{-3}	445.8	MeOH, not rep.	[69]
Cu(II)-L^1 3:2 (*7.8*)	**0.071**	**1.12×10^{-4}**	**632.1**	**EtOH/H_2O 50/50, 25**	
Cu(II)-B7[f] 2:1	1.916	1.2×10^{-3}	1597	MeCN, 25	[68]
Cu(II)-B8[g] 2:1 (*8.0*)	1.806	7.5×10^{-4}	2408	MeOH/H_2O 29/1, 20	[67]
Cu(II)-L^2 2:1 (*8.9*)	**0.387**	**1.07×10^{-4}**	**3625**	**EtOH/H_2O 50/50, 25**	
Cu(II)-B9[h] 2:1	9	2.3×10^{-3}	3913	MeOH, 20	[71]
Cu(II)-L^3 2:1 (*8.7*)	**0.157**	**3.61×10^{-5}**	**4362**	**EtOH/H_2O 50/50, 25**	
Cu(II)-B10[i] 2:1	8	7×10^{-4}	11429	MeOH, 20	[71]
ibCO[j] (*6.5*)	2293	2.5×10^{-3}	917200	H_2O, 20	[47]

[a]ligand B1: *N',N'-bis*(2-pyridylmethyl)-*N,N*-(2-hydroxybenzyl)(2-hydroxy-3,5-di-*tert*-butylbenzyl)-1,3-propanediamin-2-ol; ligand B2: *N*-(2-hydroxybenzyl)-*N',N',N-tris*(2-pyridylmethyl)-1,3-propanediamin-2-ol
[b]ligand B3: 3-(3'-methyl-2'-pyridylimino)isoindoline-1-one (MePyOIND)
[c]ligand B4: 2,6-*bis*[*bis*(pyridin-2-ylmethylamino)methyl]-4-methylphenol (BPMP)
[d]ligand B5: naproxen (nap) and 3-picoline (3-pic)
[e]ligand B6: the copper(II) complex is referred as *bis*[1,2-*O*-isopropylidene-6-*N*-(3-acetylbut-3-en-2-one)amino-6-deoxyglucofuranoso]dicopper ($H_2$3a)
[f]ligand B7: $L^{1*}SSL^{1*}$
[g]ligand B8: a pyrazolate-derived compartmental ligand bearing pyridyl arms (HL^2)
[h]ligand B9: 2,6-*bis*(R-iminomethyl)-4-methyl-phenolato type Schiff-base ligand (H_2L2^2)
[i]ligand B10: 2,6-*bis*(R-iminomethyl)-4-methyl-phenolato type Schiff-base ligand ($L2^1$)
[j]native enzyme isolated from *Ipomoea batatas*; kinetic parameters reported for catechol substrate

We also studied the performance of our complexes in longer time intervals, in presence of ~120 eq. excess of substrate ($[complex]_{tot} = 1\times10^{-5}$ M). After 1 hour, experimental turnover numbers of 41.1 h^{-1} (Cu(II)-**L^1** 3:2, pH 7.8) and 64.1 h^{-1} (Cu(II)-**L^2** 2:1, pH 8.9) was found, however these data are strongly limited by the spontaneous diffusion of air into the studied solution.

In order to have more insights into the mechanism of H_2DTBC oxidation, reaction rates were measured as a function of complex and dioxygen concentration under pseudo-first order conditions. In all cases first order dependence was observed (Figures 4.55 and 4.56), which is in agreement with many other catecholase model systems [56, 61, 66, 67]. According to the Michaelis-Menten model, the observed pseudo-second order rate constant (*k'*, slope of the complex concentration dependent reaction rate curves) is equal to $k_{cat}/(K_M + [S])$. The values calculated from the Michaelis-Menten parameters ($k'_{calc,\mathbf{L^1}}$ = 13.9 $M^{-1}s^{-1}$, $k'_{calc,\mathbf{L^2}}$ = 670.5 $M^{-1}s^{-1}$, $k'_{calc,\mathbf{L^3}}$ = 154.4 $M^{-1}s^{-1}$) are close to the measured ones

($k'_{\mathbf{L}^1}$ = 7.97 $M^{-1}s^{-1}$, $k'_{\mathbf{L}^2}$ = 495.9 $M^{-1}s^{-1}$ and $k'_{\mathbf{L}^3}$ = 272 $M^{-1}s^{-1}$), which confirms the validity of our applied kinetic model.

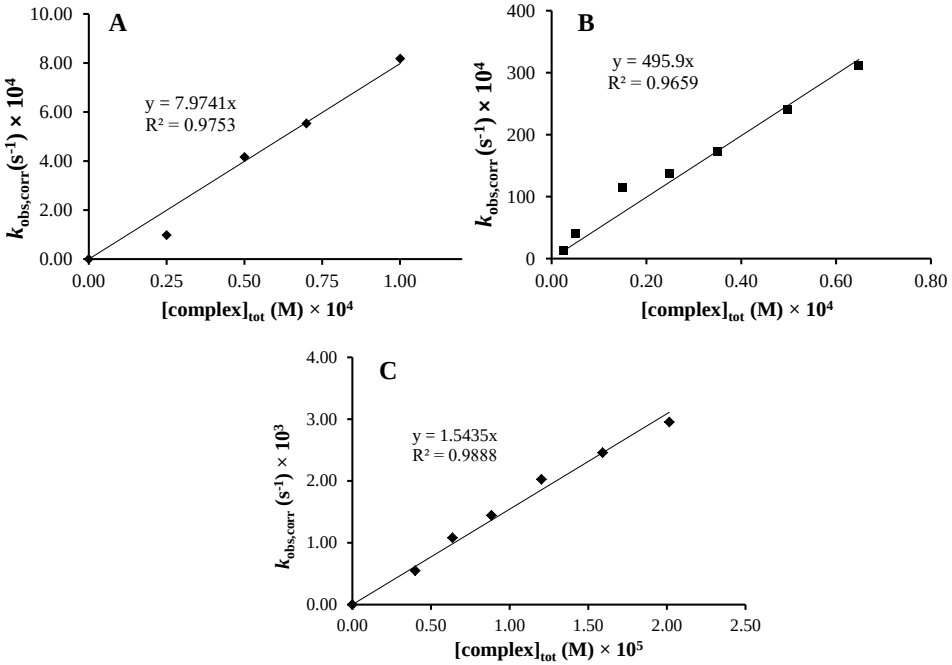

Figure 4.55. Dependence of reaction rate constants ($k_{obs,corr}$) on complex concentrations in Cu(II)-$\mathbf{L}^1$ 3:2 (**A**, pH 7.8), Cu(II)-$\mathbf{L}^2$ 2:1 (**B**, pH 8.9) and Cu(II)-$\mathbf{L}^3$ 2:1 systems (**C**, pH 7.8); applied concentrations in Table 4.12.

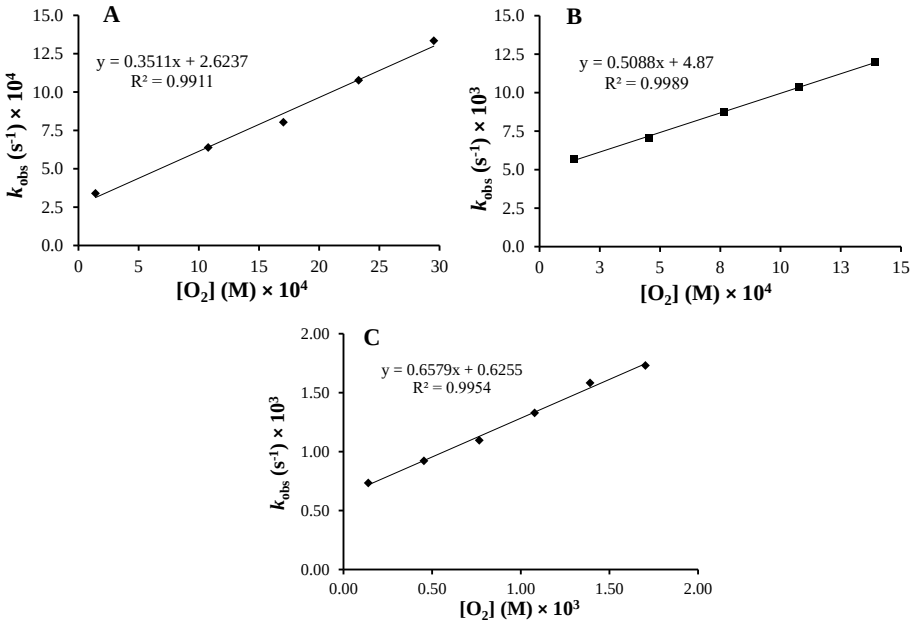

Figure 4.56. Dependence of reaction rate constants ($k_{obs,}$) on oxygen concentrations in Cu(II)-$\mathbf{L}^1$ 3:2 (**A**, pH 7.8), Cu(II)-$\mathbf{L}^2$ 2:1 (**B**, pH 8.9) and Cu(II)-$\mathbf{L}^3$ 2:1 systems (**C**, pH 8.7); applied concentrations in Table 4.12.

4.6.2. Substrate binding study in Cu(II)-L[1] 3:2, Cu(II)-L[2] 2:1 and Cu(II)-L[3] 2:1 systems

After studying the kinetic aspects of catalytic H_2DTBC oxidation by our complexes, we wished to know more about the factors influencing the catalytic cycle, and attempted to draw the mechanism of oxidation. Therefore, substrate binding and mechanistic studies have been carried out concerning the catalytically active Cu(II)-**L**^{1} 3:2, Cu(II)-**L**^{2} 2:1 and Cu(II)-**L**^{3} 2:1 systems.

The three metal centers in $Cu_3H_x\mathbf{L}^{1}_2$ complexes may raise the question about the number of bound catechols in the fast pre-equilibrium step. Therefore, we studied the binding of 4-nitrocatechol ($H_2$4NC), a widely used chromophoric probe to mimic catechol-metal ion interaction [139, 140]. Since this electron-poor catechol ligand possesses higher redox potential than H_2DTBC, its metal ion binding can be easily monitored by UV-Vis spectroscopy under aerobic conditions. First, the p*K* values and the spectral properties of $H_2$4NC have been determined in 50% EtOH/H_2O solvent (Table 4.14). The p*K* values of this ligand are considerably lower than those of H_2DTBC, thus the formation of ternary species with $Cu_3H_x\mathbf{L}^{1}_2$ complexes is expected at lower pH.

Table 4.14. UV-Vis spectroscopic parameters and deprotonation constants of 4-nitrocatechol ($H_2$4NC) substrate analog (EtOH/H_2O 50/50, T = 298 K, I = 0.1 M NaCl). Calculated individual molar spectra in Figure 4.57. insert.

	λ_{max} (nm)	$\varepsilon_{\lambda_{max}}$ ($M^{-1}cm^{-1}$)	p*K*
$H_2$4NC	350	7925	6.78(2)
$[H4NC]^-$	434	15545	11.78(1)
$[4NC]^{2-}$	512	13446	

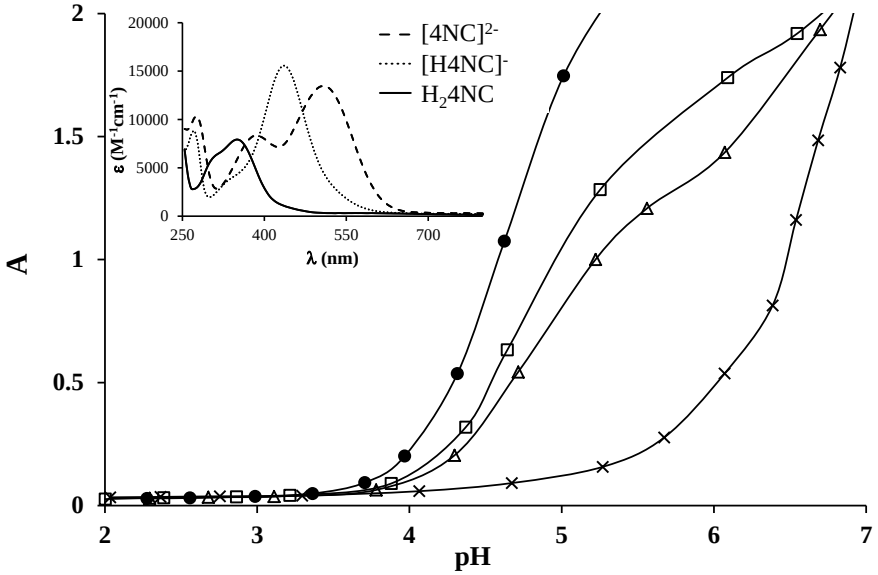

Figure 4.57. pH-dependent absorption at 434 nm at different Cu(II)-**L**^{1}-$H_2$4NC ratios: × 0:0:1, ● 3:2:1, □ 3:2:2, Δ 3:2:3 ($[H_2\text{4NC}]_{tot} = 2.5\times10^{-4}$ M, in EtOH/H_2O 50/50%). Insert: Individual molar spectra of differently protonated 4NC species.

pH-dependent absorption spectra of Cu(II)-$\mathbf{L^1}$-$H_2$4NC ternary systems were recorded at different complex-to-$H_2$4NC ratios; Figure 4.57. shows the change of absorbance at 434 nm in function of pH. At 1:1 complex-to-$H_2$4NC ratio, the pK of $H_2$4NC deprotonation is considerably shifted to the acidic region (from pK = 6.78 to ~4.5), clearly indicating direct binding of 4-nitrocatechol to the complexes resulting in metal-induced deprotonation. With decreasing concentrations of the trinuclear complexes, the deprotonation of $H_2$4NC follows a two-step process indicating that only one equivalent catecholate is coordinated under our conditions; the excess $H_2$4NC deprotonates at higher pH, without the participation of the copper(II) complexes. Since the coordination of the analogous monodentate 4-nitrophenol was not observed in a similar experiment, bidentate coordination of catechol substrates can be suggested.

We have also investigated the binding of H_2DTBC applying inert (argon) atmosphere in order to prevent the catalytic oxidation of the substrate. Figure 4.58. shows the UV-Vis spectra of Cu(II)-$\mathbf{L^1}$-H_2DTBC ternary system at pH 7.8 with increasing H_2DTBC concentrations. Three new bands appear on the electronic absorption spectra at 280, 300 and 440 nm. The wide band at 440 nm and the shoulder around 300 nm are related to the ternary species $Cu_3H_x\mathbf{L^1}_2(DTBC^{2-})$ in agreement with earlier reports on the spectral behavior of Cu^{2+}-ligand-catecholate ternary complexes [61, 71], while the band at 280 nm belongs to the absorption of H_2DTBC itself. The d-d absorption band of Cu(II) around 625 nm is almost unchanged during the experiment, only a slight blue shift indicates the alteration of the coordination sphere around the metal ion. In addition, the characteristic absorption band of the oxidized 3,5-di-*tert*-butyl benzoquinone (DTBQ) product does not appear around 400 nm. These facts indicate that under anaerobic conditions the formation of the copper(II)-catecholate ternary species is not followed by the reduction of Cu^{2+} ions and the oxidation of the substrate.

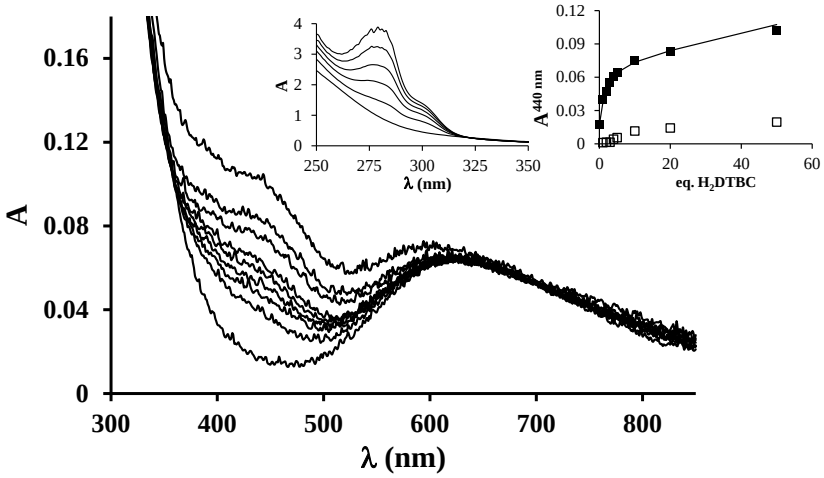

Figure 4.58. H_2DTBC-dependent UV-Vis spectra of Cu(II)-$\mathbf{L^1}$ 3:2 system under anaerobic conditions ($[complex]_{tot} = 2.4\times10^{-4}$ M, in EtOH/H_2O 50/50%, pH 7.8). Insert (left): UV region of the spectra; (right): absorbance at 440 nm in function of eq. H_2DTBC in presence (■) and in absence (□) of Cu(II)-$\mathbf{L^1}$ 3:2 system (solid line is fitted curve, see text).

Similar findings were observed during the analogous experiment in presence of the Cu(II)-$\mathbf{L^3}$ 2:1 system. Substrate dependent UV-Vis spectra (Figure 4.59. A) show two overlapping bands appearing between 350 and 450 nm upon addition of increasing amount of H_2DTBC, while the d-d band of Cu(II) shifts towards the higher energies (from ~580 to 564 nm, Figure 4.59. A). Similarly to the Cu(II)-$\mathbf{L^1}$ 3:2 system, neither the strong absorbance of DTBQ at 400 nm (which would have resulted an absorbance of ~1 within the applied experimental conditions), nor the reduction of copper(II) were found. Instead, the absorption bands (between 350-450 nm) attributed to the CT-band of copper(II)-bound catecholate [61, 72, 141, 142], and the absorbance of the free (unbound) mono-deprotonated $HDTBC^-$, present in small quantities (pK_{H_2DTBC} = 10.35 in 50/50% MeOH/H_2O medium [143]), can be observed on the UV-Vis spectra.

The CD spectra, reflecting exclusively the environment of the metal ions, also show profound changes upon addition of H_2DTBC (Figure 4.59. B), indicating important rearrangement of the coordination sphere upon substrate binding. Since the chiral perturbation arises exclusively from the ligand $\mathbf{L^3}$, the CD spectra directly prove the formation of Cu(II)-$\mathbf{L^3}$-substrate adduct.

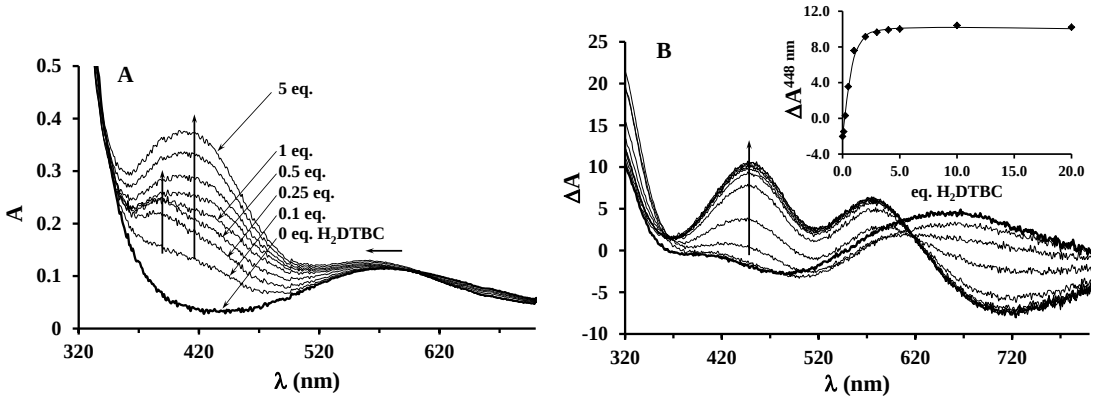

Figure 4.59. UV-Vis (**A**) and CD spectra (**B**) of the Cu(II)-$\mathbf{L^3}$ 2:1 system recorded under inert (argon) conditions, upon addition of 0-20 eq. H_2DTBC (in EtOH/H_2O 50/50%, pH_{corr} = 8.7, $[complex]_{tot} = 5.3\times10^{-4}$ M). Insert: CD intensities in function of eq. H_2DTBC (solid line is fitted curve, see text).

Based on the CT-bands related to the Cu(II)-ligand-catecholate ternary adducts (UV-Vis absorbance at 440 nm and CD band at 448 nm in Figures 4.58. and 4.59. B inserts, respectively), we could estimate the apparent stability constant (K_{app}) of the complex-substrate adduct according to the equilibrium processes $Cu_3H_w\mathbf{L^1}_2$ + H_2DTBC = $Cu_3H_x\mathbf{L^1}_2(DTBC^{2-})$ and $Cu_2H_y\mathbf{L^3}$ + H_2DTBC = $Cu_2H_z\mathbf{L^3}(DTBC^{2-})$. The non-linear regression of the data resulted K_{app} = 3570 M^{-1} and 14200 M^{-1} for the Cu(II)-$\mathbf{L^1}$ 3:2 and Cu(II)-$\mathbf{L^3}$ 2:1 systems, respectively (see solid lines of Figures 4.58. and 4.59. B inserts). These values are in good agreement with the results of our saturation kinetic measurement ($1/K_M$ = 8928 M^{-1} and 27624 M^{-1} in case of Cu(II)-$\mathbf{L^1}$ 3:2 and Cu(II)-$\mathbf{L^3}$ 2:1 systems, respectively), since the Michaelis constant corresponds to the dissociation constant of the above-mentioned adduct. It is worth mentioning that the extraordinary high binding ability of Cu(II)-$\mathbf{L^3}$ 2:1 system is not restricted to H_2DTBC; similarly high K_{app} values (> 20000

M^{-1}) were determined for catechol and 4-nitrocatechol, too, by similar CD measurements (see Appendix A.24).

Based on these results, the role of dioxygen is the oxidation of the substrate activated by the oligonuclear copper(II)-**L**^{1} and -**L**^{3} complexes, and not the regeneration of the Cu^{2+} species (re-oxidation of Cu^{+}), as it was proposed for the native enzyme [48, 49], and for many catalytic dinuclear copper(II) complexes [52]. In fact, the observed phenomenon is in agreement with an oxidation pathway pursued by mononuclear copper(II) complexes [61, 76], involving the formation of radical intermediate(s) (see later).

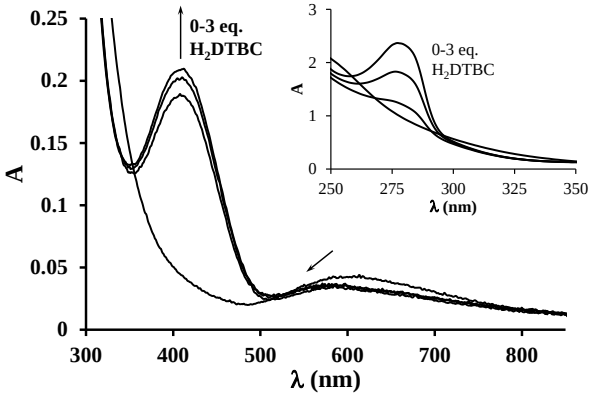

Figure 4.60. H_2DTBC-dependent UV-Vis spectra of Cu(II)-**L**^{2} 2:1 system under anaerobic conditions ($[complex]_{tot} = 2.4\times10^{-4}$ M, in EtOH/H_2O 50/50%, pH 8.9). Insert: UV region of the measured spectra.

Anaerobic UV-Vis measurements on the H_2DTBC binding were carried out in the Cu(II)-**L**^{2} 2:1 system, too. Figure 4.60. shows the recorded spectra in presence of 0 to 3 eq. H_2DTBC. The observations are fundamentally different from the previous systems: the strong absorbance of DTBQ at 400 nm appeared immediately after the introduction of 1 eq. substrate in absence of dioxygen and the intensity of the Cu(II) d-d band decreased. Though this decrease of Cu(II) band intensity is undeniable, its entire disappearance does not occur, *i.e.* the redox reaction is not stoichiometric. This is consistent with many previous observations that the reduction of copper(II) under anaerobic conditions is not complete until the introduction of considerable excess of H_2DTBC [66, 79]. These results indicate a single-step two-electron oxidation of the catechol substrate by the two cooperating copper(II) centers in the Cu(II)-**L**^{2} complexes, which is the main proposed mechanism for binuclear catecholase-like copper(II) complexes [52].

4.6.3. Peroxide, o-benzoquinone and radical formation in Cu(II)-L^{1} and -L^{2} systems. Mechanism of catecholase-like activities in the studied Cu(II)-L systems

The detection and quantification of H_2O_2 has been accomplished by treating the aqueous phase with acidic TiO^{2+}, after the elimination of the organic compounds by dichloromethane extraction. The concentration of peroxotitanyl complex can be measured spectrophotometrically at 408 nm. The formation of DTBQ and H_2O_2 has been determined

parallel during the complex catalyzed reaction of H_2DTBC. Both Cu(II)-**L**^{1} and -**L**^{2} catalytic systems show initial accumulation of H_2O_2 in the beginning of the reaction, followed by its slow decay (Figure 4.61). Moreover, the concentration of the formed DTBQ exceeds the peroxide levels considerably in both cases. This suggests a dynamic equilibrium of H_2O_2 between its formation and consumption after the initial stages of the catalytic reaction.

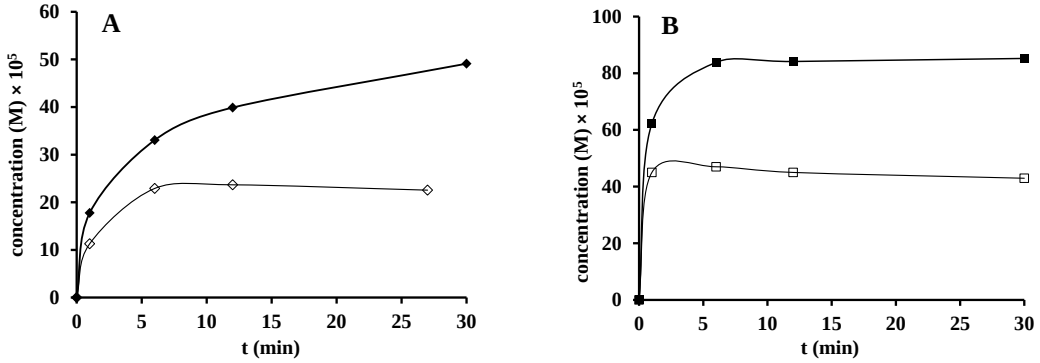

Figure 4.61. H_2O_2 (◇ and □) and DTBQ (◆ and ■) formation in presence of Cu(II)-**L**^{1} 3:2 (**A**) and Cu(II)-**L**^{2} 2:1 systems (**B**) (pH 7.8 and 8.5, $[complex]_{tot} = 5\times10^{-5}$ M, $[H_2DTBC]_o = 2\times10^{-3}$ M, I = 0.1 M).

As described above, the formation of copper(II)-catecholate unit was observed in the Cu(II)-**L**^{1}-H_2DTBC system (Figure 4.58.) under anaerobic conditions, without the subsequent redox reaction between Cu(II) and the substrate. This is consistent with mononuclear catalytic centers, where valence tautomer (VT) equilibrium between the copper(II)-catecholate and copper(I)-semiquinone adduct is strongly dependent on the donor groups and structure of the applied ligand [52, 144]. Both tautomer forms are oxygen sensitive, therefore the catalytic oxidation should proceed through the formation of radical intermediates [54] (semiquinone (SQ), superoxide radical or both), which might be detected by EPR. Although copper(II)-superoxide complexes are generally EPR silent due to the antiferromagnetic interaction [145, 146], the formation of SQ intermediates has been previously observed by EPR [56, 64, 70, 76].

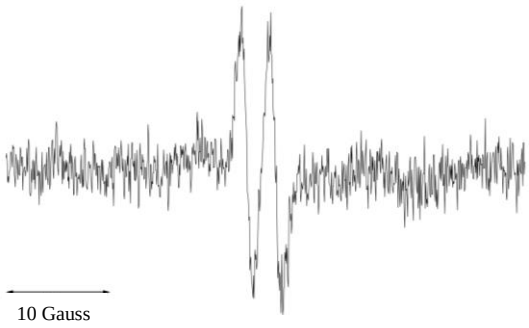

Figure 4.62. EPR spectrum of the 3,5-di-*tert*-butyl-semiquinone radical under aerobic reaction conditions, in presence of Cu(II)-**L**^{1} 3:2 complex (in EtOH/H_2O 50/50, $[complex]_{tot} = 5\times10^{-5}$ M, $[H_2DTBC]_o = 2\times10^{-3}$ M, pH = 8.0). Acquisition settings: 0.84 G modulation amplitude, 5×10^{4} receiver gain, 16 scans, 5 mW microwave power, 50 G scan width.

For that reason, we attempted to detect the formation of radical intermediate(s) in both aerobic and anaerobic conditions. In the absence of dioxygen radicals were not detected, according to the anaerobic UV-Vis measurement of the Cu(II)-$\mathbf{L^1}$-H_2DTBC system. Under aerobic conditions, however, a well-defined doublet EPR signal (g = 2.0046±0.0001, a_H = 2.67 G, Figure 4.62.) was observed, similarly to those detected earlier for intermediates of H_2DTBC oxidation [64, 70, 76]. Hence, we must conclude that in the copper(II)-$\mathbf{L^1}$-H_2DTBC system the copper(II)-bound catecholate is oxidized only in the presence of dioxygen, through the formation of oxygenated radical intermediate (Scheme 4.13).

Based on the detailed kinetic study and careful evaluation of the substrate binding experiments, the oxidation of H_2DTBC catalyzed by the oligonuclear copper(II) complexes of $\mathbf{L^1}$ and $\mathbf{L^2}$ proceeds via one- and two-electron transfer from the catechol to the copper(II) ion(s), respectively. Scheme 4.13. presents the suggested basic reaction steps of the catalytic oxidation of H_2DTBC. Under the conditions used for $\mathbf{L^1}$ (pH 7.8, Cu(II)-$\mathbf{L^1}$ 3:2) trinuclear complexes (mostly $Cu_3H_{-1}\mathbf{L^1}_2$) are the pre-active species. Nevertheless, the oxidation of H_2DTBC proceeds in a one-electron transfer pathway, with the participation of a single Cu^{2+} center. The other metal ions might have only inferior contribution in substrate binding, which is probably due to the spatial Cu(II)-Cu(II) separation in these trinuclear species (Scheme 4.2). In this system the copper(II)-catecholate/copper(I)-semiquinone valence tautomer (VT) equilibrium is shifted towards the copper(II)-catecholate form. One of these tautomers reacts with dioxygen in the rate determining step, resulting the formation of oxygenated radical intermediate(s) [54]. After a subsequent intramolecular electron transfer DTBQ and H_2O_2 are released, regenerating the copper(II) center and allowing the coordination of a new substrate molecule.

In contrast, the oxidation in the Cu(II)-$\mathbf{L^2}$-H_2DTBC system is catalyzed by two co-operating copper(II) centers, similarly to the catechol oxidase enzymes. Even though dicopper(II) species are formed already at pH 4 in Cu(II)-$\mathbf{L^2}$ 2:1 system, the tendency of catechol oxidase-like activity follows the formation of $Cu_2H_{-3}\mathbf{L^2}$. After coordination of the substrate to the dicopper(II) core, DTBQ and dicopper(I) species are formed in a fast electron transfer process. The reduced metal centers are re-oxidized by dioxygen, yielding a Cu(II)-O_2^{2-}-Cu(II) species, as it is often proposed in the literature [52]. This in turn reacts with an incoming second substrate molecule, and the dicopper(I) species is regenerated after releasing the second DTBQ and H_2O_2 (via proton transfer).

Since hydrogen peroxide does not seem to be produced in stoichiometric quantity in either catalytic system, the participation of H_2O_2 in the catalytic reaction can be suggested. Most probably, as a widely known oxidizing agent, the peroxide molecule might contribute to the reoxidation of Cu(I) center(s) to Cu(II), as it was previously described for other catalytic copper(II) complexes [79, 147].

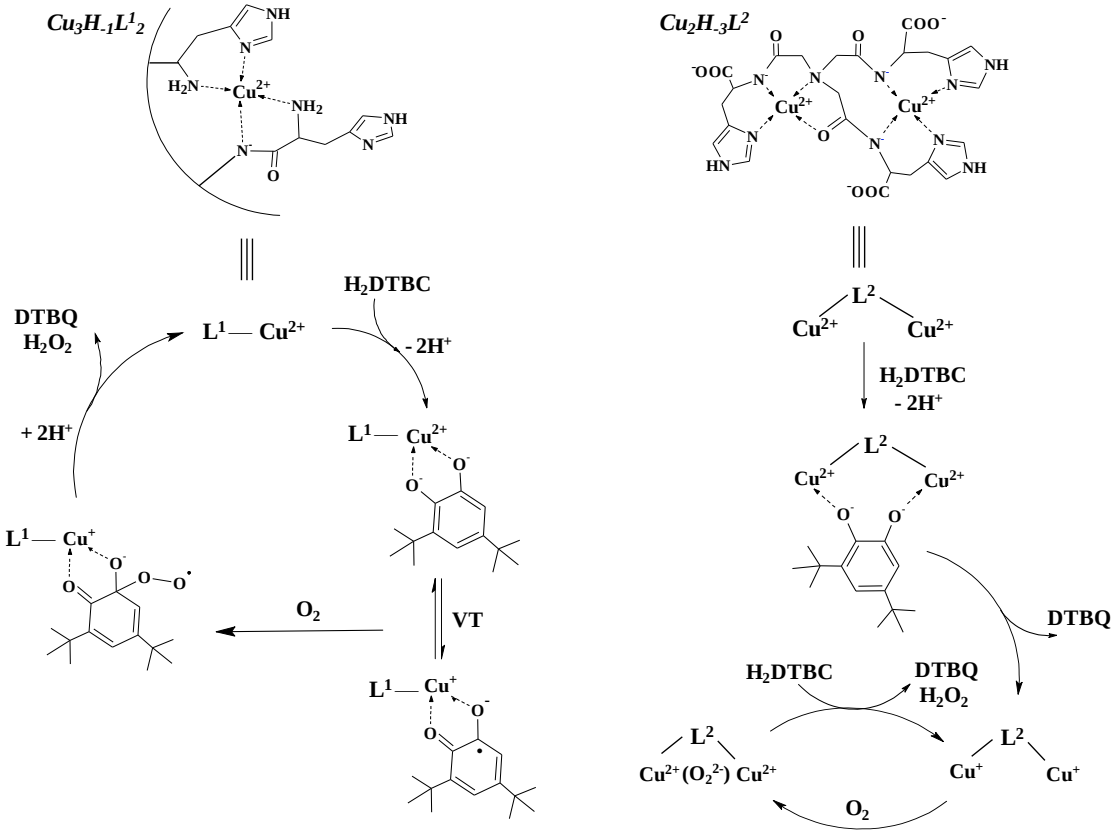

Scheme 4.13. Proposed mechanism of catalytic oxidation of 3,5-di-*tert*-butylcatechol by $\mathbf{L^1}$ and $\mathbf{L^2}$ ligand-copper(II) systems.

It is somewhat surprising that the observations in Cu(II)-$\mathbf{L^3}$ 2:1 system correspond more to the mechanistic behavior of Cu(II)-$\mathbf{L^1}$ 3:2, rather than that of the other dinuclear Cu(II)-$\mathbf{L^2}$ system. Instead of the two-electron transfer between the coordinated substrate molecule and the copper(II) centers, only the formation of the complex-substrate intermediate was observed under inert conditions. Thus, the involvement of the Cu(II)-catecholate/Cu(I)-semiquinone valence tautomerism (VT) is safe to assume in the present case, too. The presence of dinuclear complexes corresponds to the formation of a mixed-valence intermediate, which would suggest that H_xDTBC binds to only one copper ion. A similar Cu(II)Cu(II)-catecholate/Cu(II)Cu(I)-semiquinone VT was already reported in the literature [56]. Indeed, the absorption band observed between 350-450 nm (Figure 4.59. A) is in agreement with bidentate catecholate binding, however the observed very low K_M may indicate that the second copper(II) somehow assists in the substrate binding [148]. As it is suggested in the Cu(II)-$\mathbf{L^1}$ system, the VT-equilibrium is strongly shifted toward the copper(II)-catecholate state, since neither appreciable decrease of d-d band intensity, nor the EPR spectrum of semiquinone radical was observed under anaerobic conditions. Nevertheless, in presence of dioxygen the ternary adduct reacts with dioxygen in a fast rate determining step, resulting the formation of oxygenated radical intermediate(s) [54] and a subsequent intramolecular electron transfer, while DTBQ is formed and the copper(II) state is regenerated.

4.6.4. Catechol oxidation: linear vs. tripodal peptide complexes

In the past years several biochemically relevant peptide models were investigated in our research group, focusing on their coordination chemistry [43, 65, 88, 90, 116, 149]. These sequences were proved to play important roles in metal binding in native biomolecules, contributing to the function of the relevant metalloproteins in *e.g.* metal transport [149] or enzymatic processes [43, 88, 90]. By studying the redox mimicking capabilities of such strong metal binding sequences, we might gain information and estimations on redox activities of other, biologically relevant peptide fragments. Thus, it is important and desirable to reveal the redox activities of such peptide-copper(II) species.

P1 : Ac-HKHKH-NH_2
P2 : Ac-HHKHKH-NH_2
P3 : Ac-KAHEFGHSLGLDHSK-NH_2
P4 : HADHDHKK-NH_2
P5 : Ac-RHQAGPPHSHR-NH_2

Scheme 4.14. Linear peptide sequences studied in catechol oxidation.

Copper(II) complexes of several linear peptides (**P1**-**P5**, Scheme 4.14.) have been investigated as catechol oxidase mimics. These sequences, containing at least three histidyl residues, serve as decent ground of comparison with our histidine-containing tripodal peptide complexes.

In equimolar copper(II)-peptide solutions, all complexes were found to catalyze the oxidation of H_2DTBC above pH 7. Unlike the rate of autooxidation, which increases exponentially, the complex catalyzed reaction rates show maximum curves in function of pH, since the differently protonated species exhibit different catalytic efficiency (Figure 4.63). The observed pH maxima are between pH 8.2–9.8.

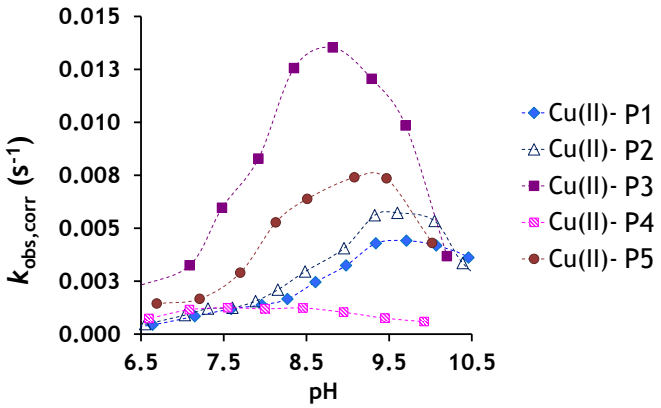

Figure 4.63. pH-dependent reaction rate constants ($k_{obs,corr} = k_{obs} - k_{obs,auto}$) observed in equimolar Cu(II)-peptide systems, in 50/50% EtOH/H_2O buffered (HEPES, CHES) solutions, $[Cu(II)]_{tot} = [\mathbf{P}]_{tot} = 5.0\times10^{-5}$ M, T = 298 K, I = 0.1 M. Individual conditions: $[H_2DTBC]_o = 3\times10^{-3}$ M for Cu(II)-**P1, -P2** and **-P3**, $[H_2DTBC]_o = 8\times10^{-4}$ M, for Cu(II)-**P4** and **-P5** systems.

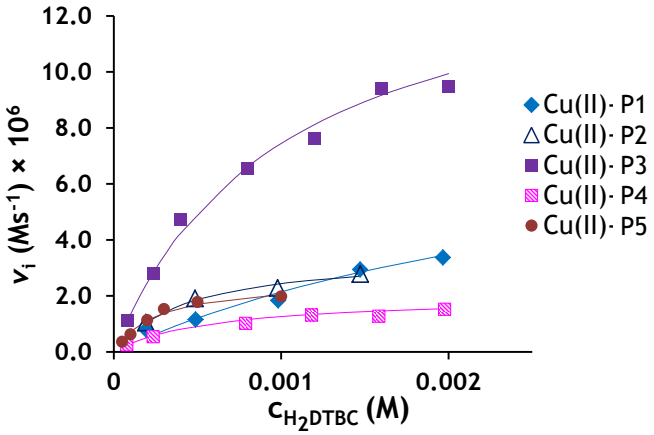

Figure 4.64. Initial reaction rates of H_2DTBC oxidation as a function of substrate concentration in presence of different Cu(II)-peptide 1:1 systems (in 50/50% EtOH/H_2O buffered (HEPES, CHES) solutions, T = 298 K, I = 0.1 M). Individual conditions: $[Cu(II)]_{tot} = 3.5\times10^{-5}$ M, pH 8.3 for Cu(II)-**P1** and **-P2**, $[Cu(II)]_{tot} = 4\times10^{-5}$ M, pH 8.9 for Cu(II)-**P3**, $[Cu(II)]_{tot} = 5\times10^{-5}$ M, pH 8.2 for Cu(II)-**P4**, $[Cu(II)]_{tot} = 6\times10^{-5}$ M, pH 9.2 for Cu(II)-**P5** systems.

Table 4.15. Michaelis-Menten parameters (estimated errors in parentheses) of H_2DTBC oxidation catalyzed by the investigated copper(II)-peptide systems, along with the composition and coordination mode of the suggested active species.

peptide (pH)	major species and its coordination mode	k_{cat} / s^{-1}	K_M / mM	k_{cat}/K_M / M^{-1}s^{-1}
P3, pH 8.9	CuL {N_{im},2N$^-$}	0.34(2)	0.90(1)	378
P5, pH 9.2	CuH$_{-2}$L {2N_{im},2N$^-$}	0.043(3)	0.25(5)	172
P2, pH 8.3	CuL {2N_{im},2N$^-$}	0.18(1)	1.6(3)	113
P1, pH 8.3	CuL {2N_{im},2N$^-$}	0.27(1)	3.7(4)	73
P4, pH 8.2	CuL {2N_{im},2N$^-$}	0.044(1)	0.8(1)	55

The pH_{corr}–$k_{obs,corr}$ profiles of the studied peptide complexes, along with the reaction rate curves in function of H_2DTBC concentration are depicted in Figures 4.63. and 4.64, respectively. The non-linear regression of the data resulted the kinetic parameters listed in Table 4.15. As it can be seen, the pre-active copper(II) species are in all cases imidazole and amide nitrogen coordinated complexes, mostly in a {2N_{im},2N$^-$} environment. This is somewhat surprising, since the increasing ligand field strength induced by the coordination of amide nitrogens, in principle, stabilizes the +2 oxidation state of copper and consequently weakens the redox activity of the complexes. Still, similar findings have been observed in earlier reports [81, 150], and we also found that the catalytically active tripodal peptide-copper(II) complexes are amide N$^-$ coordinated species (see Section 4.6.1). This seemingly general behavior prompted us to assume that the deprotonated amide nitrogens might contribute to the catalytic performance of the complexes by acid-base catalysis, *i.e.* by abstracting protons from the catechol –OH groups, and thus facilitating substrate binding (Scheme 4.15).

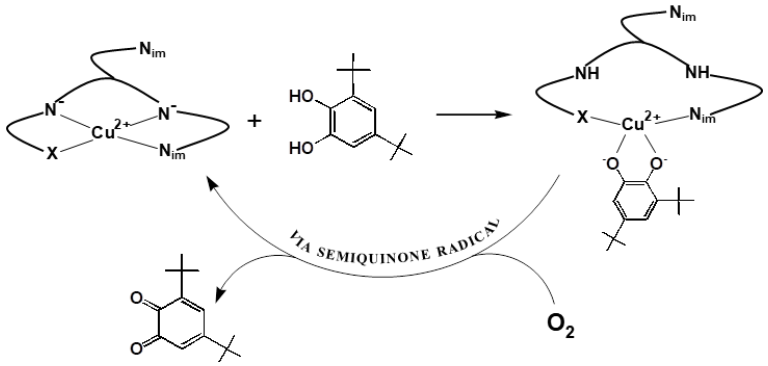

Scheme 4.15. Proposed mechanism of catalytic oxidation of 3,5-di-*tert*-butylcatechol by amide-coordinated copper(II) complexes of multihistidine peptides.

Scheme 4.15. depicts the proposed mechanism of H_2DTBC oxidation catalyzed by the studied copper(II)-peptide complexes. Since mononuclear copper(II) species are able to carry out only one-electron oxidation, the complex-substrate adduct should be transformed into a radical intermediate (*e.g.* semiquinone radical). This was indeed detected by EPR spectroscopy (see Appendix Figure A.25); a very similar doublet EPR signal was found in the H_2DTBC oxidation reaction carried out by Cu(II)-**L**$^{\mathbf{1}}$ 3:2 system (Figure 4.62), too. Since the complexes of multihistidine peptides studied here or earlier are considerably more active than those of the N-terminal α-synuclein fragments containing no histidine [80], the +1 oxidation state of copper is likely stabilized by the coordination of 2-3 imidazole rings, similarly to that suggested for the interaction of Cu(I) with Aβ peptides [151].

With this knowledge, it is worth comparing the kinetic behavior of linear and tripodal peptide complexes, with respect to the product formation rate (k_{cat}), stability of the complex-substrate adduct (K_M) and pH optimum. In cases where the catalysis involves one copper(II) center coordinated by tripodal peptides (Cu(II)-**L**$^{\mathbf{1}}$ 3:2 and Cu(II)-**L**$^{\mathbf{3}}$ 1:1), the pH optima of the reaction are considerably lower (pH < 8) than that of the linear peptide systems. While k_{cat} values of linear peptides are relatively high (k_{cat} of Cu(II)-**P3** 1:1 approaches that of the dinuclear Cu(II)-**L**$^{\mathbf{3}}$ system), their K_M value remains in the 10^{-3}-10^{-4} M range, causing generally lower k_{cat}/K_M ratio as compared with Cu(II)-tripodal peptide systems. Thus, we can conclude that the structure organizing effect of tripodal peptides influences advantageously the substrate binding and therefore, overall catalytic efficiency in catechol oxidation.

4.7. SUPEROXIDE DISMUTASE (SOD) MIMICKING WITH THE METAL-LIGAND COMPLEXES

The investigated tripodal and linear peptide-copper(II) complexes demonstrated strong ability for dioxygen activation. Such oxidative reactions may involve the formation of superoxide radical, too. Copper(II) complexes of His-containing linear peptides are well-known superoxide dismutase mimicking compounds [82, 88, 90, 91, 150, 152, 153]. Therefore, we also studied the superoxide dismutating ability of copper(II) complexes formed with the tripodal and linear His-peptides, thus gaining a deeper insight into their redox enzyme mimicking properties.

All measurements were carried out around neutral pH (7.0-7.8), in phosphate buffered solutions (I = 0.1 NaCl, T = 298 K). Superoxide radicals were generated by the xanthine-xanthine oxidase system, inhibition and IC_{50} values were determined by following the reduction of nitrotetrazolium Blue choride (NBT) at 560 nm, in presence and absence of the copper(II) complexes.

The experiments require extremely low complex concentrations (~10^{-7} M order of magnitude), therefore simulations have been performed in order to discover the distribution of the complex species under such conditions. The calculations revealed that trinuclear complexes of $\mathbf{L^1}$ do not form in dominant quantities, therefore SOD activity was determined for the monocopper(II) complexes of tren3his only. At two-fold metal ion excess, dinuclear complexes of nta3his and tren2his were found to be dominant even at such low complex concentration levels, allowing the establishment of their superoxide dismutase activity. The presence of free copper(II) ion was negligible in all Cu(II)-ligand systems.

All investigated systems, except for Cu(II)-$\mathbf{L^4}$, showed considerable SOD-like activity. Copper(II) complexes of $\mathbf{L^4}$ did not present any catecholase-like activity either, thus we can assume that the saturated, highly stable coordination sphere around the metal ion in $CuH_{-1}\mathbf{L^4}$ (Scheme 4.11.) prevents the coordination of the substrate in these catalytic tests. This finding is supported by the fact that the inhibition levels observed during our SOD experiments are even lower than that determined for free copper(II) in aqueous solutions [153].

The inhibition curves resulted by the tripodal peptide-copper(II) systems are depicted in Figure 4.65. The obtained kinetic parameters (IC_{50} and k) are presented in Table 4.16, together with that of the studied linear peptide-copper(II) systems, the native Cu,Zn-SOD and free copper(II) as comparison.

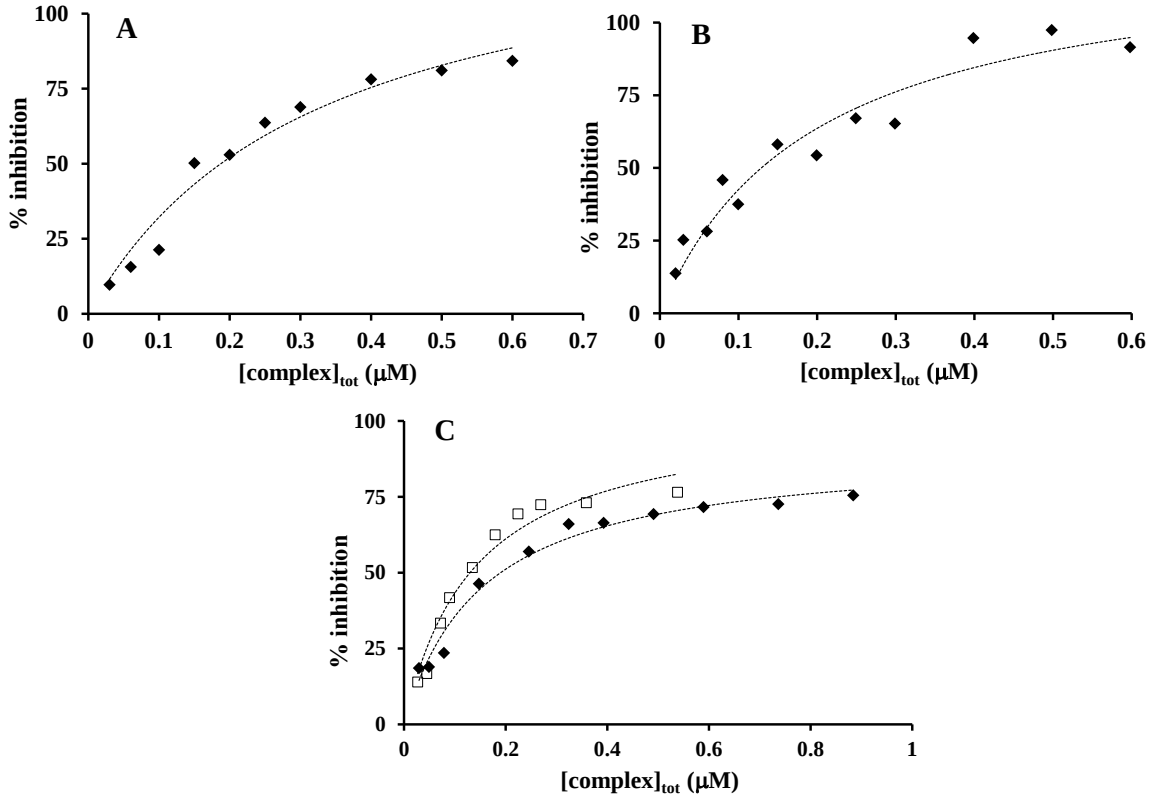

Figure 4.65. Superoxide dismutase activity of Cu(II)-**L**^{1} 1:1 (**A**), Cu(II)-**L**^{2} 2:1 (**B**), Cu(II)-**L**^{3} 1:1 (**C**, ♦) and 2:1 (**C**, □) systems at pH 7.4.

Table 4.16. IC_{50} and *k* values of Cu(II)-tripodal peptide systems, together with those of other copper(II)-linear peptide complexes and the native Cu,Zn-SOD enzyme.

complex	IC_{50} (μM)	*k* ($M^{-1}s^{-1}$)[a]	Ref.
Cu,Zn-SOD (pH 6.8)	0.0045	3.3×10^{8}	[65]
Cu(II)-**L**^{3} 2:1 (pH 7.4)	0.13	4.6×10^{7}	
Cu(II)-**P5** 1:1 (pH 7.4)	0.10	3.0×10^{7}	
Cu(II)-**L**^{3} 1:1 (pH 7.4)	0.20	3.0×10^{7}	
Cu(II)-**L**^{2} 2:1 (pH 7.4)	0.13	2.3×10^{7}	
Cu(II)-**L**^{1} 1:1 (pH 7.4)	0.17	1.8×10^{7}	
Cu(II)-**P4** 1:1 (pH 7.0)	0.11	1.4×10^{7}	[88]
Cu(II)-**P2** 1:1 (pH 7.2)	0.50	1.2×10^{7}	
Cu(II)-**P1** (pH 7.8)	0.65	9.2×10^{6}	
$Cu(HPO_4)$ (pH 7.4)	1.06	6.2×10^{6}	[153]

[a] *k* calculated as $k_{NBT}\times[NBT]/IC_{50}$ ($k_{NBT} = 3\times10^{4}$ $M^{-1}s^{-1}$, see Section 3.3.2.)

Based on the determined *k* values (which are independent of the applied NBT concentration) the highest SOD-mimicking capabilities are presented by the dinuclear complexes of **L**^{3}. Mononuclear copper(II) species of this ligand were also found to be able to dismutate superoxide radicals with high efficiency, however, the dicopper(II) complexes do not present two-fold increase in *k* over the mononuclear complexes, indicating different activities regarding the two copper cores, which is in agreement with the two copper

centers being in very different coordination environments. The observed activity is on the same level as the most active studied linear peptide system, the –H(Xaa)$_n$HXaaH– type sequence **P5**, having a {2N$_{im}$,2N$^-$} coordinated copper(II) in the relevant pH range [149]. The other linear peptide-copper(II) species have lower SOD activities, falling behind that of the other two tripodal ligand-copper(II) systems.

Altogether, it can be stated that the observed SOD activities for the copper(II)-peptide systems are significant, especially that of the tripodal peptide complexes. However, all of the obtained IC_{50} or *k* values are more or less similar; they are in the same order of magnitude, outperforming the activity of the free copper(II) phosphate solutions itself, but not approaching the efficiency of the native Cu,Zn-SOD enzyme isolated from bovine erythrocytes [65] (see Table 1.2. in Section 1.4.3). This indicates that the tripodal structure of the ligands does not affect considerably the catalytic performance of the copper(II) species in superoxide dismutation function, unlike as it was observed in the oxidation of H_2DTBC, where the tripodal platforms were found to enhance notably the substrate binding capabilities of the peptide complexes.

5. SUMMARY

In my PhD thesis, I present synthesis and characterization of tripodal peptide-type ligands, along with the extensive study on their complex formation properties in presence of copper(II) and zinc(II) ions, natural cofactors of metalloenzymes. By using His-functionalized tripodal platforms, our aim was to enhance the metal binding capabilities of linear peptide ligands, with respect to stability and structure. We applied the metal complexes of the ligands in catalytic model reactions such as catechol oxidation, superoxide dismutation or phosphoester hydrolysis, in order to establish their enzyme-mimicking behavior. Beside kinetic characterization, detailed substrate binding and mechanistic studies have been carried out, especially focusing on catechol oxidation by the copper(II)-ligand complexes.

The studied ligands provided the opportunity to (i) compare the coordination chemical properties of tripods bearing C- and N-terminal histidine units, as well as to (ii) study the effect of gradually increasing number of N-terminal His moieties. Thanks to the high number of available donor groups, formation of multinuclear species could be induced by the ligands, and some interesting self-assembling features were observed as well.

The scientific content and value of this work can be summarized in the following points:

(1) The firstly synthesized, free N-terminal histidine containing ligand, tren3his ($\mathbf{L^1}$), forms mono- and trinuclear (M_3L_2 type) complexes in presence of both metal ions. The coordination properties are directed by the highly stable *bis*-histamine-type $\{2N_{im},2\alpha NH_2\}$ coordination. Complexes with this binding mode dominate in equimolar metal-ligand solutions up to pH 8. In the basic pH range, metal induced deprotonation of the amide nitrogens takes place in presence of copper(II), while zinc(II) complexes deprotonate to form mixed hydroxo species. At 3:2 metal-to-ligand ratio, dimerization of the mononuclear units occurs with the assistance of a third bound metal ion, resulting $M_3H_{-x}\mathbf{L^1}_2$ type species. NMR study of the trinuclear zinc(II) complexes formed at pH 10 revealed that these complexes may be involved in even higher level of assembly, forming $Zn_{3n}H_{-x}\mathbf{L^1}_{2n}$ oligomer structures – while EPR measurements did not suggest such self-assembly in presence of copper(II) ions.

(2) The C-terminal histidine containing nta3his ligand ($\mathbf{L^2}$) presents different coordination properties towards copper(II) and zinc(II) ions. In the copper(II)-$\mathbf{L^2}$ system mono- and dinuclear complexes could be detected. The spectroscopic data are consistent with a highly stable, Cu(II)-Gly-His-like, $\{N_{tert},N^-,N_{im},O\}$ type coordination, dominating in the equimolar solution until pH 10. Above that, this structure transforms into the five-coordinate $CuH_{-2}\mathbf{L^2}$ complex, having an intermediate geometry between trigonal bipyramid and square pyramid. The Gly-His-type binding mode allows the binding of a second copper(II) ion at metal excess; the imidazole and carboxylic groups participate in this

coordination in the acidic-neutral, while amide nitrogens in the basic pH range. In presence of zinc(II) ions, the water insoluble Zn$\mathbf{L}^{\mathbf{2}}$ complex forms between pH 6 and 9, causing precipitation in a wide pH range. Zn^{2+}-dependent ^{1}H NMR spectra indicated different ligand exchange rates in the neutral and the basic pH range; the deceleration of the ligand exchange processes at basic pH implies the formation of the Gly-His-type $\{N_{im},N^-,NH_2\}$ coordination in $ZnH_{-1}\mathbf{L}^{\mathbf{2}}$. Accordingly, the precipitating species should be coordinated by imidazole/COO^- groups, which leads, probably due to oligo-/polymerization, to significant decrease in solubility.

(3) In the second part of the work, asymmetrically functionalized tripodal peptides have been synthesized and studied. The *bis*-histidyl tren derivative tren2his ($\mathbf{L}^{\mathbf{3}}$) forms mono- and dinuclear complexes in presence of copper(II) and zinc(II) ions. At 1:1 metal-to-ligand ratios, the *bis*-histamine-type coordination is predominant until neutral pH. In basic solutions, amide nitrogen and tertiary nitrogen coordinated copper(II) species, as well as mixed hydroxo zinc(II) complexes formed, similarly to the tren3his ligand systems. In presence of 2 eq. copper(II), $Cu_2H_{-x}\mathbf{L}^{\mathbf{3}}$ (x = 1, 2, 3) species dominate above pH 4. The formation of dinuclear species is related to the presence of two basically different metal binding sites in the molecule: aside of the *bis*-histamine-type coordination site, the primary tren NH_2, the tertiary amino group and two amide nitrogens act as secondary binding site at the center of the ligand. In presence of 2 eq. copper(II), the complex $Cu_2H_{-1}\mathbf{L}^{\mathbf{3}}$ dominates over 4 pH units. The dizinc(II) complexes have slow ligand exchange rate on the NMR time scale; the spectra indicated interesting dimerization processes, where the imidazole ring might act as bridging ligand.

(4) The *mono*-His-functionalized tren derivative tren1his ($\mathbf{L}^{\mathbf{4}}$) forms only mononuclear complexes with both metal ions. In presence of copper(II) ions, CuH$\mathbf{L}^{\mathbf{4}}$ and $CuH_{-1}\mathbf{L}^{\mathbf{4}}$ complexes are the major species with $\{N_{im},N^-,N_{tert},NH_2\}$ and $\{N_{im},N^-,N_{tert},2NH_2\}$ coordination, respectively. The latter complex is five-coordinated, similarly to tren-metal complexes, but the peptide-type functionalization causes considerable distortion in geometry. In presence of Zn^{2+} ions, the analogous $ZnH_{-1}\mathbf{L}^{\mathbf{4}}$ complex predominates in the whole pH range; the related ^{1}H NMR spectra is surprisingly complicated, due to the slow ligand exchange and the magnetically inequivalent CH_2 protons. The coordination sphere of the $MH_{-1}\mathbf{L}^{\mathbf{4}}$ complexes is completed by an axially coordinating histidine-nitrogen donor group.

(5) Catechol oxidase mimicking properties of the investigated copper(II)-ligand systems have been studied from kinetic and mechanistic aspects. We observed significant catalytic activities in the oxidation of 3,5-di-*tert*-butylcatechol (H_2DTBC) in case of copper(II)-$\mathbf{L}^{\mathbf{1}}$ 3:2, copper(II)-$\mathbf{L}^{\mathbf{2}}$ 2:1 and copper(II)-$\mathbf{L}^{\mathbf{3}}$ 2:1 systems. Reaction rates were measured in function of pH, substrate, complex and oxygen concentrations. Substrate-dependent measurements resulted saturation-like behavior in all ligand systems, allowing the Michaelis-Menten enzyme kinetic treatment. In all cases, first order dependence was detected in the reaction rates regarding oxygen and complex concentrations. Substrate

binding and other mechanistic studies revealed that Cu(II)-$\mathbf{L^2}$ 2:1 system carries out two-electron oxidation of H_2DTBC, similarly to the native enzymatic pathway. The Cu(II)-$\mathbf{L^1}$ 3:2 and Cu(II)-$\mathbf{L^3}$ 2:1 systems, despite the tri-/dinuclear pre-active complex, perform one-electron oxidation of the substrate via the formation of a semiquinone type radical intermediate.

(6) Connecting structure and activity, comparison has been made between catechol oxidase mimicking complexes of tripodal and linear peptides. As a general feature, coordinated amide nitrogens were suggested to facilitate substrate binding by the abstraction of protons from the -OH groups of the incoming substrate, serving as supporting acid-base catalytic sites in catecholase mimicking Cu(II)-peptide complexes. Furthermore, we have found that the structure organizing effect of the tripodal scaffold positively influences the substrate binding capabilities of the complexes, and therefore, overall catalytic efficiency. The studied tripodal ligands favor the formation of multinuclear species, further improving catalytic properties by allowing two-electon oxidation pathways: our dinuclear systems demonstrated impressively high k_{cat}/K_M values in H_2DTBC oxidation, even among non-peptide-type catecholase model complexes.

(7) The superoxide dismutase (SOD) mimicking properties of linear and tripodal peptide-copper(II) complexes were also studied. Except for copper(II)-$\mathbf{L^4}$, all investigated copper(II)-ligand systems showed significant superoxide dismutating ability in the modified McCord-Fridovich indirect test reaction. Their IC_{50} values are in the same range as those determined in histidine containing linear peptide-copper(II) systems; however, their activity is still almost two order of magnitudes lower than that of the native Cu,Zn-SOD.

In summary, we synthesized and investigated a new group of tripodal peptide ligands bearing histidine moieties. With thorough and systematical solution equilibrium and spectroscopic studies, we uncovered the driving forces of metal coordination, and established the impact of the tripodal structure in stability, structure and catalytic properties of the forming complexes. Our results confirm the beneficial effect of tripodal scaffolds in peptide-type ligand-metal complexes, and emphasize the possibilities lying within tripodal peptides in the field of enzyme mimicking.

6. ÖSSZEFOGLALÁS

Doktori értekezésemben peptid típusú tripodális ligandumok előállítását és jellemzését, illetve a metalloenzimekben nagy számban előforduló réz(II)- és cink(II)ionokkal alkotott fémkomplexeik tanulmányozását mutatom be. A tripodális állványzat alkalmazásával a lineáris peptidek fémkötő képességét szerettük volna továbbfejleszteni, szerkezeti és stabilitási szempontból. A képződött fémkomplexeket katalitikus modellreakciókban alkalmaztuk (pirokatechin oxidáció, szuperoxid dizmutáció, illetve foszfátészter hidrolízis), és jellemeztük enzimutánzó sajátságukat. A kinetikai vizsgálatok mellett részletes szubsztrátkötési vizsgálatokra, illetve mechanisztikus tárgyalásra is sor került, főként a réz(II)komplexek pirokatechin oxidáz aktivitására vonatkozóan.

A vizsgált ligandumok jó összehasonlítási alapként szolgáltak (i) az N- és C-terminális hisztidint tartalmazó tripodális vegyületek összevetéséhez, illetve (ii) a fokozatosan növekvő számú hisztidin-alegységet tartalmazó tripodális peptidek tanulmányozásához koordinációs kémiai szempontból. A nagyszámú donorcsoportok jelenlétének köszönhetően többmagvú fémkomplexek képződése is előidézhető volt, illetve érdekes asszociációs tulajdonságok is megfigyelhetők voltak.

A munka tudományos tartalma összefoglalható az alábbi pontokban:

(1) Az elsőként előállított és vizsgált, N-terminális hisztidint tartalmazó tren3his ligandum ($\mathbf{L^1}$) mindkét fémion jelenlétében egy- és hárommagvú (M_3L_2 típusú) komplexeket képez. A koordinációs sajátságokat a nagy stabilitású *bisz*-hisztamin $\{2N_{im},2\alpha NH_2\}$ típusú kötésmód határozza meg; az ilyen szerkezetű fémkomplexek ekvimoláris oldatukban pH 8-ig dominánsak. A lúgos pH tartományban réz(II)ionok jelenlétében amidnitrogén koordináció, míg a cink(II)-ligandum rendszerben vegyes hidroxo komplexek képződése zajlik. 3:2 fém-ligandum aránynál a monomer egységek dimerizációja következik be egy harmadik fémion megkötésével, $M_3H_{-x}\mathbf{L^1}_2$ összetételű komplexek képződéséhez vezetve. A cink(II)-ligandum 3:2 rendszerben pH 10-en felvett NMR spektrumok arra utaltak, hogy ez a folyamat még ennél is nagyobb mértékű, $Zn_{3n}H_{-x}\mathbf{L^1}_{2n}$ típusú oligomerizációhoz vezethet. Az ESR eredmények nem utaltak hasonló mértékű asszociációra a megfelelő réz(II)komplexek esetében.

(2) A C-terminális hisztidint tartalmazó nta3his ($\mathbf{L^2}$) ligandum eltérő koordinációs viselkedést mutat réz(II) és cink(II)ionok jelenlétében. A réz(II)-ligandum rendszerekben egy- és kétmagvú komplexek képződése volt észlelhető. A spektroszkópiás vizsgálatok egy nagy stabilitású, a réz(II)-Gly-His rendszerre jellemző $\{N_{tert},N^-,N_{im},O\}$ koordinációs környezetre utalnak, mely ekvimoláris oldatban pH 10-ig uralkodó kötésmód. Ez egy érdekes, ötös geometriával rendelkező $CuH_{-2}\mathbf{L^2}$ komplexszé alakul át, trigonális bipiramis és négyzetes piramis közötti szerkezettel. A Gly-His típusú koordináció lehetővé teszi egy második fémion megkötését a ligandum által, mely savas pH tartományban imidazol és karboxilát, míg lúgos tartományban amidnitrogének által koordinált. Cink(II)ionok jelenlétében csapadékképző, alacsony oldhatóságú ligandum komplexek képződnek pH 6

és 9 között. Cink(II)-függő ^{1}H NMR spektrumok a ligandumcsere sebesség megváltozására utaltak a semleges és lúgos oldatokban; a lassú cseresebesség itt is a Gly-His-szerű $\{N_{im},N^-,NH_2\}$ koordinációt valószínűsíti. Ezek alapján a semleges tartományban jellemző csapadékképző komplexben imidazol- és karboxilátcsoportok kötődnek, melyek, talán oligo-/polimerizáció révén, az oldhatóság jelentős csökkenéséhez vezetnek.

(3) A munka második felében aszimmetrikusan funkcionalizált tripodális peptideket állítottunk elő és vizsgáltunk. A *bisz*-hisztidil tren származék tren2his (**L^3**) egy- és kétmagvú komplexeket képez mind réz(II), mind cink(II)ionok jelenlétében. 1:1 fém-ligandum arányoknál a *bisz*-hisztamin típusú koordináció semleges pH-ig domináns. Bázikus oldatban amidnitrogének és a tercier nitrogén által koordinált réz(II)komplexek, illetve vegyes hidroxo cink(II)komplexek képződnek, hasonlóan a tren3his rendszerekhez. A kétmagvú komplexek kialakulása két, jól elkülöníthető fémkötő hely jelenlétéhez rendelhető a molekulában: a *bisz*-hisztamin-szerű kötőhely mellett a tren primer és tercier aminocsoportja, és a két amidnitrogén szolgáltat egy második fémkötő helyet. Az így képződő rézkomplexek közül a Cu_2H_{-1}**L^3** részecske 4 pH egységen keresztül domináns. A kétmagvú cink(II)komplexek lassú ligandumcseréjűek az NMR időskálához mérve; a spektrumok érdekes dimerizációs folyamatra utaltak, ahol az imidazolgyűrű hídligandumként betöltött szerepe is felmerül.

(4) A *mono*-His funkcionalizált tren származék tren1his (**L^4**) csak egymagvú komplexeket képez mindkét fémionnal. Réz(II)ionok jelenlétében a CuH**L^4** és a CuH_{-1}**L^4** részecskék dominálnak, az utóbbi a tren-hez hasonló, ám az amidnitrogén koordináció miatt jelentősen torzult ötös geometriával rendelkezik. A cink(II)-ligandum rendszerben a megfelelő ZnH_{-1}**L^4** komplex az egész pH tartományban domináns; a részecske NMR spektruma meglepően bonyolult, amit a lassú ligandumcsere sebesség és a különböző CH_2 csoportok protonjainak mágneses inekvivalenciája okoz. Az MH_{-1}**L^4** komplexek koordinációs szféráját egy hisztidin nitrogén axiális koordinációja egészíti ki.

(5) Jellemeztük a tanulmányozott réz(II)-ligandum rendszerek pirokatechin oxidáz utánzó sajátságait kinetikai és mechanisztikus szempontból. Jelentős katalitikus aktivitás volt tapasztalható a réz(II)-**L^1** 3:2, réz(II)-**L^2** 2:1 és réz(II)-**L^3** 2:1 rendszerekben, a 3,5-di-*terc*-butil pirokatechin (H_2DTBC) szubsztrát oxidációjában. Vizsgáltuk a reakciósebességeket a pH, illetve a szubsztrát-, komplex- és oxigénkoncentráció függvényében. A szubsztrátfüggő mérések telítési kinetikai viselkedést mutattak minden esetben, így alkalmazható volt a Michaelis-Menten kezelésmód. Minden esetben elsőrendű függést állapítottunk meg a reakciósebesség és a komplex-/oxigénkoncentráció között. Mechanisztikus és szubsztrátkötési kísérletek rámutattak, hogy a Cu(II)-**L^2** 2:1 rendszer kételektronos oxidációs mechanizmus szerint működik, hasonlóan a natív enzim mechanizmusához. Ezzel szemben a Cu(II)-**L^1** 3:2 és Cu(II)-**L^3** 2:1 rendszerek, a többmagvú preaktív fémkomplexek ellenére egyelektronos oxidációs mechanizmust követnek, szemikinon típusú átmeneti komplex képződésén keresztül.

(6) Hogy kapcsolatot teremtsünk szerkezet és aktivitás között, összehasonlítottuk tripodális rendszereink pirokatechin oxidáz aktivitását néhány lineáris peptid komplexének aktivitásával. Általánosan megállapítható, hogy a pirokatechin oxidáz utánzó réz(II)-peptid komplexekben a koordinált amidnitrogén kiegészítő sav-bázis katalitikus csoportként funkcionál, mely az -OH protonok elvonása révén elősegíti a szubsztrát koordinációját. Továbbá rámutattunk, hogy a tripodális szerkezet pozitívan befolyásolja a fémkomplexek szubsztrátkötő sajátságait, megnövelve ezzel a katalitikus hatékonyságot. A tripodális struktúra továbbá elősegíti többmagvú fémkomplexek kialakulását is, utat nyitva a nagyhatékonyságú kételektronos oxidációs mechanizmus felé: kétmagvú rendszereink még a nem peptid típusú pirokatechin oxidáz utánzó modellkomplexekkel összehasonlítva is kiemelkedő katalitikus aktivitást mutattak.

(7) Tripodális peptidkomplexeinket, valamint néhány lineáris peptid-réz(II)komplexet szuperoxid dizmutáz funkcióban is teszteltük. A Cu(II)-$\mathbf{L^4}$ rendszeren kívül az összes réz(II)-ligandum rendszer jelentős SOD-aktivitással rendelkezik az alkalmazott McCord-Fridovich indirekt tesztreakcióban. A SOD-utánzó komplexek IC_{50} értékei mind előnyösebbek a szabad réz(II)ionra meghatározott értéknél, és más, korábban vizsgált hisztidintartalmú peptidkomplexek értékeihez hasonlítanak. Aktivitásuk azonban közel két nagyságrenddel alulmarad a natív Cu,Zn-SOD hatékonyságához képest.

Összegezve tehát, a munka során a tripodális peptidek egy új, hisztidintartalmú csoportját szintetizáltuk és tanulmányoztuk. Mélyreható, szisztematikus oldategyensúlyi és spektroszkópiai vizsgálatok segítségével feltártuk a koordinációs sajátságok hajtóerejét, és megállapítottuk a tripodális állványzat hatását a komplexek stabilitására, szerkezetére és katalitikus tulajdonságaira. Az eredményeink alátámasztják a tripodális alapvegyületnek a peptidszerű ligandumok fémkomplexeire gyakorolt jótékony hatását, és rámutat a tripodális peptidek alkalmazásában rejlő lehetőségekre az enzim-modellezés területén.

RESUME FRANÇAIS

I. INTRODUCTION

De nos jours, un des objectifs importants de la recherche bioinorganique moderne est le développement d'enzymes artificielles. D'un côté, ces composés modèles de poids moléculaire faible peuvent mimer les fonctions catalytiques des enzymes avec une efficacité élevée, permettant le remplacement de ces biomolécules dans différents procédés industriels. D'un autre côté, le dévelopement d'enzymes artificielles peut nous permettre de comprendre de façon plus poussée les mécanismes d'action moléculaires existant dans les systèmes biologiques.

Les complexes de métaux de transition sont de bons candidats pour modéliser de façon structurelle et fonctionnelle les métalloenzymes. Une des stratégies concerne l'étude des séquences d'acides aminés présentes dans les centres actifs des métalloenzymes; l'étude des interactions métal-ligand avec des peptides modèles de différentes longueurs. Ces études fournissent des informations utiles quant au type des acides aminés présents dans le centre actif ainsi que sur leur rôle dans la régulation du processus enzymatique, comme la liaison avec des métaux, la liaison avec le substrat, l'activation du substrat ou les fonctions catalytiques acide/base. Les peptides linéaires, cependant, ont leurs limites dans la reconstitution des centres actifs des métalloenzymes, puisqu'ils ne possèdent pas la structure tridimensionnelle bien définie fournie par la chaîne polypeptidique repliée. Par conséquent, la stabilité de leurs complexes métalliques est relativement faible (Figure I.1), par rapport à celle du site actif natif, empêchant le développement d'une activité catalytique efficace.

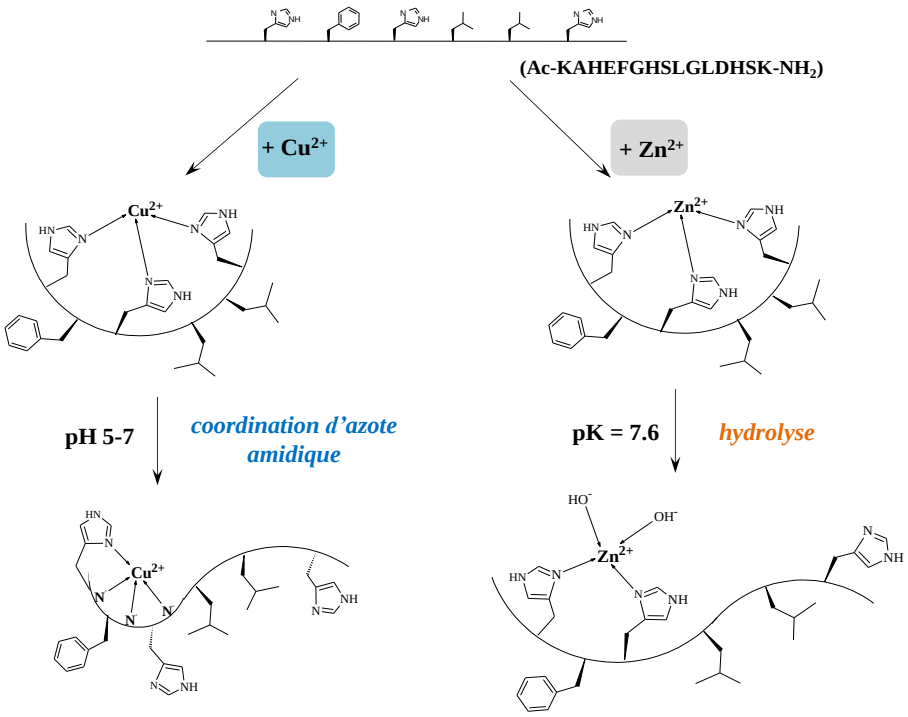

Figure I.1. Déstabilisation de l'environment multi-imidazolique en complexes de cuivre(II) et zinc(II) (du travail précédent de nos laboratoires).

La capacité de coordination des métaux par des peptides linéaires peut être améliorée, par exemple, en les attachant à une plateforme tripodale (Figure I.2). Les composés tripodaux peuvent assurer une organisation structurale rigide ou moins flexible pour des chaînes latérales des acides aminés, créant ainsi des sites de coordination pré-organisés pour les métaux. De plus, par une fonctionnalisation ciblée des ligands de nouvelles fonctions peuvent être insérées dans la molécule, telles que le site de reconnaissance du substrat ou le site allostérique de coordination du métal, ce qui peut aider à affiner l'activité catalytique. Compte tenu de tout cela, nous pouvons concevoir des ligands peptidiques tripodaux, qui pourraient former des complexes métalliques très stables avec une structure adéquate, remplissant les conditions préalables fondamentales d'un mime d'enzyme efficace.

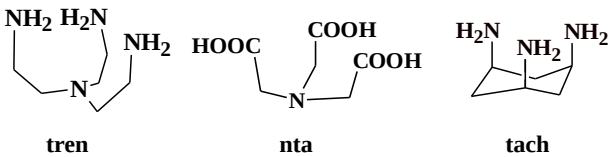

Figure I.2. Examples des ligands tripodaux simples : tren *(tris(2-aminoethyl)amine)*, nta *(nitrilotriacetic acid)* et tach *(1,3,5-triaminocyclohexane)*.

II. OBJECTIFS

Les principaux objectifs du présent travail concernent la synthèse, l'étude thermodynamique et structurale en solution de nouveaux ligands tripodaux peptidiques et de leurs complexes de cuivre(II) et de zinc(II), ainsi que leurs applications en tant que catalyseurs dans des réactions enzymatiques redox et hydrolytiques. Notre choix des ligands tripodaux fonctionnalisés par l'histidine était motivé par le fait que la coordination des métaux est assurée par les chaînes latérales des histidines dans la majorité des métalloenzymes. Nous avions l'intention de mettre autant d'effort dans l'exploration des propriétés de coordination que dans l'étude du comportement enzymatique. Par conséquent, les principaux objectifs du travail peuvent être résumés comme ci-dessous:

(1) Nous avons voulu étudier l'effet de la plate-forme tripodale sur la stabilité thermodynamique des complexes métalliques formés.

(2) Nous avons voulu identifier le rôle du tripode et d'acide aminé dans la structure des espèces formées en analysant la géométrie, le nombre de coordination et les modes de liaison dominants.

(3) Nous avons voulu comparer les propriétés de coordination des ligands contenant de l'histidine en position N- ou C-terminale et étudier l'impact de la fonctionnalisation asymétrique sur la formation des complexes.

(4) Nous avons voulu tester l'activité catalytique des complexes métalliques formés dans de simples réactions modèle enzymatique, comme par exemple dans l'oxydation du catéchol ou dans la dismutation du superoxyde.

(5) Nous avons également voulu trouver des liens entre les activités catalytiques et les structures des complexes métalliques. Dans ce but, il était important de comparer nos systèmes aux complexes catalytiques actifs formés avec des peptides linéaires. Ces résultats peuvent fournir des informations importantes pour le développement de nouveaux mimes enzymatiques plus efficaces.

III. TECHNIQUES EXPERIMENTALES ET METHODES

Synthèses des ligands

Les ligands présentés dans ce travail ont été préparés et purifiés au laboratoire de synthèse du Département de Chimie Inorganique et Analytique de l'Université de Szeged. Les ligands nta1his et nta1his-NH_2 ont été synthétisés en utilisant la méthode de synthèse peptidique en phase solide; tous les autres ligands ont été préparés par couplage peptidique en solution. Les structures schématiques des ligands synthétisés sont représentées sur la Figure II.1.

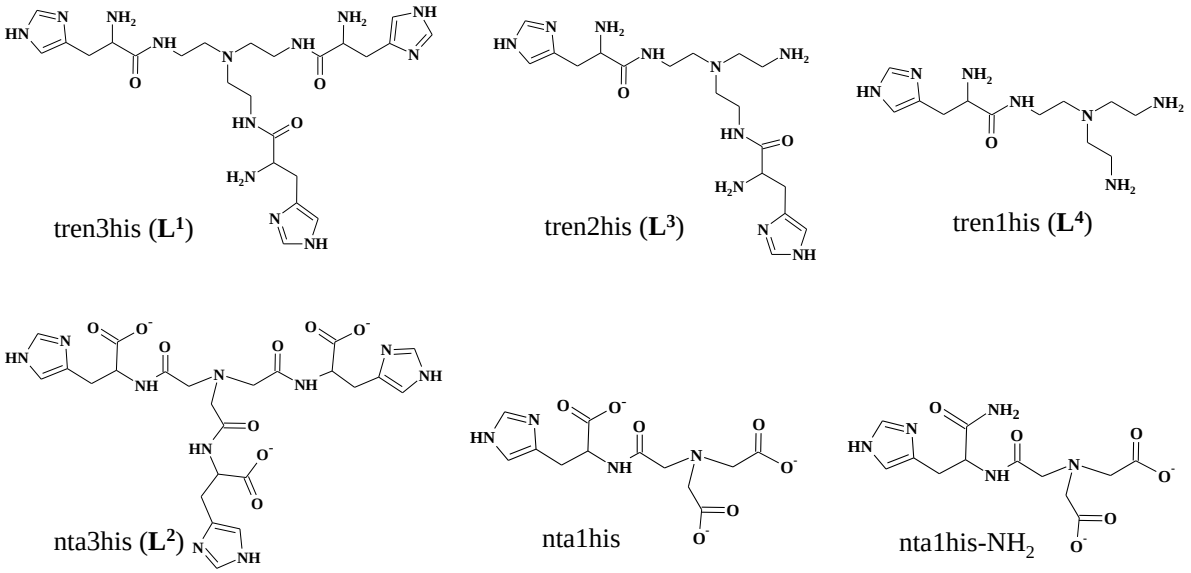

Figure II.1. Désignation et structure schématique des ligands synthétisés.

Étude d'équilibre en solution

Afin d'étudier les processus de (dé)protonation des ligands et de déterminer la stabilité des espèces métal-ligand formées, des dosages potentiométriques ont été réalisés. Les mesures ont été effectuées en milieu aqueux à différents rapports métal-ligand (force ionique NaCl de 0,1 M et à 25°C). Les résultats ont été évalués à l'aide des programmes SUPERQUAD et PSEQUAD.

Méthodes Spectroscopiques

Nous avons utilisé différentes techniques spectroscopiques pour décrire la structure des complexes métal-ligand en solution. Pour pouvoir identifier le type des atomes (groupes)

donneurs et des principaux modes de liaison dans les complexes de cuivre(II), nous avons utilisé la spectroscopie UV-visible (UV-Vis) et le Dichroïsme Circulaire (CD). Les spectres enregistrés en fonction du pH ont été traités conjointement avec des courbes de dosage potentiométriques afin d'obtenir des spectres molaires UV-Vis et CD pour les principales espèces complexées. La spectroscopie de Résonance Paramagnétique Électronique (RPE) a été appliquée pour estimer la géométrie et le nombre de groupes N-donneurs dans les complexes de cuivre(II). Nous remercions Dr Nóra May (Centre de recherche pour les sciences naturelles, Budapest, Hongrie) pour son aide précieuse dans ces mesures et l'évaluation des données. Les méthodes spectroscopiques mentionnées ont toutes été utilisées, pour étudier des complexes binaires métal-ligand, mais également dans des expériences de fixation du substrat.

L'outil principal pour étudier la formation du complexe de zinc(II) est la spectroscopie de Résonance Magnétique Nucléaire (RMN). Les spectres de ^{1}H RMN ont été enregistrés en fonction du pH pour identifier les groupements déprotonables et donneurs des ligands. Nous avons utilisé des techniques de RMN bidimensionnelles et homonucléaires (corrélation ^{1}H-^{1}H COSY, corrélation totale ^{1}H-^{1}H TOCSY, effet Overhauser nucléaire ^{1}H-^{1}H ROESY) afin de prouver certaines caractéristiques structurelles particulières. Une autre technique spéciale de la RMN, la mesure de diffusion par gradient du champ pulsé (DOSY), nous a permis de mettre en évidence certains processus intéressants d'oligomérisation induite par le métal.

Des mesures par Spectrométrie de Masse (MS) ont été utilisées pour prouver l'existence des complexes proposés à différents rapports métal-ligand. Alors que les molécules des ligands libres et des complexes mononucléaires étaient détectables par la spectrométrie de masse ESI (électrospray ionisation), la détection des espèces multinucléaires nécessitait l'application de la technique MALDI-TOF (source d'ionisation laser assistée par une matrice et un analyseur à temps de vol).

Mesures cinétiques

Les activités catalytiques des complexes métalliques ont été étudiées dans des réactions d'hydrolyse du phosphoester, d'oxydation du catéchol et de dismutation du superoxyde. Les expériences ont été réalisées dans des solutions tamponnées, à une force ionique de 0,1 M et à 25°C. Les réactions ont été suivies par spectrophotométrie; la détermination des constantes de vitesse de la réaction du pseudo-premier ordre (k_{obs}) a été réalisée selon la

méthode de la vitesse initiale. L'autohydrolyse ou le taux d'oxydation des substrats ont été pris en compte. Les paramètres cinétiques enzymatiques (k_{cat} et K_M), utilisés pour la caractérisation des activités de catéchol oxydase, ont été calculés selon l'équation de Michaelis-Menten, avec une régression non linéaire des données.

IV. NOUVEAUX RESULTATS SCIENTIFIQUES

1. Equilibre acido-basique et étude structurale du C_3 symétriques tren3his ($\mathbf{L^1}$) ligand contenant des histidines N-terminales et de ses complexes métalliques

1.1. Six déprotonations ont eu lieu dans le domaine du pH étudié (2-10,5) liées au ligand. La constante de déprotonation moyenne (p*K*) des groupes imidazolium (N_{im}-H^+) et N-terminal ammonium (αNH_3^+) est inférieure à la valeur de l'histamine. La protonation du groupe amine tertiaire (N_{tert}) n'a pas été observée même à pH acide.

1.2. La formation des complexes métal-ligand 1:1 et 3:2 a été observée en présence des ions Cu^{2+} (Figure IV.1.) et Zn^{2+}; ces complexes ont également été détectés par la technique MALDI-TOF MS (Figure IV.2). Dans la gamme de pH acide-neutre, la coordination de type *bis*-histamine {$2N_{im}$,$2\alpha NH_2$} est dominante dans le plan équatorial des métaux (Figure IV.3). Les complexes MH$\mathbf{L^1}$ présentant cette coordination ont montré une diminution des valeurs de p*K* par rapport au ligand libre, indiquant la coordination axiale du troisième «bras» du ligand.

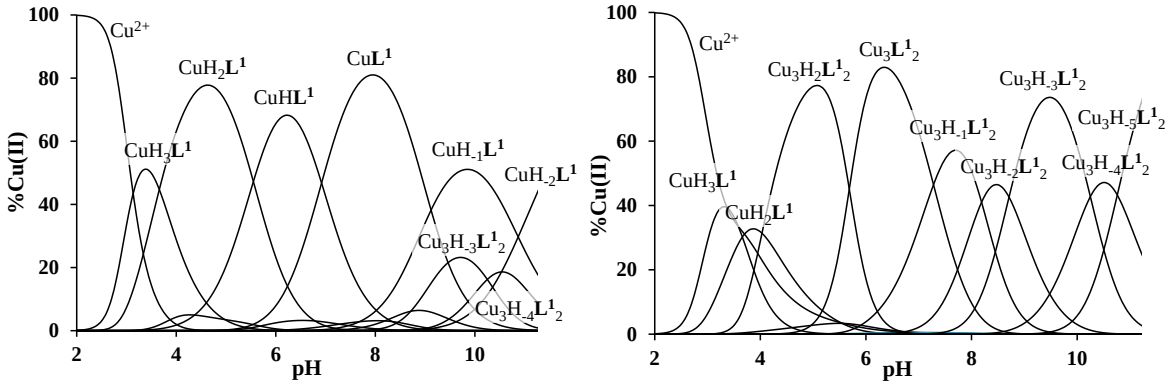

Figure IV.1. Distribution des espèces dans les systèmes Cu(II)-$\mathbf{L^1}$ 1:1 (gauche) et 3:2 (droite); $[\mathbf{L^1}]_{tot}$ = $[Cu(II)]_{tot}$ = 0.001 M et 1.5×$[\mathbf{L^1}]_{tot}$ = $[Cu(II)]_{tot}$ = 0.001 M, respectivement, *I* = 0.1 M NaCl, *T* = 298 K.

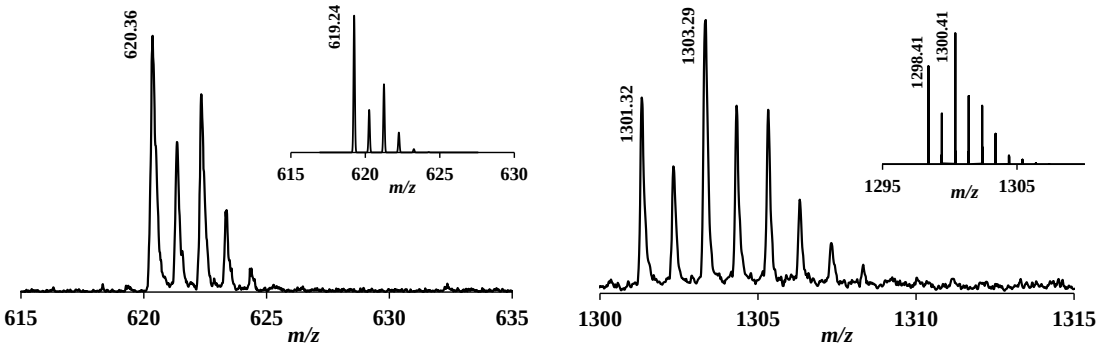

Figure IV.2. Spectres de masse MALDI-TOF mesuré dans les systèmes Cu(II)-**L**^{1} 1:1 (gauche) et 3:2 (droite). Insertion : spectres calculés pour les complexes correspondants ($[C_{24}H_{38}N_{13}O_3Cu]^+$ et $[C_{48}H_{73}N_{26}O_6Cu_3]^+$, respectivement).

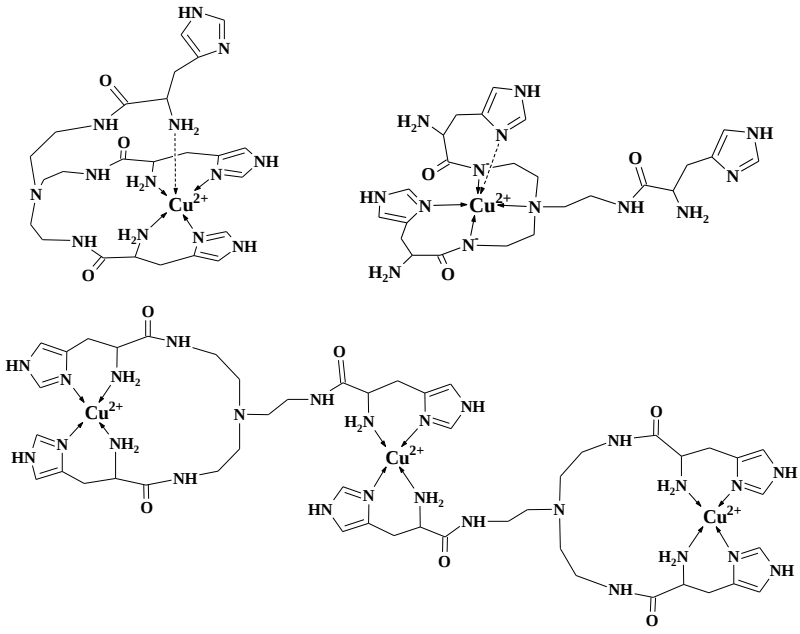

Figure IV.3. Structures proposées pour les principaux complexes de cuivre(II)-**L**^{1} Cu**L**^{1}, CuH_{-2}**L**^{1} et Cu_3**L**$^{1}_2$ (tirets indiquent de la coordination axiale possible).

1.3. A pH basique, les complexes de deux métaux subissent différents changements dans la sphère de coordination. En présence d'ions cuivre(II), les déprotonations du complexe Cu**L**^{1} de type *bis*-histamine conduisent à la coordination du groupement amide et de l'azote tertiaire (Figure IV.3). Le spectre CD du complexe CuH_{-2}**L**^{1} est très caractéristique et présente une ressemblance avec les spectres CD des complexes peptidiques modélisant le domaine «octarepeat» de la protéine prion (Figure IV. 4). Dans le système zinc(II)-**L**^{1}, l'ion métallique s'hydrolyse partiellement, conduisant à la formation des espèces mixtes-hydroxo (Zn**L**^{1}(OH) and Zn**L**^{1}$(OH)_2$) dans le domaine de pH plus élevé.

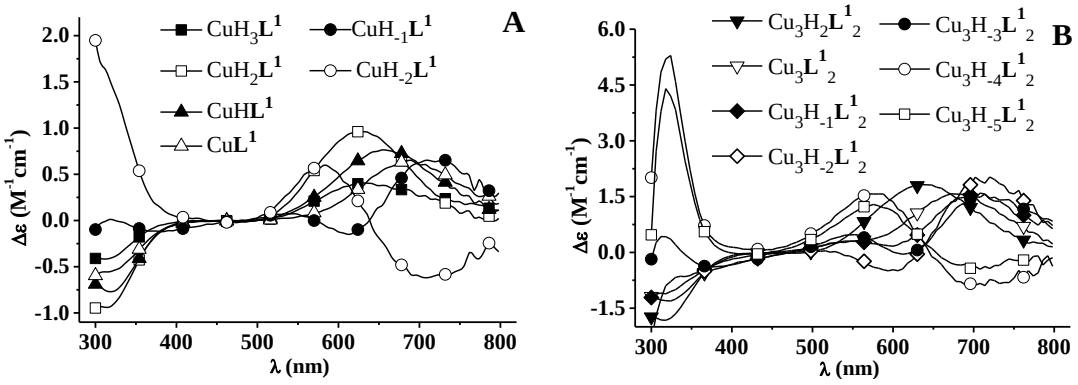

Figure IV.4. Spectres CD individuels calculés pour les complexes Cu(II)-$\mathbf{L^1}$ mononucléaires (**A**) et trinucléaires (**B**).

1.4. En présence d'excès de métal, la très stable liaison de type *bis*-histamine formée par deux bras du ligand favorise la dimérisation via le 3ème bras en complexant un troisième ion métallique. La sphère de coordination dans ces complexes métal-ligand 3:2 présente une analogie avec celle des espèces mononucléaires. Fait intéressant, ce processus devient important même dans la solution équimolaire de Zn^{2+} et $\mathbf{L^1}$; le complexe $Zn_3H_{-4}\mathbf{L^1}_2$ apparaît comme espèce majeure à pH 10 au rapport 1:1 Zn^{2+}-ligand (Figure IV.5). Les spectres de ^{1}H RMN de ce complexe présentent un ensemble de signaux d'imidazole avec un environnement chimique différent (Figure IV. 6), correspondant à des espèces échangeant leurs ligands lentement sur l'échelle de temps de la RMN. Des études de diffusion par RMN (DOSY) ont révélé que l'ensemble des pics peut être attribué à la présence de complexes oligomériques de type $Zn_{3n}H_{-x}\mathbf{L^1}_{2n}$ avec des rayons hydrodynamiques légèrement différents (Figure IV.7).

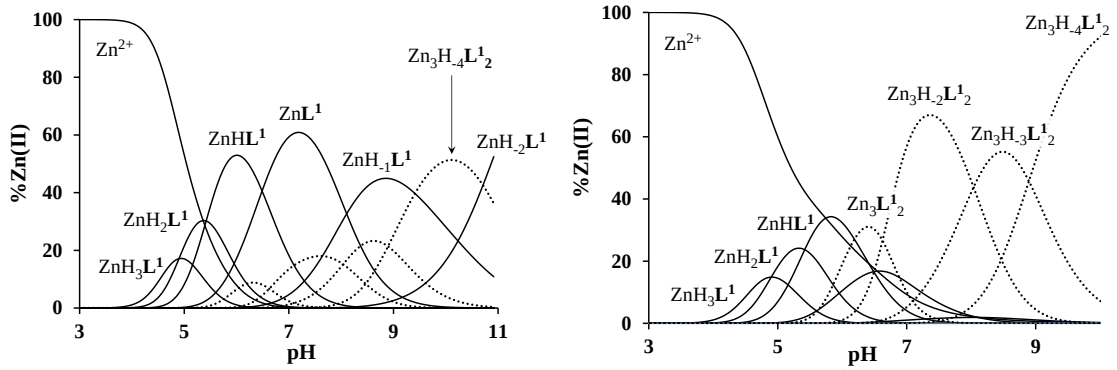

Figure IV.5. Distribution des espèces dans les systèmes Zn(II)-$\mathbf{L^1}$ 1:1 (gauche) et 3:2 (droite); $[\mathbf{L^1}]_{tot} = [Zn(II)]_{tot} = 0.001$ M et $1.5\times[\mathbf{L^1}]_{tot} = [Zn(II)]_{tot} = 0.001$ M, respectivement, $I = 0.1$ M NaCl, $T = 298$ K.

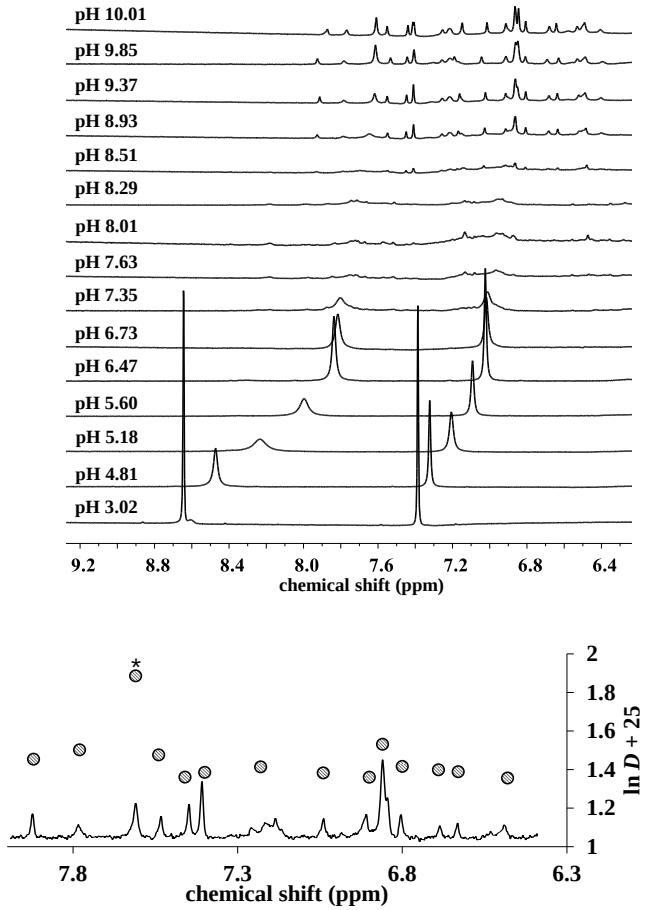

Figure IV.6. Haut : Région aromatique des spectres ^{1}H NMR en fonction du pH dans le système Zn(II)-**L^1** 3:2 (en H_2O/D_2O, $[\mathbf{L^1}]_{tot}$ = 0.0023 M, I = 0.1 M NaCl, T = 298 K). Bas : Coefficients de diffusion mesurés par ^{1}H DOSY NMR. * indique le signal C^2H du ligand libre ; le signal C^5H correspondant est mal résolu (pH = 10, $[\mathbf{L^1}]_{tot}$ = 0.0019 M, $[Zn(II)]_{tot}$ = 0.0027 M, I = 0.1 M NaCl, T = 298 K).

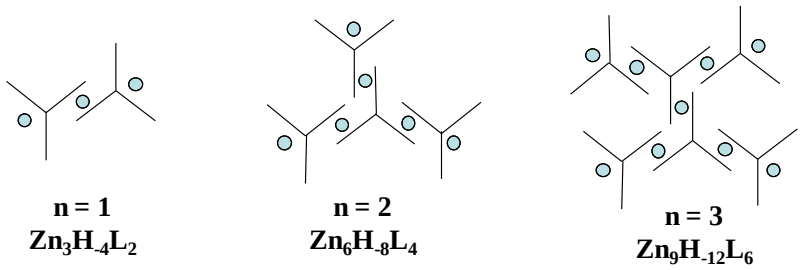

Figure IV.7. Structuration proposée pour la formation des espèces oligomères dans le système Zn(II)-**L^1** 3:2.

2. Equilibre acido-basique et étude structurale du C_3 symétriques nta3his (L^2) ligand contenant des histidines C-terminales et de ses complexes métalliques

2.1. Les processus de déprotonation du ligand impliquent les groupements carboxyliques C-terminaux et les imidazoles. Contrairement à l'acide nitrilotriacétique libre (nta), la déprotonation de l'azote tertiaire n'a pas été observée dans le domaine de pH étudié (2-10.5), probablement à cause des groupements carboxyliques plus éloignés ne permettant pas la stabilisation de l'ammonium tertiaire.

2.2. Le ligand nta3his contenant l'histidine en position C-terminale présente des propriétés de coordination très différentes vis-à-vis des ions Cu^{2+} et Zn^{2+}. Dans le système de cuivre(II)-$\mathbf{L^2}$, des complexes mono- et binucléaires ont être détectés (Figure IV.8). Les données spectroscopiques (Figure IV.9.) sont cohérentes avec une coordination de type $\{N_{tert},N^-,N_{im},O\}$ très stable (semblable au Cu(II)-Gly-His), dominant dans la solution équimolaire jusqu'à pH 10. Au-delà, cette structure se transforme en conduisant au complexe pentacoordiné $CuH_{-2}\mathbf{L^2}$ qui présente une géométrie intermédiaire entre la bipyramide à base trigonale et la pyramide à base carrée (Figure IV.10).

Puisque le mode de coordination de type Gly-His n'implique qu'un seul bras du ligand avec l'azote tertiaire, les deux autres bras histidiniques permettent la liaison d'un 2ème cuivre(II) en présence d'excès de métal; les groupes d'imidazole et carboxylique participent à cette coordination dans les zones de pH acide-neutre, tandis que les azotes amidiques prennent leur place au pH basique.

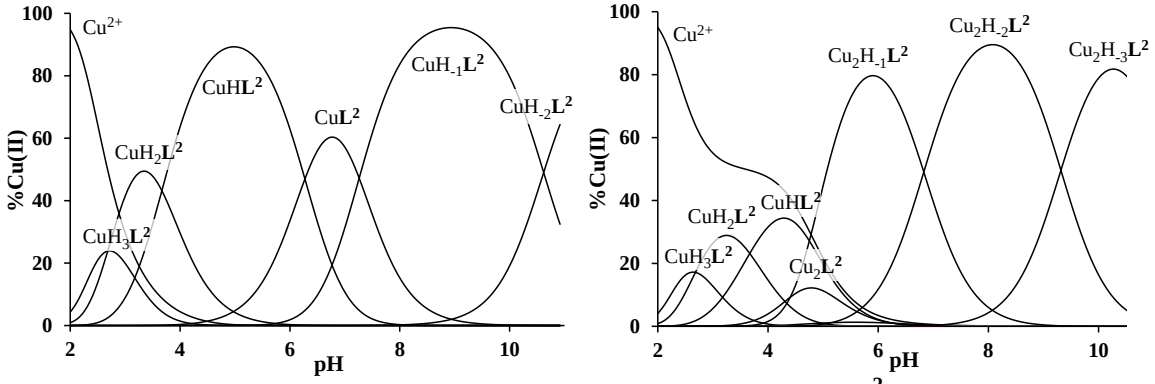

Figure IV.8. Distribution des espèces dans les systèmes Cu(II)-$\mathbf{L^2}$ 1:1 (gauche) et 2:1 (droite); $[\mathbf{L^2}]_{tot} = [Cu(II)]_{tot} = 0.001$ M et $2\times[\mathbf{L^2}]_{tot} = [Cu(II)]_{tot} = 0.001$ M, respectivement, $I = 0.1$ M NaCl, $T = 298$ K.

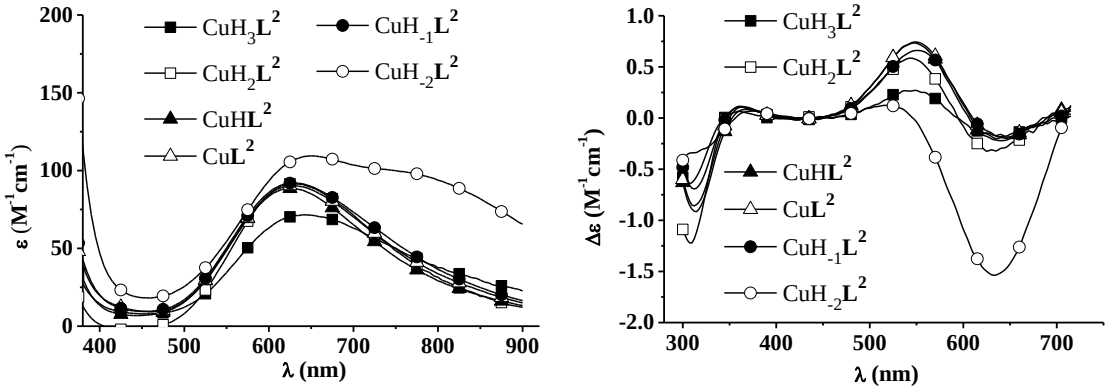

Figure IV.9. Spectres UV-Vis (gauche) et CD (droite) individuels calculés pour les complexes Cu(II)-$\mathbf{L^2}$.

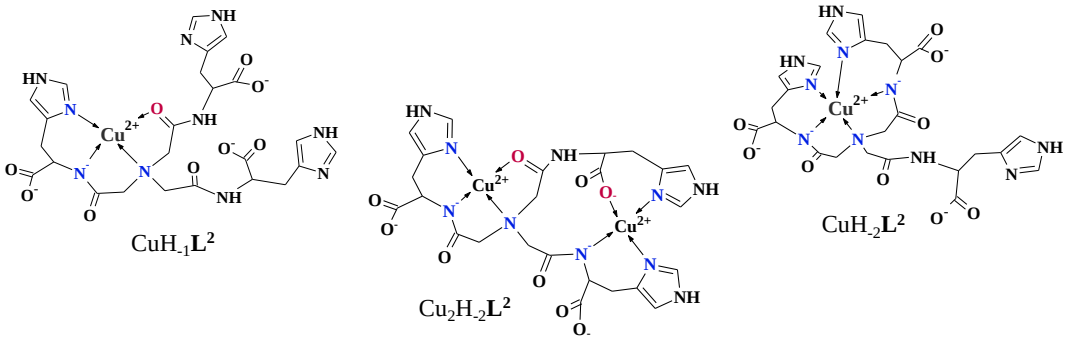

Figure IV.10. Structures proposées pour les complexes principaux de cuivre(II)-$\mathbf{L^2}$: $CuH_{-1}\mathbf{L^2}$, $CuH_{-2}\mathbf{L^2}$ et $Cu_2H_{-2}\mathbf{L^2}$.

2.3. La présence d'ions Zn^{2+} provoque la formation d'une précipité entre pH 6 et 9, même à une concentration de ligand relativement faible (~1 mM). Ce pH est trop faible pour la formation du précipité de $Zn(OH)_2$. De plus, les spectres de ^{1}H RMN enregistrés en fonction du pH ont montré une diminution significative d'intensité des signaux du ligand en montrant que le précipité correspond au complexe ligand-zinc(II). Ce phénomène peut être supprimé à l'excès de ligand (Zn^{2+}-$\mathbf{L^2}$ = 1:3,5), même si la présence de complexes *bis*-ligands n'était pas indiquée, ni par la RMN ni par des données potentiométriques. D'après des courbes de distribution simulées à un rapport métal-ligand de 1:1 (Figure IV.11), la précipitation peut être attribuée à la formation d'espèces $Zn\mathbf{L^2}$.

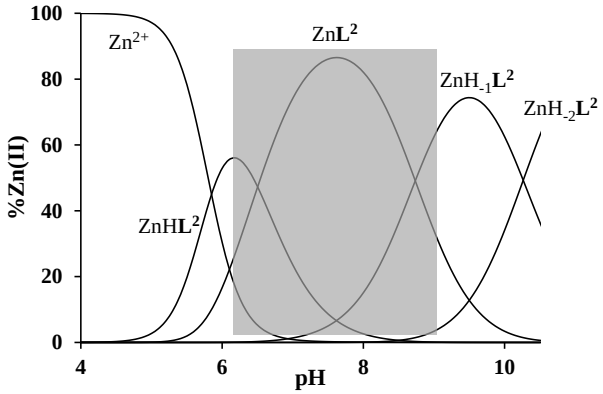

Figure IV.11. Distribution des espèces dans le système Zn(II)-$\mathbf{L^2}$ 1:1; $[\mathbf{L^2}]_{tot}$ = $[Zn(II)]_{tot}$ = 0.001 M, *I* = 0.1 M NaCl, *T* = 298 K. Champ gris indique la région du pH de précipitation.

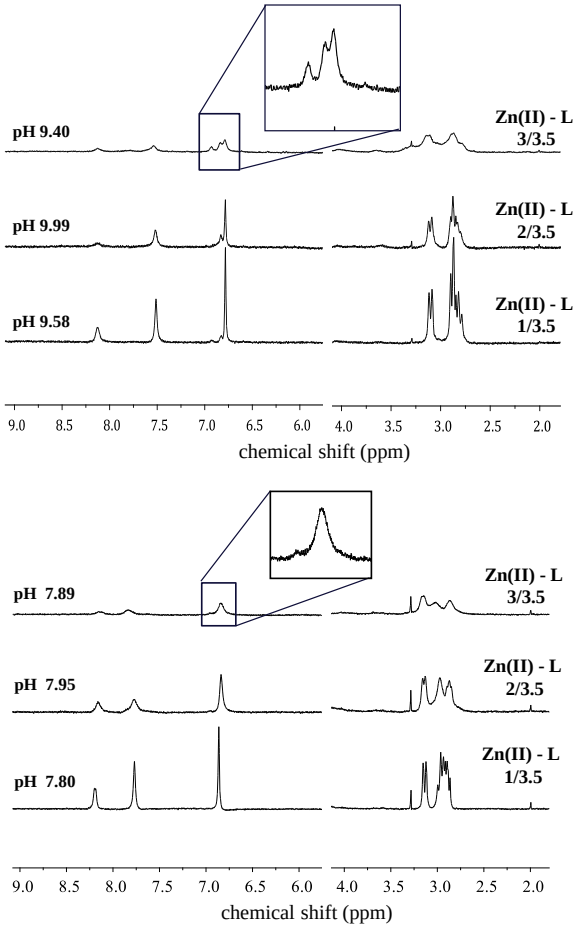

Figure IV.12. Spectres ^{1}H NMR mesurés dans le système Zn(II)-$\mathbf{L^2}$ 1:1 vers pH 10 (haut) et 8 (bas), aux rapports métal-ligand différents. $[\mathbf{L^2}]_{tot}$ = 0.0012 M, *I* = 0.1 M NaCl, *T* = 298 K.

2.4. En variant la concentration Zn^{2+} les spectres ^{1}H RMN enregistré vers pH 8 et 10 ont indiqué des vitesses différentes d'échange du ligand (Figure IV.12). En prenant compte que le dipeptide Gly-His forme l'espèce de type $\{N_{im},N^-,NH_2\}$ en présence d'ions Zn^{2+},

et en considérant la forte analogie trouvée entre les ions Cu(II)-Gly-His et Cu(II)-$\mathbf{L}^2$, renforce l'hypothèse que dans le complexe $ZnH_{-1}\mathbf{L}^2$ l'azote amidique est coordiné. Ceci explique la décélération des processus d'échange de ligands dans le domaine de pH basique. Par conséquent, dans l'espèce $Zn\mathbf{L}^2$ le métal doit être coordiné par des groupements imidazole/COO^-, ce qui conduit, probablement en raison d'oligo-/polymérisation, à une diminution significative de la solubilité.

3. Etudes thermodynamiques des ligands asymétriques nta1his et nta1his-NH_2 monofonctionnalisés contenant une histidine C-terminale libre ou protégée, et des complexes métalliques du ligand nta1his-NH_2

3.1. Des données potentiométriques ont été obtenues pour les ligands monofonctionnalisés portant une histidine, car les deux composés se sont révélés instables dans des conditions standard et leur dégradation lente n'a pu être évitée même avec un stockage soigné à basse température. Les études acido-basiques des échantillons fraîchement préparés ont révélées trois processus de déprotonation pour les deux ligands, liés à l'imidazole, à l'azote tertiaire et aux fonctions carboxyliques. Les groupements carboxyliques les plus acides se protonent seulement en dessous de pH 2.

3.2. Le ligand nta1his-NH_2 présente une spéciation très similaire avec des ions Cu^{2+} et Zn^{2+} (Figure IV.13). Le mode de coordination prédominant, de même que le système métal-$\mathbf{L}^2$, est la liaison de type Gly-His $\{N_{im},N^-,N_{tert}\}$. Cette coordination est très stable et le complexe $CuH_{-1}L$ domine plus de 7 unités de pH. Le complexe Zn(II) analogue forme plus de deux unités de pH plus élevées, car Cu^{2+} a une préférence plus importante vis-à-vis de la coordination de l'azote amidique.

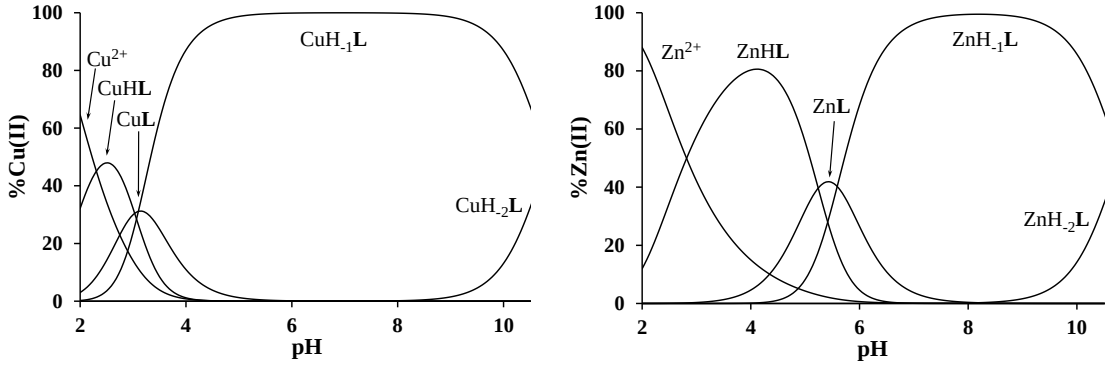

Figure IV.13. Distribution des espèces dans le système Cu(II)-nta1his-NH_2 1:1 (gauche) et Zn(II)-nta1his-NH_2 1:1 (droite) ; $[\mathbf{L}]_{tot}$ = 0.001 M, $[Cu(II)]_{tot}$ = $[Zn(II)]_{tot}$ = 0.001 M, I = 0.1 M NaCl, T = 298 K.

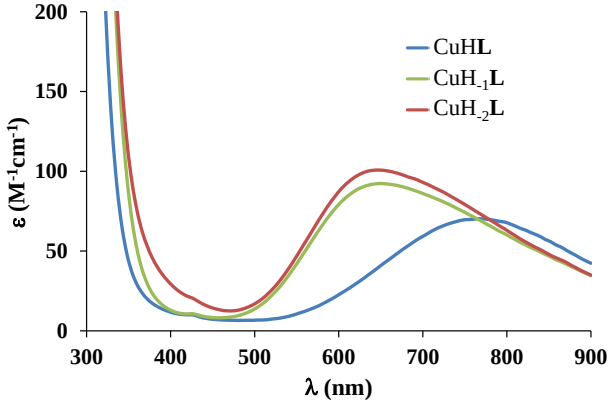

Figure IV.14. Spectres UV-Vis individuels calculés pour les complexes majeurs de Cu(II)-nta1his-NH_2.

4. Equilibre acido-basique et étude structurale du ligand tren2his (L^3) fonctionnalisé de façon asymétrique contenant des histidines N-terminales, et de ses complexes métalliques

4.1. Le ligand subit six étapes de déprotonation; la protonation du groupe amine tertiaire a également été observée, de manière unique parmi les ligands à base de tren. Les valeurs p*K* des groupements N-imidazole et N-terminal sont similaires à celles du ligand tren3his. L'amine tertiaire de type tren reste protoné en-dessous de pH 9.

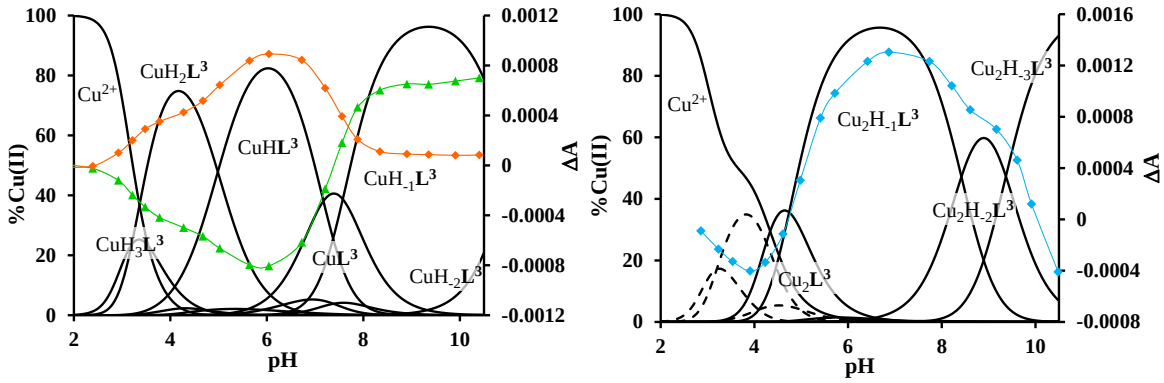

Figure IV.15. Distribution des espèces dans le système Cu(II)-L^3 1:1 (gauche) et 2:1 (droite) ; $[L^3]_{tot}$ = 0.001 M, $[Cu(II)]_{tot}$ = 0.001 M and 0.002 M, respectivement, I = 0.1 M NaCl, T = 298 K. Axe secondaire : intensités CD mesurés à 325 nm (vert et bleu) et 675 nm (orange).

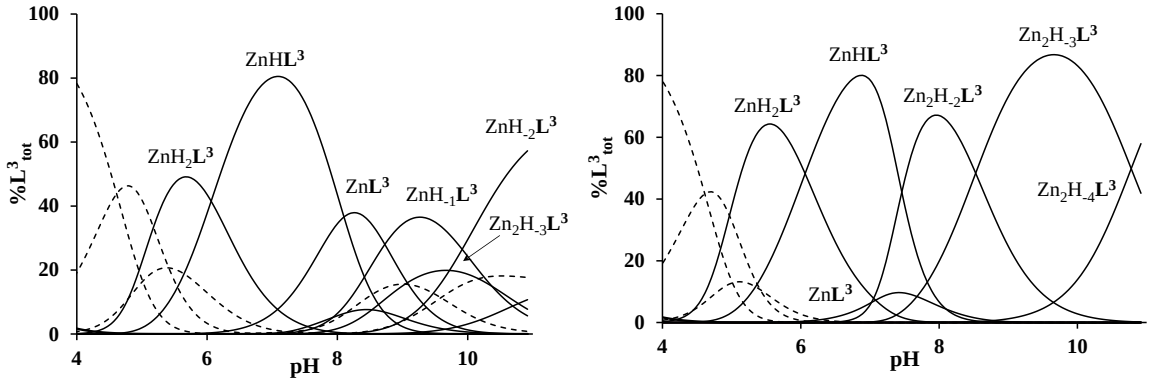

Figure IV.16. Distribution des espèces dans le système Zn(II)-$\mathbf{L}^3$ 1:1 (gauche) et 2:1 (droite) ; $[\mathbf{L}^3]_{tot}$ = 0.001 M, $[Zn(II)]_{tot}$ = 0.001 M and 0.002 M, respectivement, I = 0.1 M NaCl, T = 298 K. Les lignes pointillées représentent des espèces du ligand libre ($H_x\mathbf{L}^3$).

4.2. Nous avons observé la formation des complexes mono- et binucléaires en présence de complexes Cu^{2+} et Zn^{2+} (Figures IV.15-16). En cas du rapport 1:1 de métal-ligand, la coordination de type *bis*-histamine est prédominante jusqu'à pH neutre. A pH basique, dans des complexes formés le cuivre(II) est coordiné par des azotes amidique et tertiaire (Figure IV.17), ainsi que des complexes mixtes d'hydroxo-zinc(II) sont formés, de manière similaire aux systèmes de ligands tren3his.

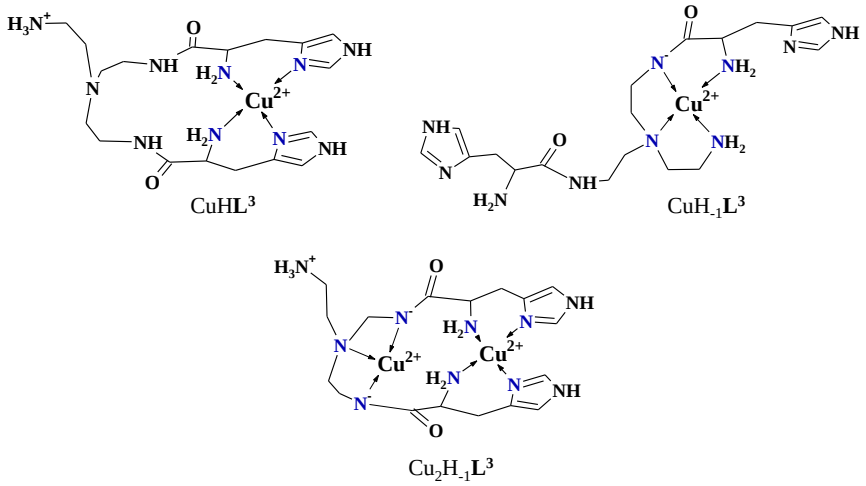

Figure IV.17. Structures proposées pour les complexes principaux de cuivre(II)-$\mathbf{L}^3$: $CuH\mathbf{L}^3$, $CuH_{-1}\mathbf{L}^3$ et $Cu_2H_{-1}\mathbf{L}^3$.

4.3. En présence d'excès de métal, les complexes binucléaires de cuivre(II) commencent à se former à partir de pH 4; l'espèce $Cu_2H_{-1}\mathbf{L}^3$ domine sur 4 unités de pH. La formation d'espèce binucléaire est liée à la présence de deux sites de coordination distincts dans la molécule: en plus du site de coordination du type *bis*-histamine, le tren NH_2 primaire,

l'amine tertiaire et les deux amides forment un 2ème site de coordination (Figure IV.18). Les complexes binucléaires de zinc(II) ainsi formés présentent une vitesse d'échange de ligand lente sur l'échelle de temps de la RMN; les spectres ont indiqué des processus de dimérisation intéressants où le cycle d'imidazole peut agir comme un pont entre deux métaux.

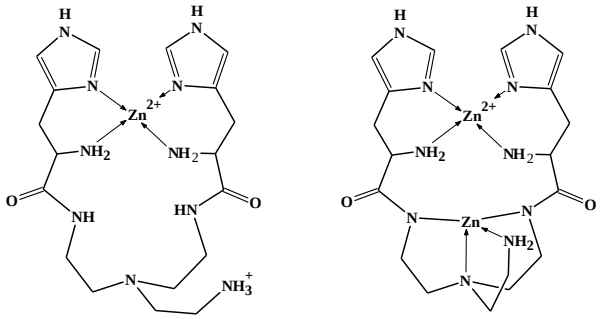

$ZnHL^3$ $Zn_2H_{-2}L^3$

Figure IV.18. Structures proposées pour les complexes $ZnHL^3$ et $Zn_2H_{-2}L^3$.

5. Equilibre acido-basique et étude structurale du ligand tren1his (L^4) fonctionnalisé de façon asymétrique contenant une histidine N-terminale, et de ses complexes métalliques

5.1. Quatre valeurs de p*K* ont été détectées pour le ligand tren1his dans le domaine de pH étudié (2-10,5), correspondant aux groupements imidazole, amine N-terminal et amine de type tren. Les p*K* des groupements analogues sont un peu plus élevés que ceux du ligand tren3his, ce qui reflète la charge globale plus faible du tren1his.

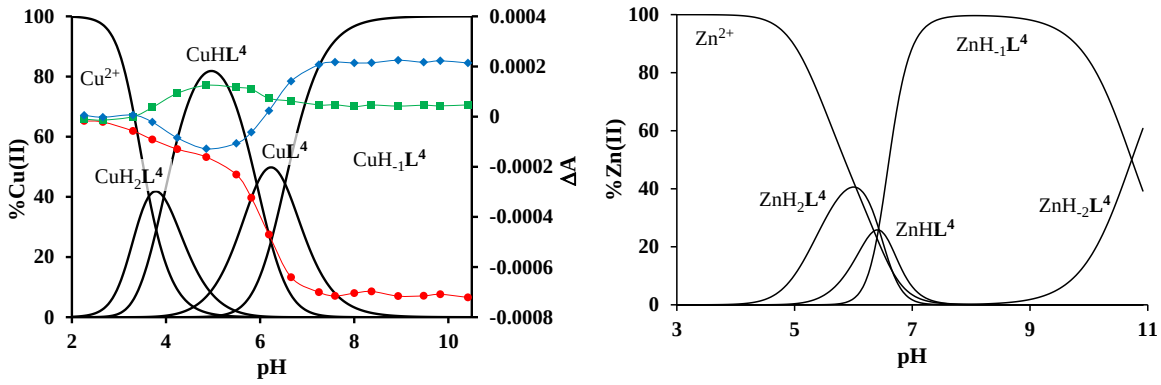

Figure IV.19. Distribution des espèces dans le système Cu(II)-L^4 1:1 (gauche) et Zn(II)- L^4 1:1 (droite) ; $[L^4]_{tot}$ = 0.001 M, $[Cu(II)]_{tot}$ = $[Zn(II)]_{tot}$ = 0.001 M, *I* = 0.1 M NaCl, *T* = 298 K.

5.2. Le ligand ne forme que des complexes mononucléaires avec les deux ions métalliques (Figure IV.19). En présence de cuivre(II), les complexes CuH**L**^{4} et CuH$_{-1}$**L**^{4} sont les espèces principales (Figure IV.20). Ce dernier est un complexe pentacoordiné de manière similaire aux complexes formé par le tren, mais la fonctionnalisation par l'histidine provoque une distorsion considérable dans la géométrie. En présence d'ions Zn^{2+}, le complexe ZnH$_{-1}$**L**^{4} analogue prédomine dans une large gamme de pH, mais les spectres de ^{1}H RMN sont étonnamment compliqués ce qui est dû à l'échange lent du ligand et aux protons CH_2 magnétiquement inéquivalents. La sphère de coordination dans le complexe MH$_{-1}$**L**^{4} est complétée par l'azote d'histidine en position axiale.

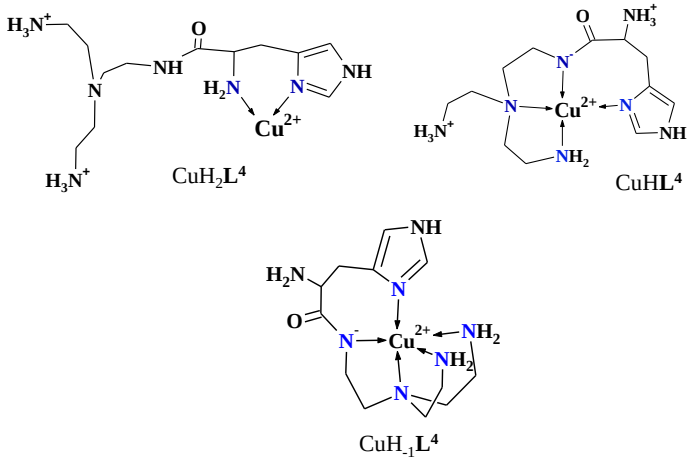

Figure IV.20. Structures proposées pour les complexes principaux de cuivre(II)-**L**^{4} : CuH$_2$**L**^{4}, CuH**L**^{4} et CuH$_{-1}$**L**^{4}.

6. Activité catécholase des complexes ligand-cuivre(II) étudiés

6.1. Nous avons observé des activités catalytiques significatives dans l'oxydation du 3,5-di-*tert*-butylcatéchol (H_2DTBC) dans le cas des complexes cuivre(II)-**L**^{1} 3:2, cuivre(II)-**L**^{2} 2:1 et cuivre(II)-**L**^{3} 2:1. La vitesse initiale de la réaction a été étudiée en détail en fonction du pH, des concentrations du substrat, du complexe et d'oxygène. Les résultats en fonction de la concentration en substrat ont montré un comportement de type saturation quel que soit le ligand (Figure IV.21), permettant appliquer le traitement cinétique enzymatique de type Michaelis-Menten (Tableau IV.1). Dans tous les cas, une cinétique de premier ordre a été déterminée concernant l'oxygène et les complexes.

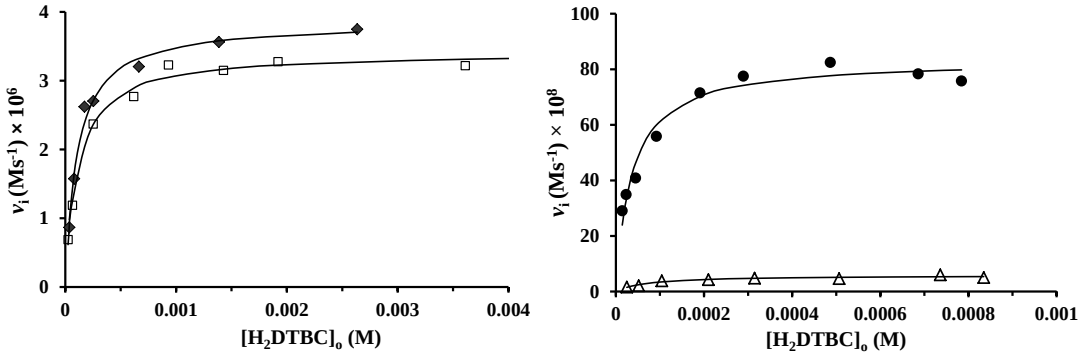

Figure IV.21. Les vitesses initiales de l'oxydation du H_2DTBC en fonction de la concentration du substrat dans les systèmes catalytiques Cu(II)-L (♦: Cu(II)-**L^1** 3:2, pH_{corr} 7.8, □: Cu(II)-**L^2** 2:1, pH_{corr} 8.9, Δ: Cu(II)-**L^3** 1:1, pH_{corr} 7.4, •: Cu(II)-**L^3** 2:1, pH_{corr} 8.7). Les lignes continues correspondent aux courbes calculées.

Tableau IV.1. L'activité catécholase de quelques systèmes cuivre(II)-L précédemment étudiés ainsi que celle de l'enzyme native.

Cu(II)-ligand systems (*pH*)	k_{cat} (s^{-1})	K_M (M)	k_{cat}/K_M ($M^{-1}s^{-1}$)	Solvent, *T* (°C)	Ref.
Cu(II)-Ac-HHGH 1:1 (*10.18*)	0.063	not rep.	not rep.	MeOH/H_2O 86/14, 25	9
Cu(II)-MDVFMKGLSKAKEGV-NH_2 1:2 (*7.4*)	0.009	1.8×10^{-3}	5.0	MeOH/H_2O 80/20, 25	37
Cu(II)-B1[a] 2:1 (*8.50*)	0.051	9.44×10^{-3}	5.47	MeOH/H_2O 97/13, 25	91
Cu(II)-B2[a] 2:1 (*8.50*)	0.0078	9.5×10^{-4}	8.1	MeOH/H_2O 97/13, 25	91
Cu(II)-B3[b] 1:2	0.00596	2.6×10^{-4}	23.37	DMF, 20	76
Cu(II)-B4[c] 2:1	0.25	6.4×10^{-3}	39.1	MeCN, 25	90
Cu(II)-L^3 1:1 (*7.4*)	**0.0056**	**7.09×10^{-5}**	**79.4**	**EtOH/H_2O 50/50, 25**	
Cu(II)-B5[d] 2:4:2	0.0426	1.45×10^{-4}	293.8	MeOH, 25	89
Cu(II)-B6[e] 2:2	2.63	5.90×10^{-3}	445.8	MeOH, not rep.	88
Cu(II)-L^1 3:2 (*7.8*)	**0.071**	**1.12×10^{-4}**	**632.1**	**EtOH/H_2O 50/50, 25**	
Cu(II)-B7[f] 2:1	1.916	1.2×10^{-3}	1597	MeCN, 25	87
Cu(II)-B8[g] 2:1 (8.0)	1.806	7.5×10^{-4}	2408	MeOH/H_2O 29/1, 20	71
Cu(II)-L^2 2:1 (*8.9*)	**0.387**	**1.07×10^{-4}**	**3625**	**EtOH/H_2O 50/50, 25**	
Cu(II)-B9[h] 2:1	9	2.3×10^{-3}	3913	MeOH, 20	68
Cu(II)-L^3 2:1 (*8.7*)	**0.157**	**3.61×10^{-5}**	**4362**	**EtOH/H_2O 50/50, 25**	
ibCO[i] (*6.5*)	2293	2.5×10^{-3}	917200	H_2O, 20	79

[a]ligand B1: *N',N'*-bis(2-pyridylmethyl)-*N*,*N*-(2-hydroxybenzyl)(2-hydroxy-3,5-di-*tert*-butylbenzyl)-1,3-propanediamin-2-ol; ligand B2: *N*-(2-hydroxybenzyl)-*N',N',N*-tris(2-pyridylmethyl)-1,3-propanediamin-2-ol
[b]ligand B3: 3-(3'-methyl-2'-pyridylimino)isoindoline-1-one (MePyOIND)
[c]ligand B4: 2,6-bis[bis(pyridin-2-ylmethylamino)methyl]-4-methylphenol (BPMP)
[d]ligand B5: naproxen (nap) and 3-picoline (3-pic)
[e]ligand B6: the copper(II) complex is referred as bis[1,2-*O*-isopropylidene-6-*N*-(3-acetylbut-3-en-2-one)amino-6-deoxyglucofuranoso]dicopper ($H_2$3a)
[f]ligand B7: $L^{1*}SSL^{1*}$
[g]ligand B8: a pyrazolate-derived compartmental ligand bearing pyridyl arms (HL^2)
[h]ligand B9: 2,6-bis(R-iminomethyl)-4-methyl-phenolato type Schiff-base ligand ($H_2L_2^2$)
[i]native enzyme isolated from *Ipomoea batatas*; kinetic parameters reported for catechol substrate

6.2. Les études mécanistiques détaillées sur les systèmes de cuivre(II)-$\mathbf{L^1}$ and -$\mathbf{L^2}$ ont révélé différentes voies réactionnelles pour l'oxydation catalytique de H_2DTBC. Dans le système cuivre(II)-$\mathbf{L^1}$ 3:2, les études de fixation du substrat ont montré la coordination d'une seule molécule de substrat malgré la présence des complexes trinucléaires. Des études de fixation de H_2DTBC réalisées en condition inerte et des mesures RPE ont prouvé que l'oxydation se déroule via la formation d'un intermédiaire radicalaire (type semiquinone), de manière similaire à d'autres complexes mononucléaires de cuivre(II) publiés dans la littérature. En revanche, le système cuivre(II)-$\mathbf{L^2}$ 2:1 effectue l'oxydation de H_2DTBC par le centre binucléaire où les cuivre(II) coopèrent, de manière similaire à la voie réactionnelle enzymatique (Figure IV.22).

6.3. Les complexes binucléaires du ligand $\mathbf{L^3}$ qui sont catalytiquement actifs présentent des capacités exceptionnellement élevées (K_M ~10^{-5} M) de fixer le substrat H_2DTBC. Par conséquent, l'efficacité catalytique globale (k_{cat}/K_M) de ce système est extrêmement élevée, dépassant même la valeur obtenue pour un complexe modèle du cuivre(II) possédant la valeur de k_{cat} la plus élevée publiée jusqu'à présent (Tableau IV.1).

6.4. Une étude comparative de l'activité catécholase entre les complexes contenant des peptides tripodaux et linéaires a été réalisée. Nous avons trouvé que l'effet d'organisation de la structure par la plateforme tripodale influence positivement la capacité des complexes de fixer le substrat, par conséquent, l'efficacité catalytique globale. La structure tripodale favorise également la formation des espèces multinucléaires qui améliore encore plus les propriétés catalytiques via l'oxydation par deux électrons.

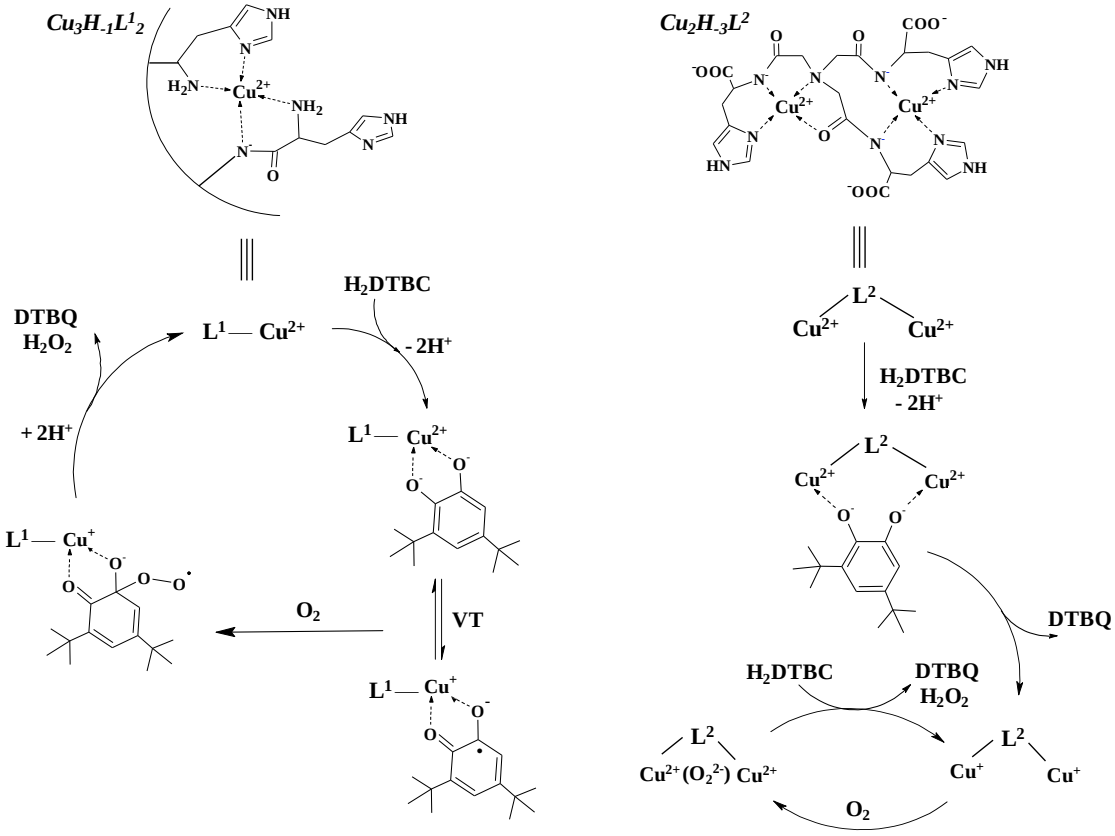

Figure IV.22. Mécanisme proposé pour l'oxydation de 3,5-di-*tert*-butylcatéchol catalysée par les systèmes cuivre(II)-**L**^{1} et -**L**^{2}.

7. Activité superoxyde dismutase des complexes ligand-cuivre (II) étudiés

7.1. À l'exception du complexe cuivre(II)-**L**^{4}, tous les systèmes ligand-cuivre(II) étudiés ont présenté des performances significatives comme mime de superoxyde dismutase (SOD) dans la réaction indirecte modifiée de McCord-Fridovich. Ils dépassent tous l'activité SOD de l'ion libre de cuivre(II). Leurs valeurs de IC_{50} sont dans la même gamme que celles déterminées dans les systèmes peptidique linéaires-cuivre(II) contenant de l'histidine; cependant, leur activité est près de deux ordres de grandeur plus faible que celle du Cu,Zn-SOD.

Publications liées au contenu de la thèse

(1) **Á. Dancs**, N. May, K. Selmeczi, Zs. Darula, A. Szorcsik, F. Matyuska, T. Páli, T. Gajda: *Tuning the coordination properties of multi-histidine peptides by using a tripodal scaffold: solution chemical study and catechol oxidase mimicking*
New J. Chem., **2017**, *41*, 808-823. IF: 3,277

(2) Gajda T., Szorcsik A., **Dancs Á.**, Matyuska F.: *Polidentát tripodális ligandumok biomimetikus fémkomplexei*
Magyar Kémiai Folyóirat, **2017**, *123 (2)*, 94-100. IF: -

(3) **Á. Dancs**, K. Selmeczi, I. Bányai, Zs. Darula, T. Gajda: *Increasing the histidine 'density' in tripodal peptides by gradual N-functionalization of tris(2-aminoethyl)amine (tren) with L-histidyl units: The effect on zinc(II) complexes*
Inorg. Chim. Acta, **2017*, in press*** (DOI: 10.1016/j.ica.2017.06.049) IF: 2,002

(4) **Á. Dancs**, K. Selmeczi, N. May, T. Gajda: *On the copper(II) binding of asymmetrically functionalized tripodal peptides: solution equilibrium, structure, and enzyme mimicking*
New J. Chem., ***manuscrit accepté*** IF: 3,269

(5) **Á. Dancs**, K. Selmeczi, D. Árus, D. Szunyogh, T. Gajda: *Catechol oxidase and SOD mimicking by copper(II) complexes of multihistidine peptides*
Int. J. Pept. Res. Ther., **2017*, in press*** (DOI: 10.1007/s10989-017-9645-x) IF: 0,904

LIST OF REFERENCES

[1] Z. Dai and J. W. Canary, *New J. Chem.* **31** (2007), 1708-1718.
[2] M. Suzuki, *Acc. Chem. Res.* **40** (2007), 609-617.
[3] N. Burzlaff, *Adv. Inorg. Chem.* **60** (2008), 101-165.
[4] G. Parkin, *New J. Chem.* **31** (2007), 1996-2014.
[5] W. A. Chomitz and J. Arnold, *Chem. Eur. J.* **15** (2009), 2020-2030.
[6] X. Hu and K. Meyer, *J. Organomet. Chem.* **690** (2005), 5474-5484.
[7] G. Rapenne, *Inorg. Chim. Acta* **362** (2009), 4276-4283.
[8] S. Tartaggia, O. De Lucchi, A. Gambaro, R. Zangrando, F. Fabris and A. Scarso, *Chem. Eur. J.* **19** (2013), 5701-5714.
[9] K. J. C. van Bommel, C. van der Pol, I. Muizebelt, A. Friggeri, A. Heeres, A. Meetsma, B. L. Feringa and J. van Esch, *Angew. Chem., Int. Ed.* **43** (2004), 1663-1667.
[10] A. Timme, R. Kress, R. Q. Albuquerque and H.-W. Schmidt, *Chem. Eur. J.* **18** (2012), 8329-8339.
[11] A. G. Blackman, *Polyhedron* **24** (2005), 1-39.
[12] R. R. Schrock, *Acc. Chem. Res.* **30** (1997), 9-16.
[13] L. H. Gade, *Acc. Chem. Res.* **35** (2002), 575-582.
[14] A. G. Blackman, *Eur. J. Inorg. Chem.* (2008), 2633-2647.
[15] E. Ristenpart, *Berichte* **29** (1896), 2526-2533.
[16] A. W. Addison, T. N. Rao, J. Reedijk, J. van Rijn and G. C. Verschoor, *J. Chem. Soc., Dalton Trans.* (1984), 1349-1356.
[17] H. Keypour, M. Dehdari, S. Salehzadeh and K. P. Wainwright, *Transit. Metal Chem.* **28** (2003), 425-429.
[18] H. Keypour, M. Dehdari and S. Salehzadeh, *Asian J. Chem.* **14** (2002), 856-866.
[19] A. D. P. Paoletti and A. Vacca, *Inorg. Chem.* **7** (1968), 865-870.
[20] W. Heintz, *Liebigs Ann. Chem.* **122** (1862), 257-294.
[21] V. L. Hughes and A. E. Martell, *J. Am. Chem. Soc.* **78** (1956), 1319-1324.
[22] G. Anderegg, *Pure Appl. Chem.* **54** (1982), 2693-2758.
[24] R. Puchta, N. van Eikema Hommes, R. Meier and R. van Eldik, *Dalton Trans.* (2006), 3392-3395.
[25] H. B. Albada, F. Soulimani, B. M. Weckhuysen and R. M. J. Liskamp, *Chem. Comm.* (2007), 4895-4897.
[26] C. Guarise, G. Zaupa, L. J. Prins and P. Scrimin, *Eur. J. Org. Chem.* (2008), 3559-3568.
[27] S. Blanc, P. Yakirevitch, E. Leize, M. Meyer, J. Libman, A. Van Dorsselaer, A.-M. Albrecht-Gary and A. Shanzer, *J. Am. Chem. Soc.* **119** (1997), 4934-4944.
[28] A.-S. Jullien, C. Gateau, I. Kieffer, D. Testemale and P. Delangle, *Inorg. Chem.* **52** (2013), 9954-9961.
[29] M. Gelinsky, R. Vogler and H. Vahrenkamp, *Inorg. Chem.* **41** (2002), 2560-2564.
[30] M. M. Ibrahim and G. A. M. Mersal, *J. Inorg. Biochem.* **104** (2010), 1195-1204.
[31] U. Herr, W. Spahl, G. Trojandt, W. Steglich, F. Thaler and R. van Eldik, *Bioorg. Med. Chem.* **7** (1999), 699-707.
[32] M. M. Ibrahim, N. Shimomura, K. Ichikawa and M. Shiro, *Inorg. Chim. Acta* **313** (2001), 125-136.
[33] A. M. Pujol, C. Gateau, C. Lebrun and P. Delangle, *J. Am. Chem. Soc.* **131** (2009), 6928-6929.
[34] A. M. Pujol, C. Gateau, C. Lebrun and P. Delangle, *Chem. Eur. J.* **17** (2011), 4418-4428.

[35] A.-S. Jullien, C. Gateau, C. Lebrun and P. Delangle, *Inorg. Chem.* **54** (2015), 2339-2344.
[36] A.-S. Jullien, C. Gateau, C. Lebrun, I. Kieffer, D. Testemale and P. Delangle, *Inorg. Chem.* **53** (2014), 5229-5239.
[37] Ł. Szyrwiel, Ł. Szczukowski, J. S. Pap, B. Setner, Z. Szewczuk and W. Malinka, *Inorg. Chem.* **53** (2014), 7951-7959.
[38] L. Szyrwiel, J. S. Pap, L. Szczukowski, Z. Kerner, J. Brasun, B. Setner, Z. Szewczuk and W. Malinka, *RSC Adv.* **5** (2015), 56922-56931.
[39] L. Szyrwiel, D. Lukacs, D. F. Sranko, Z. Kerner, A. Kotynia, J. Brasun, B. Setner, Z. Szewczuk, K. Malec and J. S. Pap, *RSC Adv.* **7** (2017), 24657-24666.
[40] A. Messadi, A. Mohamadou, I. Déchamp-Olivier and L. Dupont, *J. Coord. Chem.* **65** (2012), 2442-2458.
[41] C. Kállay, K. Várnagy, G. Malandrinos, N. Hadjiliadis, D. Sanna and I. Sóvágó, *Inorg. Chim. Acta* **362** (2009), 935-945.
[42] I. Sóvágó and K. Ősz, *Dalton Trans.* (2006), 3841-3854.
[43] D. Árus, N. V. Nagy, Á. Dancs, A. Jancsó, R. Berkecz and T. Gajda, *J. Inorg. Biochem.* **126** (2013), 61-69.
[44] I. Sóvágó, E. Farkas and A. Gergely, *J. Chem. Soc., Dalton Trans.* (1982), 2159-2163.
[45] E. Farkas, I. Sóvágó and A. Gergely, *J. Chem. Soc., Dalton Trans.* (1983), 1545-1551.
[46] M. Förster and H. Vahrenkamp, *Chem. Ber.* **128** (1995), 541-550.
[47] C. Eicken, F. Zippel, K. Büldt-Karentzopoulos and B. Krebs, *FEBS Lett.* **436** (1998), 293-299.
[48] T. Klabunde, C. Eicken, J. C. Sacchettini and B. Krebs, *Nat. Struct. Mol. Biol.* **5** (1998), 1084-1090.
[49] C. Eicken, B. Krebs and J. C. Sacchettini, *Curr. Opin. Struct. Biol.* **9** (1999), 677-683.
[50] A. Rompel, H. Fischer, D. Meiwes, K. Büldt-Karentzopoulos, R. Dillinger, F. Tuczek, H. Witzel and B. Krebs, *J. Biol. Inorg. Chem.* **4** (1999), 56-63.
[51] R. Than, A. A. Feldmann and B. Krebs, *Coord. Chem. Rev.* **182** (1999), 211-241.
[52] I. A. Koval, P. Gamez, C. Belle, K. Selmeczi and J. Reedijk, *Chem. Soc. Rev.* **35** (2006), 814-840.
[53] K. Selmeczi, M. Réglier, M. Giorgi and G. Speier, *Coord. Chem. Rev.* **245** (2003), 191-201.
[54] S. K. Dey and A. Mukherjee, *Coord. Chem. Rev.* **310** (2016), 80-115.
[55] R. Wegner, M. Gottschaldt, W. Poppitz, E.-G. Jäger and D. Klemm, *J. Mol. Catal. A: Chem.* **201** (2003), 93-118.
[56] I. A. Koval, K. Selmeczi, C. Belle, C. Philouze, E. Saint-Aman, I. Gautier-Luneau, A. M. Schuitema, M. van Vliet, P. Gamez, O. Roubeau, M. Lüken, B. Krebs, M. Lutz, A. L. Spek, J.-L. Pierre and J. Reedijk, *Chem. Eur. J.* **12** (2006), 6138-6150.
[57] E. Monzani, L. Quinti, A. Perotti, L. Casella, M. Gullotti, L. Randaccio, S. Geremia, G. Nardin, P. Faleschini and G. Tabbì, *Inorg. Chem.* **37** (1998), 553-562.
[58] W. M. Tay, J. D. Epperson, G. F. Z. da Silva and L.-J. Ming, *J. Am. Chem. Soc.* **132** (2010), 5652-5661.
[59] A. Santra, G. Mondal, M. Acharjya, P. Bera, A. Panja, T. K. Mandal, P. Mitra and P. Bera, *Polyhedron* **113** (2016), 5-15.
[60] F. Wendt, C. Näther and F. Tuczek, *J. Biol. Inorg. Chem.* **21** (2016), 777-792.
[61] K. Masahito, K. Tomohisa, K. Koji, T. Yoshimitsu, I. Shinobu and K. Shosuke, *Bull. Chem. Soc. Jpn.* **76** (2003), 1957-1964.

[62] Á. Kupán, J. Kaizer, G. Speier, M. Giorgi, M. Réglier and F. Pollreisz, *J. Inorg. Biochem.* **103** (2009), 389-395.
[63] M. J. Gajewska, W.-M. Ching, Y.-S. Wen and C.-H. Hung, *Dalton Trans.* **43** (2014), 14726-14736.
[64] J. Kaizer, T. Csay, G. Speier and M. Giorgi, *J. Mol. Catal. A: Chem.* **329** (2010), 71-76.
[65] A. Jancsó, Z. Paksi, N. Jakab, B. Gyurcsik, A. Rockenbauer and T. Gajda, *Dalton Trans.* (2005), 3187-3194.
[66] A. Granata, E. Monzani and L. Casella, *J. Biol. Inorg. Chem.* **9** (2004), 903-913.
[67] J. Ackermann, S. Buchler and F. Meyer, *CR Chim.* **10** (2007), 421-432.
[68] E. C. M. Ording-Wenker, M. A. Siegler, M. Lutz and E. Bouwman, *Dalton Trans.* **44** (2015), 12196-12209.
[69] R. Wegner, M. Gottschaldt, H. Görls, E.-G. Jäger and D. Klemm, *Chem. Eur. J.* **7** (2001), 2143-2157.
[70] T. Csay, B. Kripli, M. Giorgi, J. Kaizer and G. Speier, *Inorg. Chem. Comm.* **13** (2010), 227-230.
[71] K. S. Banu, T. Chattopadhyay, A. Banerjee, S. Bhattacharya, E. Suresh, M. Nethaji, E. Zangrando and D. Das, *Inorg. Chem.* **47** (2008), 7083-7093.
[72] S. Torelli, C. Belle, S. Hamman, J.-L. Pierre and E. Saint-Aman, *Inorg. Chem.* **41** (2002), 3983-3989.
[73] I. Monte-Pérez, A. M. Sosa, S. Bernès, N. Aliaga-Alcalde, V. M. Ugalde-Saldívar and L. Gasque, *Eur. J. Inorg. Chem.* (2012), 4739-4749.
[74] A. Patra, G. C. Giri, T. K. Sen, L. Carrella, S. K. Mandal and M. Bera, *Polyhedron* **67** (2014), 495-504.
[75] A. Guha, T. Chattopadhyay, N. D. Paul, M. Mukherjee, S. Goswami, T. K. Mondal, E. Zangrando and D. Das, *Inorg. Chem.* **51** (2012), 8750-8759.
[76] J. Kaizer, J. Pap, G. Speier, L. Párkányi, L. Korecz and A. Rockenbauer, *J. Inorg. Biochem.* **91** (2002), 190-198.
[77] D. Dey, G. Kaur, A. Ranjani, L. Gayathri, P. Chakraborty, J. Adhikary, J. Pasan, D. Dhanasekaran, A. R. Choudhury, M. A. Akbarsha, N. Kole and B. Biswas, *Eur. J. Inorg. Chem.* (2014), 3350-3358.
[78] S. Pal, B. Chowdhury, M. Patra, M. Maji and B. Biswas, *Spectrochim. Acta A* **144** (2015), 148-154.
[79] E. Monzani, L. Casella, G. Zoppellaro, M. Gullotti, R. Pagliarin, R. P. Bonomo, G. Tabbi, G. Nardin and L. Randaccio, *Inorg. Chim. Acta* **282** (1998), 180-192.
[80] S. Dell'Acqua, V. Pirota, C. Anzani, M. M. Rocco, S. Nicolis, D. Valensin, E. Monzani and L. Casella, *Metallomics* **7** (2015), 1091-1102.
[81] W. M. Tay, A. I. Hanafy, A. Angerhofer and L.-J. Ming, *Bioorg. Med. Chem. Lett.* **19** (2009), 6709-6712.
[82] S. Timári, R. Cerea and K. Várnagy, *J. Inorg. Biochem.* **105** (2011), 1009-1017.
[83] J. M. McCord and I. Fridovich, *J. Biol. Chem.* **244** (1969), 6049-6055.
[84] S. Durot, C. Policar, F. Cisnetti, F. Lambert, J.-P. Renault, G. Pelosi, G. Blain, H. Korri-Youssoufi and J.-P. Mahy, *Eur. J. Inorg. Chem.* (2005), 3513-3523.
[85] G. Csire, J. Demjén, S. Timári and K. Várnagy, *Polyhedron* **61** (2013), 202-212.
[86] M. Ciuffi, C. Cellai, S. Franchi-Micheli, L. Zilletti, M. Ginanneschi, M. Chelli, A. M. Papini and F. Paoletti, *Pharmacol. Res.* **38** (1998), 279-287.
[87] M. L. Pires dos Santos, A. Faljoni-Alário, A. S. Mangrich and A. M. d. Costa Ferreira, *J. Inorg. Biochem.* **71** (1998), 71-78.
[88] D. Árus, A. Jancsó, D. Szunyogh, F. Matyuska, N. V. Nagy, E. Hoffmann, T. Körtvélyesi and T. Gajda, *J. Inorg. Biochem.* **106** (2012), 10-18.

[89] P. Stańczak and H. Kozowski, *Biochem. Bioph. Res. Co.* **352** (2007), 198-202.
[90] Z. Paksi, A. Jancsó, F. Pacello, N. Nagy, A. Battistoni and T. Gajda, *J. Inorg. Biochem.* **102** (2008), 1700-1710.
[91] B. Bóka, A. Myari, I. Sóvágó and N. Hadjiliadis, *J. Inorg. Biochem.* **98** (2004), 113-122.
[92] T. Gajda, Y. Düpre, I. Török, J. Harmer, A. Schweiger, J. Sander, D. Kuppert and K. Hegetschweiler, *Inorg. Chem.* **40** (2001), 4918-4927.
[93] B. Bauer-Siebenlist, F. Meyer, E. Farkas, D. Vidovic and S. Dechert, *Chem. Eur. J.* **11** (2005), 4349-4360.
[94] A. Jancsó, I. Török, K. Hegetschweiler and T. Gajda, *Arkivoc* (2009), 217-224.
[95] T. Gajda, R. Krämer and A. Jancsó, *Eur. J. Inorg. Chem.* (2000), 1635-1644.
[96] D. M. Shendage, R. Fröhlich and G. Haufe, *Org. Lett.* **6** (2004), 3675-3678.
[97] L. A. Carpino and A. El-Faham, *Tetrahedron* **55** (1999), 6813-6830.
[98] M. C. F. Monnee, A. J. Brouwer and R. M. J. Liskamp, *QSAR Comb. Sci.* **23** (2004), 546-559.
[99] E. Kaiser, R. L. Colescott, C. D. Bossinger and P. I. Cook, *Anal. Biochem.* **34** (1970), 595-598.
[100] F. J. C. Rosotti and H. Rosotti, *The determination of stability constants*, McGraw-Hill Book Co. (1962).
[101] E. Högfeldt, *Stability Constants of Metal-Ion Complexes, Part A. Inorganic Ligands*, Pergamon (1982).
[102] L. Zékány, I. Nagypál and G. Peintler, *PSEQUAD for chemical equilibria*, Technical Software Distributors (1991).
[103] E. J. Billo, *Inorg. Nucl. Chem. Lett.* **10** (1974), 613-617.
[104] H. Sigel and R. B. Martin, *Chem. Rev.* **82** (1982), 385-426.
[105] L. D. Pettit, J. E. Gregor and H. Kozlowski, *Perspectives on Bioinorganic Chemistry*, JAI Press (1991).
[106] E. Prenesti, P. G. Daniele, M. Prencipe and G. Ostacoli, *Polyhedron* **18** (1999), 3233-3241.
[107] E. Prenesti, P. G. Daniele, S. Berto and S. Toso, *Polyhedron* **25** (2006), 2815-2823.
[108] A. Rockenbauer, T. Szabó-Plánka, Z. Árkosi and L. Korecz, *J. Am. Chem. Soc.* **123** (2001), 7646-7654.
[109] A. Rockenbauer and L. Korecz, *Appl. Magn. Reson.* **10** (1996), 29-43.
[110] R. G. Bates, M. Paabo and R. A. Robinson, *J. Phys. Chem. US* **67** (1963), 1833-1838.
[111] L. G. Hepler, E. M. Woolley and D. G. Hurkot, *J. Phys. Chem. US* **74** (1970), 3908-3913.
[112] D. R. Lide, *CRC Handbook of Chemistry and Physics, 88th edn*, Taylor and Francis (2007-2008).
[113] B. H. J. Bielski and H. W. Richter, *J. Am. Chem. Soc.* **99** (1977), 3019-3023.
[114] I. Török, T. Gajda, B. Gyurcsik, G. K. Tóth and A. Péter, *J. Chem. Soc. Dalton Trans.* (1998), 1205-1212.
[115] I. Sóvágó, *Metal complexes of peptides and their derivatives, Biocoordination Chemistry ed. K. Burger, Ellis Horwood, Chichester* (1990).
[116] T. Gajda, B. Henry, A. Aubry and J.-J. Delpuech, *Inorg. Chem.* **35** (1996), 586-593.
[117] B. Gyurcsik, I. Vosekalna and E. Larsen, *J. Inorg. Biochem.* **85** (2001), 89-98.
[118] N. I. Jakab, B. Gyurcsik, T. Körtvélyesi, I. Vosekalna, J. Jensen and E. Larsen, *J. Inorg. Biochem.* **101** (2007), 1376-1385.
[119] A. P. Garnett and J. H. Viles, *J. Biol. Chem.* **278** (2003), 6795-6802.

[120] E. Aronoff-Spencer, C. S. Burns, N. I. Avdievich, G. J. Gerfen, J. Peisach, W. E. Antholine, H. L. Ball, F. E. Cohen, S. B. Prusiner and G. L. Millhauser, *Biochemistry* **39** (2000), 13760-13771.
[121] P. Lubal, M. r. Kývala, P. Hermann, J. Holubová, J. Rohovec, J. Havel and I. Lukeš, *Polyhedron* **20** (2001), 47-55.
[122] G. Greiner, L. Seyfarth, W. Poppitz, R. Witter, U. Sternberg and S. Reissmann, *Lett. Pept. Sci.* **7** (2000), 133-141.
[123] K. Ősz, K. Várnagy, H. Süli-Vargha, D. Sanna, G. Micera and I. Sóvágó, *Dalton Trans.* (2003), 2009-2016.
[124] A. Myari, G. Malandrinos, Y. Deligiannakis, J. C. Plakatouras, N. Hadjiliadis, Z. Nagy and I. Sóvágó, *J. Inorg. Biochem.* **85** (2001), 253-261.
[125] Q. H. Chen, L. Chen, F. L. Jiang and M. C. Hong, *Chem. Rec.* **15** (2015), 711-727.
[126] D. L. Rabenstein, S. A. Daignault, A. A. Isab, A. P. Arnold and M. M. Shoukry, *J. Am. Chem. Soc.* **107** (1985), 6435-6439.
[127] S. Bruni, F. Cariati, P. G. Daniele and E. Prenesti, *Spectrochim. Acta A* **56** (2000), 815-827.
[128] T. Gajda, B. Henry and J.-J. Delpuech, *J. Chem. Soc., Dalton Trans.* (1993), 1301-1306.
[129] D.-H. Lee, N. N. Murthy and K. D. Karlin, *Inorg. Chem.* **36** (1997), 5785-5792.
[130] G. Facchin, M. H. Torre, E. Kremer, E. J. Baran, A. Mombrú, H. Pardo, M. P. Araujo, A. A. Batista and A. J. Costa-Filho, *Inorg. Chim. Acta* **355** (2003), 408-413.
[131] T. Gajda, B. Henry and J.-J. Delpuech, *Inorg. Chem.* **34** (1995), 2455-2460.
[132] K. Selmeczi, P. Gizzi, D. Champmartin, P. Rubini, E. Aubert, S. Dahaoui and B. Henry, *Inorg. Chem.* **49** (2010), 8222-8229.
[133] I. Sóvágó, C. Kállay and K. Várnagy, *Coord. Chem. Rev.* **256** (2012), 2225-2233.
[134] E. Farkas, I. Sóvágó, T. Kiss and A. Gergely, *J. Chem. Soc., Dalton Trans.* (1984), 611-614.
[135] N. Hakulinen, C. Gasparetti, H. Kaljunen, K. Kruus and J. Rouvinen, *J. Biol. Inorg. Chem.* **18** (2013), 917-929.
[136] R. E. H. M. B. Osório, R. A. Peralta, A. J. Bortoluzzi, V. R. de Almeida, B. Szpoganicz, F. L. Fischer, H. Terenzi, A. S. Mangrich, K. M. Mantovani, D. E. C. Ferreira, W. R. Rocha, W. Haase, Z. Tomkowicz, A. d. Anjos and A. Neves, *Inorg. Chem.* **51** (2012), 1569-1589.
[137] S. J. Smith, C. J. Noble, R. C. Palmer, G. R. Hanson, G. Schenk, L. R. Gahan and M. J. Riley, *J. Biol. Inorg. Chem.* **13** (2008), 499-510.
[138] S. Caglar, E. Adiguzel, B. Sariboga, E. Temel and O. Buyukgungor, *J. Coord. Chem.* **67** (2014), 670-683.
[139] C. A. Tyson, *J. Biol. Chem.* **250** (1975), 1765-1770.
[140] J. Kaizer, Z. Zsigmond, I. Ganszky, G. Speier, M. Giorgi and M. Réglier, *Inorg. Chem.* **46** (2007), 4660-4666.
[141] M. J. Sever and J. J. Wilker, *Dalton Trans.* (2004), 1061-1072.
[142] D. G. Brown, W. J. Hughes and G. Knerr, *Inorg. Chim. Acta* **46** (1980), 123-126.
[143] C. A. Tyson and A. E. Martell, *J. Am. Chem. Soc.* **90** (1968), 3379-3386.
[144] G. Speier, Z. Tyeklár, P. Tóth, E. Speier, S. Tisza, A. Rockenbauer, A. M. Whalen, N. Alkire and C. G. Pierpont, *Inorg. Chem.* **40** (2001), 5653-5659.
[145] P. J. Donoghue, A. K. Gupta, D. W. Boyce, C. J. Cramer and W. B. Tolman, *J. Am. Chem. Soc.* **132** (2010), 15869-15871.
[146] K. J. Reszka and C. F. Chignell, *J. Am. Chem. Soc.* **115** (1993), 7752-7760.
[147] A. Neves, L. M. Rossi, A. J. Bortoluzzi, B. Szpoganicz, C. Wiezbicki, E. Schwingel, W. Haase and S. Ostrovsky, *Inorg. Chem.* **41** (2002), 1788-1794.

[148] J. Ackermann, F. Meyer, E. Kaifer and H. Pritzkow, *Chem. Eur. J.* **8** (2002), 247-258.
[149] D. Árus, Á. Dancs, N. V. Nagy and T. Gajda, *Dalton Trans.* **42** (2013), 12031-12040.
[150] N. I. Jakab, A. Jancsó, T. Gajda, B. Gyurcsik and A. Rockenbauer, *J. Inorg. Biochem.* **102** (2008), 1438-1448.
[151] C. Hureau, V. Balland, Y. Coppel, P. L. Solari, E. Fonda and P. Faller, *J. Biol. Inorg. Chem.* **14** (2009), 995-1000.
[152] G. Facchin, N. Veiga, M. G. Kramer, A. A. Batista, K. Várnagy, E. Farkas, V. Moreno and M. H. Torre, *J. Inorg. Biochem.* **162** (2016), 52-61.
[153] L. L. Costanzo, G. de Guidi, S. Giuffrida, E. Rizzarelli and G. Vecchio, *J. Inorg. Biochem.* **50** (1993), 273-281.
[154] T. Gajda, A. Jancsó, S. Mikkola, H. Lonnberg and H. Sirges, *J. Chem. Soc. Dalton Trans.* (2002), 1757-1763.

ACKNOWLEDGEMENTS

I am grateful to the head of Department of Inorganic and Analytical Chemistry, Dr. Gábor Galbács, as well as the leader of the Bioinorganic Research Group, Prof. Tamás Kiss, for allowing me to carry out my PhD work in their laboratories at the University of Szeged. Equally, I thank Prof. Philippe Gros for accepting me as doctoral student in his group of Laboratoire Structure et Réactivité des Systèmes Moléculaires Complexes (SRSMC UMR 7565), in the University of Lorraine. I wish to acknowledge the financial support provided by the French Government and Campus France, enabling my co-tutelle PhD program.

I wish to express my gratitude to my main supervisor, Prof. Tamás Gajda, who assisted in my scientific development since my second undergraduate year. His advice and scientific knowledge accompanied and helped me along my doctoral years. He spent considerable amount of his time on the interpretation and discussion of my results, would that be either for presentations, papers or my BSc/Master/PhD thesis.

I am thankful to Prof. Bernard Henry and Dr. Florence Dumarçay, my supervisors from the University of Lorraine, for accepting the direction of my PhD thesis, as well as for their advice, corrections and opinions.

My deepest gratitude goes to my co-supervisor, Dr. Katalin Selmeczi. Her joining in the direction of my work was a real inspiration; I am thankful for her valuable help around my experiments, as well as for the scientific discussions and the corrections of papers and manuscripts. Her assistance and support was imperative in the months of my stay in Nancy, not to mention her huge contribution to my improvement regarding French language.

Many thanks to all our scientific partners in the University of Szeged, the Biological Research Centre in Szeged (Dr. Zsuzsanna Darula, Dr. Tibor Páli), the University of Debrecen (Dr. István Bányai) and the University of Lorraine (Dr. André Merlin, Dr. Gabriel Krier, Lionel Vernex-Loset, Sophie Poinsignon, Fabien Lachaud, Pascal Lemière). I am especially thankful to Dr. Nóra May from the Hungarian Academy of Science, for her help in the EPR measurements and evaluations, and also to Stéphane Parant, for his technical help in the laboratory concerning my experiments.

I owe thanks to my family, highlighting my mother, and my partner, Balázs. Their continuous support gave me strength even in the hardest moments. I wish to thank the invigorating presence of my friends, especially: Gergely Samu, Attila Kormányos, Nóra Grecsó, Gabriella Fiser and Fernanda Haffner. Every single coffee/tea/pizza we've had together contributed to this work! Finally, thank you all, fellows in the PhD room, for the laughs and chats: Orsi, Ria, Edit, Dani, Levi, Feri. You of all people know the best the joys and hardship of this journey.

APPENDIX

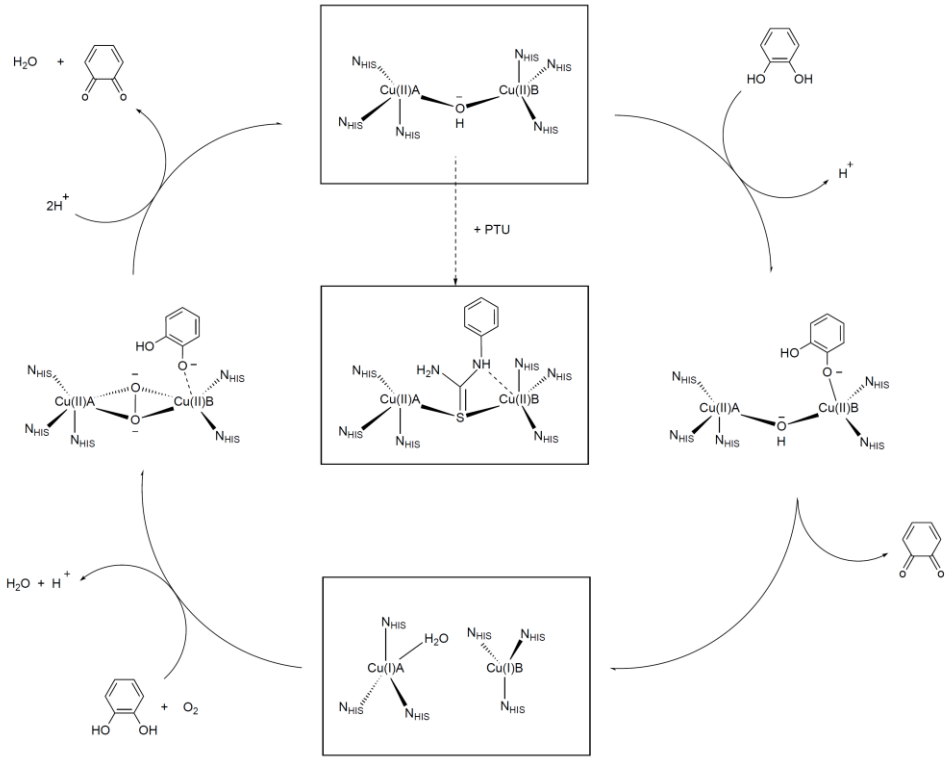

A.1. Catalytic cycle of catechol oxidase isolated from sweet potato *(Ipomoea batatas)*, as proposed by Krebs and co-workers [49]. Boxes indicate structurally characterized steps.

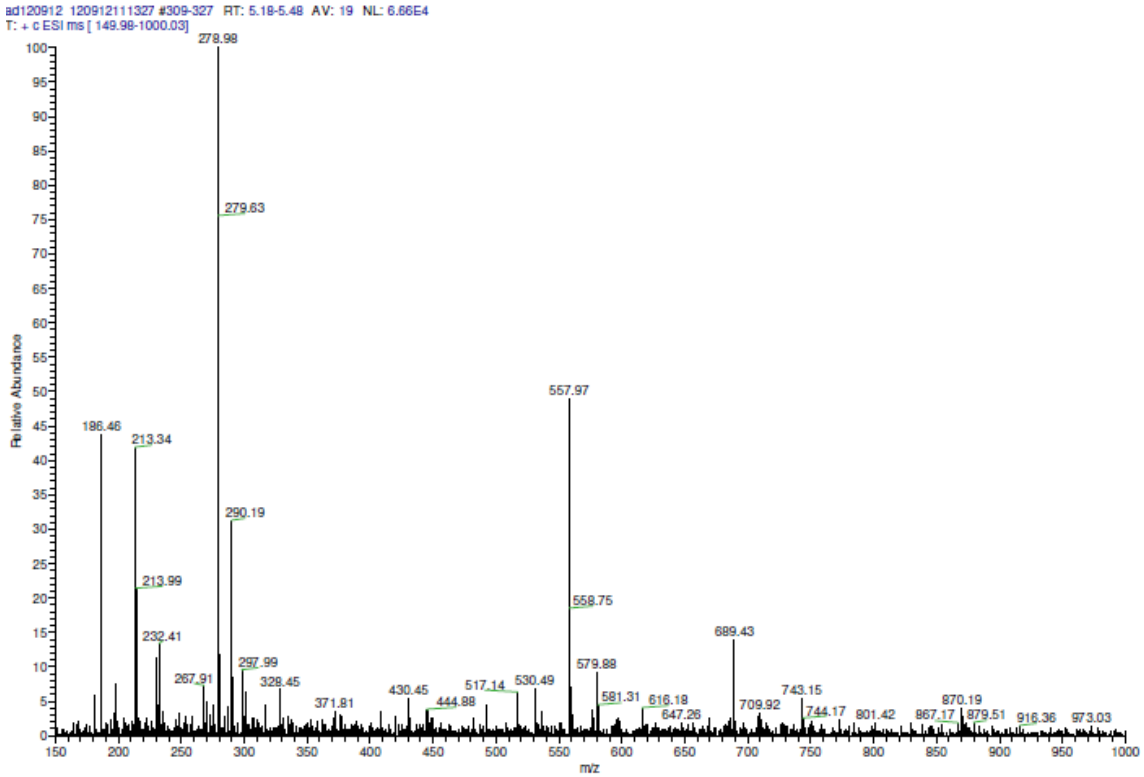

A.2. ESI-MS spectrum of the ligand tren3his (**L**[1]); *m/z* values of 557.97, 279.99 and 186.46 correspond to $[M + H]^+$, $[M + 2H]^{2+}$ and $[M + 3H]^{3+}$, respectively.

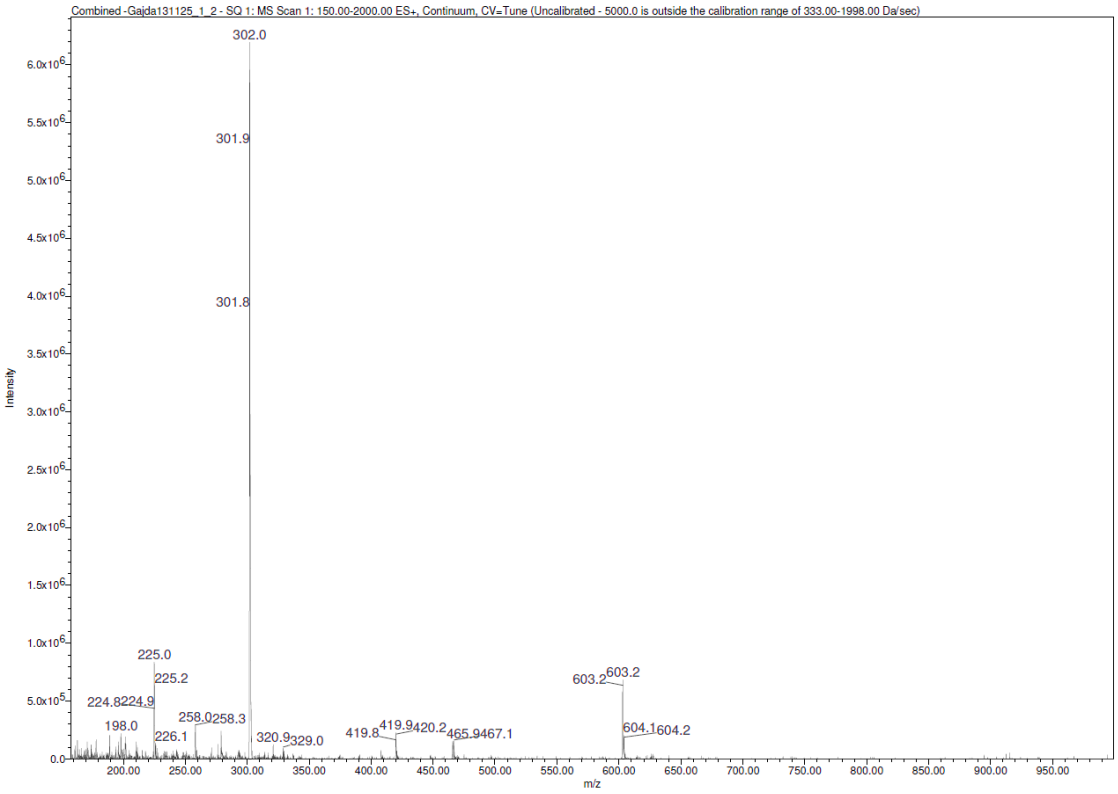

A.3. ESI-MS spectrum of the ligand nta3his (**L**^{2}); *m/z* values of 603.2 and 302.0 correspond to $[M + H]^{+}$ and $[M + 2H]^{2+}$, respectively.

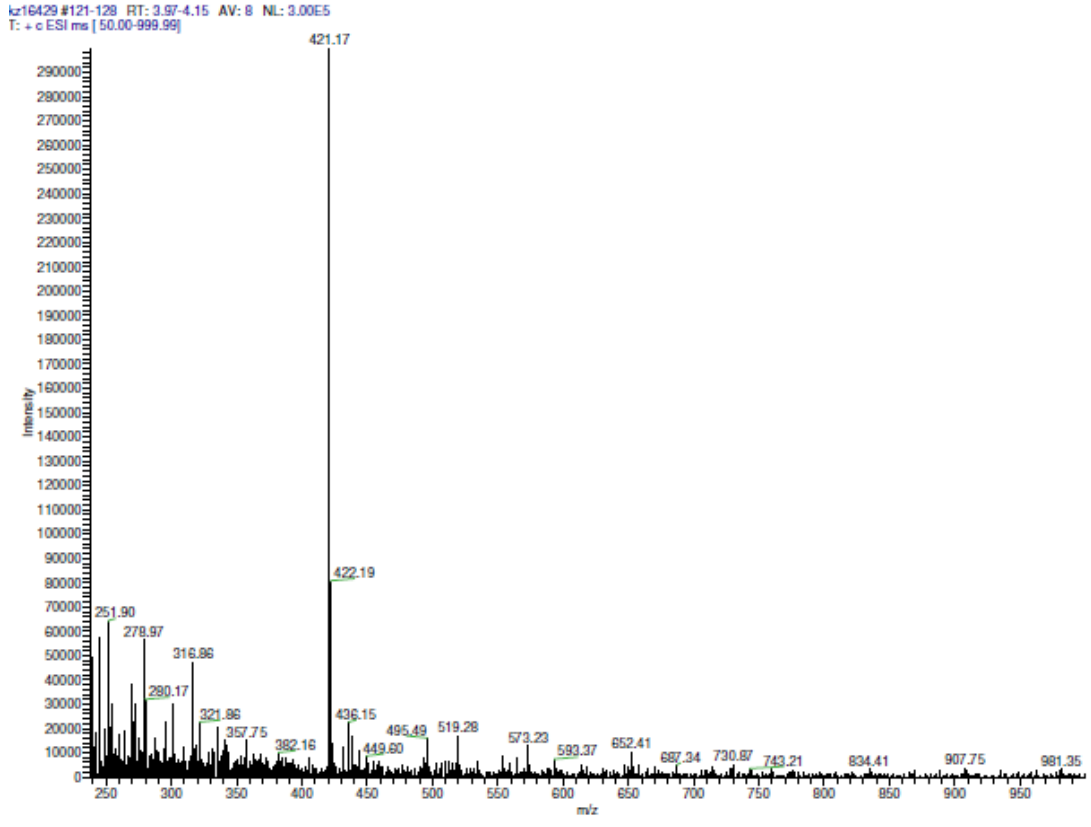

A.4. ESI-MS spectrum of the ligand tren2his (**L**^{3}): *m/z* value 421.17 corresponds to $[M+H]^{+}$.

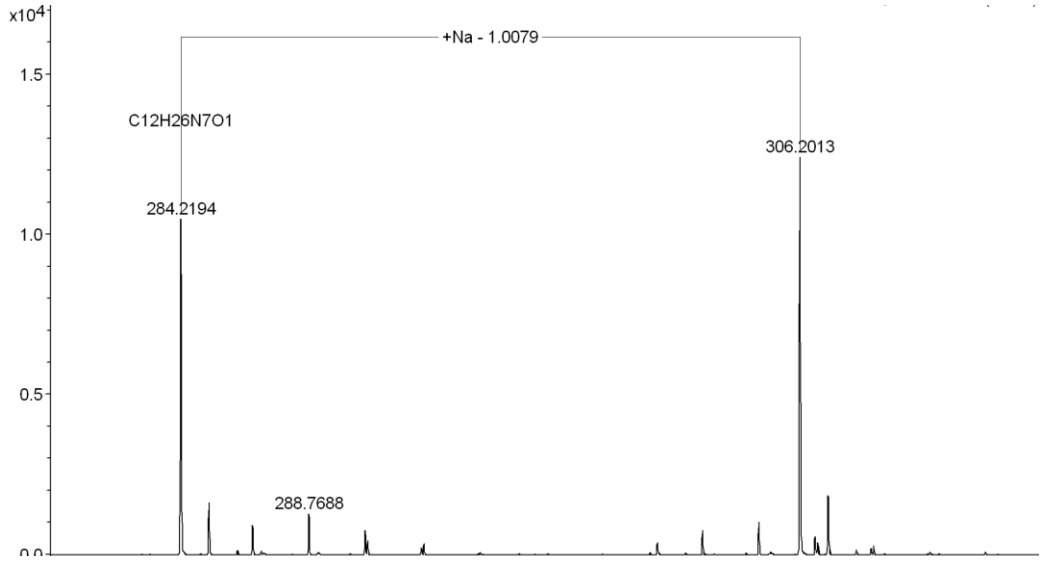

A.5. ESI-MS spectrum of the ligand tren1his ($\mathbf{L^4}$): *m/z* values 284.22 and 306.20 correspond to $[M+H]^+$ and $[M+Na^+]^+$, respectively.

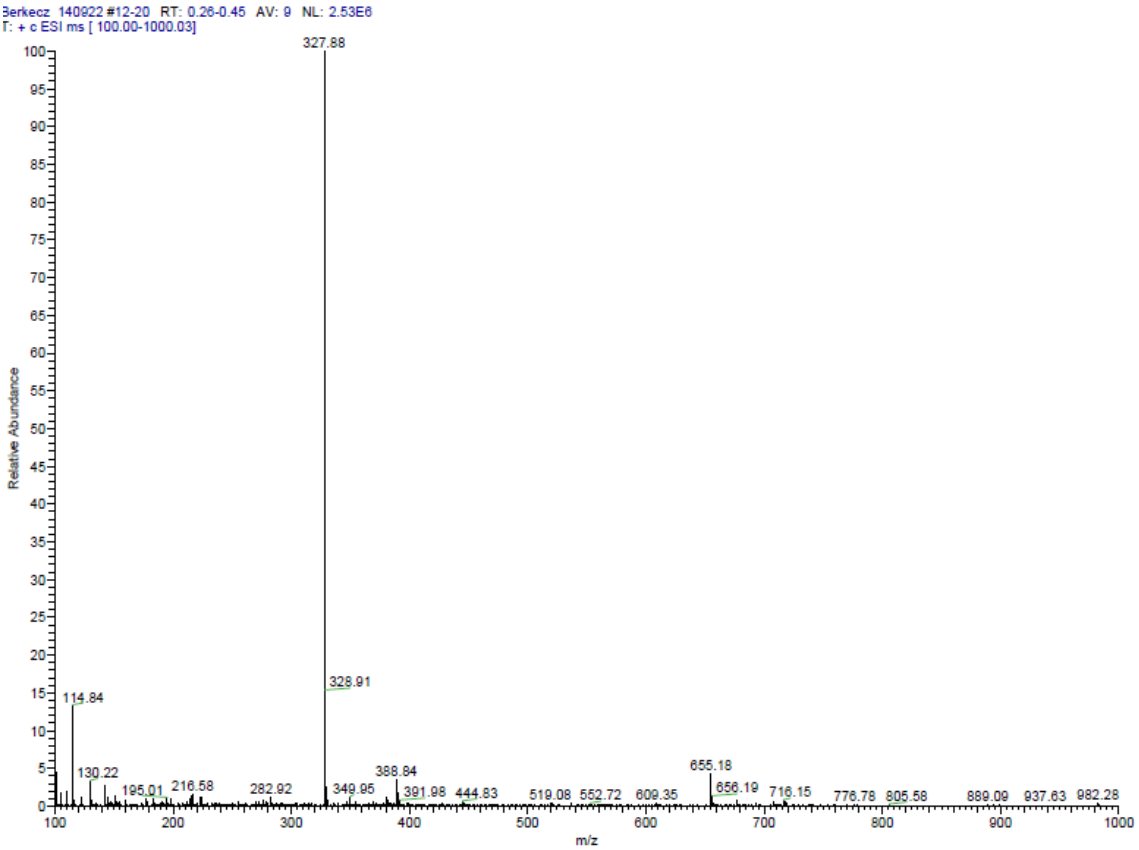

A.6. ESI-MS spectrum of the ligand nta1his-NH_2: *m/z* value 327.88 corresponds to $[M+H]^+$.

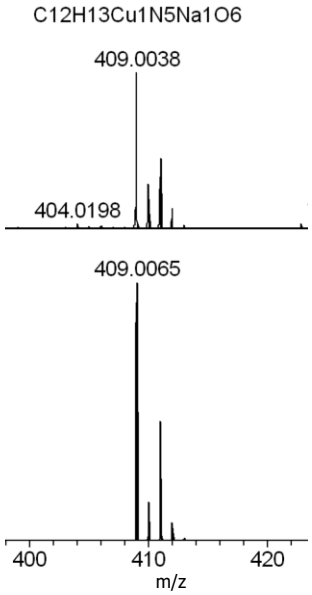

A.7. Measured (up) and calculated (down) ESI-MS spectrum of Cu(II)-nta1his-NH_2 1:1 complex: *m/z* value 409.0 corresponds to $[CuH_{-2}L+Na^+]^-$.

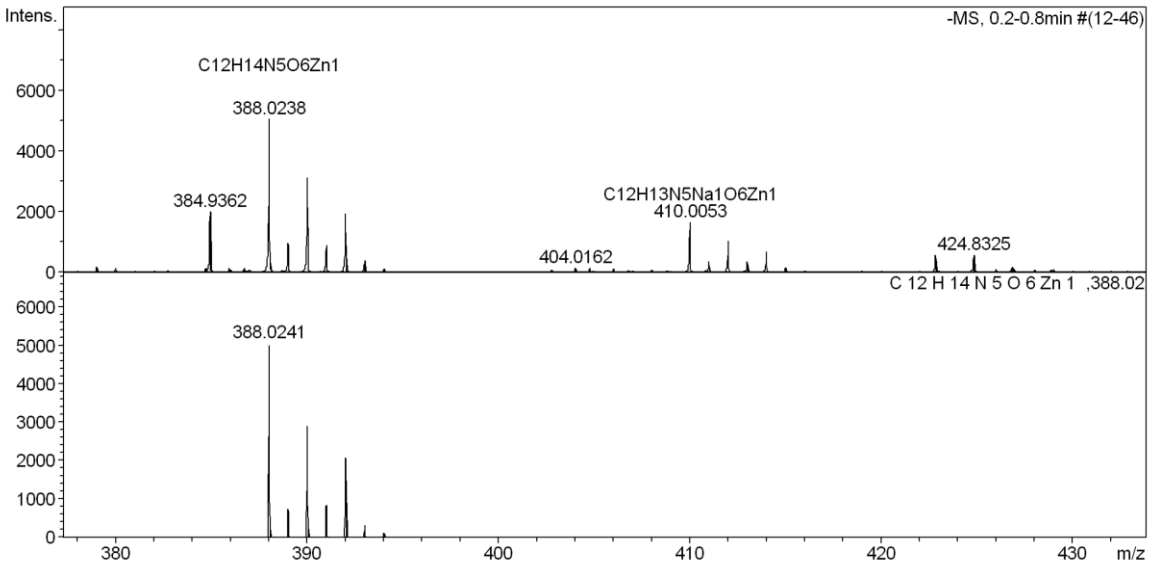

A.8. Measured (up) and calculated (down) ESI-MS spectrum of Zn(II)-nta1his-NH_2 1:1 complex: *m/z* values 388.0 and 410.0 correspond to$[ZnH_{-1}L]^-$ and $[ZnH_{-2}L+Na^+]^-$, respectively.

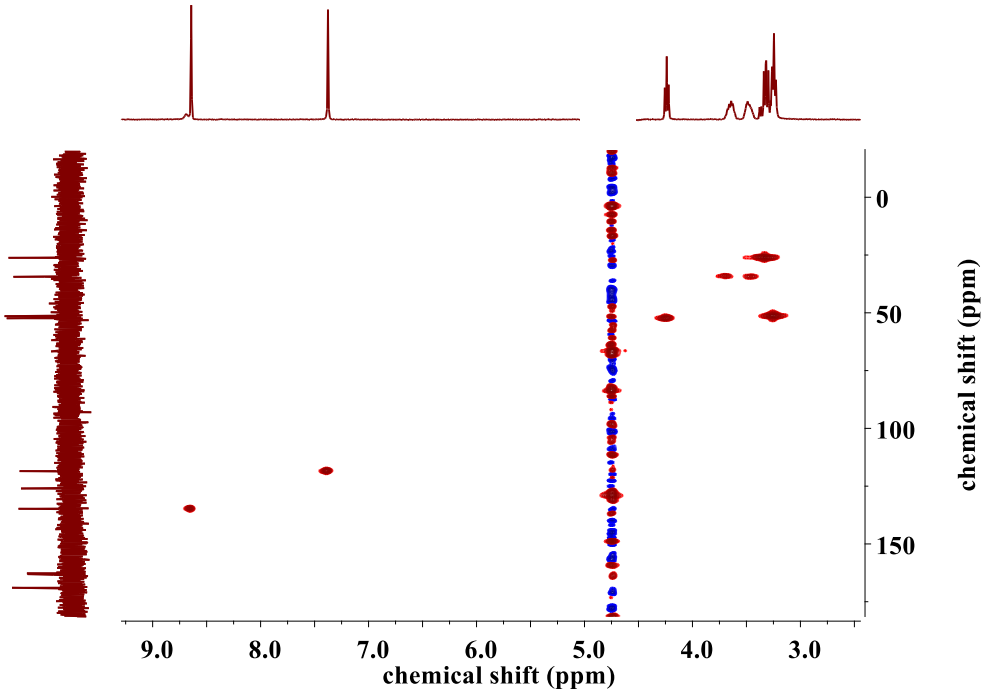

A.9. HMQC spectrum of tren3his (**L**[1]); in H_2O/D_2O 50%-50% solvent, pH 3.21, internal reference: acetonitrile (δ = 2.00 ppm).

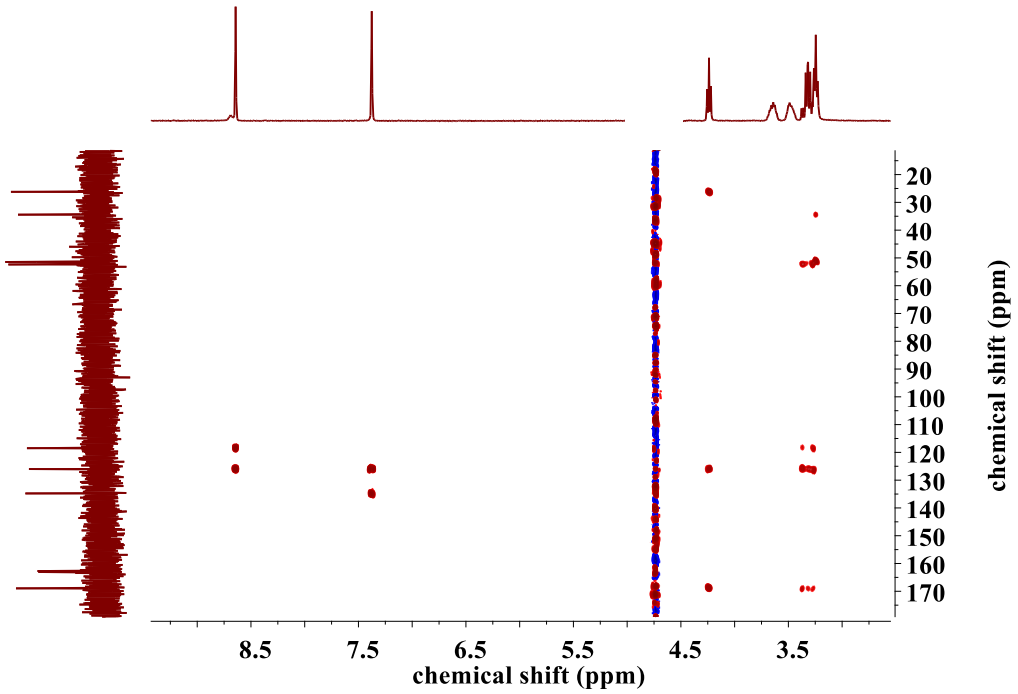

A.10. HMBC spectrum of tren3his (**L**[1]); in H_2O/D_2O 50%-50% solvent, pH 3.21, internal reference: acetonitrile (δ = 2.00 ppm).

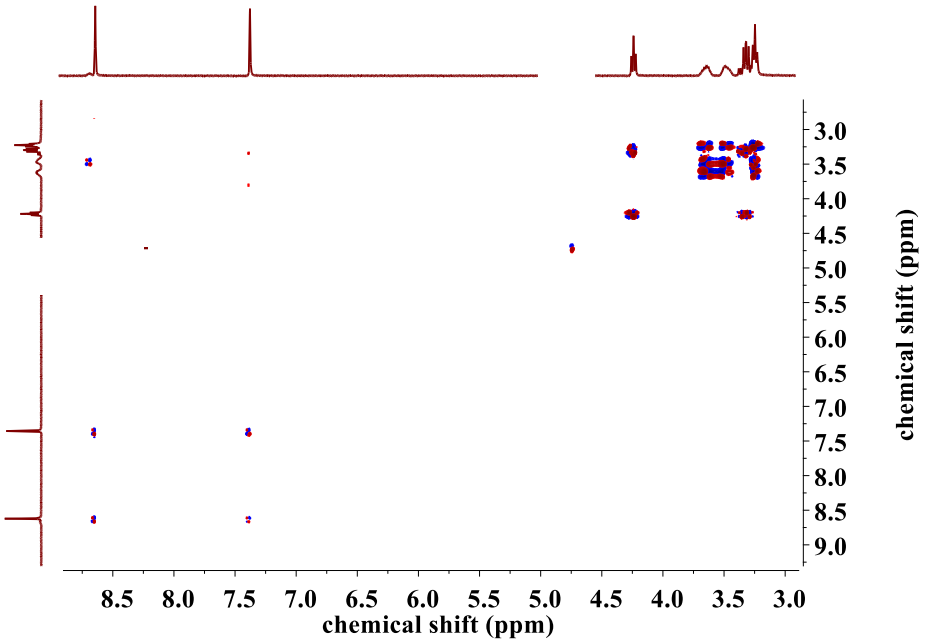

A.11. COSY spectrum of tren3his ($\mathbf{L}^1$); in H_2O/D_2O 50%-50% solvent, pH 3.21, internal reference: acetonitrile (δ = 2.00 ppm).

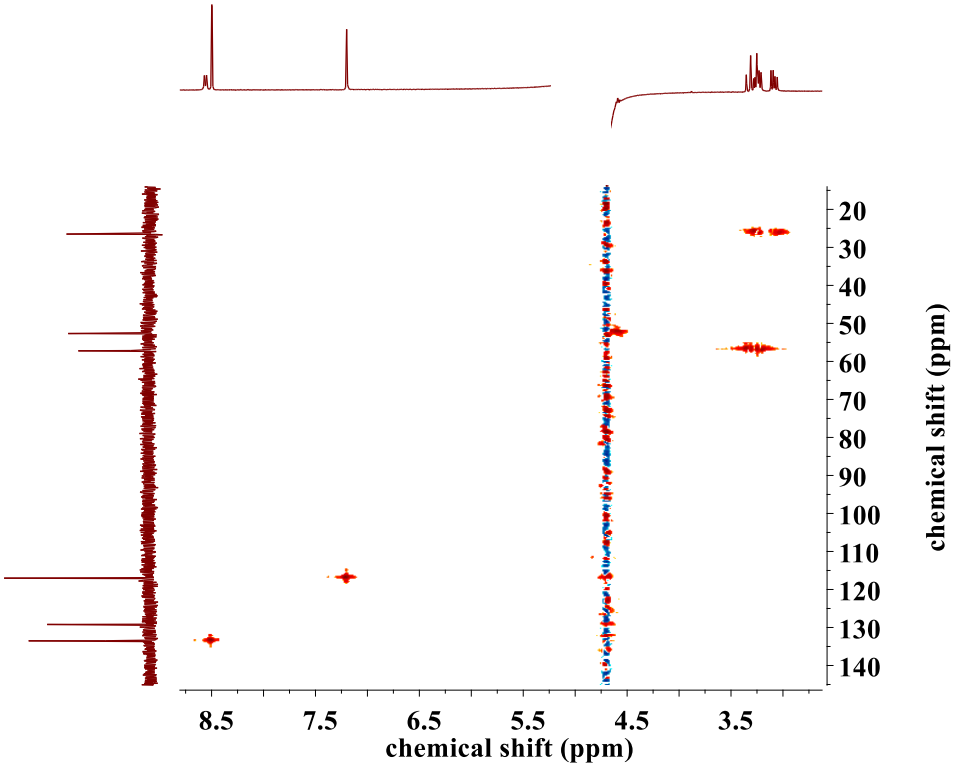

A.12. HMQC spectrum of nta3his ($\mathbf{L}^2$); in H_2O/D_2O 50%-50% solvent, pH 2.80, internal reference: acetonitrile (δ = 2.00 ppm).

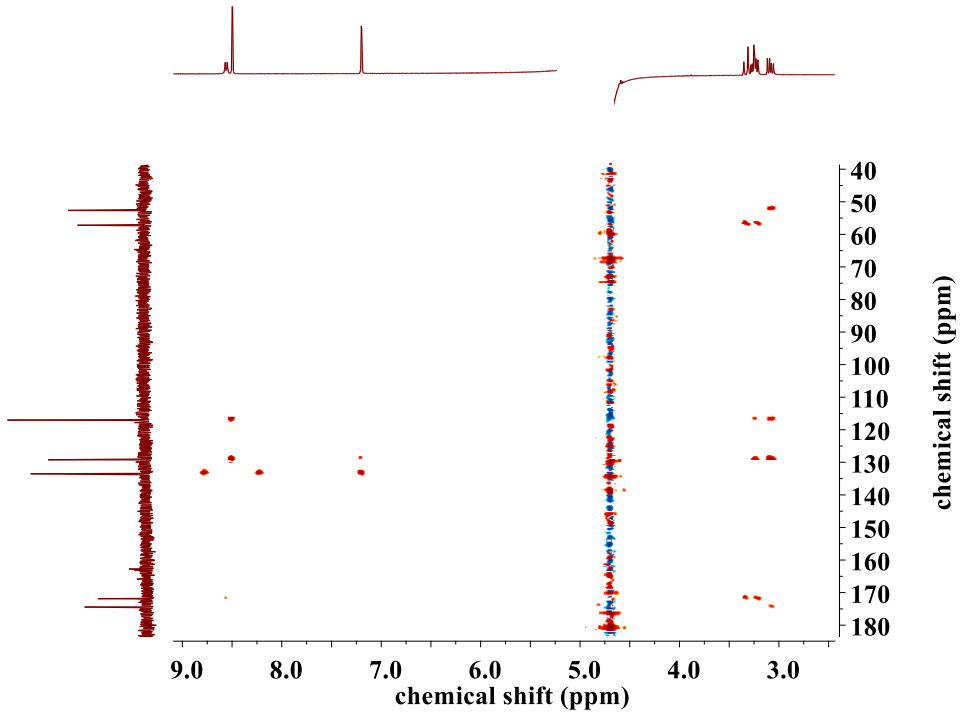

A.13. HMBC spectrum of nta3his ($\mathbf{L}^2$); in H_2O/D_2O 50%-50% solvent, pH 2.80, internal reference: acetonitrile (δ = 2.00 ppm).

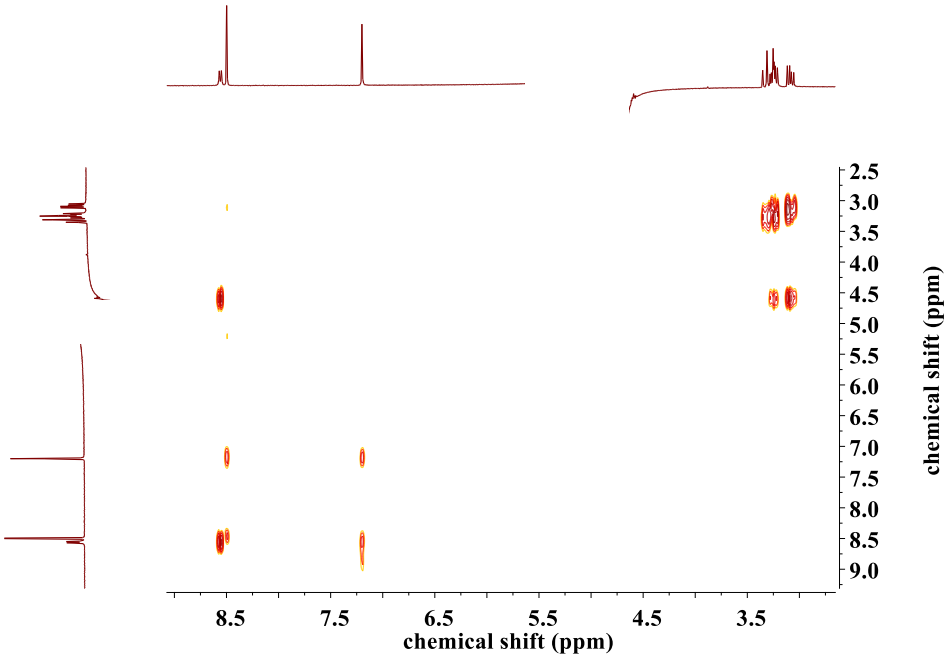

A.14. COSY spectrum of nta3his ($\mathbf{L}^2$); in H_2O/D_2O 50%-50% solvent, pH 2.80, internal reference: acetonitrile (δ = 2.00 ppm).

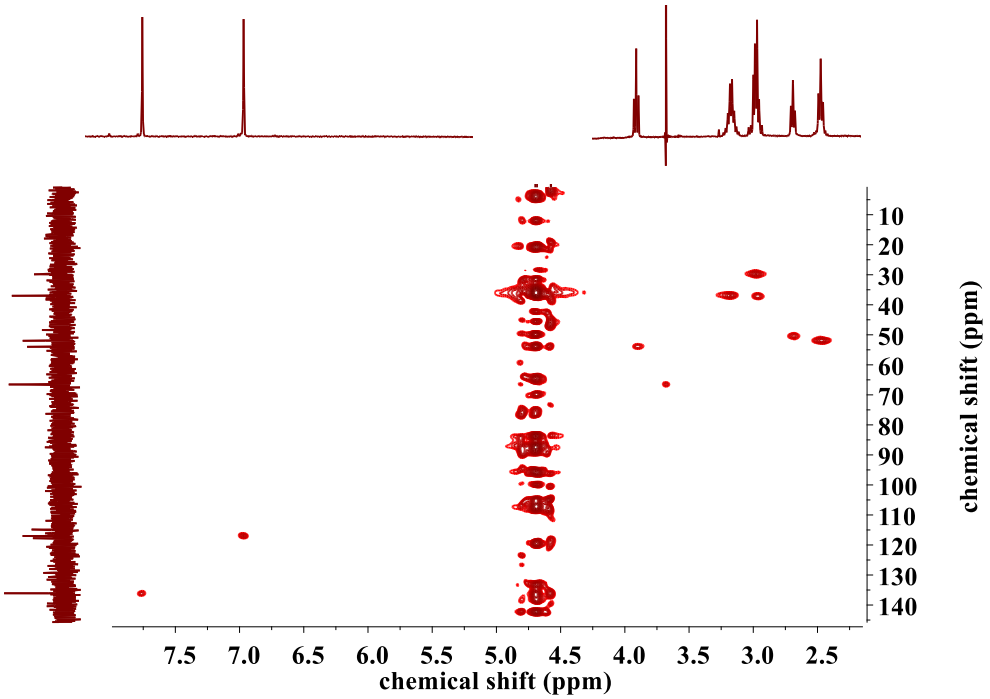

A.15. HMQC spectrum of tren2his ($\mathbf{L}^3$); in H_2O, pH 6.64, external reference: dioxane (δ = 3.70, 66.5 ppm).

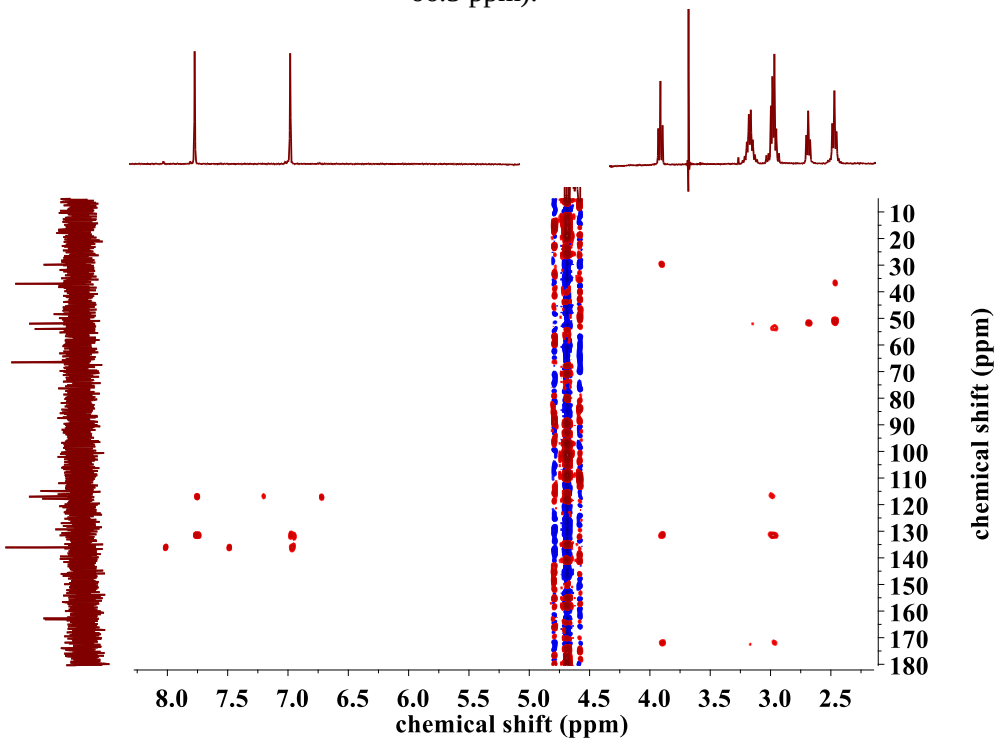

A.16. HMBC spectrum of tren2his ($\mathbf{L}^3$); in H_2O, pH 6.64, external reference: dioxane (δ = 3.70, 66.5 ppm).

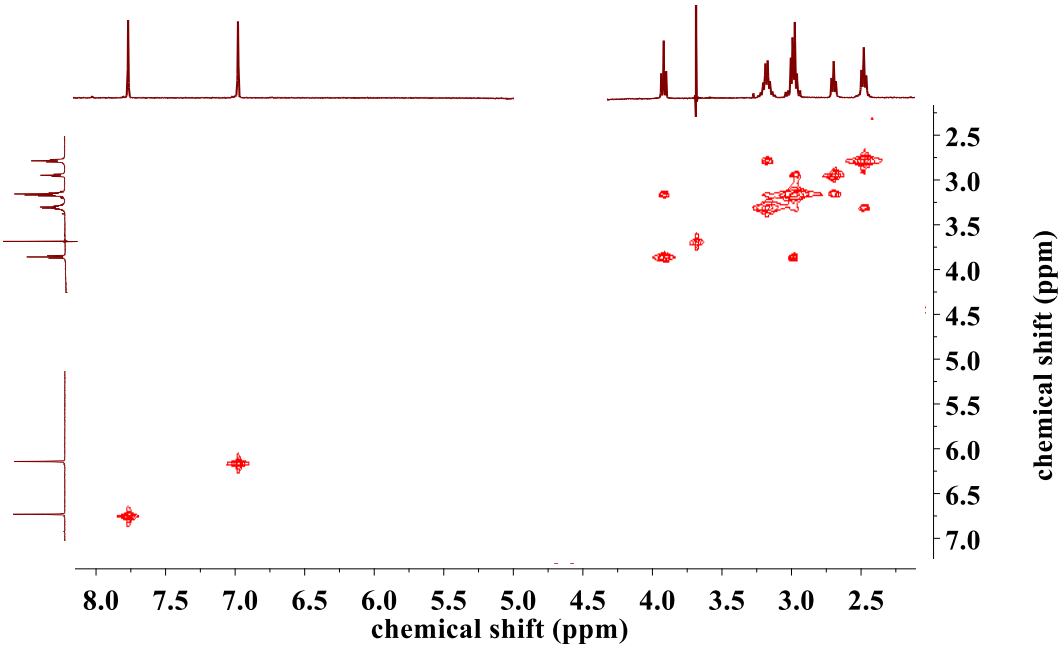

A.17. COSY spectrum of tren2his (**L**^{3}); in H_2O, pH 6.64, external reference: dioxane (δ = 3.70 ppm).

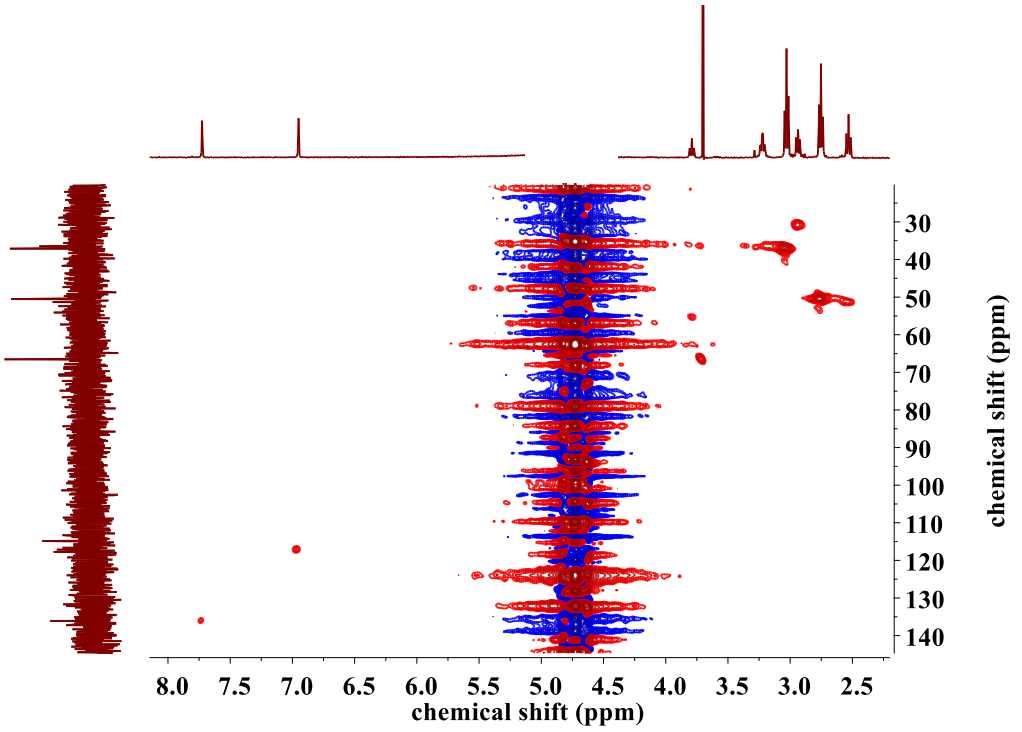

A.18. HMQC spectrum of tren1his (**L**^{4}); in H_2O, pH 7.12, external reference: dioxane (δ = 3.70, 66.5 ppm).

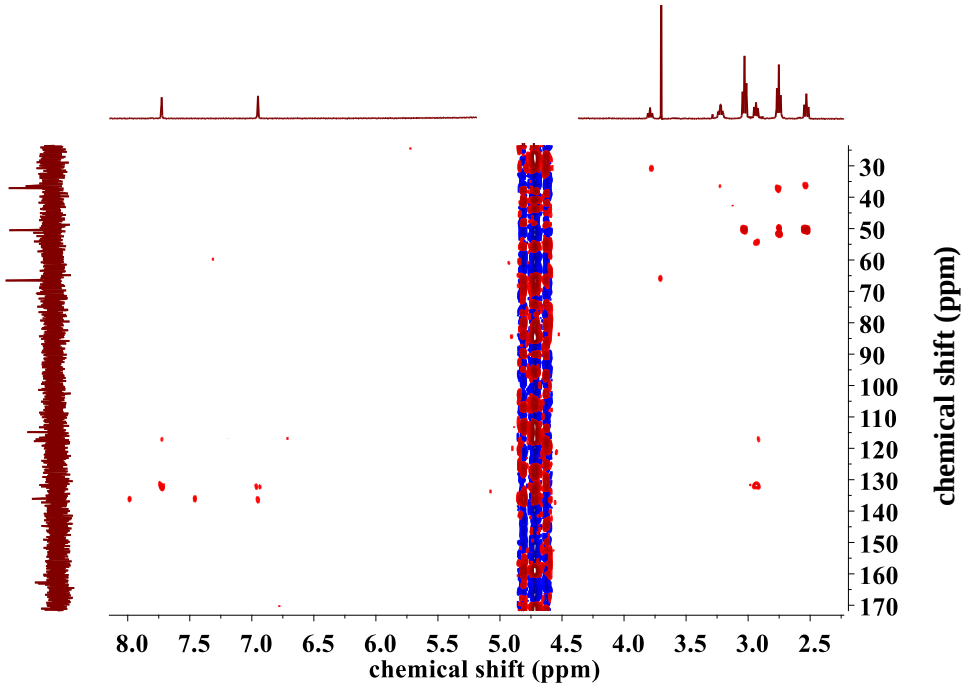

A.19. HMBC spectrum of tren1his (**L**^{4}); in H_2O, pH 7.12, external reference: dioxane (δ = 3.70, 66.5 ppm).

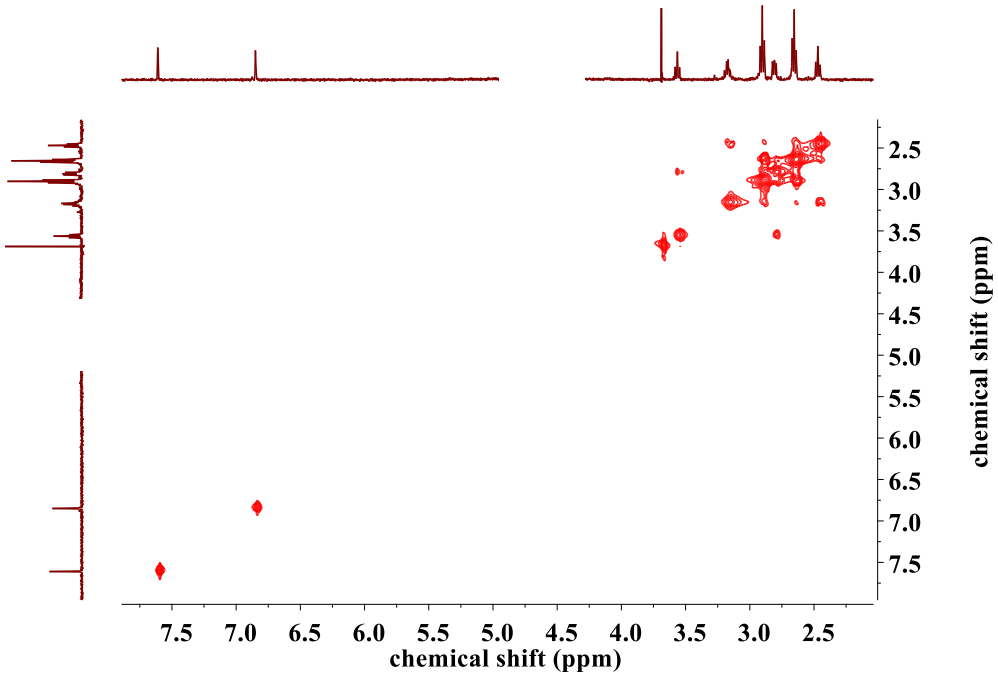

A.20. COSY spectrum of tren1his (**L**^{4}); in H_2O, pH 7.12, external reference: dioxane (δ = 3.70 ppm).

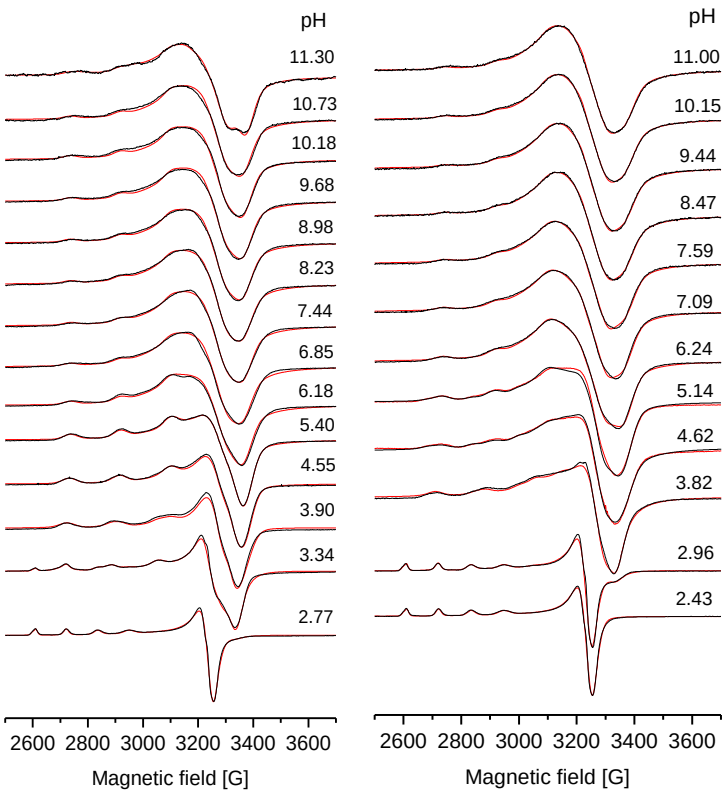

A.21. Measured (black) and calculated (red) EPR spectra in Cu(II)-tren3his 1:1 (left) and 3:2 (right) systems (77 K).

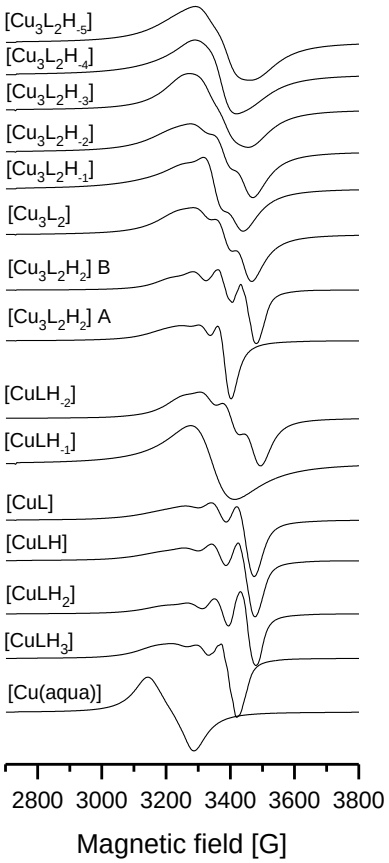

A.22. Individual EPR spectra of Cu(II)-tren3his 1:1 and 3:2 complexes at room temperature.

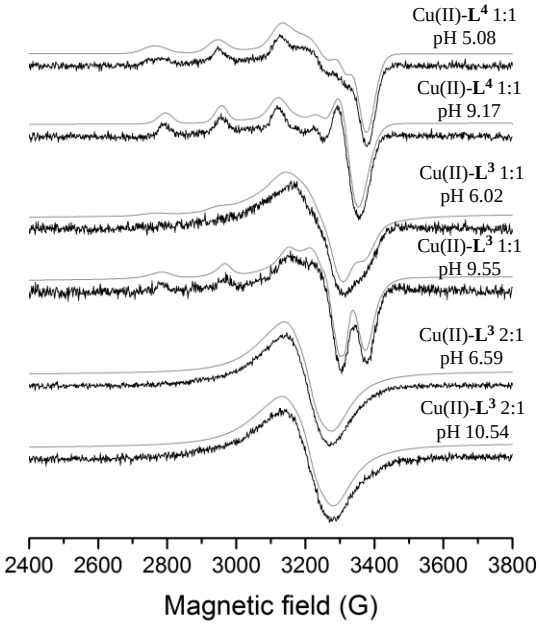

A.23. Anisotropic EPR spectra recorded at 77 K in Cu(II)-**L**^{3} and Cu(II)-**L**^{4} systems ([**L**^{4}]$_{tot}$ = [Cu(II)] = 0.0016 M in Cu(II)-**L**^{4} system, [**L**^{3}]$_{tot}$ = 0.0018 M, [Cu(II)]$_{tot}$ = 0.0018 M or 0.0036 M in Cu(II)-**L**^{3} systems, *I* = 0.1 M NaCl, gray: simulated, black: measured). Calculated parameters are listed in Table A.1.

Table A.1. Calculated EPR parameters of individual samples of Cu(II)-**L**^{3} and Cu(II)-**L**^{4} recorded at 77 K.

		Anisotropic parameters[a]							Calculated parameters[a]
		g_x	g_y	g_z	A_x /G	A_y /G	A_z /G	%	$g_{o,\,calc}$
Cu(II)-**L**^{4} 1:1	pH 5.08	2.036(1)	2.090(1)	2.212(1)	32(1)	25(3)	177.9(6)	100	2.113
Cu(II)-**L**^{4} 1:1	pH 9.17	2.053(2)	2.072(2)	2.210(1)	41(2)	46(5)	157(1)	100	2.112
Cu(II)-**L**^{3} 1:1	pH 6.02	2.036(1)	2.090(1)	2.212(1)	32(1)	25(3)	177.9(6)	15	2.113
		2.096(2)			153(5)[b]			85	
Cu(II)-**L**^{3} 1:1	pH 9.55	2.033(1)	2.063(1)	2.197(2)	4(3)	19(3)	178(2)	100	2.097
Cu(II)-**L**^{3} 2:1	pH 6.59	2.106(1)			128(5)[b]			100	
Cu(II)-**L**^{3} 2:1	pH 10.54	2.108(1)			137(5)[b]			100	

[a] $g_{o,calc} = (g_x+g_y+g_z)/3$, [b] full width at half maximum

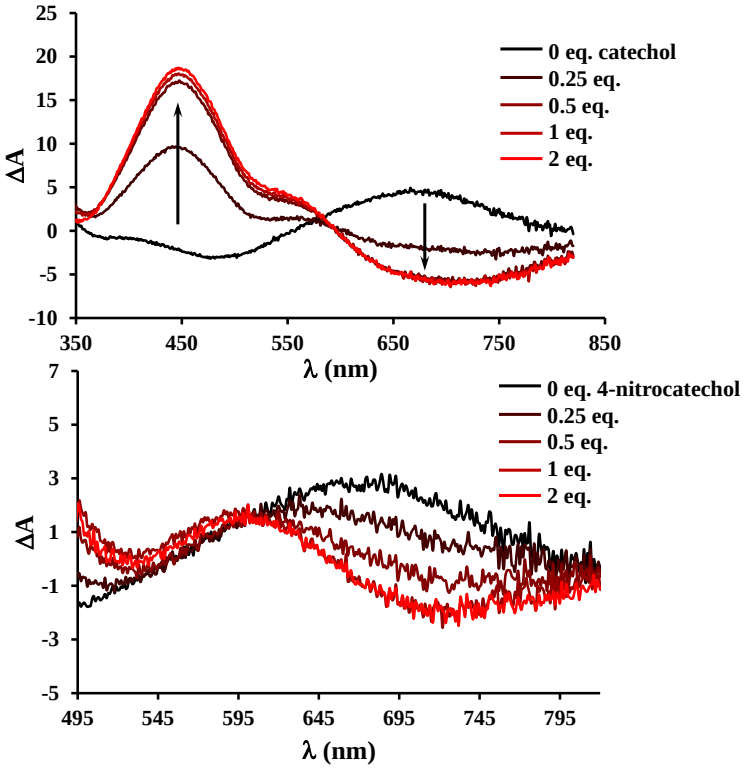

A.24. Catechol (up) and 4-nitrocatechol (down) dependent CD spectra of Cu(II)-**L**^{3} 2:1 system under anaerobic conditions ([complex]$_{tot}$ = 5.4×10^{-4} M and 3.5×10^{-4} M, respectively, in EtOH/H_2O 50/50, pH$_{corr}$ = 8.7).

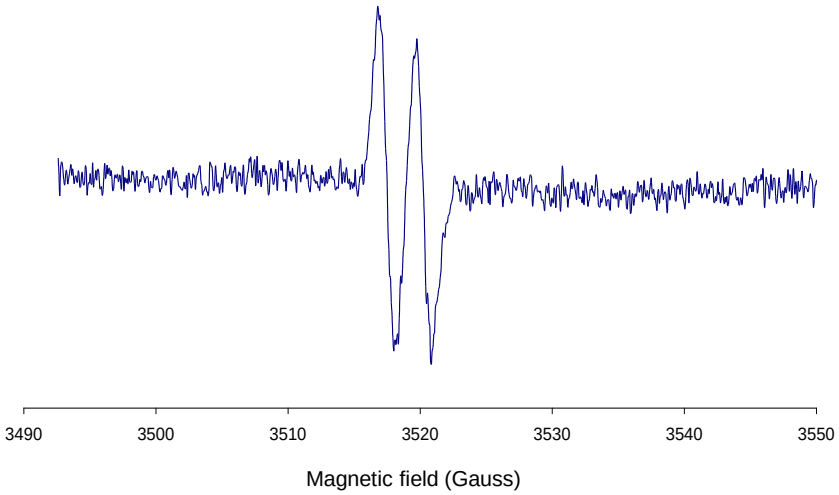

A.25. EPR spectrum of the semiquinone radical intermediate formed in the Cu(II)-**P3**-H_2DTBC-O_2 system ([H_2DTBC] = 2×10^{-3} M, [complex]$_{tot}$ = 4×10^{-4} M, pH = 8.9).

A. 26. Hydrolytic cleavage of phosphoesters in Cu(II)/Zn(II)-ligand systems

Copper(II) and zinc(II) complexes of $\mathbf{L^1}$ and $\mathbf{L^2}$ symmetrical tripodal ligands have been tested in hydrolytic functions, using the activated phosphoesters BNPP, NPP, HPNP and DNPEP. The experiments were carried out in aqueous, buffered solutions at T = 25 °C, adjusted to the pH corresponding to major metal-ligand species (see Table A.2). The formation of the colored products was followed spectrophotometrically at 400 nm. Observed pseudo-first order and pseudo-second order reaction rate constants ($k_{obs,corr}$, k') were calculated according to the initial reaction rates method, and given in Table 4.17. All values have been corrected with the rate constant of autohydrolysis ($k_{obs,corr} = k_{obs} - k_{auto}$).

Considering the obtained rate constants, and taking into account the magnitude of catalytic activity of efficient phosphoesterase mimics from the literature [92, 94, 154], the investigated metal-ligand systems demonstrate low-medium hydrolytic activities. Generally, it can be stated that copper(II) complexes exhibit somewhat higher hydrolytic activities; species formed at higher pH perform better than those in the acidic/neutral pH range. The relatively weak activities are most likely related to the high number of donor groups of the tripodal ligands, and thus the saturated coordination sphere around the metal ion, preventing the formation of the nucleophilic OH^- group and the coordination/activation of the substrate.

Since none of the studied systems presented significantly high or selective hydrolytic properties, further detailed kinetic investigation was not pursued.

Table A.2. Pseudo-first and -second rate constants ($k_{obs,corr}$, k') observed in the hydrolysis of activated phosphoesters in presence of different Cu(II)/Zn(II)-**L** systems.

system, pH	major complex and coordination	BNPP		NPP		DNPEP		HPNP	
		$k_{obs,corr}$ (s^{-1})	k' ($M^{-1}s^{-1}$)	$k_{obs,corr}$ (s^{-1})	k' ($M^{-1}s^{-1}$)	$k_{obs,corr}$ (s^{-1})	k' ($M^{-1}s^{-1}$)	$k_{obs,corr}$ (s^{-1})	k' ($M^{-1}s^{-1}$)
Cu(II)-**L**^{1} 1:1, pH 7.6	Cu**L**^{1} {$2NH_2$,$2N_{im}$+ax.NH_2}	2.64×10^{-8}	8.10×10^{-5}	2.15×10^{-7}	6.97×10^{-4}	9.03×10^{-7}	2.93×10^{-3}	8.29×10^{-7}	2.68×10^{-3}
Cu(II)-**L**^{1} 1:1, pH 9.2	CuH_{-1}**L**^{1} {$2NH_2$,N_{im},N^-}	2.81×10^{-7}	8.65×10^{-4}	-	-	4.62×10^{-7}	1.35×10^{-3}	3.31×10^{-6}	1.07×10^{-2}
Cu(II)-**L**^{1} 1:1, pH 10.2	CuH_{-1}**L**^{1}/CuH_{-2}**L**^{1} {N_{im},N^-,N_{tert},N^-}	2.01×10^{-7}	6.32×10^{-4}	-	-	3.83×10^{-7}	1.12×10^{-3}	-	-
Zn(II)-**L**^{1} 1:1, pH 7.2	Zn**L**^{1} {$2NH_2$,$2N_{im}$+ax.NH_2}	3.87×10^{-9}	1.18×10^{-5}	1.26×10^{-7}	3.86×10^{-4}	1.23×10^{-7}	3.77×10^{-4}	2.53×10^{-7}	8.52×10^{-4}
Zn(II)-**L**^{1} 1:1, pH 8.2	ZnH_{-1}**L**^{1} {$2NH_2$,$2N_{im}$,OH^-}	-	-	1.95×10^{-7}	6.00×10^{-4}	1.74×10^{-7}	5.34×10^{-4}	6.37×10^{-7}	2.15×10^{-3}
Zn(II)-**L**^{1} 1:1, pH 10.2	Zn_3H_{-4}**L**$^{1}_2$ {$2NH_2$,$2N_{im}$+μ-N_{im}^-}	-	-	-	-	9.69×10^{-8}	3.25×10^{-4}	-	-
Cu(II)-**L**^{2} 1:1, pH 5.0	Cu**H**^{2}**L**^{2} {N_{im},N^-,N_{tert},O}	2.06×10^{-8}	1.92×10^{-4}	-	-	-	-	-	-
Cu(II)-**L**^{2} 1:1, pH 7.0	Cu**L**^{2} {N_{im},N^-,N_{tert},O}	1.75×10^{-8}	1.62×10^{-4}	-	-	-	-	-	-
Cu(II)-**L**^{2} 1:1, pH 9.0	CuH_{-1}**L**^{2} {N_{im},N^-,N_{tert},O}	9.46×10^{-8}	8.79×10^{-4}	6.57×10^{-7}	6.57×10^{-3}	-	-	-	-
Cu(II)-**L**^{2} 2:1, pH 7.0	Cu_2H_{-2}**L**^{2} {N_{im},N^-,N_{tert},O;N^-,$2N_{im}$}	1.59×10^{-7}	1.67×10^{-3}	-	-	-	-	-	-
Zn(II)-**L**^{2} 1:1, pH 9.0	ZnH_{-1}**L**^{2} {N_{im},N^-,N_{tert},O}	1.46×10^{-7}	1.53×10^{-3}	3.32×10^{-7}	3.49×10^{-3}	-	-	-	-

Abstracts

One of the most important directions of modern bioinorganic research is the development of artificial enzymes. One pathway of enzyme modeling strategy is the study of amino acid sequences present in the active centers of metalloenzymes. Linear peptides, however, have their limitations in reconstituting the active centers of metalloenzymes, since they do not possess the well-defined three dimensional structure, therefore their structure is vulnerable towards amide nitrogen coordination/hydrolysis. Improvement of metal binding capabilities of linear peptides can be obtained by *e.g.* their functionalization with tripodal ligands. Tripodal compounds may provide a rigid, less flexible platform for the coordinating amino acid side chains, creating pre-organized metal binding sites.

In my thesis, I present synthesis and characterization of histidine containing tripodal peptide ligands and their complex formation in presence of copper(II) and zinc(II). Solution equilibrium was studied with pH potentiometric measurements, and several spectroscopic methods were used for structural characterization (UV-Vis, CD, ESR, NMR and MS methods). Beside thermodynamic and structural characterization, enzyme mimicking catalytical properties of the complexes have also been investigated (catechol oxidation, superoxide dismutation).

Our results demonstrated that tripodal peptide ligands are capable of enhancing the stability of metal-peptide complexes, and they may provide convenient structures to efficiently mimic the catalytic functions of enzymes. With thorough and systematical solution equilibrium and spectroscopic studies, we uncovered the driving forces of metal coordination, and established the impact of the tripodal structure in stability, structure and catalytic properties of the forming complexes. Our findings confirm the beneficial effect of tripodal scaffolds in peptide-type ligand-metal complexes, and emphasize the possibilities lying within tripodal peptides in the field of enzyme mimicking.

Keywords: tripodal ligands, peptide complexes, copper(II), zinc(II), enzyme mimicking

De nos jours, un des objectifs importants de la recherche bioinorganique moderne est le développement d'enzymes artificielles. L'étude séquentielle des acides aminés présents dans le centre actif des métalloenzymes peut présenter une voie possible de la stratégie de modélisation enzymatique. Cependant, les peptides linéaires ont leurs limites lors de la reconstitution des centres actifs des métalloenzymes : ils ne possèdent pas la structure tridimensionnelle bien définie, par conséquent leur structure est vulnérable vis-à-vis de la coordination ou de l'hydrolyse des azotes amidiques. La capacité de coordination des métaux par des peptides linéaires peut être améliorée, par exemple, en les attachant à une plateforme tripodale. Les composés tripodaux peuvent assurer une organisation structurale rigide ou moins flexible pour des chaînes latérales des acides aminés, créant ainsi des sites de coordination pré-organisés pour les métaux.

Dans cette thèse, la synthèse et la caractérisation des ligands peptidiques tripodaux contenant de l'histidine et la formation des complexes en présence de cuivre(II) et de zinc(II) sont présentées. Les propriétés acido-basiques ont été étudiées par potentiométrie et différentes techniques spectroscopiques ont été utilisées pour la caractérisation structurale (UV-Vis, CD, ESR, RMN et MS). Outre que la caractérisation thermodynamique et structurale, des propriétés catalytiques des complexes en réaction enzymatiques (oxydation du catéchol, dismutation du superoxyde) ont également été étudiées.

Nos résultats ont démontré que les ligands peptidiques tripodaux sont capables d'améliorer la stabilité des complexes métalliques et qu'ils peuvent fournir des structures adéquates pour mimer efficacement les fonctions catalytiques des enzymes. Grâce aux études approfondies et systématiques des propriétés acido-basiques et spectroscopiques, nous avons mis en évidence les forces motrices de la coordination des métaux et établi l'impact de la structure tripodale sur la stabilité, la structure et les propriétés catalytiques des complexes formés. Nos résultats confirment l'effet bénéfique des plateformes tripodales durant la complexation des métaux, et soulignent les possibilités qui s'offrent aux peptides tripodaux dans le domaine de la biomimétisme.

Mots-clés: ligands tripodaux, complexes peptidiques, cuivre(II), zinc(II), mime enzymatique